ON-LINE MEASUREMENT OF SIZE DISTRIBUTION AND VOLUMETRIC CONCENTRATION OF PNEUMATICALLY CONVEYED SOLIDS USING DIGITAL IMAGING TECHNIQUES

A Thesis Submitted to The University of Kent
for the Degree of Doctor of Philosophy
in Electronic Engineering

By

Robert M. Carter BEng

April 2005

On-Line Measurement of Size Distribution and Volumetric Concentration of Pneumatically Conveyed Solids Using Digital Imaging Techniques

Robert M. Carter, PhD 2005

Abstract

This thesis describes the design, implementation and experimental evaluation of a digital imaging based system for the on-line, non-intrusive, measurement of size distribution and volumetric concentration of solids, in a dilute pneumatic suspension. Inferential establishment of mass flow rate, derived from the combination of solids concentration and electrostatic cross-correlated velocity information, is also covered.

A review of methodologies and technologies for the optical measurement of the parameters in question is presented, together with their advantages and shortcomings. Both the fundamental validity and industrial applicability of each technique are discussed. Based upon this review an imaging arrangement based upon the novel application of perpendicular laser sheet illumination is proposed. The strategy is intended to avoid depth of field issues experienced with diffuse illumination and circumvent particle movement issues experienced in conventional laser sheet work. Novel processing algorithms are developed and the feasibility of particle shape quantification is investigated. A static interrogation system with front illumination is used to allow the basic limits of measurement to be established. Subsequently, a full on-line prototype instrument is produced and practical concerns are discussed and addressed. Throughout the work emphasis is placed on practical methodologies and cost-effective implementations that would be applicable in an industrial environment.

The results of extensive experimental evaluation of the system, based on laboratory testing and industrial trials using a pulverised coal/biomass mixture, are presented and discussed. Comparisons between off-line and on-line results are presented and reference data, recorded with an industry standard laser diffraction instrument, are considered. The performance of the system is discussed and suggestions given for the future development of the methodology.

Acknowledgements

The author wishes to express grateful thanks to the following:

Professor Y. Yan — My supervisor, whose encouragement and experience in the field of particulate flow metering drove the project to progress at all times.

Mr A. W. Dodson — Research technician at the University of Greenwich, for his excellent advice and technical support throughout the project.

Staff at the Wolfson Centre for Bulk Solids Handling Technology, in particular; Dr T. Deng, Dr I. Bridle and Dr R. Farnish for their help in providing laser diffraction test results.

RWE npower, in particular, staff and technicians at the Combustion Test Facility in Didcot for their help during industrial testing.

A number of academic and support staff at the University of Greenwich with particular thanks to Mr I. C. Cakebread and Professor A. R. Read.

Staff at the University of Kent where the project was completed.

The British Coal Utilisation Research Association for providing funding during part of the project.

Mitsui Babcock – industrial collaborators in relation to the BCURA grant, in particular to Dr S. D. Cameron.

My fellow researchers at both the University of Greenwich and the University of Kent, particularly; Dr H. C. Bheemul, Dr I. R. Barratt, Dr J. Shao, Dr G. Lu and Dr L. Xu.

This thesis is dedicated to my parents, Bobbie and Tom, for their encouragement, help and support throughout the project also to my late Grandfather, Jack Whitehead and to Paddy.

Contents

Chapter 1

Requirements for Particle Size and Mass Flow Rate Measurement of Pneumatically Conveyed Solids

1.1 Introduction

Granular or particulate materials are used in many industrial processes. The transportation of such materials within industrial plant is an important technical requirement and methods suitable for such transportation vary widely, encompassing mechanical, hydraulic and pneumatic techniques. Pneumatic conveyance is an important methodology used widely in many industries from foodstuffs preparation to power generation and the steel industry. Such conveyance consists typically of two phase solids/gas suspensions commonly employing air as the gaseous transport medium and represents an efficient, high performance material handling technology. In order for pneumatic conveyors to achieve their full potential, in terms of conveying efficiency and the prevention of material degradation, it is necessary to measure the parameters of the flow. Such information may then be used for purposes ranging from off-line quality control sampling to, more importantly, on-line process optimisation and control.

Mass flow rate determination in particulate flows has been a subject of interest for the Advanced Instrumentation and Control Research Group at the University of Greenwich (headed by Professor Y. Yan) for some time. Previous work has concentrated on electrostatic and radiometric methodologies and the author joined the group in September 2000 with the aim of extending the group's portfolio of flow sensor types with digital imaging (imaging had previously been applied to flame imaging but not flows). For the first two and a half years of the work only part-time funding was available but in 2003 a grant was secured from the British Coal Utilization Research Association (BCURA) for full time study. This source of funding may help to explain the slight bias towards pulverized coal metering that may be observed in the work presented here. In 2004 the group moved to the University of Kent where the project was completed.

1.2 The Importance of Particle Size and Mass Flow Rate

Two of the most important parameters of pneumatic flows are the size, or size distribution, of the particles within the duct and the mass flow rate of material – a measure of the quantity that is flowing through the system. In order that the importance of these parameters can be better understood an example of an industrial pneumatic conveyor is required. Figure 1.1 shows a typical feeding arrangement for pulverised coal or fuel (PF) as used in the power generation industry and highlights desirable locations for sensor systems as letters A through D.

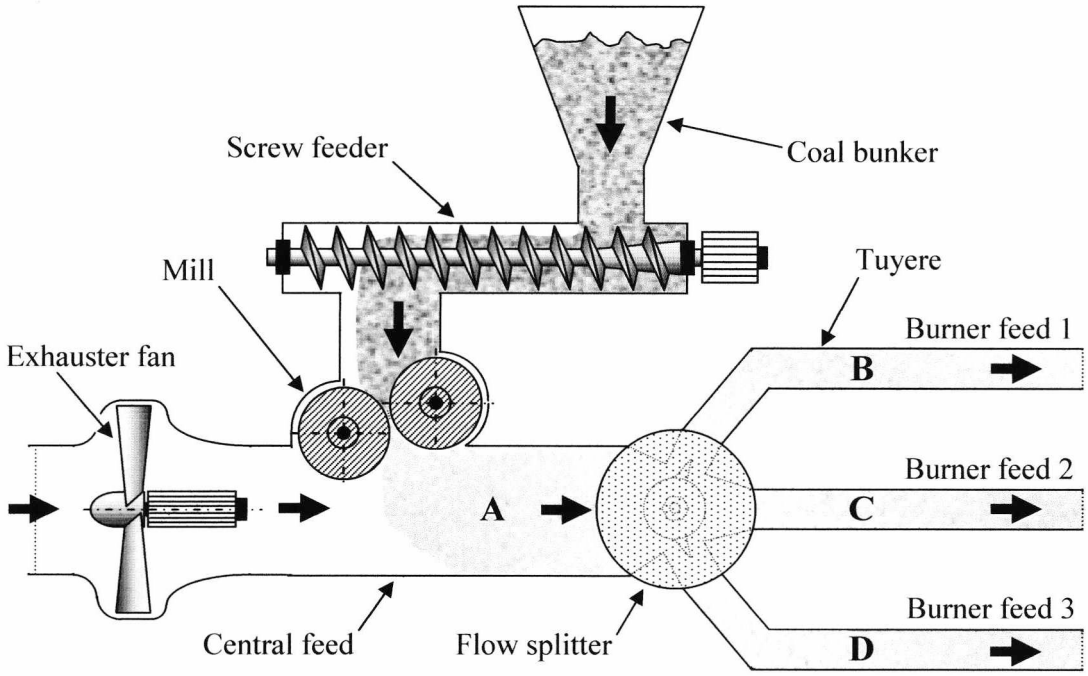

Figure 1.1 Schematic diagram of a PF feed system for power generation

Hot furnace exhaust air, mixed with cool fresh air, is drawn into the conveying system, from the furnace, through the use of a powerful exhauster fan. Lumps of coal are drawn from storage bunkers using an adjustable screw feeder and ground to a fine powder (particles being around 40μm in size typically) in the mill. The air stream and pulverised fuel are then combined. At this stage, on the central feed duct, it would be desirable to install a particle size and mass flow rate measuring instrument (location A in figure 1.1) the inclusion of which would allow optimisation of fan speed, feeder rate and mill power. It is accepted that the optimisation of coal particle size can lead to a reduction in NO_x and

CO_2 emissions and carbon in ash levels (DTI 2001, Advanced Power Generation Technology Forum 2004). Next the flow is split using a system of valves into a series of smaller ducts known as Tuyeres that each feed a burner. The inclusion of mass flow rate meters in the tuyeres (locations B, C and D) would allow the flow splitting valves to be adjusted in such a way as to allow accurate division of the fuel/air mixture. Balanced material feed to the various burners in a furnace can lead to reduced flame 'blow outs' and the reduction of both NO_x formation and slagging (Yan 1996).

The usefulness of particle size and mass flow rate measurement, on an on-line basis, is not limited to the power generation industry (see chapter 4 section 4.5 and item 16 in the dissemination section – p289). In general the measurement of these parameters allows closed loop control of industrial processes in order that these processes can be optimised. This will lead to improvements in product quality, greater process efficiency and balanced, reliable control over plant operation.

1.3 Major Technical Challenges

The main technical difficulties involved in producing an instrumentation system to fulfil the requirements suggested above, or that are likely to be faced by such a system, will now be introduced briefly. In-depth analysis of these difficulties and the identification of suitable solutions will, where appropriate, be dealt with in later chapters.

1.3.1 On-Line Operation

It is clear from the introduction to pneumatic conveyance presented here that an instrumentation system for the measurement of particle size must operate on an on-line continuous basis if its usefulness is to be maximised. Whilst it is possible to take samples of material from the flow and analyse the size of particles by off-line means (coal particle size in power generation is often established through sieving) it is much more desirable to have an on-line indication of this parameter. Only when on-line data are available can a process be optimised in real-time. Real-time optimisation will lead to the greatest benefits in process efficiency improvement. Mass flow rate measurement must always, by the very nature of this parameter be acquired on-line.

On-line operation presents a number of challenges when compared to off-line work. Both the environment within the duct and nature of the flow itself will affect the operation of the instrument. Similarly the instrument, if poorly designed, may affect the flow, causing perturbations in the process and this effect must be minimised.

1.3.2 Non-Intrusive Measurement

In general it is the aim of any instrumentation engineer to avoid changing the parameter that a new instrumentation system is trying to measure. For example; attempting to measure the temperature of a tiny fragment of material using a large, cold mercury thermometer will yield results that are far from accurate. On this basis alone it can be argued that an instrument designed to interrogate pneumatic flows must not intrude into the duct as this will cause a change in effective area and other aerodynamic properties leading to modified flow conditions.

Another, equally important, consideration is that of wear. In a pneumatic conveyor a vast number of particles are moving at very high velocities – in the power generation example cited previously particle velocities vary typically between 10 and 40m/s (Yan 2001). Under these conditions any instrument that protrudes into the flow will find itself under conditions similar to those created for sand blasting operations – needless to say even the most robust of designs would not last long. In order that reliable operation over a useful time period is achieved, non-intrusive operation is a must.

1.3.3 Dilute Phase Conveying

The range of industries in which pneumatic conveying is employed is large. Within this range there is scope for a tremendous range of differing conditions to prevail within flow ducts. One of the most important parameters is phase density. Phase density is defined as the ratio of solids to conveying air mass flow rates – in general it is a measure of the amount of material in the duct, though this should not be confused with solids concentration (more on this in section 1.4.3). In industry phase densities of greater than 40 are known as 'dense phase' and below 20 as 'dilute phase'. It is dilute phase conveyance that has traditionally presented the greatest challenge to instrumentation

systems. Though in general having a phase density of less than 20 dilute phase systems typically vary between one and 20. This yields volumetric solids concentrations in the region of 0.3 to 6% by volume. In the example of pulverised fuel conveyance concentrations lie, typically, toward the low end of this range (Yan 2002).

1.3.4 Irregular Velocity Profiles/Inhomogeneous Flow

Particles flowing through a duct do not always maintain perfectly even, or 'homogeneous' distribution of concentration and velocity. A pneumatic conveyor is a complex system containing bends, varying duct orientation, imperfections in the duct walls, misaligned joints and other phenomena. These factors act together and may cause the flow to exhibit inhomogeneous distribution. Common forms of inhomogeneous flow are stratification and roping. Stratification represents a situation in which material is drawn by gravity to the bottom of the duct, there being greater concentration of material at the bottom that at the top. In this situation the velocity of particles will be higher in the areas of low concentration and vice versa. Roping is a particularly difficult phenomenon in which the flow forms a tight clump or bundle causing a peak in both velocity and concentration at this location (there being, effectively, no material elsewhere in the duct). In power generation, roping is widely suspected as hampering efforts to reduce NO_x emissions and carbon in fly ash levels (Yilmaz and Levy 1998).

The ability to identify inhomogeneous flow regimes would be useful in an instrumentation system. This would allow not only for these phenomena to be studied but also for appropriate corrective action to be taken in industrial situations. Notwithstanding possible detection of these regimes it is clear that an instrument should be unaffected by changes in solids distribution in respect to the measurement of fundamental flow parameters such as particle size and mass flow rate.

1.3.5 Particle Deposition

One important factor that can affect an instrumentation system is material deposition. Due to the physical characteristics of the material in the duct and also static electricity that may build up there, it is not unknown for a small percentage of particles to deposit

themselves upon the duct walls, forming a coating. A successful instrumentation system must either be insensitive to this coating of material or be provided with some means of dispersing it if reliable operation is to be assured.

1.3.6 Cost-Effectiveness/Rugged Technology

It has been made clear in preceding discussions that an instrumentation system for measuring particle size and mass flow rate is as much use in industry as under laboratory conditions. In the past various measurement techniques have been suggested (see section 1.5) and these, whilst performing well under controlled experimental conditions, are not always suitable for practical application due to a lack of robustness, the requirement for complex and frequent re-calibration or simply prohibitive cost, as well as a number of other factors. Clearly future systems should address these factors and aim to produce an instrumentation system that is of use to industry. This rules-out the use of exotic scientific components on the basis of cost and efforts should be made to ensure the physical and conceptual robustness of the system.

1.4 Key Flow Parameters

1.4.1 Particle Size

The definition of particle size is not as straightforward as it might at first appear. The size of a given particle is generally expressed using a single number – for example, a particle may be stated to be 1mm in size. It is generally understood that this single number usually refers to the particle's diameter but, unless the particle is a perfect sphere there is no clear and unambiguous diameter to be measured. Any diameter quantification for arbitrarily shaped particles must therefore represent an 'equivalent diameter' based upon an accepted definition (this issue is discussed in Appendix A).

Another issue, of more practical relevance to particle size measurement, is the range of sizes likely to be encountered. In pneumatic conveyance this ranges from a few μm in the case of, for example, laser printer toner, to tens of millimetres in the food or mineral

handling industries. An intrinsically wide turn-down ratio (the ratio between the largest and smallest sizes that can be measured) is therefore an important requirement for any particle size analyser.

1.4.2 Particle Shape

It has already been suggested that the shape of particles will have an effect upon size measurement. This, however, is not the only consideration as particle shape is important in its own right. It is possible for a number of particles of the same equivalent diameter to be of varying shapes. Particles may be elongated or rounded, smooth or rough and these variations may be of importance in respect to process quality control. Such shape variation may even be critical in ensuring consistent properties of materials in the chemical processing industry where the surface area of particles involved in reactions is of great importance. It is desirable, therefore, to provide some indication of particle shape as well as size. If particle size definition is difficult, involving as it does such a simple physical characteristic, then it can be readily appreciated that the numerical definition of shape, a fundamentally subjective concept, is even more complex. The investigation of shape measurement would justify an entire programme of work in its own right and since the present work concentrates on size and concentration measurement, shape coverage will be limited here. Nevertheless a brief discussion on shape measurement is presented in chapter 3 as no particle analysis work can be complete without some coverage of this important issue.

1.4.3 Mass Flow Rate and Solids Concentration

The fact that the amount of material flowing through the duct is of importance has already been introduced. In a real situation a more accurate definition of the amount of material present than a simple statement of dense or dilute phase flow is required and this is provided by mass flow rate and/or solids concentration. Mass flow rate is a measure of the quantity of material flowing with respect to time (expressed in kg/hr or kg/s) and is an important parameter in process control. Solids concentration (or solids loading) is defined as the percentage of the duct's volume that is occupied by solids (or, more accurately, the ratio of solids volume to total duct volume, expressed as a percentage).

In industry it is mass flow rate that is of primarily of interest and much research work has been undertaken in respect to the on-line measurement of this quantity. Many of the possible techniques used in such work have been reviewed in the past in articles such as those written by Yan (1996) and Green and Thorne (1996). In much of this work it has been found necessary to establish mass flow rate inferentially through the mathematical combination of solids concentration, material velocity and absolute material density (a constant). Thus it is solids concentration and velocity that are often measured in order to establish mass flow rate. Particle velocity measurement is well established but absolute solids concentration remains a challenging parameter. An imaging based system is capable of measuring solids concentration and is therefore suitable for inferential mass flow rate measurement where velocity information is available (See later chapters). From a practical viewpoint, during experimental trials, it is easier to find a reference mass flow rate value than a solids concentration value (e.g. by measuring the amount of material that has flowed through the duct during a certain time period). The inferential mass flow calculations may then be used in reverse to establish the accuracy of solids concentration measurement (see chapter 5).

1.5 Techniques for Particle Flow Sensing

The study of particulate flow metering is of wide interest in both scientific and industrial settings. Much of the work in this field concentrates on measuring absolute mass flow rate. A great number of sensing techniques and topologies have been employed in the past, including electrostatic, optical and acoustic attenuation and scattering, capacitance, radiometric, microwave and magnetic resonance. These and others have been extensively reviewed elsewhere (Yan 1996, Green and Thorne 1998) and will not be discussed further here. Some recent work has shown great promise. A good example of this lies in the work of Barratt et al. (2001) who describe a gamma ray based system for the measurement of solids loading that also offers sensing of inhomogeneous flow conditions. Another example is that of Zhang et al. (2004) who discuss an electrostatic system. Despite the presence of this and similar work it is generally accepted that such systems are susceptible to time varying dependency factors (such as temperature and material moisture content) resulting in a mass flow measurement that is more relative than

absolute (Barratt 2000). This has led to increased interest in finding methods for establishing absolute solids concentration, rather than mass flow rate – this quantity can be combined with readily available velocity information to yield true absolute mass flow rate data (see chapter 5). Measuring solids concentration is challenging but may lead to increased reliability of measurement when compared with attempts to establish mass flow rate directly (Yan 1996). This increased reliability stems from the possibility offered by solids concentration measurement systems, such as imaging, to operate in a direct sense rather than inferentially, producing a result that is virtually free of calibration requirements – a comprehensive review of this application of imaging is presented in chapter 2.

The size of particles is also of interest in both process optimisation and scientific study. In the power generation industry the necessity for on-line size measurement is generally recognised (Laux et al. 2001). The study of on-line particle size measurement is not new and in the past many techniques have been suggested ranging from the analysis of particle impact force on an mechanical target (Nakajema 1967) through electro-optical techniques (e.g. Ricci et al. 1969) to novel concepts such as ultrasonic extinction (Hess et al. 2003) and flow turbulence analysis (Beck et al. 1973). More recently electrostatic methods have shown great promise – an example of this methodology that has been developed commercially is presented by Laux et al. (1999) though a more interesting study has been presented by Zhang and Yan (2003). In general laser diffraction based methods have shown the greatest popularity and the various methods employed have been reviewed extensively in the past (e.g. Black et al. 1996). Some instruments have been developed commercially (the Malvern 'Insitec' for instance) though these are usually intrusive to some degree. The benefits of direct, rather than inferential, measurement of particle size through image analysis have been recognised for a number of years and despite early work in this field (e.g. Ow and Crane 1980) it is only recently that computers and imaging equipment have become suited to this purpose. A good, recent, example of on-line imaging based particle sizing has been presented by Nishino et al. (2000). Unfortunately such studies often employ complex optics and processing that would be impractical and/or prohibitively expensive in industry and so, despite wide acceptance of the benefits of such a system, a practical industrial imaging based particle sizer remains elusive – imaging based sizing is reviewed in more depth in chapter 2.

1.6 Proposed Research Programme

The proposed research consists of the design and implementation of both the software and hardware aspects of an on-line imaging based particle interrogation system. Dedicated software is to be developed using object orientated techniques and visual C++. Novel algorithms are to be created that enable high speed processing for real time operation using readily available and cost-effective processing hardware – one of the main driving forces behind the research is to establish the industrial applicability of such an imaging based instrument and so general cost effectiveness and robustness are preferred for both hardware and software. Sensing head design should concentrate on simple interrogation geometry for non-intrusive operation and ruggedness in use (such geometry will also ensure cost-effectiveness, minimising the use of expensive custom optics etc).

A small pneumatic conveying test rig is to be constructed in the laboratory and an extensive experimental programme is to be conducted using this apparatus. In addition the sensing hardware must be compatible with available industrial test facilities and some testing is to be performed under industrial conditions. Comparative results are to be generated using accepted off-line instrumentation.

In general past work in the field of particle imaging has consisted of complex scientific systems that are largely unsuited to industrial application (see chapter 2). In view of this, the limits of operation of a simple sensing setup using modern, low-cost components, have not been established and at each stage of the research programme such limits should be investigated.

The main parameters to be measured will be particle size and solids concentration (in that order of importance) although other parameters, such as shape, will be investigated where applicable and convenient. Of some interest are inhomogeneous flow regimes, roping in particular, and investigations will be undertaken into the detection of such regimes through the study of spatial variances in the measured solids concentration data. Finally a reference velocity measurement will be combined with solids concentration results so that instantaneous mass flow rate can be found.

1.7 Research Programme Objectives

In the light of the general scope of the research programme, as described above, the following objectives were defined:

- To review the state of the art in the field and identify research objectives.
- To develop novel algorithms for the analysis of particle images.
- To establish the limits of measurement for a basic particle imaging system (using the new algorithms) and compare results achieved with those from accepted off-line instrumentation.
- To create an optimised on-line imaging arrangement and develop this into a practical sensor.
- To assess the performance of the on-line sensor through an extensive experimental programme.
- To investigate the detection of roping flow regimes using the on-line sensor.
- To test the system under real industrial conditions in the field of power generation.

1.8 Thesis Outline

The natural progression of the research programme has lead to a division of the thesis into seven chapters. These are as follows:

Chapter 1 introduces the importance of particle size and concentration measurement, covers the technical requirements of such measurement and outlines the proposed research programme and objectives.

Chapter 2 reviews optical instrumentation for particle flow sensing with emphasis on imaging techniques and discusses the problem of representative material sampling.

Chapter 3 discuses the technical difficulties of analysing particles with imaging techniques and presents novel processing algorithms that have been developed to deal with these problems. In the interests of simplicity the example of an off-line static system

is used here and the underlying accuracy of measurement is assessed. In this way the principles and limits of performance are investigated.

Chapter 4 presents a practical off-line arrangement and the design of the software is covered. Optical considerations are discussed and new algorithms required in order to deal with real-world difficulties are introduced. In short, the requirements and problems associated with transitioning from the theoretical to the real are covered.

Chapter 5 covers the transition from static to on-line operation and any problems and difficulties are presented along with the necessary solutions. Practical sensor and flow rig design is discussed and inhomogeneous flow detection and inferential mass flow rate measurement are introduced.

Chapter 6 provides the results from extensive laboratory evaluation and these results are discussed in some depth. In addition the results from initial industrial trials are presented and discussed.

Chapter 7 draws conclusions from the work that has been presented and provides suggestions for the continuation of the work in the future.

Chapter 2

Review of Optical and Imaging Techniques for On-Line Measurement of Particle Size and Solids Concentration

2.1 Introduction

In chapter one it was suggested that a great range of instrumentation types has been applied to flow measurement. In view of this it would be unrealistic to review all of these methodologies and so this review will concentrate on techniques that are of relevance to the present research. Such a review will ensure the originality of the present work by establishing the state of the art and identifying ways in which to proceed that build upon work that has gone before.

Many of the techniques developed for particle size and concentration measurement are inferential in nature – for instance an electrostatic sensor may be employed to measure particle size (e.g. Zhang and Yan 2003) but the resulting information is inferred through analysis of variations in the signal. Such methods can yield good results with suitable calibration but can be susceptible to give unreliable results with changing conditions in the duct. Methods which directly size particles are considered intrinsically more desirable. Imaging is such a method – it can be readily appreciated that measuring a particle's size from an image of that particle can provide greater confidence than deriving the probable size through mathematical analysis of a seemingly unrelated signal. Some techniques, such as laser based methods, whilst not as simple in concept as imaging do provide results that are clearly of a less inferential nature than electrostatic and other systems and have become popular in recent years. Off-line laser diffraction based systems have become accepted instruments in laboratory environments and in later chapters the results from the present research are compared to those generated by such a system. In view of this laser based systems will be briefly reviewed here.

The definition of particle size is not as straightforward as it might appear. Defining the size of a three dimensional object with a single number will always be a subjective process and there are a number of definitions in common use. The calculation of mean particle size is equally complex there being a number of common definitions for this also. These problems are widely accepted and understood and so they will not be discussed here. Nevertheless an understanding of these difficulties is important in the work that follows and in the interests of convenience (also so that the definitions used throughout the present work are clear) a brief discussion of these issues is presented in Appendix A. One issue that is discussed in this chapter, in reference to fundamental size measurement concepts, is that of representative sampling. This issue is of direct relevance to the discussions that follow and is therefore included in this review.

Solids concentration is important as well as size and this is where laser diffraction is of limited usefulness. Imaging represents a methodology that has the potential to measure both particle size and concentration, being able to view a cross section of the duct and count the particles within it. The location of the particles is also found and so inhomogeneous flow regimes may be identified. The ability to 'image' a cross section of a duct is widely accepted as desirable and there has been much work undertaken in the past on tomographical reconstruction of cross sections through the flow. Such tomography may be based on many techniques from capacitance to gamma ray systems and whist not the same as imaging with a camera does produce flow images that may be used to establish solids concentration and flow distribution. Tomography is, therefore, of interest here and is briefly reviewed.

The chapter concludes with a discussion on the various systems reviewed and highlights why the technique used in the present research was decided upon. The form taken by the present work is also explained.

2.2 Representative Sampling

The representative nature of particle size data is an important concern in any attempt to measure this parameter and the inability to provide this may be a limiting factor in a given instrument's performance. If a material is to be sized then a sample of this material must be analysed – how large must this sample be in order that measurements made are representative of sizes in the material as a whole? This problem is mainly an issue with off-line analysis as for on-line work all of the material is generally sampled over a period of time (Single Particle Counter type instruments may have difficulties – see section 2.3.2). Nevertheless it is of great interest here and must be considered. The analysis of this problem requires much statistical knowledge which would be beyond the scope of this document but has been reported in the past by Masuda and Iinoya (1971, 1972) with similar work undertaken by Tate (1982). Further analysis of such work led Masuda and Gotoh (1999) to perform in-depth simulations of particle sampling and their results suggest that typical powders require that between a few thousand and a few tens of thousand particles must be sampled if the measured size information is to be considered representative at the 95% confidence interval. This result is important to bear in mind during the discussions that follow and in later chapters.

2.3 Non-Imaging Laser Based Techniques

Laser based particle sizing techniques are possibly the most widespread in use today. They can be broadly divided into Single Particle Counters (SPCs) and ensemble instruments which analyse multiple particles simultaneously. There are many variations on each technique and only the main or key techniques will be outlined here – a full discussion on the various set-ups would be beyond the scope of this review as it is only necessary here to discuss laser based systems so that their basic operation and shortcomings, in relation to imaging systems, can be discussed. Fuller reviews of laser based systems have been presented in the past, notably by Hirleman (1988 and 1991) and Black et al. (1996).

2.3.1 General Theory

In general laser based systems operate by observing the interactions between the laser beam and the particles in the sample. These interactions take the form of scattering and diffraction of the beam and can be described in mathematical terms. The most frequently employed theories for such work are Lorenz-Mie Scattering and Fraunhofer Diffraction.

Lorenz-Mie theory is derived by solving Maxwell's equations describing electromagnetic radiation for the light scattered by a homogeneous sphere under uniform illumination. Through understanding this light scattering it is possible to calculate the particle size. The full mathematical development of this theory is complex and has been described fully elsewhere (Hulst 1957, Kerker 1969 and Borhen and Huffman 1983) and algorithmic implementations have also been presented (Barber and Hill 1990). It is important to note that this theory assumes a spherical particle under uniform illumination (plane light waves). Assuming such illumination is acceptable where particles are very much smaller than the laser beam but when they approach similar size inaccuracies are introduced. This issue has been dealt with in a modification of the theory known as Generalised Lorenz-Mie Theory (GLMT) that was developed by Gouesbet, Grehan and Maheu (1986, 1991). A general summary of the technique is presented by Gouesbet (1994). It is explained that the plane light assumption becomes significantly erroneous in a real situation when the particle size approaches 10% of the focused laser beam width. GLMT allows the particle size to approach the beam diameter before this problem is manifest although it does so at the expense of complex calculation that may be time consuming.

Whilst the scattering of light by the particles is the phenomenon which allows particle size to be calculated it is necessary for this scattering to be measured and this is often achieved, in the near forwards direction, through the study of the patterns produced on a focal plane when light is scattered by the particles. Such diffraction patterns, described through Fraunhofer diffraction theory, are in the form of a series of light and dark rings that decrease in intensity with increasing radial position. The pattern produced by a particle or particles is not related to the optical properties of the material but represents the size or size range of material in the sample. Information on particle size is extracted through analysis of the intensity of the diffraction pattern at a number of radial locations

(exact details vary). The methodology relies on scattered light and therefore any transmitted light (through a transparent particle for instance) can cause difficulties. It is also of importance to note that non spherical particles will not produce perfectly circular diffraction patterns and will therefore introduce measurement inaccuracies. The general concept of a diffracted light scattering pattern is illustrated in figure 2.1.

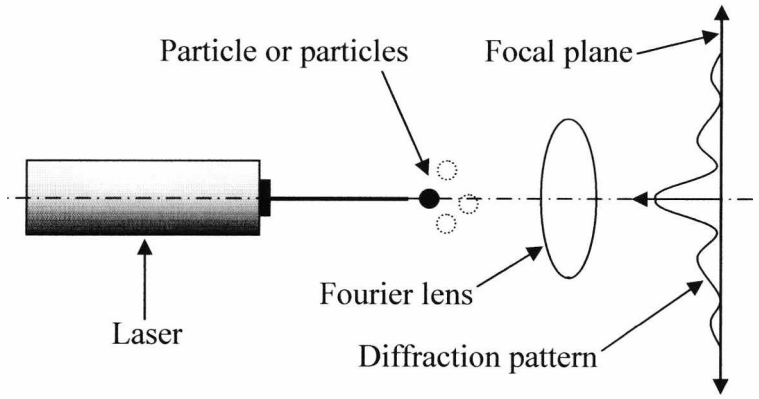

Figure 2.1 Diffracted light scattering patterns

A Fourier transform lens is a standard lens used in such a way that the angle of incident scattered light corresponds to a particular annular position in the focal plane.

2.3.2 Single Particle Counters

In a single particle counting (SPC) instrument a very small sample volume is interrogated and material number density is limited so that only one particle will be interrogated at a time. Such instruments may provide exact experimental size distributions (acquired over a period of time) and are popular in both laboratories and industry. There are a number of methodologies commonly employed for SPC instruments and the most popular of these will now be discussed. Fuller reviews may be found elsewhere (e.g. Black et al. 1996). All SPC instruments may determine solids concentration through particle counting, though they are limited to determining this parameter only over a period of time and at a single point within the flow field. Attempts to find the distribution of solids concentration within a duct require the use of some form of physical scanning – this will be discussed in section 2.5.

2.3.2.1 Intensity Based Methods

These systems measure the intensity of light scattered by particles as they pass through the sample volume. The general layout of a typical absolute intensity based instrument is illustrated in figure 2.2.

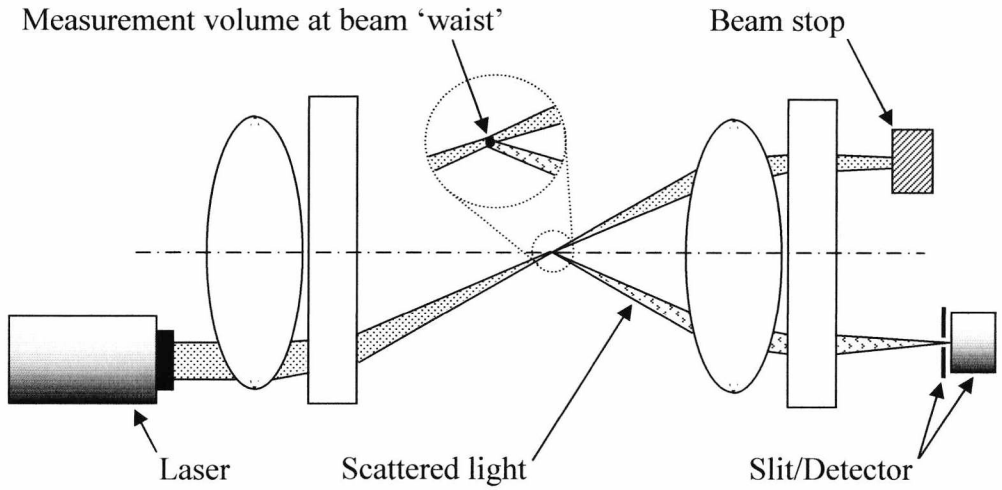

Figure 2.2 Geometry employed by a typical absolute intensity SPC instrument

It can be seen that the measurement volume is tiny, typically being around $0.001cm^3$ – $0.0001cm^3$ in size (Black et al. 1996). In general an SPC will only achieve representative sampling over a period of time and, due to the extremely limited sampling volume, will be sensitive to inhomogeneous flow regimes when operated on-line. As suggested in the discussion on Lorenz-Mie theory such systems are also sensitive to particle shape. Other inaccuracies are introduced by sensitivity to the path which the moving particle takes through the measurement volume. Particle size is determined from the maximum intensity of the scattered light as a particle passes through the sample volume. A response function is programmed into the instrument that is based upon Lorenz-Mie theory and the corresponding size is logged. Since the operation is based upon absolute intensity it is necessary to calibrate the instrument with a suitable reference. This reliance upon absolute values also means that the instrument will be highly sensitive to changes in optical conditions which, for instance, may be caused by material fouling of access windows in an on-line system. Despite the many problems the technique in general is popular since individual particles are sized also, by assessing the time it takes the particles to cross the measurement volume, velocity can be measured simultaneously. For

this reason such instruments are often referred to as PCSVs (Particle Counter Sizer Velocimeter) and have found their way into commercial products such as those manufactured by Malvern-Insitec, which achieve accuracies (for particle sizing) in the 5-10% range. A summary of the PCSV instruments that are available is given by Holve and Meyer in 'Combustion Measurements' (1991) where it is pointed out that practical PCSV instruments often have to resort to the use of two or more optical assemblies, each characterised for a different range of particle sizes, in order that a sufficient turndown ratio is achieved – a typical system might use a small beam to measure particles from 0.5-2μm and a larger one for 3μm to a few hundred. Due to the popularity of the technique much research has been performed in the interests of reducing the associated shortcomings, usually by applying ever more complex analysis of the scattered light. Holve and Self (1979) and later Holve and Davis (1985) studied the nature of the sample volume characteristics for SPC systems and this greater understanding has lead to techniques such as intensity deconvolution (Holve and Annen 1984) which reduces sensitivity to the path taken through the sample volume. Other techniques developed by Holve et al. (1979) have lead to reduced sensitivity to particle shape allowing particles with aspect ratios of up to 2:1 to be studied.

The fundamental reliance upon absolute intensity and the related problems of calibration and changes in optical conditions can be reduced through the use of a relative intensity measurement system. Hodkinson (1966) originally suggested such a method and in practice one way in which this can be achieved is through the use of two polarised laser beams, called a Polarised Intensity Ratio (PIR) technique. The general layout is shown in Figure 2.3 where it should be noted that the detector contains the necessary optics to detect the intensity ratio between polarisations in the scattered light.

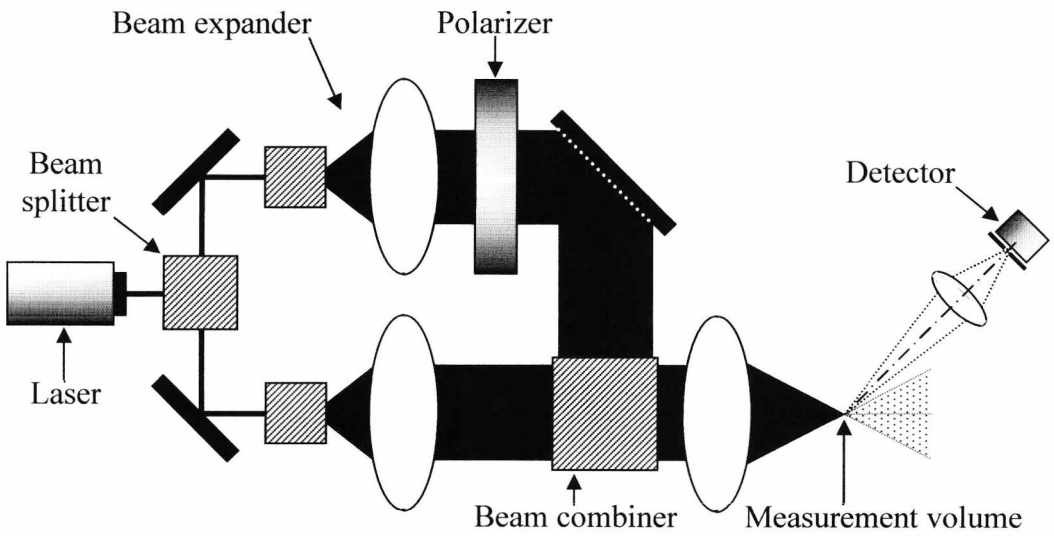

Figure 2.3 Geometry employed by a typical PIR system

Whilst solving the problem of absolute intensity sensitivity, ratio based systems have been found to suffer from problems related to particle light extinction, leading to sizing errors as high as 40% in some cases (Boron and Waldie 1978) and limited measurement range (Azzazy and Hess 1985). In general the increase in complexity over a PCSV system is rarely considered worthwhile unless absolute intensity consistency presents a significant problem.

Despite the many possible problems with intensity based instruments they remain popular due to their simplicity and a number of studies have been carried out using these instruments. Notably Bonin (1992) and later Bonin and Queiroz (1990, 1991, 1996) have published a number of papers on the use of PCSV instruments on industrial scale pulverised coal boilers and work on the formation of fly ash during PF combustion has also been presented (Baxter 1992).

2.3.2.2 Phase Doppler Technique

One of the most well known laser based particle analysis techniques is Laser Doppler Velocimetry (LDV – sometimes referred to as Laser Doppler Anemometry – LDA). Since LDV systems measure velocity their importance here might not be clear but the basic LDV technique can be expanded to form Phase Doppler Analysers (PDA) which are capable of measuring particle size. LDA systems operate by focusing two laser beams on

a single point in the flow. Where the beams cross an interference pattern is created defining the measurement volume and particle velocity is found by analysing the frequencies in the light scattering signal as the particle crosses this space. In PDA systems the scattered light is collected at two or more spatial locations and particle size information can be extracted through analysis of the phase shift between frequencies in the two signals (these frequencies are produced by intensity variations as the particle passes through the interference fringes and should not be confused with the frequency of the laser beams). The general arrangement of a PDA system is shown in figure 2.4.

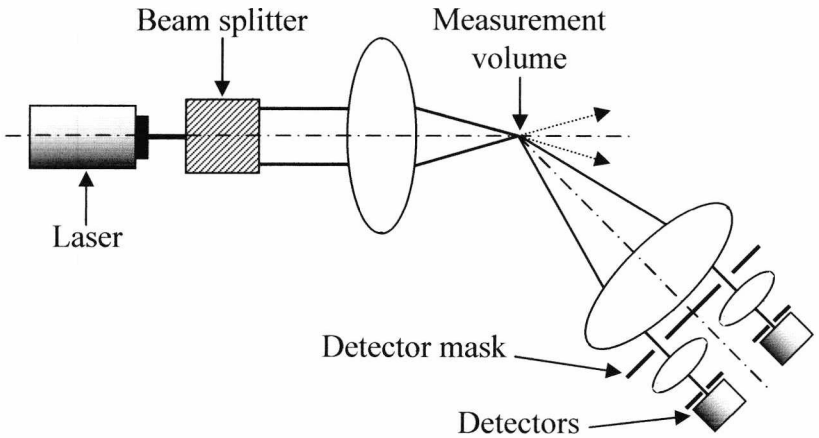

Figure 2.4 Geometry employed by a typical PDA system

The PDA technique is popular and has been developed into commercial instruments by companies such as Aerometrics and Dantec. Reasons for this popularity include reliable velocity and size measurement on a particle by particle basis and high accuracy sizing and velocimetry that does not require calibration – the results are a function of known instrument parameters and are insensitive to the intensity of scattered light. Despite these advantages PDA systems are only applicable to spherical particles – Alexander et al. (1985) have shown that a change in particle aspect ratio of only 0.29 can cause a 45% error to be introduced into PDA results. Under ideal conditions, however, velocity can be measured to within 1% and particle size to within 4%.

In general PDA techniques are most useful for laboratory analysis, often of turbulence in two phase flows. Many studies have been carried out using such systems, notably by Sommerfeld and Qiu (1991, 1992) and Sommerfeld et al.(1993) who studied two phase swirling flows such as those found in pulverised coal boilers. Fuller analysis of PDA

principles, techniques and limitations may be found elsewhere (e.g. Durst and Naqwi 1993 and Sankar and Bachalo 1995).

2.3.3 Ensemble Methods

Single particle counters may be able to achieve good experimental size distributions through analysis of each individual particle in a sample but this is achieved sequentially suggesting that it may take some considerable time to achieve a representative distribution result. Also such instruments are limited to point measurements and are therefore sensitive to local variations in a flow. These shortcomings are addressed by another group of laser based instruments known as ensemble sampling systems. These systems interrogate a group, or ensemble, of particles simultaneously and do so though the use of a larger sampling volume than that employed by SPCs.

2.3.3.1 Diffraction Based

Probably the most widely used method of ensemble sampling employs the Fraunhofer diffraction principle. A schematic representation of the general arrangement employed is shown in figure 2.5. The general principle is a follows: A laser beam is expanded to create a field of parallel radiation which is passed through a two phase particulate suspension (usually solids in air). The light that is scattered by all the particles is collected by a Fourier transform lens and focussed onto an array of detectors where a diffraction pattern is formed. The angle of scattered light from each particle is related to its size and so by analysis of the signals from the detectors it is possible to determine the size distribution of particles in the sample.

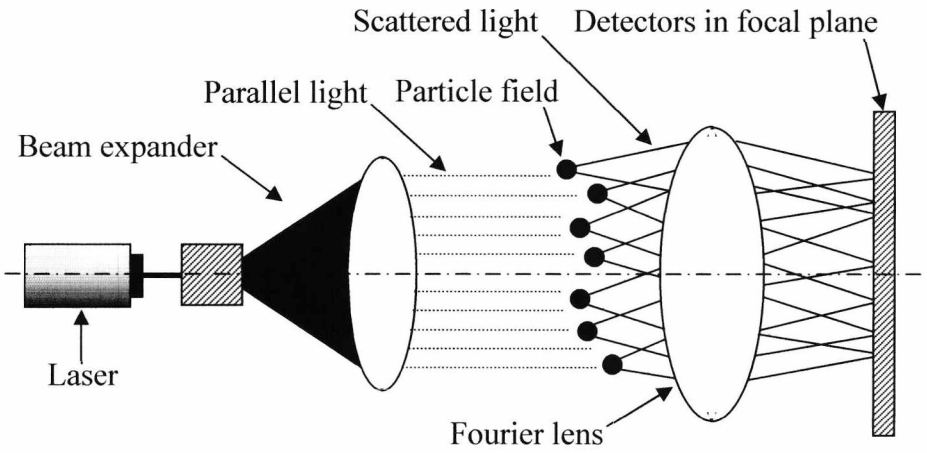

Figure 2.5 Geometry employed by a laser diffraction ensemble sizer

The methodology was originally developed by Swithenbank et al. (1977) and this work led to the well known Malvern Mastersizer range of instruments. One of the key challenges for such instruments lies in analysing the signals from the detectors to create a meaningful result. There are two means of achieving this; iterative-numerical and analytical methods. Iterative methodology has been employed traditionally and this has been explained in some depth in the past (e.g. Bayvel and Jones 1981). Analytical methods are more recent, the main pioneers in the field being Knight et al. (1991) who showed that analytical methods produce comparable or in some cases superior results to the traditional procedures.

As with other laser based systems the diffraction methodology is sensitive to particle shape, the use of non spherical particles resulting in larger errors (Black et al. 1996). Laser diffraction instruments are widely accepted for off-line analysis under laboratory conditions and may be used as a source of reference data for other sizing systems. It is, however, widely accepted that where non-spherical particles are concerned it is virtually impossible to state that one system measures size erroneously when compared to another but simply that there is a variance in results (e.g. Boyko et al. 1993). One study of particular interest was performed by Nathier-Dufour et al. (1993) and compared Malvern Mastersizer results with sieving – general agreement was good but some discrepancies were found that were accredited to the fundamental differences in the measurement techniques, in particular the fact that the Malvern instrument makes an in-flight averaged particle size measurement whereas sieving identifies the minimum dimension of a particle. Another interesting study was performed by Kanerva et al. (1993) who

compared sizing results from a diffraction based technique to manual microscopy (see section 2.4). It was shown that the diffraction system was unreliable for absolute measurements when the aspect ratio of particles was extreme, clearly highlighting the unsuitability of laser based systems for analysis of non-spherical particles. In all of these studies, particle shape was highlighted as the dominant factor in variations between results although sensitivity to inhomogeneous flow regimes and differences in the representative nature of the sampling were also cited.

Despite the difficulties laser diffraction systems remain popular and some have been developed for on-line use. Malvern-Insitec are well known in this field and have produced a number of instruments of this nature. Early examples required that a probe be inserted into the flow which may suffer from wear related problems in long term installation (a pneumatic conveyer carrying, for instance, sand at 40m/s will quickly destroy any intrusive probe irrespective of what material it is made from and it is certain that any lens assembly would soon be rendered useless). Such instruments are often marketed as mobile or temporary systems (Powder Handling and Processing: Editorial, 2003). Other designs are advertised as non-intrusive but in reality either reduce the diameter of the duct to some degree or require that a small side chain flow be extracted from the main duct (Crawley 2003). The use of laser diffraction instruments in industry has received much interest in recent years and fuller summaries of available systems and their benefits and shortcomings have been presented elsewhere with good examples being Weiner and Fairhurst (1992), Wedd (1993), Pohl (2001) and Odreitz and Behrens (2004).

2.3.3.2 Transmission Based

Transmission based systems are capable of measuring solids concentration and not particle size. A number of the ensemble laser sizing systems already discussed adopt some form of transmission based principle in order that they can also measure concentration. A basic transmission based setup is shown in figure 2.6.

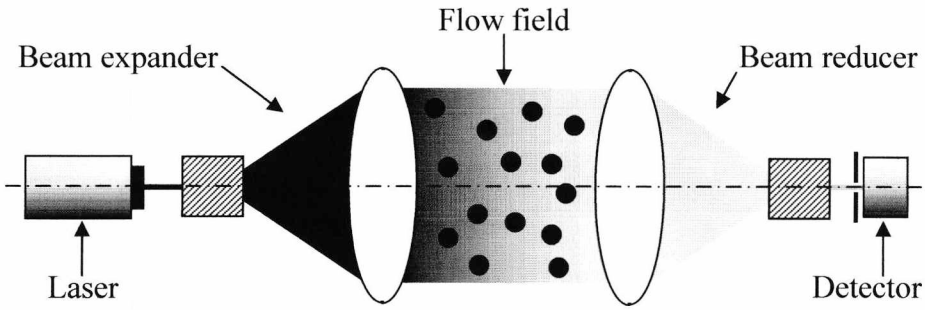

Figure 2.6 Basic transmission based concentration measurement setup

The general principle of transmission based concentration measurement is as follows: A beam of light (usually a laser, though tungsten lamps and xenon strobes have been used in the past) is shone through the particle field. As the light moves through the particles it is attenuated due to absorption and scattering. This attenuation can be measured and related to particulate concentration through the application of Bouguer's law (Siegel and Howell 1992) which may be written as:

$$I = I_0 \exp(-\tau) \qquad [2.1]$$

Where I_0 is the incident radiance, I is the transmitted radiance and τ is the pathlength (note that this is sometimes described as Lambert's law). The technique has been used widely for measuring soot concentrations in flames but its use in other two phase flows is limited. Insitec manufacture a combined ensemble diffraction based particle size and transmission based concentration instrument known as the TESS (Transmission particle method for Extinction-Scattering with Spatial resolution) which determines size and concentration through studying the ratio between scattered and transmitted light. Holve et al. (1992) have studied the application of such a system and discussed its capabilities. It was shown that useful concentration measurements can only be achieved when particles in the 1-100μm range are used – outside this range calibration must be undertaken on a per-material basis. It should also be highlighted here that transmission based systems are highly sensitive to changes in absolute intensity and are, therefore, affected by such phenomena as window fouling and component aging – measurements must always rely on calibration for accuracy. This limits the usefulness of such systems in industrial situations.

2.4 Imaging Techniques

Flow and particle imaging is a technique that is not new. Work has been reported from over 50 years ago in which photographic images were acquired and analysed manually (York and Stubbs 1952). This simple form of image based particle analysis was an extension of manual microscopy in which particles are scattered over a flat objective and analysed by an operator. Manual microscopy is an extremely time consuming and labour intensive technique that is subject to variation with operator experience and fatigue – even an experienced operator will only be able to size around 2000 particles per day (Rawle 2001) and this is barely acceptable for representative sampling as discussed in section 2.2. Despite this limitation microscopy is suitable for use with non-spherical particles and provides robust measurements which may be treated with a high degree of confidence through good empirical understanding of the fundamental methodology. In view of this the automation of image analysis using computerised image processing is an area of great interest allowing the fundamental benefits of microscopy to be combined with consistent high speed operation.

So far only imaging based methodologies that employ some form of camera, therefore representing imaging in the generally understood sense, have been introduced. In addition other systems will be briefly reviewed that are based on tomographical imaging. An image may be defined as a two dimensional array of information, usually of luminance and or chrominance (in the case of a visible light based system) but it is possible for instance to build up an 'image' from localised analysis of solids concentration in a duct – this is of interest here and will be discussed in section 2.4.3.

2.4.1 PTV and PIV

The most well known forms of particle imaging are, unquestionably, Particle Tracking Velocimetry (PTV) and Particle Image Velocimetry (PIV). As the names suggest these techniques focus mainly upon velocity measurement but attempts have been made in the past to derive size information as well. In addition the general methodologies employed by such systems for physically acquiring particle images are of interest and so they are of relevance here.

In both techniques sets of two temporally separated images are acquired and suitable processing employed in order that maps of localised velocity may be produced. These are of great interest for scientific study in, for example, the analysis turbulence in flows. The two techniques differ on one point: PTV identifies individual particles in the images and tracks their velocity by matching them from frame to frame, whereas PIV performs a regional spatial correlation in order to extract velocity information and is not aware of individual particles. PIV cannot provide particle sizing information and whilst it may be possible to assess solids concentration through regional image intensity, no quantitative work has been found in this area. The qualitative differentiation between dense and dilute phase flow has been attempted in the past (e.g. Lackermeier et al. 2001) but this provides no useful information as to the absolute amount of material that is present. Despite the lack of knowledge of individual particles in PIV processing the images used for this work are often of good enough quality that individual particles could be identified if desired and similar physical image acquisition arrangements are frequently used for both PIV and PTV.

Since these techniques are primarily intended for velocity calculation it is necessary for two images to be captured with well defined temporal separation. For this reason a pulsed light source is used. It is possible to achieve pulsed illumination using some form of diffuse back lighting technique employing a xenon strobe as the light source (more on this in section 2.4.2) but it is more common to make use of a 'sheet' of laser light that is pulsed in nature due either to the use of a pulsed laser or through modulation of a continuous wave device. Such a sheet of light is generated by passing the circular laser beam through an arrangement of barrel lenses so that it is spread out into a fan of light with very little thickness (thickness used varies from a fraction of a millimetre to several millimetres depending on the application). As particles pass thought the laser sheet they scatter light (due to Lorenz-Mie scattering) and this scattered light may be imaged with a camera. The illuminated section of flow may be considered to be two dimensional in nature and clear, well-defined, images are produced without depth of field related problems. The technique is widely accepted, a good example of its application being presented by Putorti et al. (2003) in a recent paper prepared for the US National Institute of Standards and Technology.

Figure 2.7 shows the general arrangement of a PIV/PTV system employing laser sheet illumination. It should be noted that particle motion is in the 2D plane of the laser sheet rather than through it (i.e. not perpendicular to it).

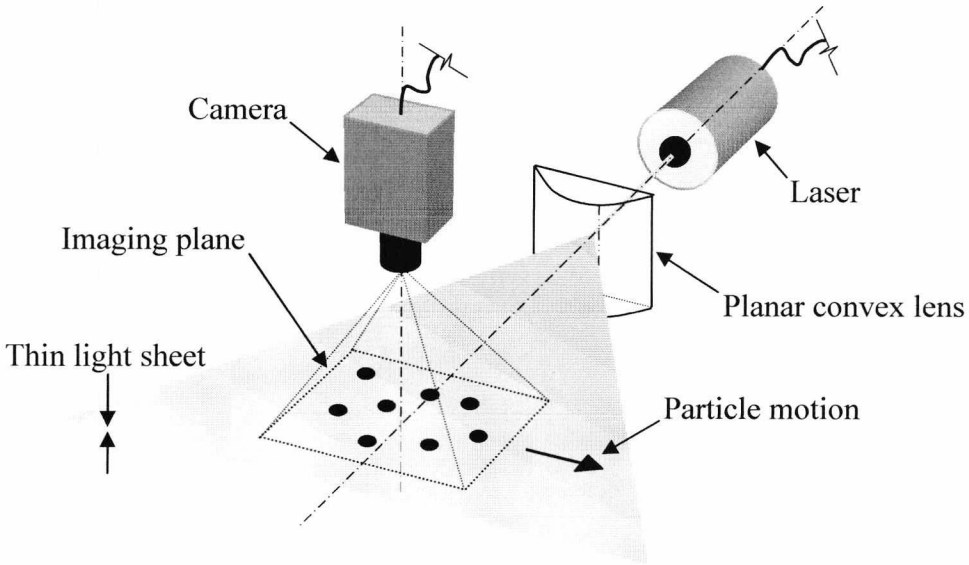

Figure 2.7 Typical arrangement of laser sheet illumination based PIV/PTV system

Whilst this illumination technique has been used successfully for both PIV and PTV the measurement of particle size rather than velocity is of interest here. PIV by its very nature cannot provide size information and the only work that has been found that brings particle size information and PIV together concerns simultaneous multiphase flow velocimetry. Different sizes of particle are used for each phase and a simple processing pass is applied to the image to separate out the two sizes into two separate images before PIV techniques are applied to each (Wang et al. 1995) – accurate sizing is not considered but rather the simple classification into two groups. Due to this limitation of PIV discussion will now centre on PTV which, whilst not always used for sizing, may be readily adapted for this task.

Early work on particle tracking for the analysis of complex turbulent and swirling flow (a stirred tank is often employed during development work it being a simple matter to introduce baffles etc to create complex eddies) relied upon manual identification of particles and was extremely time consuming – such work is of little interest here. Some of the first automated particle tracking research was reported by Chang et al. (1984, 1985a and 1985b) from before the term 'PTV' had been coined. Clear interest was shown in the

technique not only in scientific communities but also in industry. Other pioneers in the field are Adamczyk and Rimai from the Ford Motor Company who applied an enhancement of the technique to the analysis of flow structures inside carburettors (Adamczyk and Rimai 1988a) – by this time PTV was widely accepted. One limitation of PTV that was speedily identified was that it only acquired a 2D velocity map – measurements had to be made at a number of angles in order to fully understand a 3D flow structure. This shortcoming was addressed with 3D PTV, commonly employing two or more cameras to achieve full 3D flow field visualisation. Adamczyk and Rimai (1988b) developed a 3D two camera arrangement and a thorough analysis of two-camera (stereo) PTV has been presented by Nishino et al. (1989). Others have developed means of optically compressing two angularly separated views onto a single CCD sensor (e.g. Pan et al. 2002). A particularly elegant solution to this problem was implemented by Padilla-Sosa et al. (2002) who combined 2D PTV with analysis of the particles Lorenz-Mie scattering to achieve depth information – over the course of successive frames a full 3D flow field was reconstructed, though depth information was limited to the depth of the laser illumination (it should be noted here that 3D PTV does not give the same accuracy as 2D methods and is treated with suspicion in some circles – often the robustness of a 2D method is preferred over the promise of a greater quantity of less reliable data that is provided by 3D analysis).

Much of the PTV work mentioned above does not observe the particles that constitute the flow medium (if the flow medium were a liquid there would be no particles to observe) but tracer particles are introduced, which take up the motion of the surrounding flow, having controlled optical properties for easy identification and tracking (for example brightly coloured or white particles may be used to ensure good image contrast – latex or nylon are widely used for this purpose). This reliance upon tracer particles would render particle sizing attempts pointless. One reason for the use of tracers is that a smaller number of them can be used than there would be if the primary flow material was observed. This reduction in numbers speeds processing and originated in manual attempts at particle tracking. With the increasing power of computers tracking more particles becomes practical allowing not only improved velocity map resolution but also introducing the possibility of particle size measurement. Attempts to combine PTV with sizing using laser sheet illumination have been made in the past with the studies of Herpfer et al. (1995 and 1997) and Kadambi et al. (1998) being of particular interest.

Results from these studies were mixed and in some cases contradictory – some investigators have suggested that the use of laser sheet illumination and scattered light imaging are unsuitable for particle sizing (Cao et al. 1999). It is not, however, the fundamental methodology (of laser sheet illumination) that is in question but rather the details of its application. There are two methods of implementing PTV, dual flash imaging and streak photography and many sizing studies have employed the latter. In the dual flash method very short bursts of illumination are employed so that particles are 'frozen' at a single point in space as far as the images are concerned – two such images are acquired with a known interval between them and the change in position of particles is used to calculate their velocity. In the streak method a single image is used and a longer burst of illumination is employed – particles move an appreciable amount during the illumination burst and appear in the images as streaks. The lengths of the streaks can be analysed to find velocity information. The general idea is shown in the simulated images of figure 2.8.

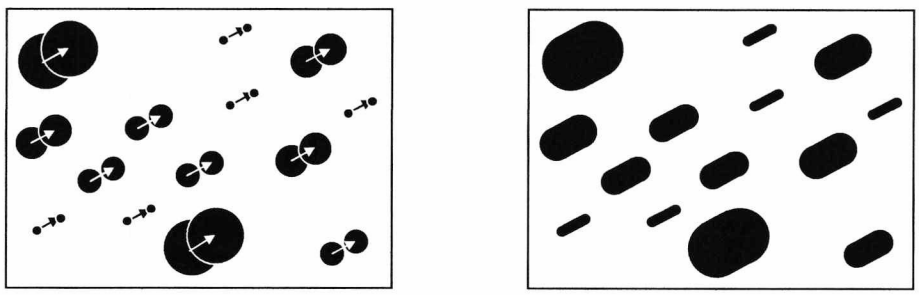

a) Dual images b) Single streak image

Figure 2.8 Comparison of PTV techniques for the same motion

It should be noted that figure 2.8a shows two separated images superimposed with particle matching shown in the form of arrows – real images would show distinctly separate particles in each of two frames. The use of dual flash images allows very accurate velocity measurements to be made based upon the movement of individual particles' centre of mass locations – it is insensitive to particle shape and the images provided by such systems would be ideal for sizing attempts. Such methods, however, require complex image matching algorithms to be employed which may be procedural (e.g. Nishino et al. 1989) or based on natural algorithms such as fuzzy logic (e.g. Shen et al. 2001). Streak imaging has its origins in manual particle tracking and, though providing simpler processing than dual flash imaging, demonstrates little consideration to particle

shape, since particles are stretched into a streak that represents their maximum width. This causes some ambiguity as to the centre of mass of particles that will lead to reduced velocity accuracy. Also, whilst the width of such streaks may be taken to represent the diameter of circular (spherical) particles for sizing purposes, arbitrarily shaped particles will not be sized correctly. The use of streak imaging could explain the varied results obtained in the sizing studies previously mentioned.

Another problem in relation to reliable particle sizing caused by laser sheet illuminated PTV is that of the particles' positions within the thickness of the light sheet. Since particles travel in the plane of the light sheet they move an appreciable distance during the measurement interval in the case of streak imaging and from one measurement to the next for the double pulsed technique. This movement will not necessarily be in two dimensions – there may be some vertical movement within the light sheet. This phenomenon will cause problems with particle sizing as a particle that is only just within the bounds of the sheet during the first measurement may appear smaller than it does in the second measurement by which time it has moved into full illumination. This problem will also produce variable sizing results with particles of similar size that move with planar motion at different depths within the sheet. This problem has been investigated recently by Putorti et al. (2003). The exact geometry of the laser sheet is of importance and this factor will also have contributed to variable nature of results recorded in previous sizing studies.

Whilst many researchers have abandoned light sheet illumination for sizing, due to the problems discussed above, it is widely admitted that there is still room for research in the field (Nishino et al. 2000) as a light sheet solves many depth of field problems that have been found to plague other techniques (see the next section). In particular it seems likely that considerably better results could be achieved if velocity measurement were to be abandoned and the technique used purely for sizing. In this case the particles could move through the light sheet at right angles to it allowing an accurate cross section of the particle to be collected by the camera during its passage through the sheet. This would solve both problems discussed above (at the expense of the loss of velocity data). Despite the possible advantages no work has been found on this use of light sheet illumination.

The solids concentration of material is another problem that can be addressed with PTV type systems. In general it is possible to count the particles present in the images for this purpose. Some work has been found on particle counting in such systems (e.g. Kim and Lee 1990) though this seems to be for the purposes of producing particle size distributions rather than solids concentration data and no thorough investigation into the suitability and accuracy of such systems for measuring this parameter as a goal in its own right seems to have been performed.

2.4.2 Other Camera Based Particle Size Analysers

Despite the fact that the most well known imaging based particle measurement systems focus on velocity information there has been much work in the past on imaging systems that primarily measure particle size. Imaging systems are insensitive to particle shape and due to the fundamental straightforwardness of their operating principles offer good robustness of measurement. Imaging based sizing systems consist of two parts: Imaging hardware, including some means of particle illumination and image acquisition and the image processing software that extracts the required particle parameters. Such systems may be intended for off-line static analysis or on-line live flow work. For static work particles are placed on a flat focal plane and imaged with a camera – there are two methods of diffuse illumination that may be employed: front lighting and back lighting (or shadow imaging). A front lighting scheme illuminates the particles from behind the camera and reflected light is collected by the lens – this is the same mechanism through which we see the world on a daily basis and detailed 'photographic' images of the particles are produced. This approach is extremely simple to implement in terms of hardware setup. A difficulty with this approach, however, is that image contrast is low and defining the exact location of particle boundaries (i.e. determining which image pixels represent particles and which background) will require complex, time consuming, processing that is difficult to perform consistently. For this reason the benefits of simple hardware are often ignored in favour of simple processing requirements and back lighting is generally favoured (Nishino et al. 2000). A back lighting scheme introduces diffuse illumination from behind the particles so that images acquired represent their silhouettes (or 'shadows'). Such images are virtually in binary form and contain crisp particle boundaries – this simplifies image processing software considerably but at the expense of

a more complex lighting arrangement (further discussion on the difference between front and back lighting is undertaken in chapter 3). Figure 2.9 illustrates the differences between front and back lighting and simulated particle images are shown.

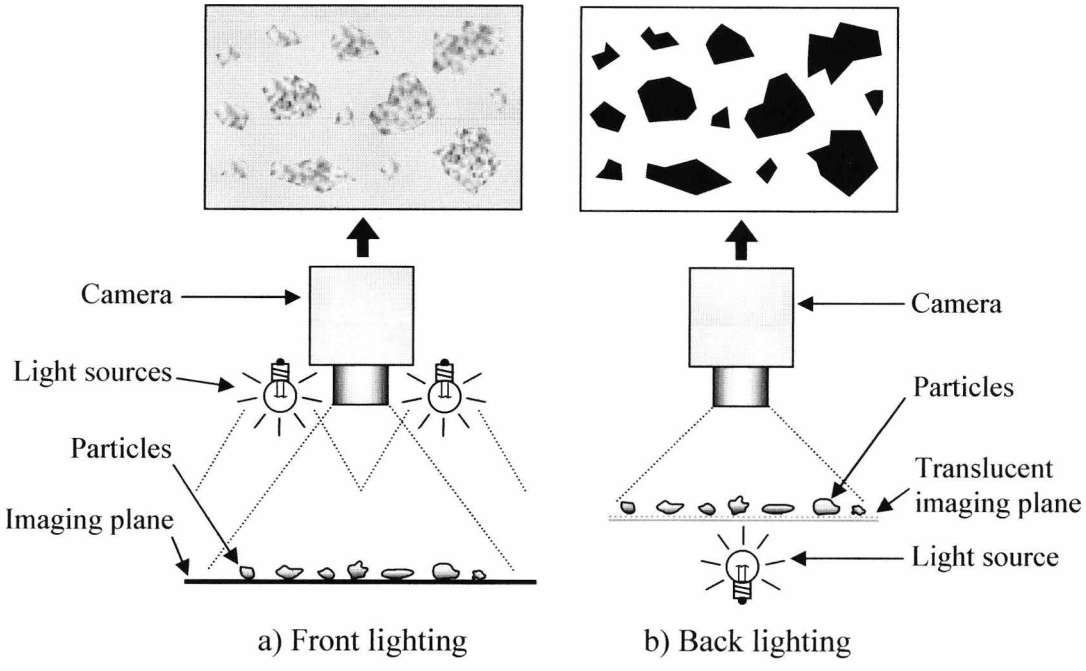

Figure 2.9 Off-line imaging arrangements and simulated particle images

The backlighting arrangement is susceptible to fouling and deterioration of the translucent imaging plane which may result in inconsistent results. Despite this, back lighting is generally favoured for static analysis applications, which may be considered as automated microscopy, as complex image processing is avoided. It is also possible to provide consistent imaging conditions in the controlled laboratory environment where an automated microscopy system is likely to be used.

There are a number of commercial automated microscopy systems on the market, a good example being the PharmaVision830 from Malvern Instruments. The exact operating principles of such systems are not in the public domain but one interesting point in regard to the Malvern device is that it appears to require manual trimming of the threshold level used to separate particles from background (Malvern Instruments 2005a). This could lead to inconsistent results depending upon the particular operator who makes this determination. Little information is supplied in regard of the sizing accuracy of such

systems and in general, no thorough assessment of the accuracy and consistency of static imaging based systems seems to have been performed.

Due to the simplicity of image processing necessary for static systems research work has tended to concentrate on more complex areas of study where in-flight particle measurements are made (Nishino et al. 2000), with particular emphasis on droplet sizing (Chigier 1991). Such systems may be for off line analysis, with a finite sample being suspended in some form of fluid stream, or for full on-line operation. In-flight systems employing laser sheet illumination have already been discussed in section 2.4.1 but it is also possible to use diffuse light. The main problem when imaging in-flight materials is that the particles do not all exist in a single plane that is easy for a camera to focus on. In practice back lighting is the only practical approach (other than laser sheets) in such circumstances and has been used widely in research work in the past (Chigier 1991). A typical imaging set-up is shown in figure 2.10.

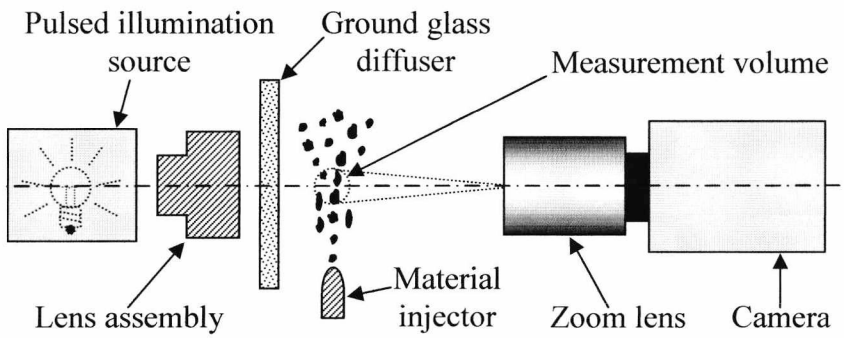

Figure 2.10 Typical back lighting arrangement for in-flight measurements

Particles are illuminated with pulses of diffuse light and imaged with a camera. A high magnification lens is usually employed together with a relatively small aperture (high F-stop number) in order to provide a large but crisply defined working depth of field. Some of the earliest work for in-flight measurements with diffuse illumination was performed by Ow and Crane (1980, 1981) who used a vidicon based camera (An old fashioned camera technology that may be considered to be the inverse of a cathode ray tube. Images are acquired by scanning a target with an electron beam – as with CRTs some distortion is inherent with this technique). They reported difficulties with measured particle size being dependant on the depth within the measuring volume and suggested depth of field tests so that particles in extreme positions could be ignored. Weiss et al. (1984) introduced a

focus test based upon the gradient of the brightness level of each particle image and this was refined by Bertollini et at. (1985). The difficulty of defining a suitable working depth of field and establishing which particles are within it is widely accepted and represents the main source of error in this type of work (Oberdier 1984, Chigier 1991).

Despite the complexity of the depth of field issue research in the field of diffuse illuminated in-flight measurements has continued and a good, recent, example of this work may be found in Nishino et al. (2000). In this work a two camera stereo imaging setup was used so that particle depth could be established. Particle sizing was accurate to around 5% when using precision calibration images. The setup required two full imaging arrangements and these required physically clumsy long focal length optics. A measurement volume of only $3mm^3$ was achieved which limited its usefulness to laboratory analysis – no discussion on the possibility of on-line industrial work was undertaken. It was found that despite the back lighting arrangement many materials yielded poor contrast images similar to those achieved with static front lighting or laser sheets and so complex image processing was still required. Much effort was placed on camera coordinate calibration due mainly to the stereo nature of the work. Equations used were based on those proposed by Murai et al. (1980) – such work was originally developed for aerial cartography applications for which accurate spatial positioning from images taken at arbitrary angles is required.

The measurement of solids concentration using diffuse back lighting is difficult due to the depth of field issues and related particle validity concerns (Oberdier 1984) and research has concentrated on sizing. Concentration is of importance however as there will be a limit to the concentration that can be measured by any optical imaging system – If there are too many particles present there will be difficulties with overlapping particles in the images causing sizing inaccuracies. Nishino et al. (2000) state that they believe their technique can reliably measure particle size with concentration of up to 0.1% (with a sensing volume of $3mm^3$ only six 100μm particles could be sized at a time – this would have caused difficulties with the representative nature of the size result). Whilst this effect is widely recognised (e.g. Song et al. 1999) there seem to have been no systematic studies made in order to establish the upper limits of operation. The usual response to the problem is to attempt to recognise overlapped particles and either ignore them or separate them. Shen et al. (2001) separated overlapped particles using a method that was only

applicable to spherical shapes. The Malvern PharmaVision instrument that was discussed earlier attempts some particle separation but details are not in the public domain and, if advertising brochures are to be believed, the method appears to ignore the portions of the particles that are underneath one another.

Despite the difficulties with diffuse illuminated in-flight systems a small number of commercial instruments have become available. These are of no use for on-line flows but are for laboratory studies. The Malvern FPIA-2100 instrument uses this technique. Materials are suspended in a liquid solvent and imaged with an arrangement similar to the figure 2.10 setup. The system is intended for very fine materials that are prone to clumping under dry conditions (e.g. laser toner – Malvern Instruments 2005b). Maximum working concentration is stated only vaguely and in the unusual units of particulate number density per μL. Another system is produced by Oxford Lasers which is intended mainly for droplet sizing in sprays (Oxford Lasers 2005). Neither manufacturer mentions depth of field effects in their advertising literature. In general there would appear to be no imaging based systems intended for routine day to day measurements when installed permanently under industrial conditions.

2.4.3 Tomography

As suggested in previous sections optical camera based methods are not the only widely accepted form of imaging. If a set of chordal density values over a defined cross section can be found then it is possible to build up a 2D 'image' of the density of material present. These chordal densities have been found in the past using attenuation of X-rays, gamma rays and untrasound and also through the study of changes in electrical capacitance (Electrical Capacitance Tomography – ECT) and resistance (Electrical Resistance Tomography – ERT) within the measuring volume (Yan 1992, Barratt 2000). Such techniques were originally developed for radio astronomy (Bracewell 1956) though their most well known application lies in medical imaging (Hounsfield 1973). These techniques have also been applied to particulate flows where capacitance based methods are particularly common. Figure 2.11 shows the general arrangement of an ECT system as applied to a circular cross sectioned pipe.

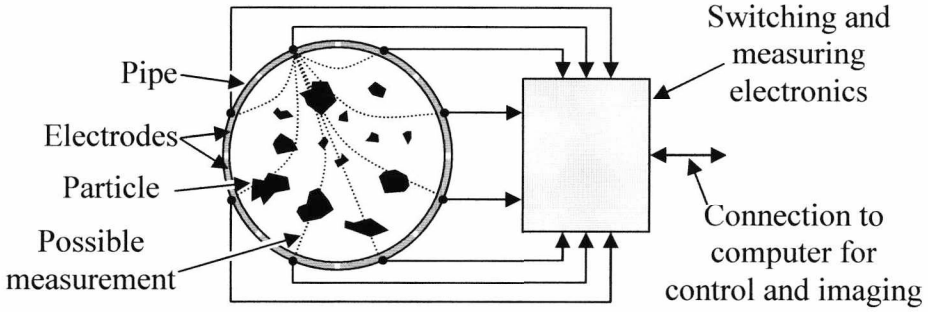

Figure 2.11 Capacitance based tomography system

It should be noted that only seven out of a possible 28 capacitance measurements are shown in this diagram in the interests of clarity. These measurements require complex and time consuming switching between electrodes which limits the upper number of electrodes that may be employed – other limiting factors include the lowest limit of capacitance value and, therefore, electrode area that can be used. Such limitations mean that, in ECT, a larger number of electrodes does not necessarily yield higher spatial resolution. Also to be considered is the processing required to re-construct a cross sectional image from these data – more measurements require more processing. Similar practical limitations on the number of measurements possible are to be found with other measurement techniques (Barrett 2000).

The spatial resolution of tomographic systems is very low – certainly individual particles cannot be resolved by such techniques, leaving little scope for particle sizing work. This is not a problem for solids concentration measurement or flow distribution study (e.g. Yang and Liu 2000) – radiometric instruments have been known to provide promising solids concentration data in the past though require dense flows to be successful (Barrett 2000).

The lack of particle sizing limits the relevance of tomography here. Despite this no review on flow interrogation would be complete without mentioning this widespread technique – tomography allows real time study of flow distributions within the duct that would not be possible by other means. Fuller reviews of tomography can be found elsewhere (e.g. Barrett 2000) and the application of ECT techniques to gas/solids flow measurement in particular is covered in an interesting article by Yang and Liu (2000).

2.5 Discussion

Particle size and solids concentration are important parameters in particulate flow measurement. These parameters often go hand in hand and whilst instruments that can measure solids concentration but not particle size have been created in the past the opposite is not generally the case.

A considerable number of particles must be analysed (thousands to tens of thousands) if representative size distributions are to be achieved. When the number and area of particles are known the solids concentration may be calculated easily as a ratio of total particle area to total interrogated area (or volumes for 3D systems). In practice the usefulness of many particle size analysers as concentration instruments is limited by their small interrogation volume, yielding a result that is not representative of concentration across the duct.

Laser diffraction based techniques are well established in both the research community and industry. SPC instruments analyse each particle individually and give good experimental size distributions but rely on temporal averaging to achieve representative results. Despite this, commercial instruments have appeared but are used mainly for research work rather than in industry. This type of instrument always suffers from sensitivity to particle shape that ever more complex data analysis techniques and optical geometries have been unable to eliminate. The highly localised single particle measurements using SPCs are not ideal in most situations and ensemble systems have been developed to allow a large number of particles to be sized at once. Whist giving good sizing results the laser diffraction based systems have seen limited success as concentration measuring setups – SPCs requiring long time averaging yielding point measurements (thus being highly sensitive to inhomogeneous flow) and ensemble systems relying on transmission based techniques for this functionality. In off-line laboratory conditions ensemble laser sizing systems are widely accepted, there being ISO standards to define their accuracy and applicability (e.g. ISO13320). For industrial measurements there are a number of on-line systems but these are not truly non-intrusive and are often designed only for temporary installation during initial process set-up. Off-line laser diffraction systems have, however, been used for at-line measurements (Pohl et

al. 2001) analysing samples taken from ducts in less time than it would traditionally take to send such samples to a laboratory for analysis. Under such situations the limited coverage and spatial sensitivity of both SPC and ensemble systems are overcome by taking multiple material samples from across the duct. This may be achieved manually or by automatic mechanical means through the use of the widely accepted Rotorprobe apparatus (Yan 2002, ISO9931). In general true on-line operation for laser diffraction based systems remains problematic and the basic sensitivity to particle shape and spatial flow variation is a fundamental problem with these methodologies.

Optical imaging based systems promise to eliminate particle shape sensitivity (whilst widely accepted this fact has yet to be thoroughly tested in a quantitative manner) and have the capability to observe a significant area of the flow, thus removing the spatial sensitivity also. Systems based on laser sheet illumination are well established for velocity measurement but sizing work is limited. Where sizing is attempted velocity measurement is invariably retained leading to sizing errors due to vertical movement of particles through the laser sheet. The elimination of velocity measurement and concentration upon size, so that particle movement issues can be resolved by the use of a perpendicular light sheet, is a promising technique that requires investigation. Despite the widely accepted benefits of laser sheet illumination thorough investigation into the practicalities of an industrial sizing system have yet to be performed and there has been little work reported on concentration measurement with this technique.

The use of diffuse illumination for particle measurement systems offers an alternative to the laser sheet. Automated microscopy systems are commercially available for static particle analysis and these usually employ back lighting to simplify image processing requirements. The limits of measurement accuracy are not well defined for such systems. In-flight analysis may also be achieved with diffuse back lighting but such attempts are plagued by depth of field related errors which can only be minimised with complex, costly and delicate optical arrangements – laser sheets are preferable in this respect. Some commercial instruments have been produced but these are used for laboratory analysis and research work rather than for industrial operation. Again, little work on concentration measurement has been undertaken, this capability of imaging systems remaining poorly defined.

One point of interest in relation to all sizing systems and solids concentration is the range of applicable concentrations at which sizing can be achieved reliably. Laser based SPCs require that only a single particle should exist within the sample volume at any given time – this limits the maximum concentration that can be used to around 10^5 particles per cm^3 for most instruments (Black et al. 1996). Ensemble systems are limited at the upper end of the range by multiple scattering phenomena and the concentration is usually limited to that which causes laser beam extinction of no more than 50% – the resulting concentration will vary depending upon the material in question and is therefore poorly defined (Black et al. 1996). For camera based imaging systems the lowest measurable concentration is defined as a single particle within the measurement volume (which would be a tiny concentration considering the relatively wide duct coverage offered by such systems). All camera based imaging systems are limited at the upper end by particle overlapping effects. Despite wide acceptance no thorough investigation into the effects of this phenomenon and the resulting limits of measurement has been undertaken. In general imaging systems are suited to dilute phase flows (an excellent example of such a flow being pulverised coal in the power generation industry).

Tomographic systems typically require dense flow in order to achieve concentration measurement (Barratt 2000). Such systems cannot be used to measure particle size as their spatial resolution is extremely low (orders of magnitude below a camera based imaging system). Their usefulness lies in the on-line visualisation of spatial concentration variation phenomena (inhomogeneity). Tomography systems are fundamentally non-intrusive in operation.

The measurement of non-spherical particles is problematic in general. Laser diffraction systems are adversely sensitive to shape and only provide accurate data when measuring spherical particles. Imaging systems can, in theory, measure non-spherical particles without difficulty but one point of interest that has been shown here is that sizing results can never be said to have absolute accuracy where non-spherical particles are concerned – results simply have relative variances from one instrumentation system to another.

In general imaging based particle analysis offers many potential benefits over laser diffraction systems. Based on the work reported in the past a system using a perpendicular laser sheet seems to offer the greatest promise. Complex image processing

difficulties could be overcome through the use of a front illuminated static system during software development. Investigations into the limits of measurement for both particle size and solids concentration need to be conducted and the insensitivity to particle shape must be quantitatively proven. Comparability of measurements with accepted off-line laser diffraction instruments must be investigated. The possibility of a simple, rugged, non-intrusive and cost effective industrial instrument based on this technique is interesting and this too requires investigation.

2.6 Summary

This chapter began by explaining the requirement for representative particle sampling – an issue that affects the validity of measurements made by various sizing systems. Various optical particle analysers have been reviewed and their benefits and shortcomings presented and discussed. It has been established that, despite the popularity of laser diffraction methodologies, imaging based systems represent the state of the art upon which further work must build. The shortcomings of past imaging systems have been analysed and the course to be taken by the present work, in order that such shortcomings are addressed through the application of novel techniques, has been identified. It has been shown that there is a need for quantification of the measurement limits for imaging systems in general, such work representing a useful contribution to this field of study. The practical implementation of the present work, based upon the requirements identified here, will be presented in the chapters that follow.

Chapter 3

Image Processing Techniques for 2D Particle Analysis

3.1 Introduction

Whilst the main purpose of this work is to develop an on-line system, many of the basic principles are more easily considered in an off-line, static analysis, context. For this reason this chapter presents the basic concepts of particle image analysis using the example of a static set-up (no physical details are discussed until Chapter 4). The problems and solutions involved in analysing each particle parameter are discussed and the method used in each case is detailed with emphasis on novel methodologies. The possibility of particle shape measurement is investigated along with size and concentration. Finally the underlying accuracy of the measurements is assessed. In this way the principles and limits of performance, for an imaging based system, are investigated without the additional complexity of on-line operation. Chapter 4 will take a more practical look at static analysis and in Chapter 5 the conversion to full on-line operation will be discussed.

3.2 Particle Sizing

3.2.1 Definition of the Problem

The size of particles is the most obvious parameter to be measured. Defining the size of an irregular shaped item is not as easy as it might at first appear. There are many possible ways of defining particle size (see Appendix A) in respect to its dimensions, volume, density etc. When working with images of particles the most practical method of defining size is to measure the area of each particle in the image. This can then, if necessary, be

used to calculate the particles 'equivalent diameter'; the diameter of a perfect circle of the same area, which is a widely used quantification (Rawle 2001).

It must be assumed for the purposes of this chapter that some kind of imaging arrangement is available whereby particles are laid in a flat sheet and images of them are acquired by a camera (similar 2D images can be achieved on-line with the use of a laser sheet – see Chapter 5). The general arrangement is illustrated schematically in figure 3.1.

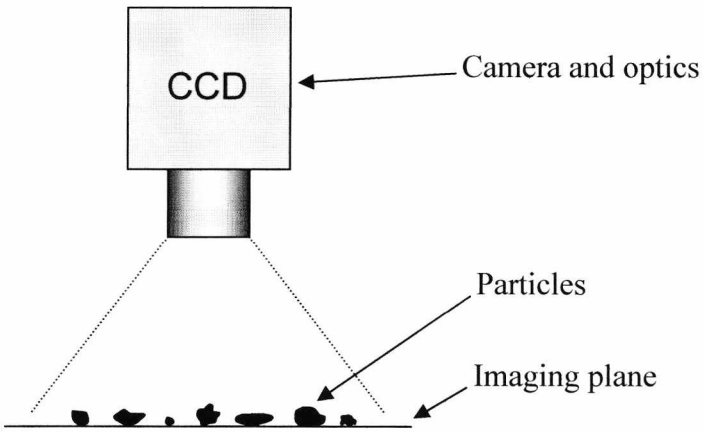

Figure 3.1 Imaging arrangement concept

In the past research work involving imaging based particle sizing has used back lighting, shadow imaging or other idealized lighting schemes (Nishino et al. 2000) that, though simplifying particle sizing for research purposes, do not lend themselves to practical use, or indeed to ready conversion for an on-line system (see chapter 2, section 2.4.2). Since one aim of the work presented here is to investigate a practical 'real world' set-up it was thought relevant to use a more realistic lighting approach. For this reason a front illumination scheme is used. The general arrangement is illustrated in figure 3.2.

The use of front illumination provides practical benefits – the lighting and camera can exist as a single unit, thus simplifying installation – and complex lighting optics are not required. The problem with this method, however, lies in the quality of the particle images. When using back lighting or shadow imaging the particle images generated are virtually in binary form already – i.e. the boundaries between particles and background are distinct. With front lighting the images demonstrate less favourable characteristics.

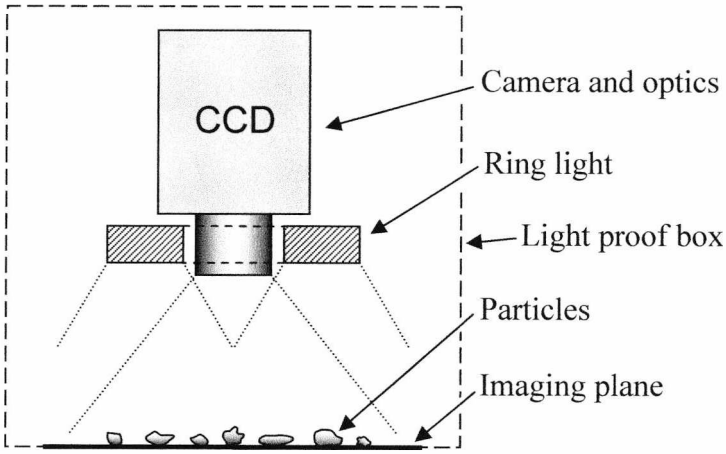

Figure 3.2 Imaging arrangement with front lighting

The edges of particles may not be distinct, there may be gradients or 'blurred' edges. The problem of determining the true particle boundary, and hence the particle size, thus becomes difficult when non idealized lighting is used. This is the main complexity in imaging based particle sizing. Figure 3.3 shows two particle images: - 3.3a shows an idealized, virtually binary, image of a type that would be generated by shadow imaging and 3.3b shows a practical image acquired with front lighting. It is clear to see that deciding on accurate particle boundaries for a real image is no easy task.

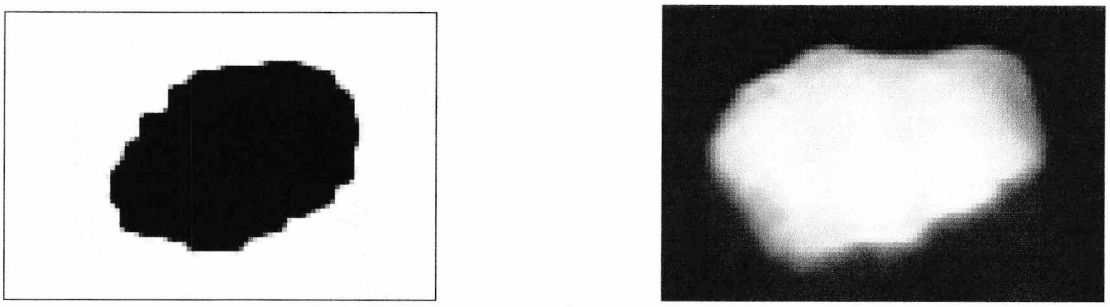

a) Particle shadow image

b) Front illuminated image

Figure 3.3 Illuminated particles

3.2.2 Particle Separation Methods

Once a physical setup of camera and optics is established it can be worked out what area each image pixel represents (see section 3.5). It is, therefore, necessary to in some way differentiate between image pixels that represent background and those that represent

particles. The number of pixels making up each particle can then be counted and the area of the particle simply defined:

$$A_p = \sum_{i=1}^{n_{pix}} A_{px} \qquad [3.1]$$

Where A_p is the area of a particle, n_{pix} is the number of pixels making up the particle and A_{px} is the area of each pixel.

When an equivalent diameter is called for this is defined, for the purposes of the present work, as the diameter of the circle that has the same surface area as a given particle's projected area. This relationship can be defined mathematically:

$$D_{eq} = 2\sqrt{\frac{A_p}{\pi}} \qquad [3.2]$$

Where D_{eq} is the equivalent diameter of the particle (Sometimes referred to as d_a – see Appendix A).

It can be seen that, once the number of pixels in each particle is known the derivation of size is a simple matter. Determining the exact location of the particle's boundary, and from there the number of pixels within it, represents, as has already been intimated, a problem of no little complexity.

There are three main methods of separating the particles from the background (i.e. determining the particle's boundary); Shape based methods, Thresholding and Smart gradient based perimeter detection. Shape based methods, such as Hough transforms, have been used widely for particle separation in the past (Shen et al. 2001). These methods rely on known particle characteristics in order to work – the approximate size and shape (in the case of Hough transforms all particle images must be circular) of the particles must be known already. This rules the method out for real world use where particles vary widely in terms of both size and shape. In order to assess the other two methods it is necessary to demonstrate the definition of the particle's boundary or perimeter and to provide an exaggerated example of a particle image with a heavy gradient.

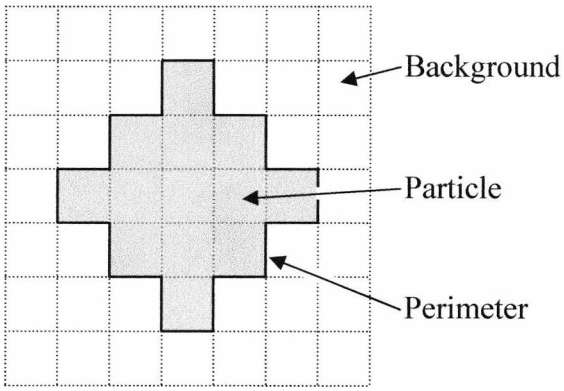

Figure 3.4 Particle Perimeter definition

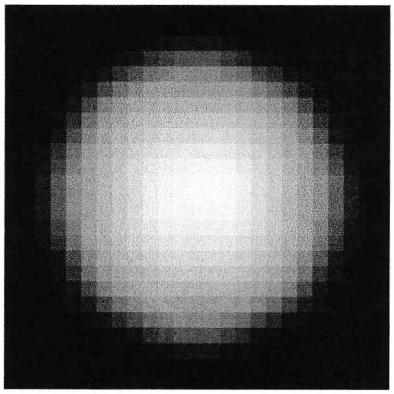

Figure 3.5 Particle image with exaggerated intensity gradient

From figure 3.4, in which pixel sizes are exaggerated for clarity, it can be seen that an exact definition of background and particle pixels is required. The boundary between particle and background is known as the perimeter.

Figure 3.5 shows a synthetic particle image that demonstrates an intensity gradient from the centre to the edge. Since the particle's edge blends smoothly into the background, defining a perimeter must always be a subjective procedure. What is required is consistent subjectivity in order that errors are systematic and can be trimmed out.

Since, in general, the background is dark and the particle is light, it is possible to determine an intensity level above which all pixels must represent part of a particle. This is known as thresholding. Thresholding is a very simple procedure requiring little computer time but it is not ideal; it can be very difficult to define a suitable threshold level (e.g. Kumar and Kannan 1994). Figure 3.6 shows that by using a varied threshold setting the particle from figure 3.5 can be seen to vary in size dramatically.

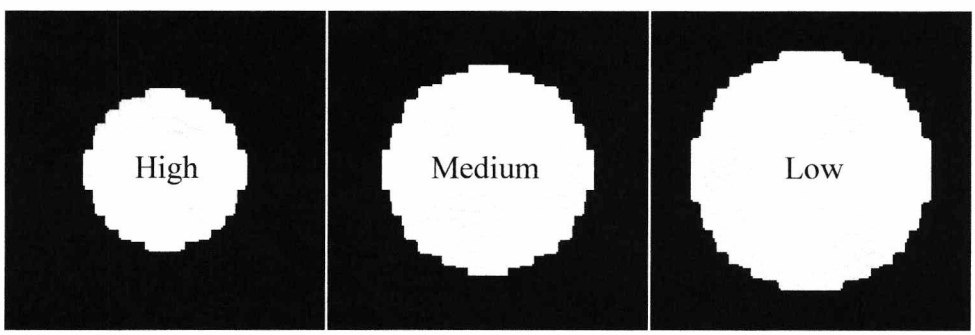

Figure 3.6 Thresholding the particle image from figure 3.5 at three different settings

If a repeatable procedure can be established for determining a suitable threshold level then, for on-line work, the method's low processing overheads become attractive. It should also be noted that thresholding is insensitive to particle shape – very irregular shapes with central holes or folded back features will be thresholded as reliably as simple circles.

The problem of deciding on a suitable threshold setting can be considered prohibitive to the use of thresholding and for this reason some particle imaging work has used smart gradient based perimeter detection (Bertollini et al. 1985). Gradient based perimeter detection, in its basic form, senses the changes in gradient of particle image intensity and assumes that there will be an inflection point in this quantity at the particle boundary. Figure 3.7 shows the change in intensity across the particle image of figure 3.5.

It can be seen from figure 3.7 that the boundary of the particle has been located. This location, though more insensitive to intensity variations than thresholding, is still based on a subjective determination. Some particles may exhibit 'crisp' well defined edges that will confuse this detection method. Furthermore, complex shapes or internal features may not be processed correctly (Nishino et al. 2000).

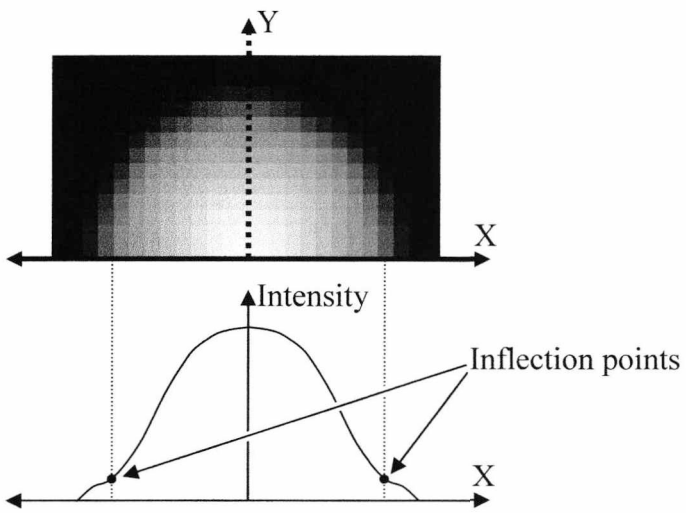

Figure 3.7 Change in intensity across a particle image

In order to assess the gradient of the particle it must first be tentatively located using thresholding – the gradient method refines the thresholded data. This means that any gradient processing must be performed in addition to thresholding and the gradient scanning is, in itself, a computer intensive task requiring many particle radii to be

processed. Table 3.1 presents a comparison between thresholding and gradient based edge detection. Thresholding is split into two groups: – simple and auto. Auto thresholding represents a theoretical system in which a suitable threshold level is determined automatically by the software.

Table 3.1 Comparison between thresholding and gradient based edge detection

Characteristic	Simple Thresholding	Auto Thresholding	Gradient Based Edge Detection
Complexity of algorithm	Simple	Medium-High	High
Processing requirements	Low	Low	Heavy
Complex shape handling	Excellent	Excellent	Poor
Variance of detected size with change in processing parameters	Large	Small	Small
Variance of detected size with change in image intensity	Large	Small	Small

After comparison of the various methods of particle detection it was considered desirable to devise an auto thresholding scheme, specifically tailored to particle imaging, for the current system.

3.2.3 Automatic Threshold Setting

Automatic threshold setting is a well known area of study in the field of image processing (Sankur and Sezgin 2002). Unfortunately general study of this field focuses more on scenic images (Milstein 1998) than scientific image analysis. The field of image segmentation for Optical Character Recognition (OCR) in desktop scanners would, at first, appear relevant as characters must be separated from a background. The problems addressed, however, do not include an accurate and consistent boundary characteristic – since this is not required for OCR – but focus mainly on ignoring real world scanning defects such as inconsistent background colours (Savakis 1998).

In view of a lack of suitable existing work on the subject it was necessary, for this work, to develop a novel auto thresholding method especially for particle imaging (see dissemination section items 2, 3 and 16). To this end, the first step was to analyse particle

images in order to understand their characteristics. Figure 3.8 shows a comparison between the synthetic particle image of figure 3.5 and a real particle image. The figure is split into four parts: (a) a close-up of the inside of the synthetic image, (b) the background of this image (which has been brightened by 20% for clarity), (c) the inside of a real particle image and (d) a real background (again, brightened by 20%).

It can be seen clearly that the real images contain noise. There is random intensity variation in both the particle and the background. When considering the change in threshold level it is easy to think that particles in the image will vary in size based on threshold setting until, at the extremes, they either blend into the background or the background becomes the same as the particles. The presence of noise in the images means that this behaviour becomes more complex. Consider the simulated noisy particle image of figure 3.9a. The approximate intensity distribution of this image is shown in figure 3.9b.

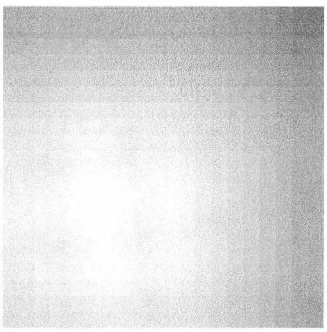

a) Synthetic particle close-up

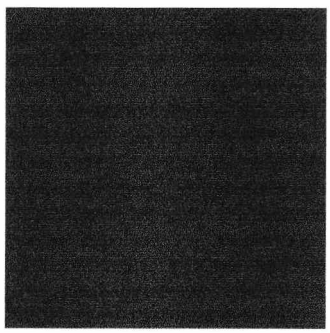

b) Synthetic background close-up

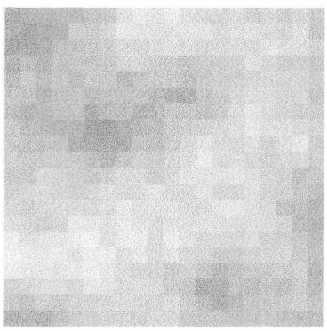

c) Real particle close-up

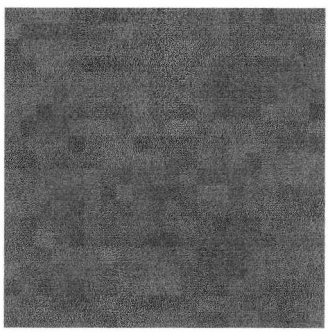

d) Real background close-up

Figure 3.8 Particle image close-ups

It can be seen from the intensity distribution that, though there is noise present, the particle pixel values are distinct from the background pixel values. If a threshold level is used from within the central 'dead' area then the particle will be separated successfully. The relevance of this realisation to automatic threshold level setting may not be apparent immediately but a little analysis of the intensity curve's characteristics will help here.

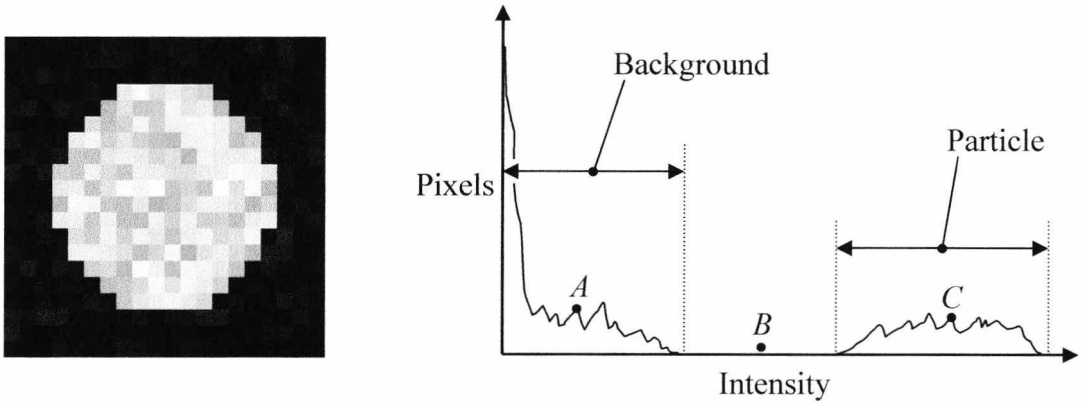

a) Noisy particle image

b) Approximate intensity distribution for (a)

Figure 3.9 Particle image intensity range

Consider a situation where the image is thresholded multiple times starting at zero intensity and ending at the maximum possible value. Initially there will be only one detected 'particle' in the resulting image since all pixels lie above the threshold level, but as the setting increases the noisy background will begin to break through. Some pixels will be above the threshold level but a large number of pixels, that are isolated from one another, will lie below it. This means that the number of detected 'particles' in the image will increase dramatically (these will not be real particles but noise related artefacts). The number of detected particles will drop, to the correct number (in this case one), once the central 'dead' area is reached. As the threshold value passes through the 'dead' zone, though the correct number of particles will be detected, their sizes will change slightly due to edge gradients, as discussed in the previous section. Once the threshold value enters the area of values that represents the particle then the particle will begin to 'break up' due to noise breaking through and the detected 'particle' numbers will again increase dramatically. This explanation is expressed diagrammatically in Figure 3.10a. This figure shows the figure 3.9a image thresholded at three key levels, indicated on figure 3.9b as A, B and C. Figure 3.10b shows the result of applying the same threshold settings to the same particle image but this time without added noise (i.e. an ideal synthetic image).

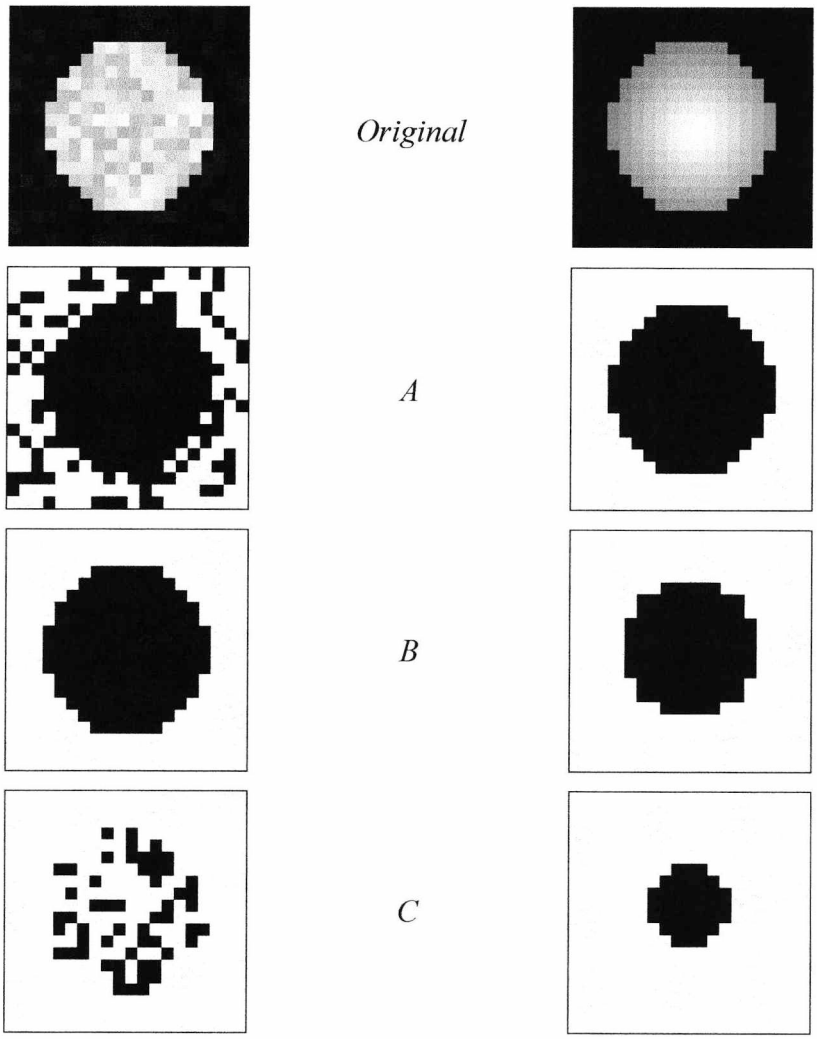

a) Thresholding a noisy image b) Thresholding an ideal synthetic image

Figure 3.10 Thresholding at three key levels

The effect in figure 3.10 is clear. The noisy image breaks up at thresholding extremes. If some way can be found of detecting this break up then a range of suitable thresholding values can be defined automatically. It can be assumed that, for a controlled particle imaging set-up, once a threshold level has been decided upon, the same value can be used until conditions change in some way. This change may be due to lighting variations, material type change or even variations in equipment over time. This leads, in turn, to the realisation that a noise breakthrough type threshold level setting would not need to be performed for every frame but that most frames could be processed using simple, high performance, thresholding (using the detected level).

Since it was anticipated that the analysis software would have to locate each particle within the image, in order to find its characteristics, the software would need to be capable of particle counting. When a particle counting processing algorithm is available then a sample input image can be thresholded at all possible settings and the number of detected 'particles' counted at each setting.

Through differential analysis of the resulting data a suitable thresholding range can be established. Figure 3.11 shows a theoretical result curve and highlights points of interest upon it – an approximate second order derivative curve is also shown.

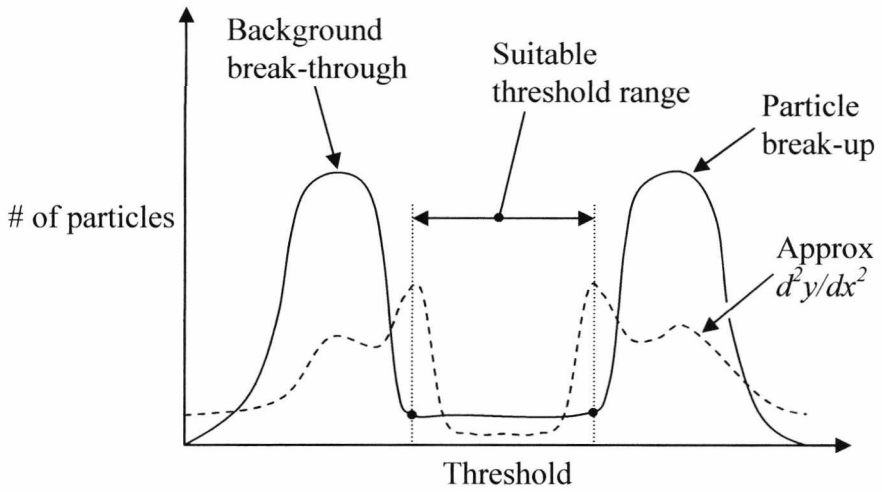

Figure 3.11 Theoretical threshold analysis curves

This graph indicates clearly; the initial increase in detected 'particle' numbers due to background breakthrough, the suitable range of thresholding values and the final particle number increase due to noise related break-up.

When requested to set the threshold level automatically the current software analyses the number of 'particles' present at each threshold setting. These data are then filtered, in order to avoid false detections, using a rolling average filter:

$$\overline{x_d} = \frac{\sum_{i=-W/2}^{W/2} x_d}{n} \qquad [3.3]$$

Where x_d is the data value, $\overline{x_d}$ is the averaged result and W+1 is the width of the filter window (W must be an even number). A window width of 21 has been found, through experiment, to give good results. Values at the extremes are padded with the initial or final value in the data set. Inaccuracy at these extremes is unimportant since these parts of the curve lie beyond the useful range for auto thresholding. Rolling average filters use no complex math routines and, therefore, execute swiftly and efficiently.

The continuous gradient of the filtered data is now found. Again, a window type operation is performed and in this case a width of seven has been found to be suitable. The operation is described in Equation 3.4.

$$M = \frac{\left(x_d + \frac{W-1}{2}\right) - \left(x_d - \frac{W-1}{2}\right)}{W} \qquad [3.4]$$

Where M is the gradient data, W is the window width (which must be an odd number in this case) and x_d is the filtered particle numbers data (from equation 3.3). The points of interest on the curve must now be found and this is performed by the software through the use of a systematic search algorithm. The software searches for four points, or features, on the curve, two of which represent the thresholding range extremes. The location of these points is illustrated in figure 3.12. The search algorithm is shown diagrammatically in figure 3.13 and its explanation follows.

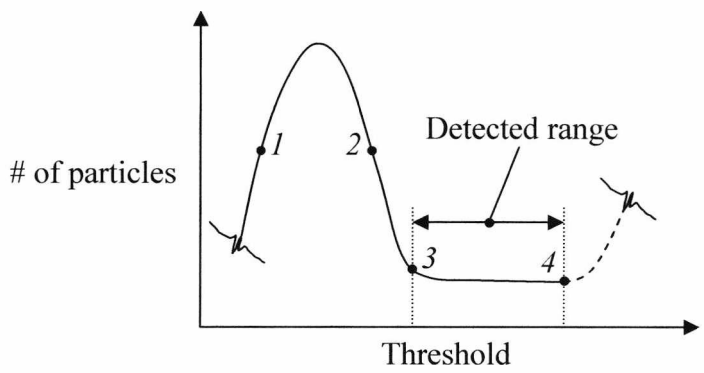

Figure 3.12 Points of interest for the search algorithm

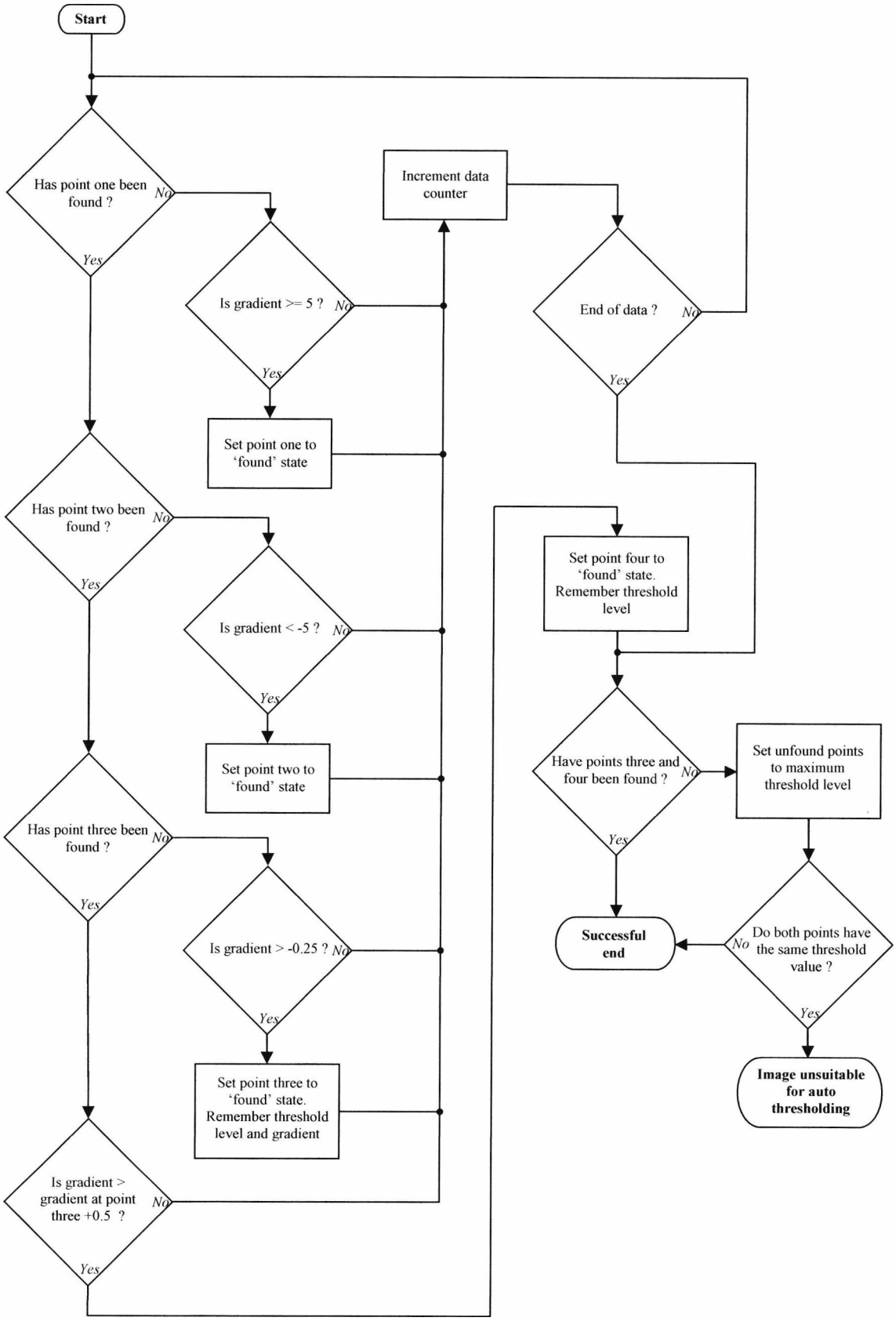

Figure 3.13 Threshold range search algorithm

The first point (marked '1' in figure 3.12) represents the initial increase in particle numbers due to background breakthrough and is detected in the software by searching through the values until a gradient of greater than five has been found. Once this point has been located point two can be found. Point two represents the fall from the initial background breakthrough peak and is detected by finding the first instance of a gradient of minus five or less (after point one – the initial point cannot be ignored since, in some data, a dip has been observed before the initial peak which can lead to false detections). Point three represents the beginning of the suitable thresholding range and is characterised by having a gradient of greater than or equal to -0.25. Point four is the end of the thresholding range and is detected when the gradient becomes greater than the gradient at point three plus 0.5. The values chosen for these gradients have been selected after observing many sets of data and have been found to be reliable in most instances.

There are some data sets – i.e. images – that do not lend themselves to auto thresholding in this manner. Such images are characterised by containing little noise and consisting of clearly distinguished particles. These images can, in most cases, be assigned a threshold value manually – a reliable method due to their well defined nature.

A more difficult problem is presented by a third group of images that are not well defined and do not contain strong enough features to be processed successfully using auto thresholding. For these images an operator must subjectively judge the thresholding curve and decide on suitable values through experience. The software will warn the operator when an image is not suitable for auto thresholding by adopting a simple methodology; points of interest that are not found by the search algorithm are assigned their maximum possible value. If points three and four have the same value at the end of processing then the image was unsuitable for automatic processing. It is possible in some instances for point four to be close to the end of the data set – in such cases the final peak of particle break-up does not exist.

Figure 3.14 shows actual results of applying the auto thresholding algorithm. Figure 3.14a is a typical particle image (the material is maize) and figure 3.14b shows the thresholding curve generated by the software. Figures 3.14c & d are similar but use a clean, synthetic, image that was unsuitable for auto thresholding. The thresholding curves indicate chosen thresholding extremes with circular points. The small dots around the line represent

unfiltered data (visible mainly in figure 3.14b) – the smooth curve is filtered. The software warned of an unsuitable image in the case of figures 3.14c & d.

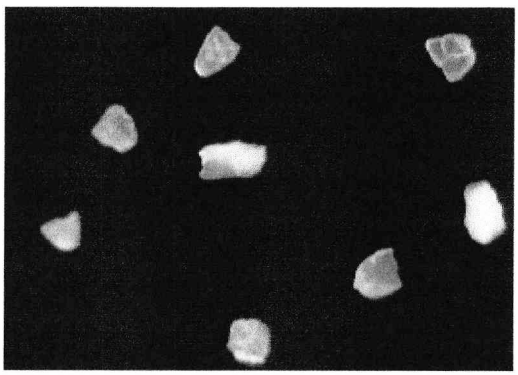

a) Typical particle image

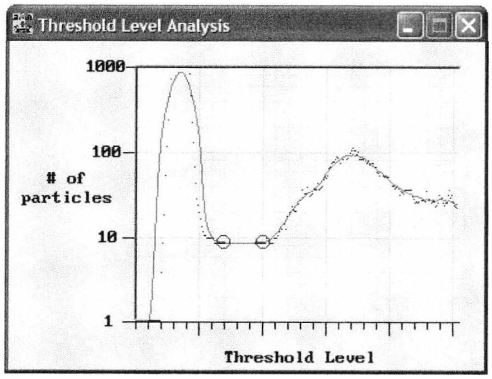

b) Threshold curve and points for (a)

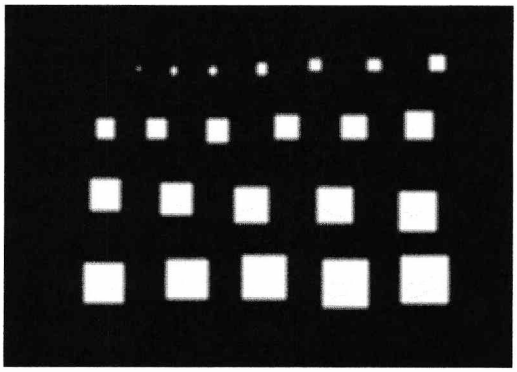

c) Unsuitable synthetic image

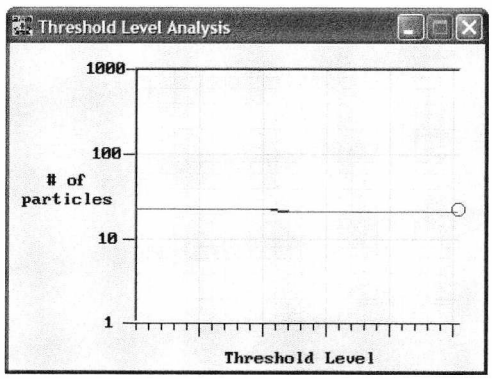

d) Thresholding for (c)

Figure 3.14 Automatic thresholding curves

It has been seen that the auto thresholding technique used is dependant on the availability of a particle counting algorithm. A few words of explanation will now be offered in respect to the particle counting system used in the current software. Particle counting is used after the thresholding has taken place. This means that the image is in a binary form – i.e. particle pixels are represented by one intensity level and background pixels by another. In the current software a dynamically allocated memory array is set-up to contain information on various particle parameters such as area (in pixels) and centroid (in x, y co-ordinates). The algorithm used for particle counting also fills in the other data in the array thus performing several steps at once and saving on processing time. The algorithm operates as follows:- Scan through the image starting at the origin (top left) and working through line by line. When the current pixel is a particle pixel increment the particle

count, store the current co-ordinates for future use and perform a flood fill on the current particle. During the flood fill note is taken of the number of pixels filled and the minimum and maximum x and y co-ordinates in the particle and the relevant information is filled into the particle parameter array. After the flood fill (which fills the particle with a third intensity level that will not be detected as a particle) the algorithm jumps back to the stored scanning co-ordinates and continues the scan. After the entire image has been scanned the parameter array contains information on all particles in the image. The number of data sets in the array, and hence the number of particles in the image, is known. This methodology provides high performance processing, acquiring all information from the image in one pass. The operation of this algorithm is clarified diagrammatically in Figure 3.15.

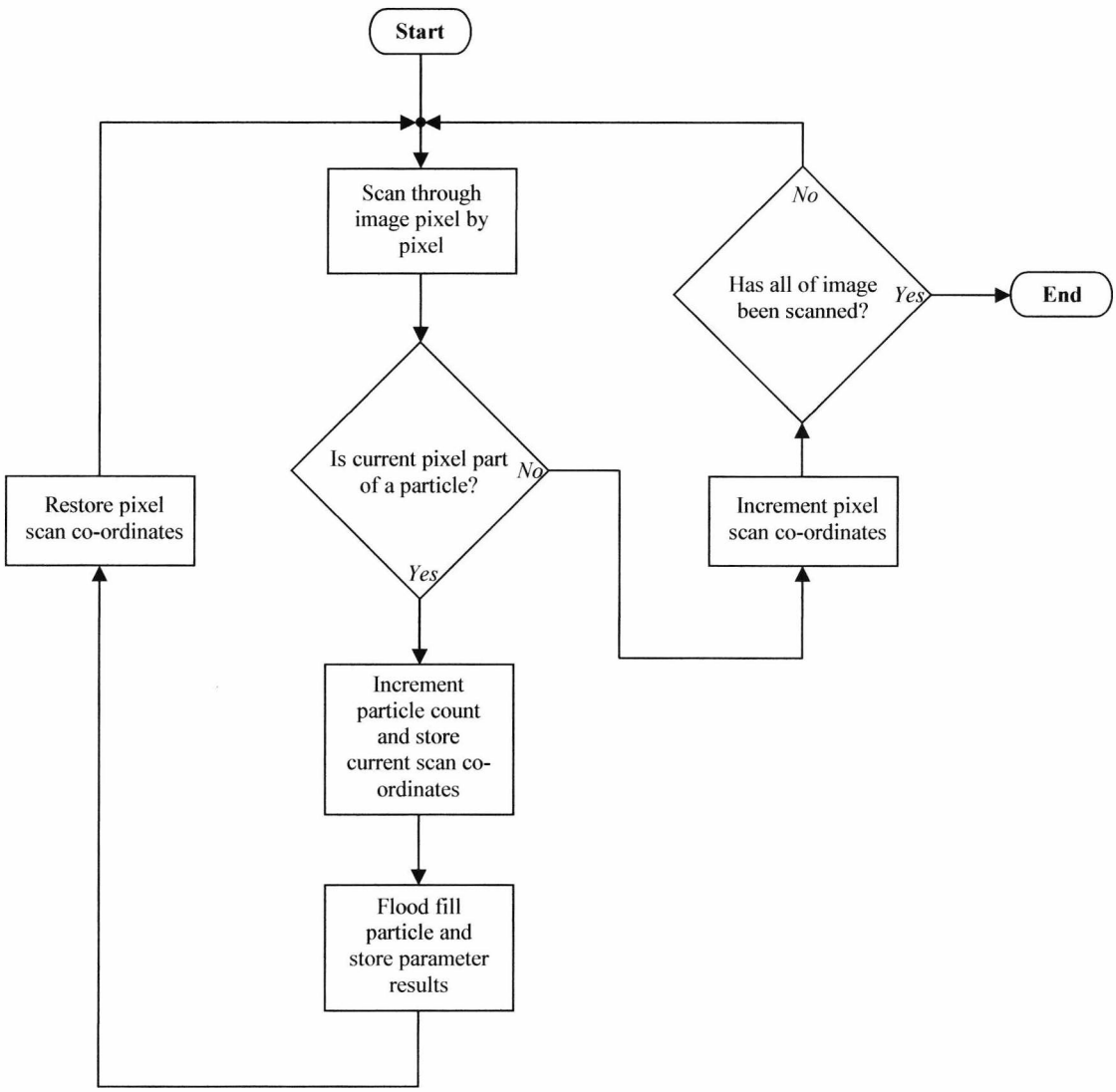

Figure 3.15 Particle scan algorithm

3.2.4 Fuzzy Processing – Spatial and Temporal Variance of Threshold

The previous section detailed a method of establishing a range of suitable thresholding values. Within that range, detected particle size could be expected to vary slightly. Figure 3.16 shows a typical variation of detected particle size through a typical thresholding range. This result was generated using a static calibration image as discussed in the next section. The detected thresholding range was about 90 to 170 (pixel intensity values may vary from 0 to 255) – the first and last data points show particle size falloff (due to noise breakthrough – the detected particle size decreases as the numbers increase).

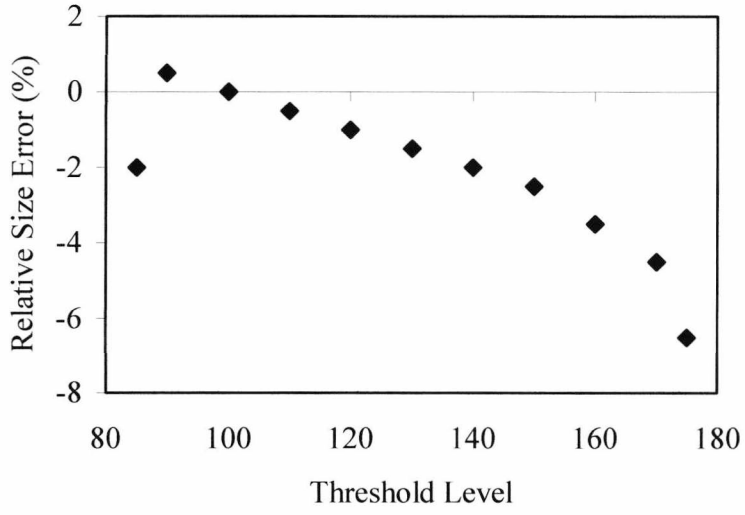

Figure 3.16 Variation of particle size through detected thresholding range

It would be possible to simply use the threshold level in the centre of the thresholding range. In the example of figure 3.16 this would give a relative error of about -2% which would be acceptable in an industrial environment. This, however, is not an ideal solution and it was decided to develop a novel method which would allow the whole thresholding range to be utilised in order that errors may be reduced.

Manual microscopy is one of the most well established particle sizing techniques in existence and is believed, by some, to offer many potential benefits (Rawle 2001). In microscopy the principals are similar to those employed here except that processing is performed, not by an arithmetic digital computer, but by an associative analogue system – the human brain. The human brain does not work with 'crisp' digital data but 'fuzzy'

quantities. Fuzzy computing techniques that imitate the approach taken by natural systems are becoming increasingly popular in improving the performance of scientific systems (e.g. Shen et al. 2001). Such techniques can, in concept, be applied here. Although the system developed is not a fuzzy logic system in the generally accepted sense (i.e. there are no fuzzifiers or fuzzy data sets etc.) it certainly uses a 'natural algorithm' approach. The system works on the following assumptions:-

1) If manual microscopy is considered accurate then making the system imitate human judgement will improve its performance.

2) When a person examines particles visually they will always, subconsciously, use a slightly different set of parameters to define the perimeter of each particle.

Point one can be deduced from the preceding discussion but point two is more interesting. It suggests that when a person analyses a particle image they will oversize some particles and undersize others – these errors will, over the entire image frame, provide a consistent mean particle size measurement. When an automatic system, with a fixed threshold level, analyses an image it will either oversize or undersize consistently. This will result in a fixed offset error. Such systematic errors can be trimmed out, where reference data are available, but it is preferable for a system to be free of such errors from the outset.

If the threshold level used by an automatic system is varied randomly within the suitable thresholding range then, over several frames, this 'fuzzy' approach will give results similar to human microscopy. Furthermore, if the threshold level is varied randomly across each individual frame (still within the suitable range) – i.e. varied spatially as well as temporally – then the same result can be achieved on a frame by frame basis. In theory this approach could be adopted on a per-pixel basis although this would require the generation of a pseudo random number, and the associated processing, for every pixel in the image. With hundreds of thousands of pixels in each image this would slow the system down considerably and so, in the present system, the image is split into a grid of 50 rectangular zones each of which uses a random variation of the detected threshold values. With many thousands of operations reduced to just 50 the processing performance impact, with this approach, is minimal – there is, however, a possible shortcoming: The fewer the number of zones then the slower the response to changes in particle size

distribution – if there is no spatial variance at all then that is the same as using just one zone – and averaging only occurs between frames and not on a frame by frame basis. The number of zones must be decided upon arbitrarily and, in practice, the use of 50 zones has proven to represent a good compromise between processing speed and averaging performance.

When threshold values are automatically varied within the detected range the complete thresholding process becomes automated. Under most circumstances no user interaction is required in order to establish particle separation parameters. This leads to consistent performance.

3.2.5 Sizing Performance

In order to establish the basic accuracy of the system it was deemed necessary to examine particles of known size and calculate system errors. Since the present system works on two dimensional images it was possible to use an alternative to the usual reference materials used to calibrate sieves and other particle sizing apparatus. Reference materials are expensive and hard to find – the present system uses synthetic images of particles printed in sheets using an ink jet printer.

Using printed images is an undertaking that is not without potential problems. Particle images can be generated readily using image editing software and, if a sufficiently high resolution is used aliasing (jagged edges) of the particles will not be a problem. If the images are printed accurately the exact size of the 'particles' will be known. This leads to the next problem; the printing process. For the current work a consumer ink jet 'photo' printer was used. The device offers a resolution of 2880dpi, suggesting accuracy to better than one thousandth of an inch (<0.025mm). It is unlikely that this accuracy can be relied upon, for scientific purposes, and so the order of magnitude rule was used: It was decided that the minimum size of printed particles should be 250μm. The highest quality ink and 'matte' paper were used and the images appeared 'crisp' without signs of running. An example image is shown in Figure 3.17.

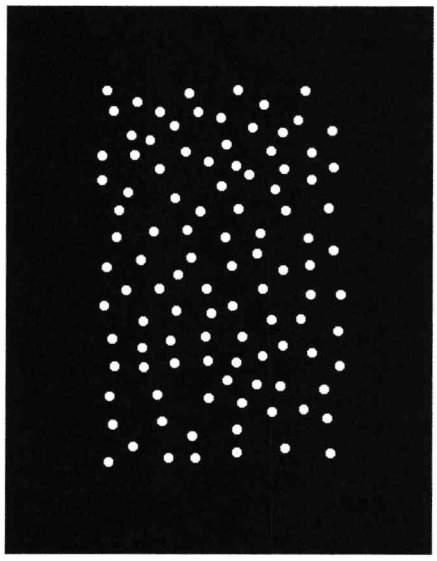

Figure 3.17 Example reference image – when printed these 'particles' are 1mm in diameter

Various images were generated covering four particle sizes and several concentrations of particles (particulate concentration is covered in the next section) at each size. Details of the images generated are given in table 3.2.

Table 3.2 Details of reference images

'Particle' sizes (μm)	Approx. concentration range (%)	Number of 'particles' in images
250	0.005-0.7	1-128
500	0.02-1.7	1-80
1000	0.08-3.3	1-40
2000	0.3-3.3	1-10

For the smaller sizes of particle the number of particles in the images became unmanageable at higher concentrations and so upper limits were set – the lower limits were, of course, set by the sizes of the individual particles. Ten images were created for each particle size (ten concentrations).

The printed reference images were placed under a camera and lighting setup similar to the conceptual arrangement illustrated in figure 3.2 (exact details of the imaging arrangement will be discussed in chapter 4). The auto thresholding process was initiated for each image and the system was allowed to take multiple frames until the size measurement had stabilised (required due to spatial averaging) – a total of 90 video frames were taken for

each measurement result. Each size result represents the mean of those achieved for all reference images featuring a given particle size. Since there were ten images for each size the data points shown on the following graphs represent mean data from 900 video frames.

Figure 3.18 shows the basic linearity of the system. Deviations from the linear are shown more clearly in figure 3.19 which presents the relative errors from figure 3.18.

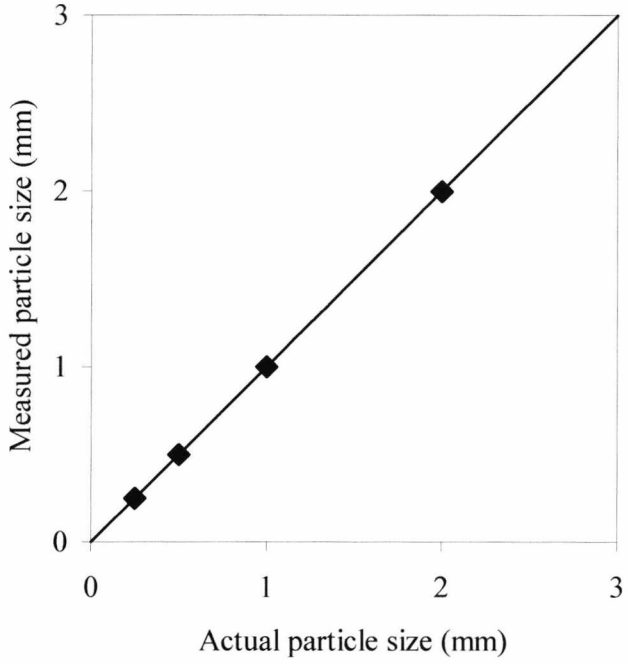

Figure 3.18 Comparison of measured and actual particle size

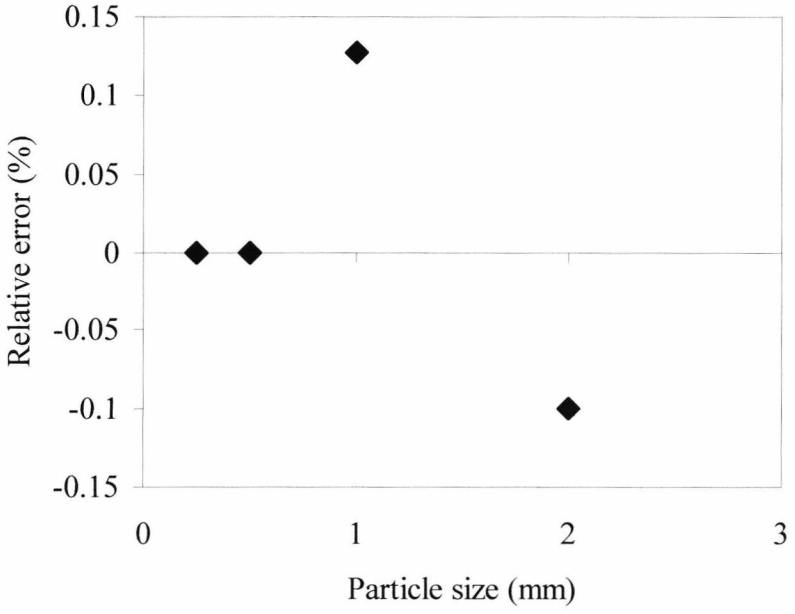

Figure 3.19 Relative errors of figure 3.18

It can be seen that the system exhibits excellent linearity with relative errors of less than ±0.15% in all cases. The first two data points in figure 3.19 suggest that the system is perfectly accurate, i.e. there is zero error, and some words of explanation will now be offered in respect to this issue. The software logs size data results in millimetres to an accuracy of three decimal places. When the ten test images featuring, for example, 250μm particles were tested the resulting size values varied from 0.242mm to 0.254mm. When the mean of these ten values was calculated it was exactly 0.250mm – a similar situation occurred in respect of the 500μm particles. Clearly, there must be an error here as no system is perfect – if more decimal places were available then a small calculated error would emerge (if we add a decimal place then the worst case actual mean value would be either 0.2495 or 0.2504mm giving *maximum* relative errors of -0.2% or +0.16%, respectively, which is in line with the other errors and still very low). The decision to limit the software's output to three decimal places was made in order that it would not appear to be more accurate than it can realistically be expected to be.

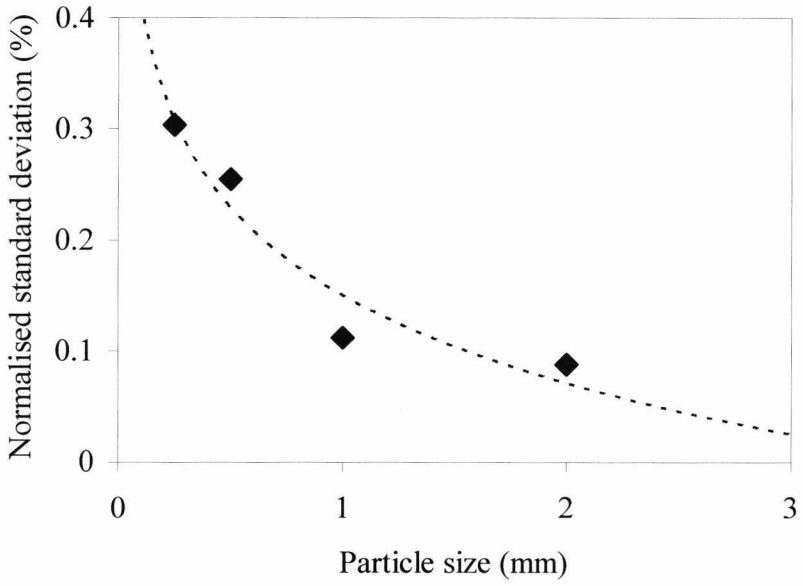

Figure 3.20 Normalised standard deviation of the particle size measurements

In order that the repeatability of the measurements could be quantified the standard deviation of each set of size readings, normalised to their mean value, was found. This is presented in figure 3.20. It can be seen that, in all cases, the repeatability is better than 0.3%. The increase in the standard deviation for the smaller particles is attributed, in part,

to an effect of the normalisation process but can also be explained readily in more practical terms. Repeatability issues will cause consistent variations in the lower decimal places of the results irrespective of the size of particles being measured. The effect, expressed as a percentage, of these variations will, naturally, be higher for smaller particles than for larger ones.

3.3 Concentration Measurement

It has been explained already that an imaging based particle measurement system must be aware of the number and size of particles in the images. It is possible, therefore, to specify the quantity of particles as an end result in its own right and not just a step in the sizing process – this is the concept of concentration measurement.

3.3.1 Basic Principle – Solids Concentration

The quantity of particles present in each image could be simply specified as a number – i.e. the numerical quantity of particles present. This quantity, however, is of limited use. In the bulk solids handling industry the quantity of particulate material present in a flow system, at any one time, is commonly defined as the Volumetric Concentration of Solids or $\beta_s(t)$. This represents the total quantity of moving solids within a pipe or duct and is defined as the cross sectional area occupied by the moving solids, normalised to the entire cross sectional area of the pipe or duct as a percentage:

$$\beta_s(t) = \frac{A_s(t)}{A} = \frac{\iint \beta(x,y,t)dxdy}{A}(\times 100\%) \qquad [3.5]$$

Where A is the area of the pipe or duct, A_s is the area occupied by solids and $\beta(x,y,t)$ is the local solids concentration. $\beta_s(t)$ represents the instantaneous solids concentration (for one frame) and, in practice the time averaged value is more useful:

$$\overline{\beta_s} = \frac{1}{t_1}\int_0^{t_1} \beta_s(t)dt \qquad [3.6]$$

The imaging approach to particle interrogation can, of course, establish both of these quantities quite readily. It has already been shown that the size of particles can be determined with some accuracy and that the number of particles present is known. The solids concentration, therefore, can be defined as the ratio of particle pixels to total pixels, expressed as a percentage:

$$\beta_s(t) = \frac{\sum_{1}^{x_{pix} \times y_{pix}} P_i}{x_{pix} \times y_{pix}} (\times 100\%) \qquad [3.7]$$

Where x_{pix} and y_{pix} represent the x and y image size in pixels, respectively, and P_i represents the currently interrogated pixel, this quantity being equal to one if the current pixel is part of a particle and zero if it is not. It is also possible to express this in terms of the total measured area occupied by particles in relation to the total area interrogated by the camera:

$$\beta_s(t) = \frac{\sum_{0}^{n} A_p}{x_{mm} \times y_{mm}} (\times 100\%) \qquad [3.8]$$

Where n is the number of particles in the image, A_p is the area of each particle and x_{mm} and y_{mm} are, respectively, the x and y size of the interrogated area in mm.

Since all necessary data are provided by previous processing of the image no further explanation of method is required here – the software can derive instantaneous solids concentration information through the application of equation 3.7 or 3.8 and a time averaged value can be achieved through averaging the result over a number of video frames.

3.3.2 Concentration Measurement Performance

In order to assess the basic accuracy of solids concentration measurement, tests were performed using the static calibration images described in section 3.2.5.

The printed reference images were placed under the same camera and lighting setup as used for the sizing performance measurements. The auto thresholding process was initiated for each image and the system was allowed to take multiple frames until the concentration measurement had stabilised (required due to spatial averaging) – a total of 90 video frames were taken for each measurement result. At each concentration level four particle sizes were available (where possible) and the results from all sizes were averaged in order to achieve a mean concentration value. Most data points, therefore, consist of data from four test images – or 360 video frames. Some of the higher points only consist of data from two test images due to the problems of large particle numbers for smaller particles.

Figure 3.21 shows the basic linearity of the system. Deviations from the linear are shown more clearly in figure 3.22 which presents the relative errors of the measured solids concentration.

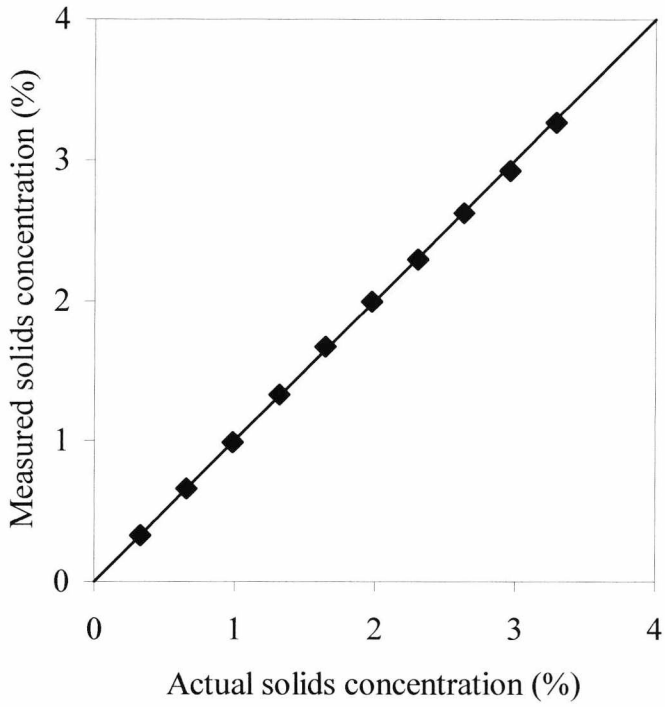

Figure 3.21 Comparison of measured and actual solids concentration

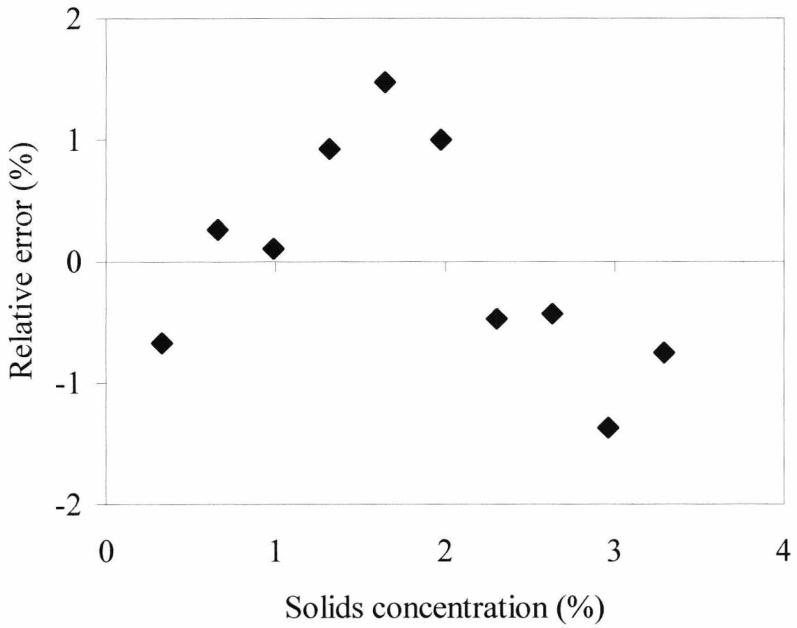

Figure 3.22 Relative errors of concentration measurement

It can be seen that linearity is very good. The relative errors are larger than those experienced for particle sizing, but this is to be expected – if there is a sizing error for each particle then these errors will affect the solids concentration result in a cumulative manner. All errors lie within ±2%.

In order to assess the repeatability of the measurements the normalised standard deviation of each concentration reading was found. This is presented in figure 3.23.

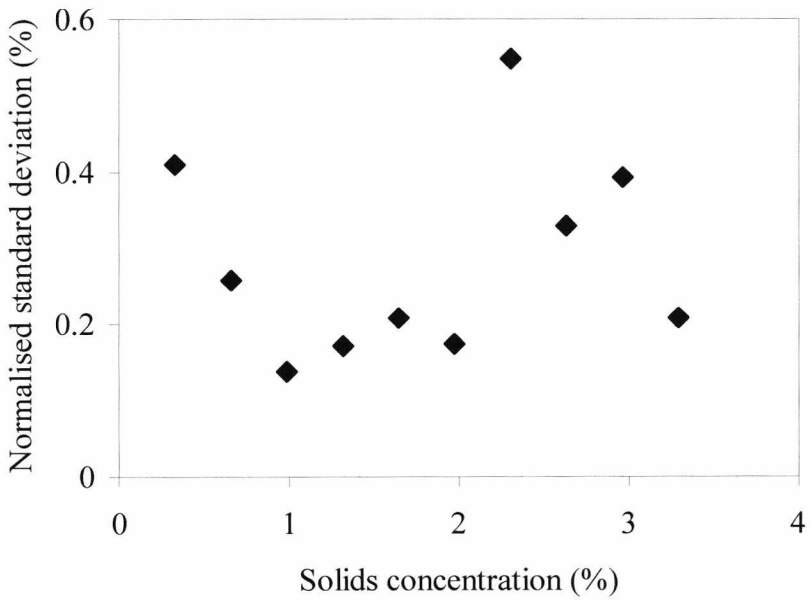

Figure 3.23 Normalised standard deviation of the concentration measurement

It can be seen that, in all cases, the repeatability is better than 0.6%. There is no increase in standard deviation for the lower values here. This is due to the fact that the concentration measurement is heavily linked to size measurement results and the increase in standard deviation of sizing results (for smaller particles) has been eliminated here as a result of averaging the concentration measurements from several different particle sizes.

3.4 Particle Shape Quantification

The size and quantity of particles are not the only useful data that are needed. It is possible that two different particles may exhibit the same size but be of completely different shapes. This variation of shape could result in a change of actual (3D) surface area – this could be a very important parameter in, for example, the pharmaceuticals industry, where the surface area of particles may affect the rate of reaction of a given mixture of chemicals. The importance of particle shape in industry is widely accepted (see for example Davies 1975 or Lohmander et al. 2001) not only in terms of product quality (broken particles would exhibit jagged edges for instance) but also the handle-ability of particles in bulk form (Human 1992, Leung et al. 1996).

An imaging based approach can be used to provide some quantification of shape – obviously only a cross sectional view of the particles is available but, within these bounds, it is possible to produce some relative indication of the shapes of particles within each image. Such work is not new (e.g. Poczeck 1997) but the present work would not be complete without a study of the ability of a cost-effective imaging system to measure this characteristic under realistic conditions. It is accepted that past attempts at shape characterisation leave room for improvement (Bowman et al. 2000).

3.4.1 The Concept of Quantified Shape

The problem in quantifying shape lies in what to quantify. The difficulty lies in reducing the two dimensional image of a particle's shape to a single figure or meaningful set of figures. This problem is not new and the work of many researchers in the field has been reviewed in the past (Clark 1981). Since the present research concentrates upon particle

size and concentration it would not be appropriate to provide a full review of particle shape characterisation here. A brief overview will be given, however, in the interests of completeness and convenience. The problem can be better understood through considering the four 'particles' shown in Figure 3.24.

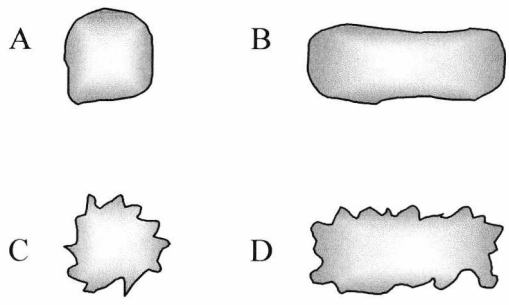

Figure 3.24 Particles of differing shapes

In this figure it can be seen that particles A and C are both of roughly the same area and general form factor – they are both 'rounded'. Particles B and D may be similarly compared though, of course, these particles are both elongated in shape. It is also possible to liken A to B and C to D since these two combinations are smooth and rough respectively. Since these four particles' shapes are interrelated it is clear that definition of shape with a single parameter is difficult.

Early work on the quantification of particle shape centred upon morphology studies in the field of soil mechanics. Wadell (1932) defined a 'roundness' characteristic of particles (the ratio of the curvature of the corners and edges of the particles to that of the overall particle) whilst Krumbein (1941) defined 'sphericity' (the ratio of a particles volume to that of the smallest circumscribing sphere). Both of these parameters required complex subjective analysis of particle features and were applied, for practical purposes, through the use of comparative charts (developed, respectively, by Krumbein 1941 and Rittenhouse 1943). Heywood (1954) suggested a shape coefficient which used measurements of surface area and volume to categorize particles into rough categories such as 'tetrahedral', 'sub-angular' and 'rounded'. Work in the field has continued and more recently image analysis techniques have been suggested working on a number of principles, from the comparison of individual particles to standard forms (Poczeck 1997) to fractal analysis (Vallejo 1995) and Fourier analysis of particle perimeters (Bowman et

al. 2000). In much recent work definitions of particle form and texture originally created by Barrett (1980) are used though there is still no generally accepted, standardised, method through which particle shape may be quantified by image analysis.

It is not the intention with the present research to solve the long standing problem of particle shape definition, or indeed to attempt to standardise on a particular definition, but rather to assess the ability of an imaging based system to consistently measure *a shape measurement of some kind* and prove its usefulness. In keeping with the rest of this work a parameter that lends itself to high performance processing is required. In order to explain the choice of shape factor decided upon a general discussion on the problems of shape definition will now be presented.

In order to accomplish a meaningful shape measurement in the case of the four particles presented in figure 3.24 two aspects of the images must be taken into account; the form factor or 'aspect ratio' (a widely understood concept) of particles and also the 'roughness' of their perimeters. In practice, whilst the first parameter is reliable the measurement of surface roughness is not. In its basic form this requires some kind of frequency domain analysis of particle perimeter data. Such analysis will consume much computer time and will produce complex results – a spectrum of frequencies appearing in the particles' perimeters will be generated rather than a single numerical result (this may be of use in certain situations, e.g. Thomas et al. 1995, but is generally of little use in industry). Consider the three particles in Figure 3.25.

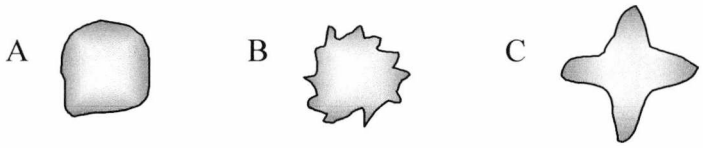

Figure 3.25 Particles of varying surface 'roughness'

Clearly these particles have similar aspect ratios and surface areas (from the 2D point of view) but the perimeter 'roughness' varies. The perimeter of particle A contains very low frequencies whereas that of particle B contains higher frequencies. It might be thought that simply producing an average frequency result would be sufficient but then the analysis of particle C, which presents both high and low frequencies, would produce a

misleading result. Clearly, from the points of view of both processing complexity and ambiguity of results a simper method of perimeter complexity quantification is required. It is for this reason that a 'shape factor' must be defined that is simpler to calculate, producing clearer numerical results than a frequency domain analysis alone. This factor should represent a calculated definition of particle shape rather than a matrix based comparison with known shapes such as that suggested by Poczeck (1997).

The following section describes how aspect ratio and 'shape factor' are defined in this instance and explains a novel algorithm that has been developed which allows both quantities to be found using just one scan of each video image. Using a single scan allows faster processing – one of the aims of the current research being to concentrate on practical, real time, analysis techniques.

3.4.2 Definition of Parameters

3.4.2.1 Aspect Ratio

The aspect ratio of a shape is a very simple concept and is, in general, defined as the ratio of that shape's long dimension to its short dimension. This may also be expressed as a single figure, rather than a ratio, that is defined as the minimum dimension divided by the maximum. This is shown in equation 3.9.

$$R_a = \frac{x}{y} \qquad [3.9]$$

Where R_a is the aspect ratio, and y and x represent Cartesian dimensions. This is shown diagrammatically in Figure 3.26.

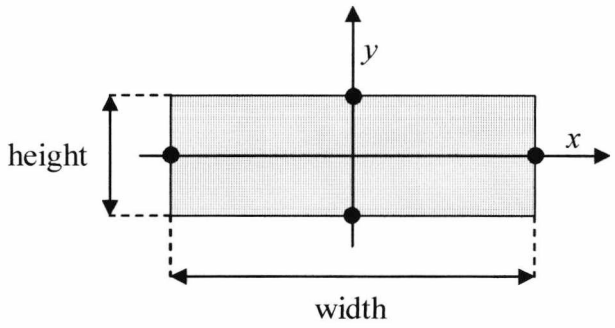

Figure 3.26 Basic aspect ratio measurements

In theory and for objects with known orientation it is easy to specify the longest and shortest measurements. In practice, when examining particles, this is not as simple since particles of various shapes and orientations will be present – it will involve examining particles at various different angles. The variation in results between different aspect ratio measurements is an accepted problem (e.g. Lohmander et al. 2000) that is worthy of research in its own right. For the purposes of the current work it is necessary only to define the particular aspect ratio determination technique employed here and justify this choice. Consider the particles in Figures 3.27 a, b and c – note that measurements are illustrative rather than technically accurate.

In this figure we see three possible ways of defining the minimum and maximum dimensions of a particle. Figure 3.27a shows an external method of achieving this – it works in a similar way to using callipers to size an object. Two parallel lines are drawn that touch the particle's opposite boundaries, the particle is then rotated and the minimum and maximum distances between the lines are recorded.

Figures 3.27 b and c show internal methods of finding the necessary dimensions. When the location of the particle's centre of mass is known (this information is generated during particle sizing – see section 3.2) it can be used as a 'fulcrum' through which the measurements must pass. It is then possible to find the minimum and maximum distances to the particle's boundary, as in figure 3.27b, or find the maximum distance to the boundary and then find the distance to the boundary that is perpendicular to this as in figure 3.27c.

The 'calliper' method is the most intuitive. In practice, however, problems may be caused if there are other particles close by – this method would translate into a fairly complex processing algorithm. The internal methods are more promising since the algorithm has a starting point (the centre of mass) and need only scan within the bounds of the particle. Although the perpendicular method of figure 3.27c looks 'neatest' it is, in reality, less valid then the simpler figure 3.27b method since the minimum measurement is not a true minimum but is dependant on the location of the maximum value. It should be noted that these two methods will give very similar results in the case of elongated particles (with a large aspect ratio) – the non-perpendicular method serves to highlight minor differences between similar particles when the aspect ratio is not large).

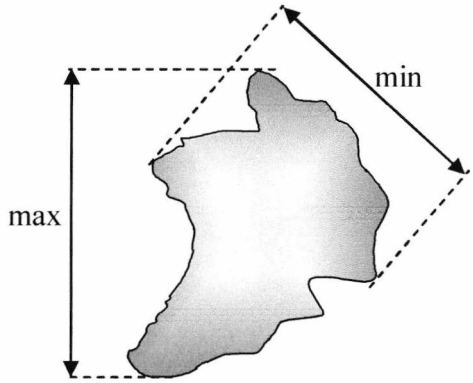

a) External maximum and minimum dimensions of a complex shaped particle

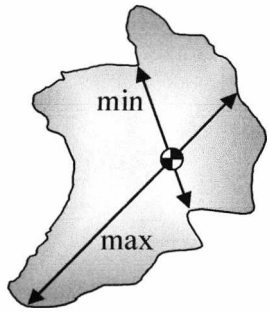

b) Internal dimensions of a complex particle passing through the centre of mass

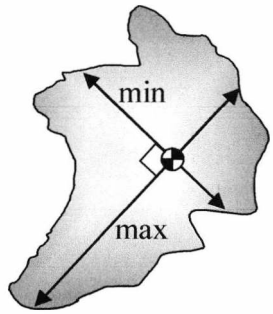

c) Internal dimensions passing through the centre of mass and remaining at right angles

Figure 3.27 Aspect ratio measurement strategies

The properties of these three methods are summed up, for ease of comparison, in Table 3.3. It can be seen that the internal non-perpendicular method has the best combination of features. It is this method that was chosen for implementation in the present research.

Table 3.3 Summary of aspect ratio measurement methods

Method	Intuitiveness	Ease of processing	Ability to resolve small variances
External – 'Calliper'	Best	Poor	Good
Internal – non perpendicular	Poor	Best	Best
Internal – perpendicular	Good	Good	Poor

3.4.2.2 Shape Factor

To define a 'shape factor' is, by its very concept, a proprietary undertaking. In general the type of shape factor required here can be described as 'deviation from round' or 'circularity'. It is not, therefore, insensitive to changes in aspect ratio but should be considered *with* aspect ratio in order to provide fuller information.

The information necessary in order to calculate the shape factor is full data on the variations of the perimeter of the particle. As with aspect ratio it would be possible to use an external calliper-like method or an internal method taking advantage of the known location of the particle's centre of mass. The pros and cons of these two approaches have already been discussed – it was decided to use the internal method in this case.

If the lengths of a large number of particle radii (passing through the centre of mass) are found, then the variations in these lengths can be quantified in some manner. A diagrammatic representation of these radii is shown in Figure 3.28.

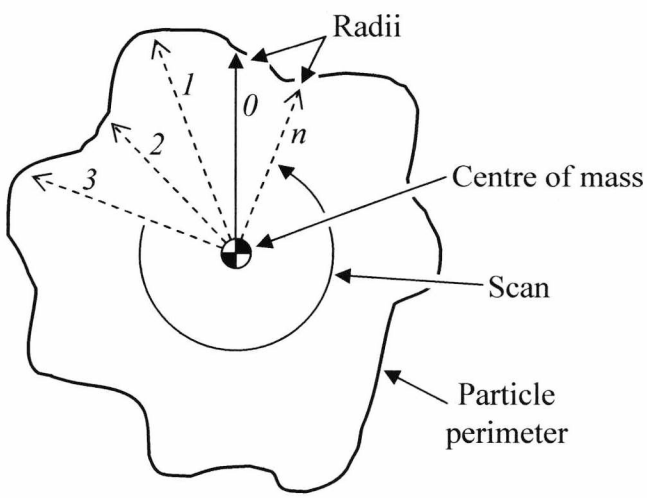

Figure 3.28 Particle radii

Once radii data are available it is possible to calculate the shape factor. In this case the shape factor is defined as the Root Mean Square (RMS) deviation in radii length divided by the mean length. It should be noted that the RMS deviation is the RMS value of the *deviation* in radii lengths and *not the RMS radius length*. This can be defined mathematically as:

$$r_{rms.d} = \sqrt{\frac{(r_{\max} - r_{mean})^2 + (r_{mean} - r_{\min})^2}{2}} \qquad [3.10]$$

Where $r_{rms.d}$ is the RMS deviation of radii lengths and r_{min}, r_{mean} and r_{max} are, respectively, the minimum, mean and maximum radii lengths.

The shape factor itself can now be defined:

$$S_F = \frac{r_{rms.d}}{r_{mean}} \qquad [3.11]$$

Where S_F is the shape factor. This definition of shape factor has been found to give consistent results and is simple enough to allow high performance processing. It is also of greater relevance to irregular shaped particles than other shape factors (or 'circularity' definitions) that are commonly defined in such a way as to give a result equal to one for a perfect circle – as the shape deviates from the circular the resulting figure becomes smaller. This is acceptable where objects are expected to be circular and any deviations from this are small but, when working with particles that are consistently irregular in shape, the results will consist of very small numbers where accuracy to several decimal places is important – this is not considered desirable, effectively limiting the amount of deviation that can be recorded, and so the current definition was set up differently: Perfectly circular particles will generate a value of zero and this figure will increase with the deviation from circular of the particles. This means that there is no limit to the variations in shape that the present definition will allow to be highlighted – it will, in theory, produce a single, unsigned, figure that can vary from zero to infinity which describes particles varying from a perfect circle to infinitely non-circular (i.e. a 1D line).

It may be noticed that one factor affecting the accuracy and consistency of the shape factor measurement has not yet been discussed: How many radii should be scanned? Clearly the greater the number of radii scanned the smaller the variations in perimeter shape that can be detected. This important factor is discussed in the next section.

3.4.3 Processing Algorithm

In order to realise fast, efficient processing a single scan of the particle image produces all information necessary for both aspect ratio and shape factor calculation. It has been shown already that in order to calculate the value of these quantities it is necessary to scan particle radii, passing through the centre of mass, and to find the maximum, minimum and mean length of these dimensions. It is, therefore, these radii scans that must be performed on the image in one processing pass.

Before scanning can commence it must be decided how many radii to scan. Clearly a small number will result in high performance but low resolution and a large number will result in good resolution but low performance. If a fixed number of radii are scanned for each particle then the resolution, in terms of the distance along the particles' perimeters between scan points, will vary according to particle size – this could lead to inconsistent results. It was decided that a method of automatically varying the number of radii, in order to achieve optimum resolution according to particle size, was required.

There are several methods by which the number of radii can be decided upon automatically. It would be possible to define a look-up-table with an appropriate number of radii for particles of various sizes; this is a clumsy method which requires the explicit programming of a large number of cases and provides consistency that is only as good as the programming of the look-up-table. Ideally, for optimum resolution, the radius length for every pixel around the particle's perimeter should be scanned. This could be achieved by working along the particle perimeter and 'back calculating' the radius at each location. Whilst giving optimum resolution this would require fairly complex calculation at every stage and would translate into a complex algorithm. A simplification of this method is required that lends itself to higher speed processing. A fixed number of radii must be scanned (with constant angular separation) for each particle but the fixed number to use

must be dynamically calculated for each particle in the image. A novel method has been developed for achieving this: The area, in pixels, is found during particle sizing. If this area is used to calculate the circumference of a circular particle of identical area then this figure (in pixels) may be considered to be the number of radii that must be scanned. This compromise has been found to give good results in practice. The application of simple circle calculations allows this relationship to be defined mathematically:

$$N_{rad} \approx C_{pix} = 2\pi\sqrt{\frac{A_{pix}}{\pi}} \qquad [3.12]$$

Where N_{rad} is the number of radii to scan, C_{pix} is the circumference of the particle in pixels and A_{pix} the area of the current particle in pixels.

Once the number of radii to scan has been decided upon the actual scan can commence. This must be optimised for performance. In order to halve the number of processing iterations required it was decided to scan double length radii. This means that the diameters (through the centre of mass) are being found, rather than the radii, during each program loop iteration. It is, therefore, only necessary to scan through a 180 degree field in order to process the entire particle. This concept is illustrated in Figure 3.29 which should be compared with Figure 3.28 where single length radii are used.

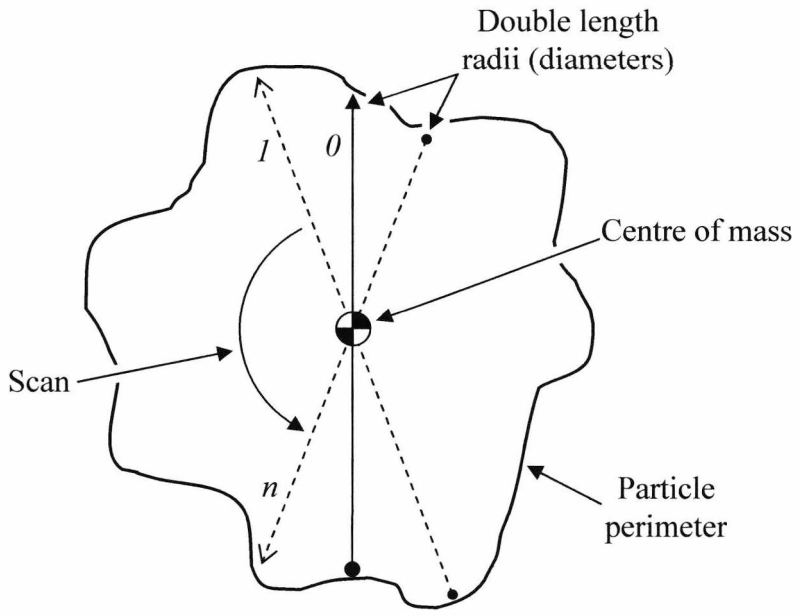

Figure 3.29 Scanning using double length radii (diameters)

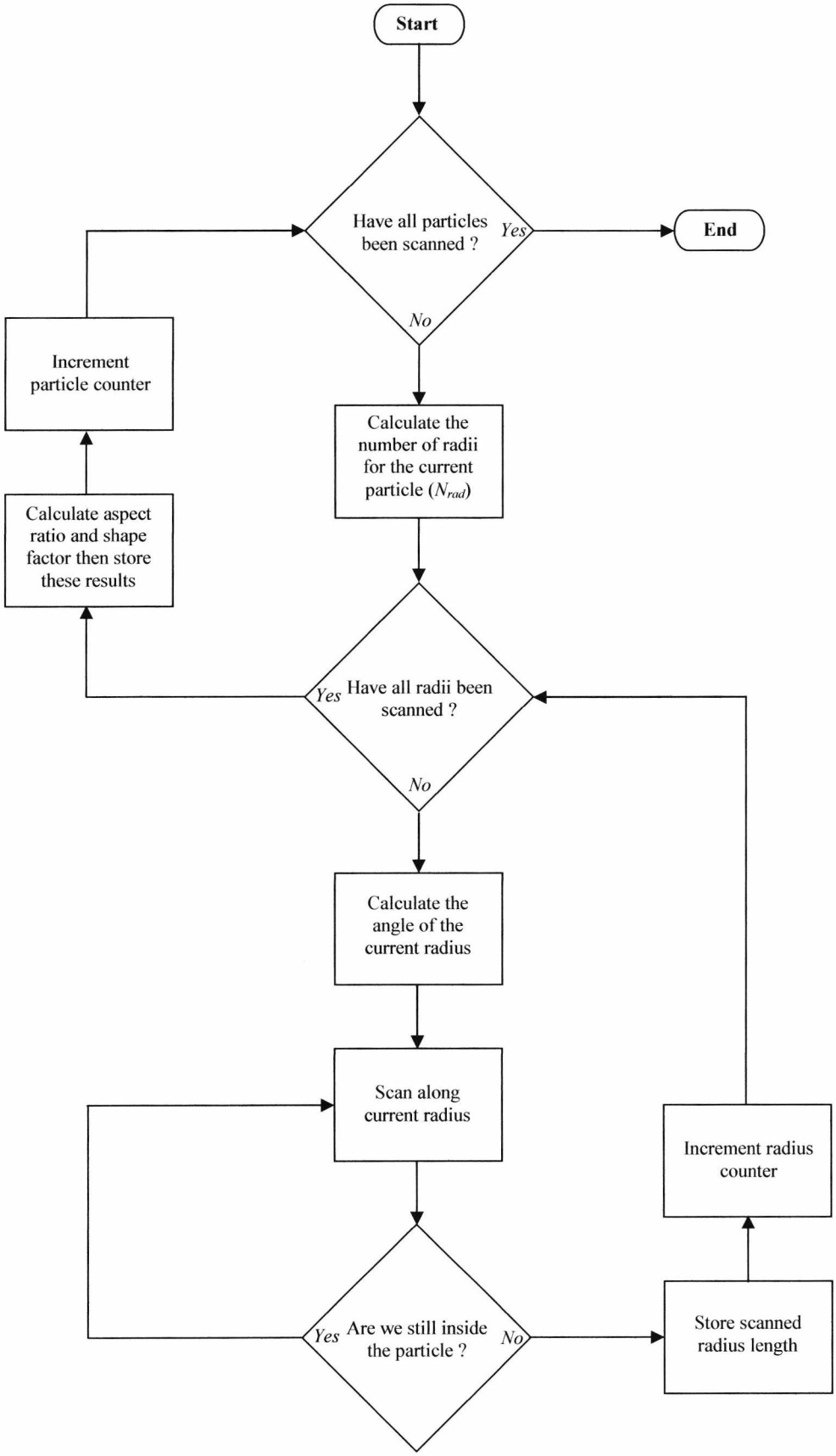

Figure 3.30 Particle radii scan algorithm

The actual determination of radius length is performed by scanning up and down each radius, starting from the centre of mass, until the current pixel is no longer inside the particle. The length of the current radius is then known and the next can be scanned. This continues until the whole particle has been completed at which point its aspect ratio and shape factor can be calculated and stored. The process then repeats for all other particles in the image. This is represented diagrammatically in figure 3.30.

Scanning along the radii is achieved through the use of simple trigonometric functions in conjunction with the angle of the current radii from the vertical axis, on a per-pixel accurate basis. In this way an X offset and a Y offset are created that can be added to the stored centre of mass location data in order to find the absolute pixel location to be examined, in image co-ordinates. It should be noted that by the time this processing is performed the image is already in a binary form (with particles separated from background) and so the points at which radii terminate are easily defined.

3.4.4 Performance of Shape Measurement

In order to assess the performance of the shape measurement a series of test images were produced in a similar way to those used for size and concentration testing. Aspect ratio can be quantified absolutely and so system errors can be calculated easily. Shape factor, however, is arbitrary and can have no real error but must be judged on consistency of measurement. When testing the performance of the system at measuring these two parameters it was thought necessary to test that the aspect ratio and shape factor could be measured consistently independent of the shape, size and orientation of particles in the images. For this reason the test images created consisted of five different shapes, each at four sizes and at four rotation angles. The shapes used were a circle, square, five pointed star, cross and complex 'explosion' shape. Examples of these are shown in figure 3.31.

Figure 3.31 Examples of the shapes used for shape measurement testing

The exact sizes used for the shapes were not considered important – it is consistency during the test that must be considered. Sizes that were convenient for testing were used. The four sizes chosen depended on the particular shape – a graphics package was used to create the shape images and the baseline (100%) shape size was based on a 3x3 grid using the package's arbitrary grid units – the images were scaled during printing to produce images sizes suitable for static imaging. Shape sizes of 100% (3x3), 125%, 133%, 150%, 166%, 175% and 200% were used. Each shape size was then rotated through 15°, 30° or 45° to provide four different angles – rotations greater than this would have resulted in repetition. Three examples of image sequences used are shown in figure 3.32, where size choices are clarified.

The images were viewed using the same physical setup as used for previous tests. The measured aspect ratio and shape factor for each shape image were recorded as well as the mean values of these quantities.

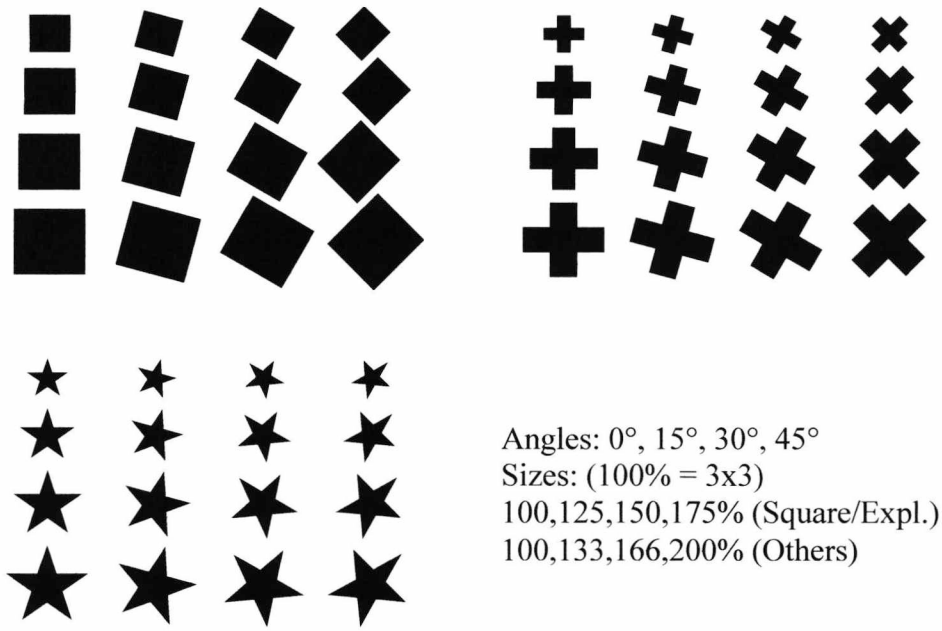

Figure 3.32 Shape test image examples (not to scale)

Whilst no reference data is available for shape factor (other than that the circle should give a value of zero) the fact that the shapes were based on a 3x3 grid allowed the theoretical aspect ratio to be calculated for the circle (always 1), square and cross. Measured mean values and, where possible, errors are shown in table 3.4.

Table 3.4 Mean shape measurement results

Shape	Aspect Ratio			Shape Factor		
	Theoretical	Measured	Error (%)	Theoretical	Measured	Error
Circle	1.000	0.97	3.0	0	0.01	0.01
Square	0.707	0.71	0.4	N/A	0.19	N/A
Star	N/A	0.60	N/A	N/A	0.26	N/A
Cross	0.447	0.48	7.4	N/A	0.34	N/A
Explosion	N/A	0.49	N/A	N/A	0.36	N/A

It can be seen that, although the aspect ratio results are reasonable the errors in terms of percentage are quite high. This will be discussed in depth later but is thought to be related to image quantisation effects. The shape factor results are difficult to judge. It should be noted that the shapes have been arranged, in table 3.4, in order of complexity (based on the number of 'sides' each possesses) and a clear relationship can be seen between complexity and measured shape factor. This relationship can be seen more clearly in figure 3.33.

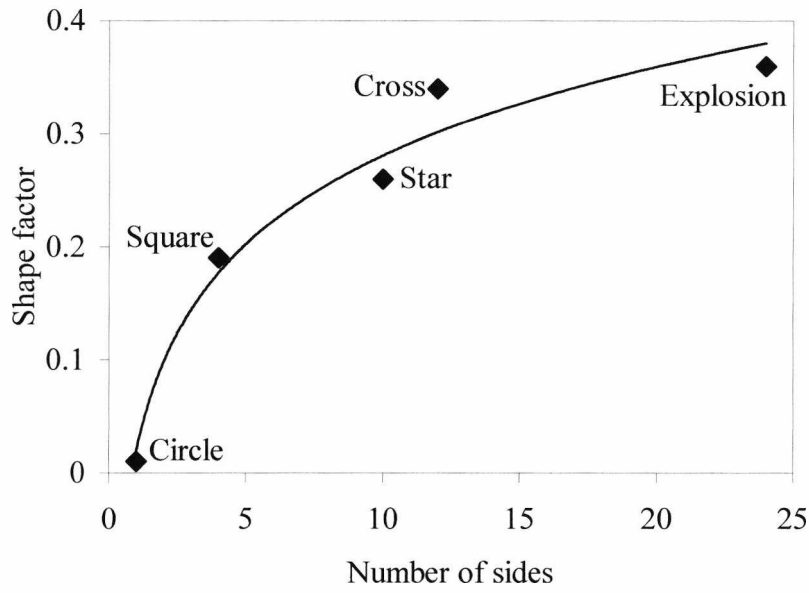

Figure 3.33 Relationship of measured shape factor to shape complexity

The existence of such a relationship may be viewed only as an indicator that the defined shape factor is a useful way of quantifying shape – a direct, reliably quantifiable, relationship between the number of sides of a shape and its shape factor was not the

intention. It should be remembered that the present definition of shape factor takes into account the depth of features on the particles' perimeters, so that it may be possible for a shape featuring a relatively small number of sides but large jagged transitions to result in a shape factor that is higher than a shape with more sides but less well defined features. This is illustrated in figure 3.34 where particle A would result in a greater shape factor than B despite having fewer sides – in practice this is not an issue since the overall, perceived, complexity of A is clearly greater than B and so the higher shape factor is rightly deserved. The introduction of the concept of 'sides' as an indicator of complexity was undertaken merely to provide some scientific justification of the shape factor results obtained, in relation to the shapes used, thus proving the usefulness of an arbitrary quantity that is, by its very nature, difficult to analyse.

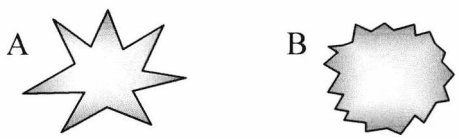

Figure 3.34 Relationship of shape factor to perimeter feature depth

The main purpose of testing the shape measurement system was to determine the independence of the shape measurement from shape size and orientation. During the tests four sizes and orientations were used for each shape.

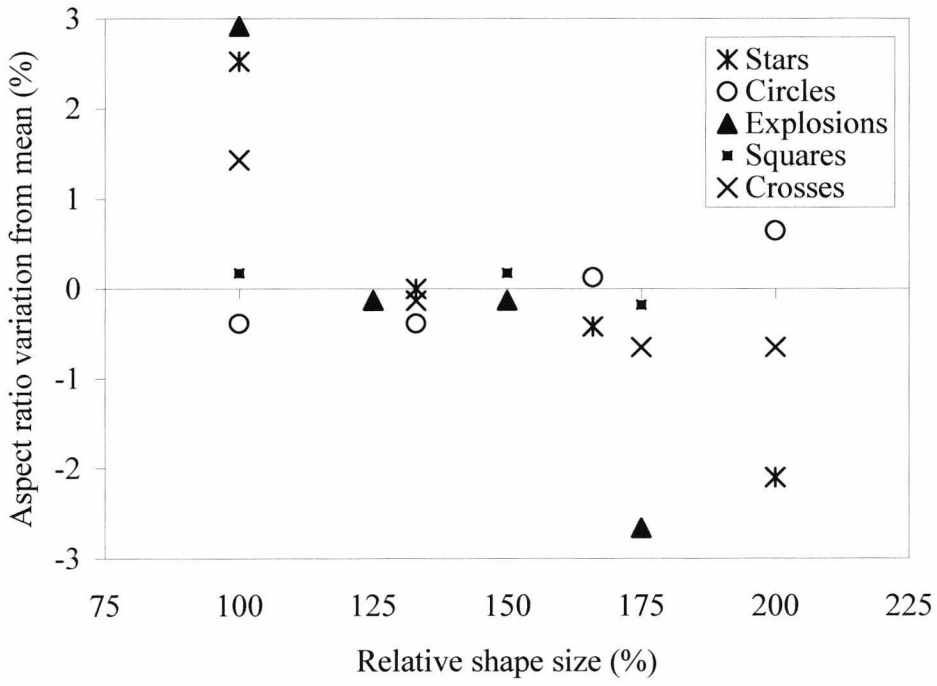

Figure 3.35 Aspect ratio measurement in relation to size

Figure 3.35 shows the results of the size dependence tests for aspect ratio measurement – each data point represents the mean value of all four particle orientations for each particular size.

It can be seen that, through a 100% increase in size, variations remain below ±3%. All shapes show variation that is, in essence, linear. The circle and square, which are the simplest shapes, show the least change in relation to size. These are followed by the cross, which is more complex but is limited to 90° corners, and then by the shapes featuring very 'sharp' corners or features – the star and explosion. The size dependant change in aspect ratio can be explained by considering the quantised nature of the video images used by the system – as the sizes of the shapes change they must be represented by the nearest combination of whole pixels that is available. The square is the only shape that can be represented realistically with a Cartesian grid of pixels and it is the square that shows the least variation here. The curved circular shape must always be an approximation when represented by a pixel based system – this approximation will improve with size and although hard to see in figure 3.35, which shows variation in relation to the mean value, this statement was found to be correct when studying the raw results since the small variation caused the value to tend towards 1.0 for the larger sizes. Pixel related limitations of the image will have the greatest effect on shapes with sharp corners since approximations in shape will cause relatively large percentage changes in shape dimensions at the points. Despite the effects of the real world images the variations of ±3% are thought to be acceptable.

Continuing the discussion on size dependence, Figure 3.36 shows the fluctuation from the mean value of shape factor measurements in relation to particle size. Again, each point represents the mean of four different orientations at each particular size.

A pattern similar to that seen in figure 3.35 can be seen here. Again, a small linear variation with respect to size is evident which can be explained by the effects of quantisation in the images. As before the square is the least affected shape. Interestingly, the circle showed a relative error here in the order of ±20% (too high to plot on the graph without swamping the other values).

This is due to an unfortunate consequence of the particular shape factor definition used here – the shape factor of a circle should be zero and so all the results for the circle were very small numbers, this means that a very small absolute change in one of the circle's dimensions, caused by pixilation, will result in a large change in the relative shape factor percentage variation. In general the variation here is acceptable, lying within ±6%.

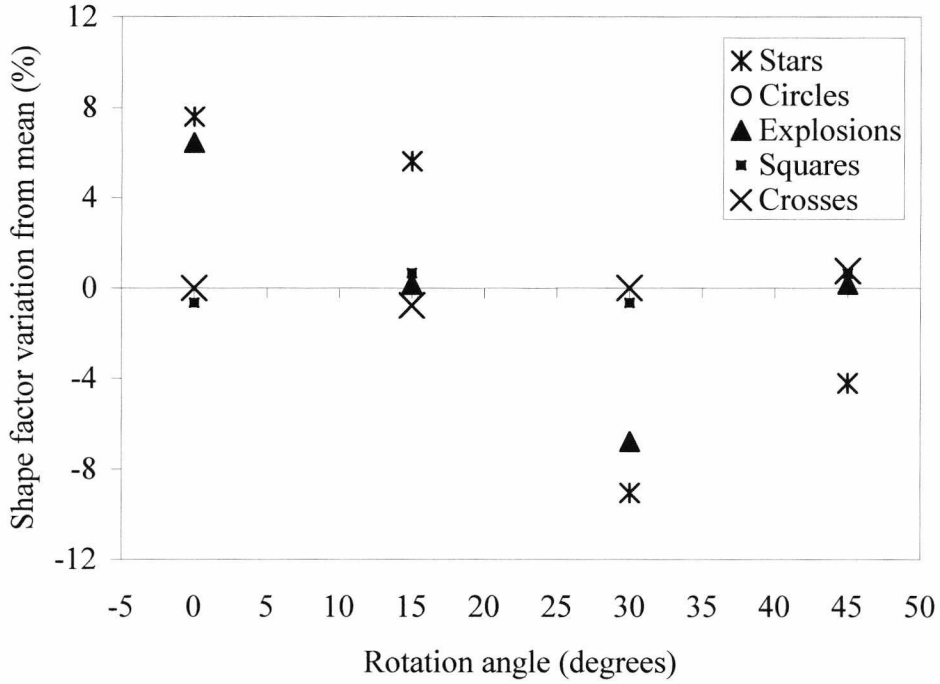

Figure 3.36 Shape factor measurement in relation to size

Variations in orientation must now be considered. Figure 3.37 shows the fluctuation from the mean value of shape factor measurements in relation to particle orientation. Each point represents the mean of four different sizes at each particular orientation.

A similar pattern to before is apparent here. The shapes with the sharp points suffer most from rotation. This can again be explained in image quantisation effects – anyone with experience in representing lines (and other geometric shapes) using a low resolution display will understand the errors that are, unavoidably, introduced. The circle cannot be seen here due to the shape factor related effect that has already been discussed. Whilst the two jagged shapes – the explosion and the star – suffer from errors as high as ±8%, it is unlikely that particles showing this much variation in perimeter would be found in a real situation. The less complex shapes give much better results here with variations lying within ±1%.

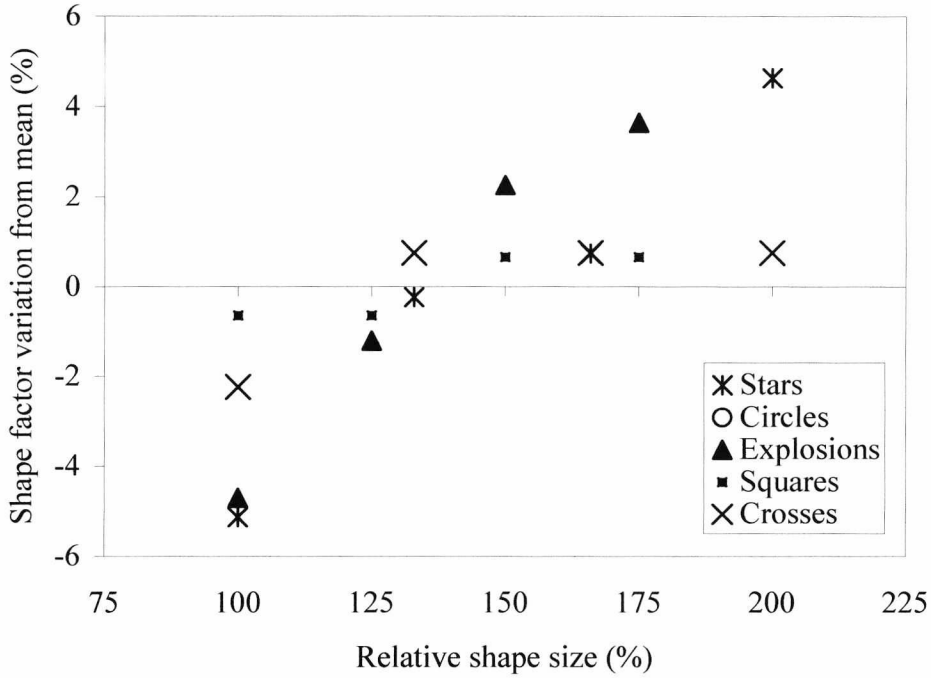

Figure 3.37 Shape factor measurement in relation to orientation

Figure 3.38 shows the fluctuation from the mean value of aspect ratio measurements in relation to particle orientation. Again, each point represents the mean of four different sizes at each particular orientation.

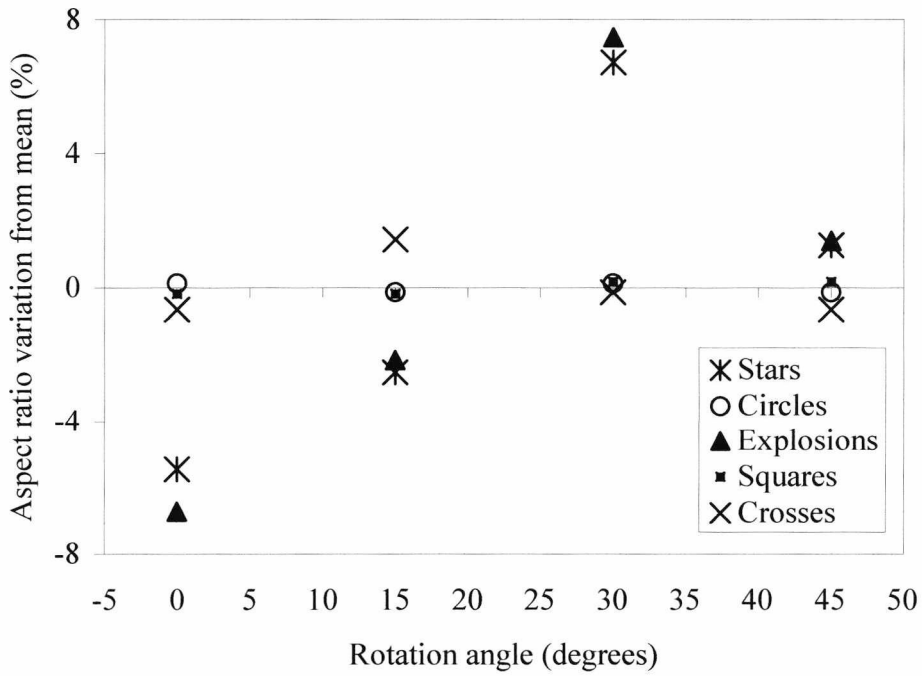

Figure 3.38 Aspect ratio measurement in relation to orientation

The pattern here is very similar to before – the simpler shapes show very good results whilst the more complex ones show slight linear variation with orientation change. The circle is shown once more as the measurements presented here are for aspect ratio. In general the variations are no larger than ±1.5% for the realistic shapes and lie within ±7% for the extremely complex ones.

3.5 Summary

This chapter has presented the basic principles and processing requirements of imaging based particle analysis using a single camera to acquire 2D particle images. The main problems have been identified and, where relevant, novel processing methods have been suggested in order to surmount these problems. The main quantifiable particle parameters have been identified (size, concentration and shape) and methods have been detailed for measuring these parameters.

One of the main benefits of an imaging based system is its ability to be calibrated and checked for basic accuracy using accurate printed test images. This advantage has been identified and exploited and the basic, underlying, accuracies of size, concentration and shape measurement have been investigated. Sizing has been found to be accurate to within ±0.15%. Concentration measurement has a lower accuracy of ±2% and this reduction, which is caused by the interrelation with shape measurement, has been explained. The accuracy of shape measurement is more difficult to quantify but, in general is accurate to within ±2-4% for realistically shaped particles. The reduction in shape measurement accuracy due to the quantised nature of the images has been identified and discussed.

This chapter has, in general, focussed on theoretical rather than practical issues. The next chapter will discuss a practical implementation of a 2D test system and highlight problems that have not been discussed here. More specific descriptions of the software structure will also be given in addition to the simple theoretical algorithms that have been shown in this chapter.

Chapter 4

Design and Implementation of a Static Test Setup and System Software

4.1 Introduction

So far, discussion has centred on theoretical descriptions of principles and processing strategies. During performance testing, in Chapter 3, it was suggested that a real physical test set-up was available and results were obtained using this system. No practical details were given as discussion in Chapter 3 focused on the basic theory of imaging based particle analysis.

In this Chapter the physical set-up will be introduced. Physical and optical considerations will be explained, the structure of system software will be discussed and any processing algorithms, necessary in order to avoid real world problems, will be detailed. In short, the requirements and problems associated with transitioning from the theoretical to the real will be covered. It should be noted that this chapter is still dealing with static particle analysis – on-line work will be discussed in the next chapter.

4.2 Practical Setup

4.2.1 Physical Arrangement

The physical arrangement used for static observation of particles and test images consists of a camera, an imaging surface and a front-lighting arrangement. Details of the set-up used are shown in figure 4.1.

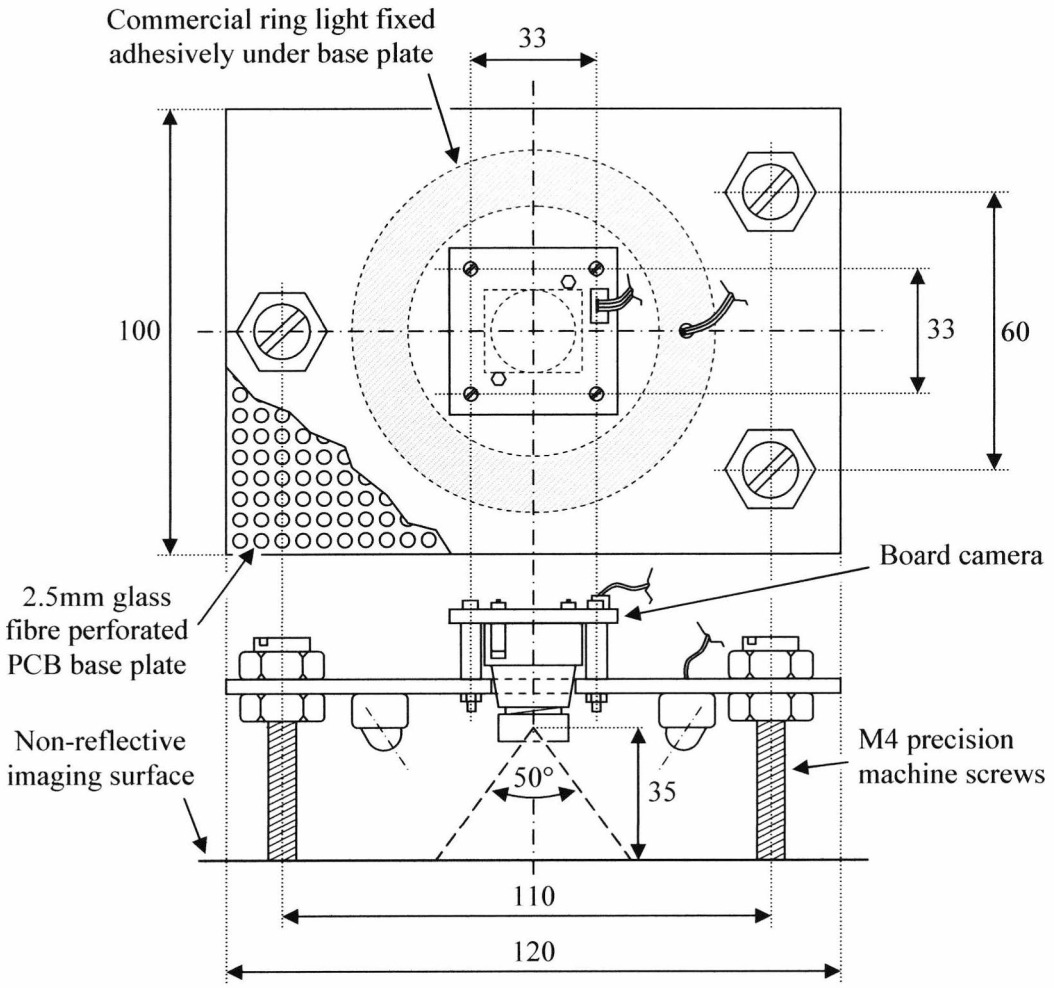

Figure 4.1 Physical arrangement for static analysis of particles

The arrangement used was designed to be simple, cost-effective, robust and reliable. The use of three bolts, each provided with two nuts for locking, allowed the height and level of the base plate to be adjusted accurately. The thick glass fibre PCB material proved to be both flat and rigid – any slight imperfections in the board's flatness could be trimmed out with the three point supports. For use, the entire assembly was placed on a matte black surface, onto which calibration images or particles could be placed (where dark coloured particles were measured a matte white surface was used and the resulting image made negative) and enclosed within a lightproof box.

4.2.2 Camera/Optical Considerations

In order that the viability of the system for real industrial applications could be judged it was decided to use a cheap and readily available board camera module, originally intended for closed circuit television use, rather than an exotic scientific camera. This would impose several difficulties on the system but was thought relevant in this case. A device was found that provided the full CCIR resolution – a full list of specifications is given in Table 4.1.

Table 4.1 Camera specifications

Image sensor	1/3" Sony monochrome CCD
Video system	CCIR, interlaced
Effective resolution	768 x 576
Minimum illumination	0.25 Lux / F2.0
Signal to noise ratio	> 48dB
Electronic shutter speed	$1/50^{th}$ to $1/100000^{th}$ of a second
Power source	12V DC 120mA
Lens type	M12 x 0.5 miniature board camera lens
Dimensions	38 x 38mm
Weight	15g
Cost	< £40

This camera provides excellent performance for the price with a resolution exceeding that of many relatively expensive scientific cameras. It does, however, suffer from three problems when used for scientific applications: The device features automatic gain control (which cannot be disabled), automatic shutter speed setting (which cannot be overridden) and interlaced video scanning. The effects of these difficulties were investigated as part of the present work, thus establishing the viability of a cost-effective physical implementation. (See chapter 5, section 5.2.3 and chapter 6)

The on-board electronics adjust the gain control and shutter speed settings in order to achieve the maximum range of pixel values for any given illumination conditions. This behaviour may be ideal for security applications but could result in an uncontrolled change in imaging conditions when applied to scientific uses. In practice, for static

analysis, this is not a problem as a physical steady state condition is achieved with respect to particles and lighting. The auto threshold setting feature, in the processing software, will avoid possible problems with the variance in steady state conditions from test to test (see chapter 3, section 3.2.3).

The third limitation of this camera is its use of interlaced video scanning. To describe the exact nature of interlaced video would be beyond the scope of this work and so it will only be introduced briefly here in the interests of clarity. A video image consists of an array of pixels. When this image is transmitted from one place to another (from a camera to a PC for instance) it must, necessarily, be broken down and transmitted serially, one pixel at a time. The most obvious way is to transmit the image line by line until the whole has been transmitted – this is known as progressive scanning and is available in expensive scientific cameras. Cheaper cameras, designed to produce 'standard' video signals do not, however, utilise progressive scanning but, instead, perform an interlaced image scan. This method splits the image into two 'half-height' frames consisting of odd then even numbered image lines (or rows) which are transmitted one after the other (they are re-assembled or 'interlaced' at the receiver). This complex and seemingly unnecessary approach stems from the early days of television – it is a method of reducing display 'flicker'. Television images are updated 25 times a second in order that the illusion of fluid movement is maintained. Unfortunately at a refresh rate of 25Hz the image, though smoothly animated, will appear to flicker to a distracting degree. In the early days of television there were no digital memory circuits that could store each image and refresh it at a rate independent of the update in incoming frames as in today's PCs and so an alternative had to be found – the image was interlaced. This means that an entire image is built up from two frames. The image update rate is still 25 times per second but the frame refresh rate is doubled to 50Hz – this drastically reduces visible flicker without increasing the required transmission bandwidth.

The use of 'half and half' interlaced images can represent a problem in scientific applications since, in practice, cameras tend to scan odd lines and transmit the data then scan even lines and transmit the data and so on – the result is that the two interlaced frames do not represent the same time period. For moving applications this means that the camera can only be used at half its vertical resolution but at a frame rate of 50Hz. So long as there is no movement in the subject the full vertical resolution may be used. In the case

of static particle analysis this means that there must be no significant vibration and the particles must remain stationary during imaging – these two conditions are easily met and so, in this case, the interlaced nature of the cameras operation does not, once understood, present a problem.

Once the camera had been decided upon a suitable lens had to be found. Board cameras use a miniature M12 x 0.5 lens fitting and the types of lenses available for them are somewhat limited. Furthermore many of these lenses use extremely cheap plastic optics which produce significant non-linearity in the resulting images. This limits the availability of suitable lenses still further since properly ground glass lenses must be used for this application. The lens chosen for this work is a multi element, fixed aperture, glass lens with a focal length of 6.3mm (a choice of two suitable lenses was available and this lens was chosen as it provides good area coverage at a reasonable working distance). The exact specifications are given in Table 4.2. Unfortunately no details of the exact configuration of the individual elements are available. This means that the exact working distance cannot be known and this will affect the software. Such effects will be discussed in the software section (section 4.4.3.1).

Table 4.2 Lens specifications

Type	Multi element ground glass with anti reflective coating
Aperture	Fixed – f2.0
Effective angular field of view (1/3" image sensor)	50°
Focal Length	6.3mm
Working distance	25mm – ∞
Cost	< £20

The range of working distances that board camera lenses are capable of is very wide. More specifically, they can be focussed on subjects that are extremely close at hand. This would not be the case with larger cameras featuring a C-Mount lens system – a highly specialised (and expensive) macro lens assembly would be required. This is another reason to use the board camera as in use it was found that the selected lens would focus on the subject at working distances down to eight millimetres. Such close-up focussing could be useful for the sensing of very small particles.

4.2.3 Lighting

The illumination sub-system is a critical part of the imaging set-up. The illumination produced must be uniform over the whole interrogation surface otherwise the results may suffer from spatial dependencies. The best method of achieving such a uniform and diffuse illumination field was found to be through the use of a ring light. This has the double advantage of allowing the camera to be placed in the centre of the light source – in its basic form a ring light consists of a ring (i.e. a circle with no centre) with light sources (usually LEDs) arranged around it so as to provide consistent illumination. Commercial ring lights are widely available, though expensive. Equally good results were found to be obtainable using a carefully arranged ring of separate, diffuse, large format LEDs. It is important that all LEDs are driven in series or, at least, that they are all driven with well regulated and identical currents, in order that uniform light intensity is achieved. A commercial ring light was used for all experiments recorded here.

It was thought necessary to check the spatial uniformity of illumination and to establish if there was any correlation between this and any spatial non-uniformity in the particle sizing results. To this end a test image was produced featuring a regular grid of 'particles' – this is shown in Figure 4.2.

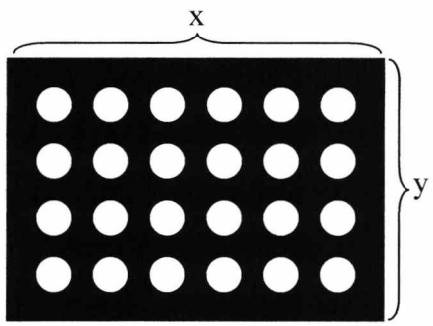

Figure 4.2 Spatial dependency test image – when printed these 'particles' are 2mm in diameter

This image was printed and then placed under the imaging arrangement. In the resulting video image the intensity at the centre of each 'particle' was noted. The results are shown in Figure 4.3. It can be seen that variations in intensity are small, lying within ±3% for the most part. The greater dips towards the corners of the image can be attributed to a slight optical 'vignetting' effect caused by the lens.

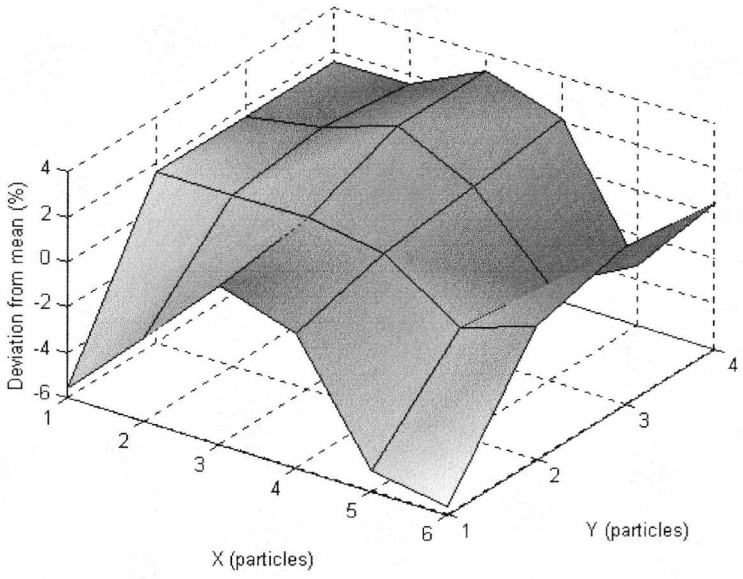

Figure 4.3 Illumination intensity across sensing area

Despite the fact that variations in illumination intensity can be seen to be small it was thought necessary to continue the analysis of the test image and analyse the size of each particle individually. In this way any correlation between illumination variations and size variations can be explored. The results are shown in Figure 4.4.

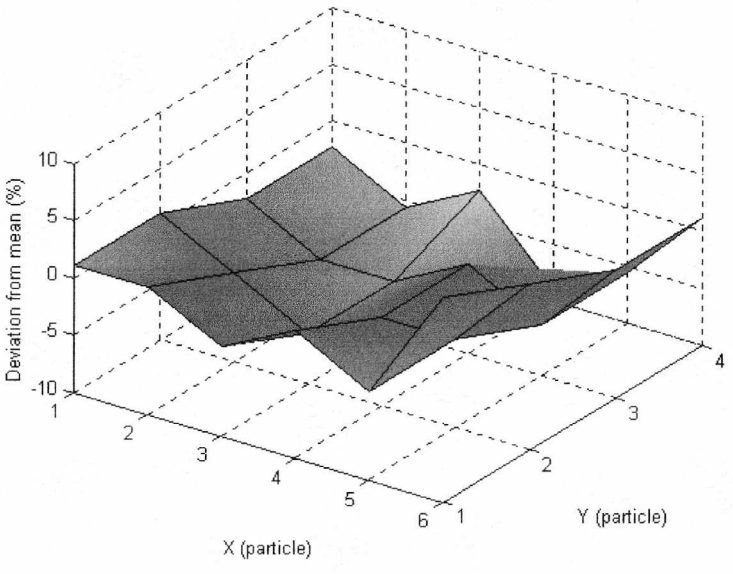

Figure 4.4 Measured particle size in relation to position

It can be seen that there are variations in measured particle size in relation to the particles' positions in the image but these variations are very small. In general they lie within ±2%.

It is clear that there is no correlation between these variations and the variations in intensity shown in figure 4.3. These small variations can be considered random and will be of no concern in a real situation where the results from large numbers of particles are averaged.

4.3 Fundamental System Limitations

For any kind of instrumentation system it is important to know the limits of its measurement capabilities. In Chapter 3 the basic accuracy of the imaging based particle analyser was discussed but limits of performance were not. This chapter deals with physical aspects of the system and since performance limits are related to the specific hardware setup used it was thought best to discuss them here. There are two aspects of the particle images for which limits must be defined: Density of particle images (solids concentration) and particle size.

4.3.1 Concentration Limits – Overlapping Particle Images

The concentration of particles within the images is an important parameter and in Chapter 3 it was shown that variations in concentration could be measured with some accuracy but the limits of suitable concentration were not established – these will be discussed here.

In theory there is no reason why an imaging based system should not measure concentrations from as low as one small particle right up to 100%. In practice this is not the case. For lower concentrations, although the concentration will be measured accurately, there may not be sufficient particles in the image to obtain a representative particle size result. This lower limit of concentration is, therefore, dependent upon the requirements of size measurement and not concentration. It must be determined on a per-material basis and so no fixed value can be given here (this issue will be revisited in later chapters). The upper concentration limit presents a more interesting problem.

In order to understand why it is not possible to measure concentrations right up to 100% it is necessary to consider the mechanisms through which inaccuracies may be introduced.

When static test images are used 'particles' are always placed so that they do not touch one another. In a real situation where a particulate material is sprinkled onto an imaging surface this will not always be the case and some particles may overlap one another. It is not possible to use vibration to separate such particles since the material will tend simply to collect at the nodes and so the problem is aggravated. It must be accepted that overlaps will occur and that this will lead to measurement errors. Some work has been conducted in the past in order to attempt to detect and separate joined particle images (Song et al. 1999, Shen et al. 2001). Much of this work either assumes that all particles are of uniform shape (usually circular) or makes subjective decisions as to which particles to separate. This may lead to incorrect separation in the case of extremely rough particles which will cause as much error as the overlapped particle in the first instance. It was decided for the current system that no particle separation would be attempted as when a large number of images are used it is unlikely that occasional overlaps will cause any extreme biasing of the results. If, however, the concentration is high, overlaps may not be occasional and could lead to significant errors. These errors will manifest themselves as a) a reduction in the measured solids concentration (which is impossible to detect) and b) an increase in measured mean particle size due to the presence of many large 'conglomerated' particles.

In order to establish the upper concentration limit of the present set-up a test was conducted. A particulate material (table salt) was sieved in order to produce a consistent mean size and then observed using the imaging system. The concentration was steadily increased, through random sprinkling onto the imaging surface, whilst the mean size result was noted. The results of this experiment are shown in figure 4.5. The material used, when performing the experiment passed through a 355μm sieve but was stopped by a 300um mesh. The mean size was therefore assumed to be the midpoint between these quantities – 328μm. This expected mean size is marked as a straight dotted line on the figure 4.5 graph.

It can be seen that the measured mean size not only agrees closely with the expected size but remains constant (with a little random variation) irrespective of concentration until the concentration reaches approximately 2-3%. After this value the mean measured size rises sharply as particle overlaps become significant.

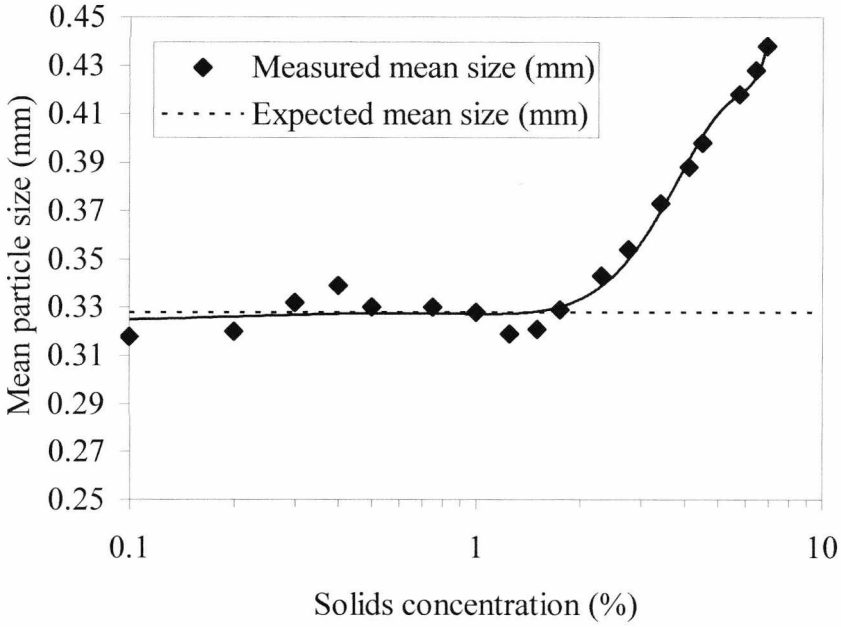

Figure 4.5 Establishing the upper concentration limit

For this particular set-up, the upper concentration limit must be placed at about 3%. At 4% concentration the sizing error has risen to 10%. An image taken at approximately 4% concentration is shown in Figure 4.6 where several areas of overlapping particles can be seen clearly.

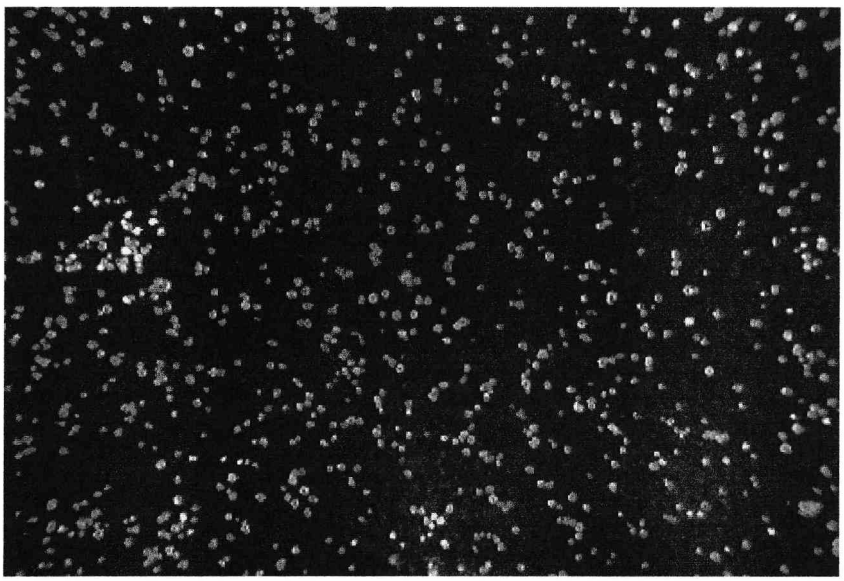

Figure 4.6 Table salt at about 4% concentration

4.3.2 Particle Size Limits – System Rangeability

In previous sections the basic accuracy of size measurement has been assessed but, so far, no discussion has been undertaken in respect to the absolute limits of size that an imaging based system can detect. For the current system the maximum measurable particle size is limited only by the area that the camera can observe; if the particle can fit into the image then it can be analysed. From a practical viewpoint the maximum size may be lower than this as analysing one particle at a time may not be helpful and so it would be necessary to establish the minimum number of particles that must be used for a particular application and set the maximum size accordingly.

The minimum working particle size presents a more complex problem. In theory a particle that occupies one image pixel could be accurately sized. In practice the accuracy of measurement for such a small particle could not be relied upon unless the particle happened to be square in shape and exactly centred on the image pixel. If the particle were to overlap two pixels it may not be recognised at all (if it overlapped each pixel more or less evenly the resulting intensity level might be too low to register). Also per-pixel noise would affect particles this small. In practice the smallest particle that such a system can be expected to analyse must occupy several pixels.

In order to establish the minimum measurable size through experiment it would be necessary to use accurate calibration images of very small particles. As explained in Chapter 3 the minimum size of particles producible by inkjet printing must, with the current equipment, be limited to 250μm. In order to assess the problem fully, smaller particles than this are required. In order to solve this difficulty it was decided to use particles in the 0.25mm – 10mm range but to lift the camera to a greater than usual interrogation distance so that the particles appeared ten times smaller (in the range 25μm – 1000μm). This, in effect, produces smaller particles but does cause some practical problems: In order to fit the system into the available light proof container a wider angle lens had to be used – wider angle lenses introduce more distortion by their very nature and also the particular lens in question was of the cheap plastic variety. Also the lighting arrangement was not designed to work at this distance and so some variation in lighting intensity was unavoidable. Despite these problems an experiment was carried out and the

relative errors of size measurement, when detecting particles in the size range indicated, were recorded. The results are shown in figure 4.7 along with the number of pixels in each particle.

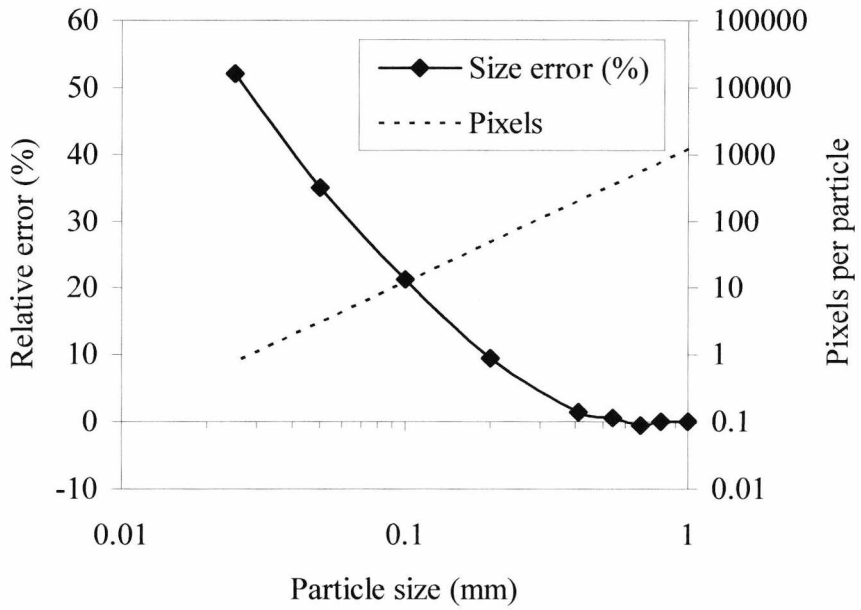

Figure 4.7 Measurement of small particles

It can be seen that errors are in general higher than seen in Chapter 3 but this is to be expected due to the use of a low quality lens and an ill suited lighting arrangement. Fortunately the absolute value of the errors is not as important as the general trend. It can be seen that errors stay fairly low and constant until about 300 – 400μm is reached and then they start to increase dramatically. In Chapter 3, with the good quality lens working at a small objective distance, the measurement of particles down to 250μm was made with an error of no more than 0.2%. By adjusting the figure 4.7 results in order to reflect this known performance it is possible to construct a projected relative error curve that gives a truer representation of the system's small particle measurement capabilities. Figure 4.8 shows this adjusted curve along with the theoretical error caused by a one pixel change in the measured particle size (the smallest error that is theoretically possible for one particle). Again, the number of pixels per particle is also shown.

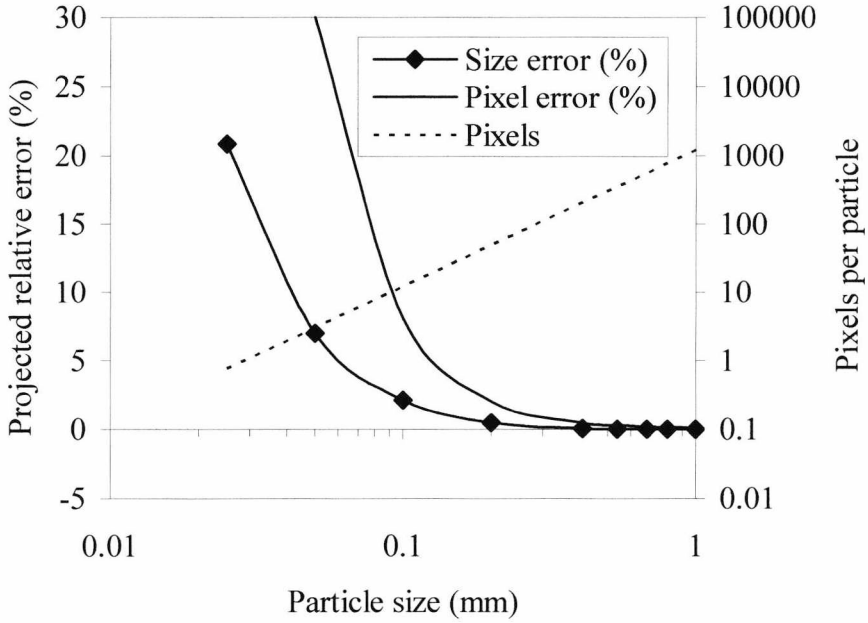

Figure 4.8 Projected relative error of small particle measurement

The projected relative error in figure 4.8 shows that errors start to rise dramatically at around the 100μm point. At 100μm the relative error has risen to about 2% from 0.2% at 250μm. A 100μm particle occupies around nine pixels (i.e. a 3x3 grid) and so, based on these results it can be argued that a 3x3 pixel particle is the minimum size allowable for reliable particle measurements. It is interesting to note that the actual relative error falls below the theoretical value for a single pixel per-particle error. When the experiment was performed images containing four particles were used and it is thought that this reduction in relative error below the theoretical minimum is due to averaging effects across the four particles (one extra pixel in one particle would cancel out the effect of one too few in another).

In order to establish if the relative error in relation to the number of pixels per particle was constant and repeatable it was decided to run the experiment again, but this time to reduce the resolution of the camera by half. This was achieved artificially, by creating a small processing routine that gives every 2x2 block of pixels the mean value over all four elements. The errors would be expected to increase roughly by a factor of two, in general, although the smallest particle will now be smaller than one pixel which should cause a non-linear change in the results. The results from this experiment are shown in figure 4.9. Again, this curve shows the projected error in relation to the Chapter 3 results.

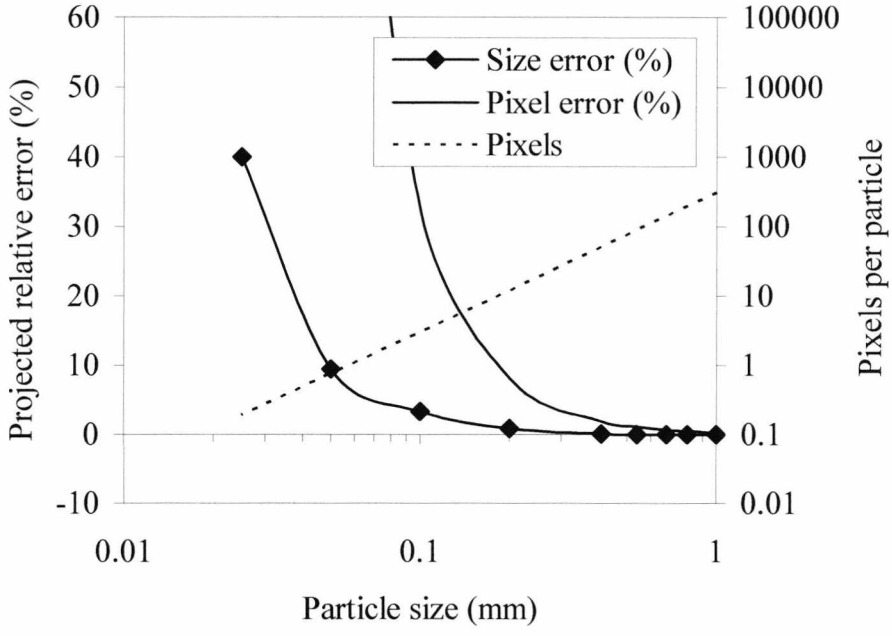

Figure 4.9 Errors generated using halved resolution imaging

It can be seen that the errors follow the same pattern but are higher than before. The smallest particle was detected sporadically during the tests causing a disproportionate rise in the error. The 3x3 pixel rule still holds true with a roughly 2% error at 9 pixels. This can be seen more clearly in Figure 4.10 in which the scale has been expanded. It can be seen that the low resolution curve is less than double its counterpart for smaller particles. This is believed to be due to the fact that image noise will be much reduced with the pixel averaged resolution reduction used here and is not representative of true behaviour.

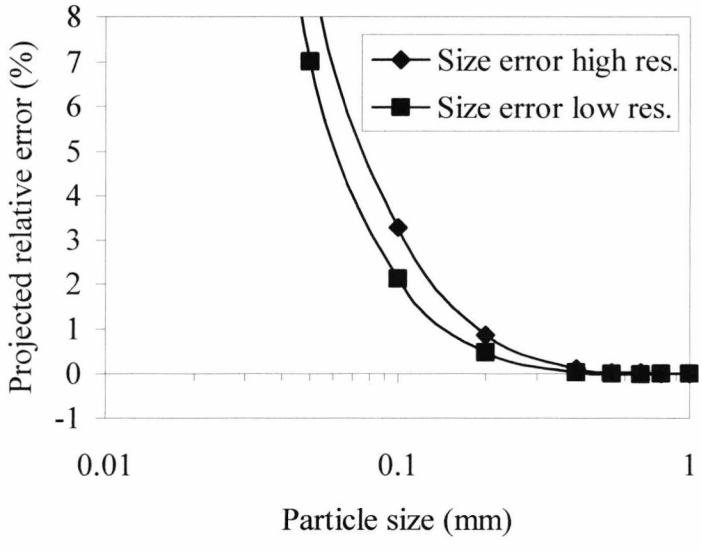

Figure 4.10 Size errors at two resolutions

4.4 System Software

The software created for this work consists of a full Windows application that has been custom written. It is beyond the scope of this account to deal with the software's user functionality and Windows programming features in detail and so they will not be shown here unless to back up a particular point (to show, for instance, the format in which results are presented). So far various algorithms have been presented that are used to implement key image processing features. In this section the general structure of the software system will be discussed and any algorithms and methodologies that have not been detailed already will be explained. In keeping with other, previous, sections emphasis will be placed on processing performance and efforts to increase processing speed will be presented. Software listings of the more important routines are presented in Appendix B.

The software used for real-time image analysis is linked inexorably with the imaging hardware. In the present system an image 'frame grabber' produced by Matrox Graphics has been used. This board is provided with a software imaging library that allows simple and reliable access to the captured images within software. Once images are available within a memory buffer, custom software can take these images and process them. The Microsoft Visual C++ compiler was used for all software development and object orientated techniques were used. The general arrangement of the software is illustrated, in block form, in Figure 4.11.

Since specific details of the user interface will not be discussed and the Matrox imaging library is a commercial product there is only one block in figure 4.11 that needs to be explained: the image processing class (the other blocks will only be mentioned in so far as their interactions with the image processing class). By separating the image processing into its own class, which is written in ANSI standard C++, the portability of the software is assured. To convert the software for another target environment would require only that the interface portions of code be re-written.

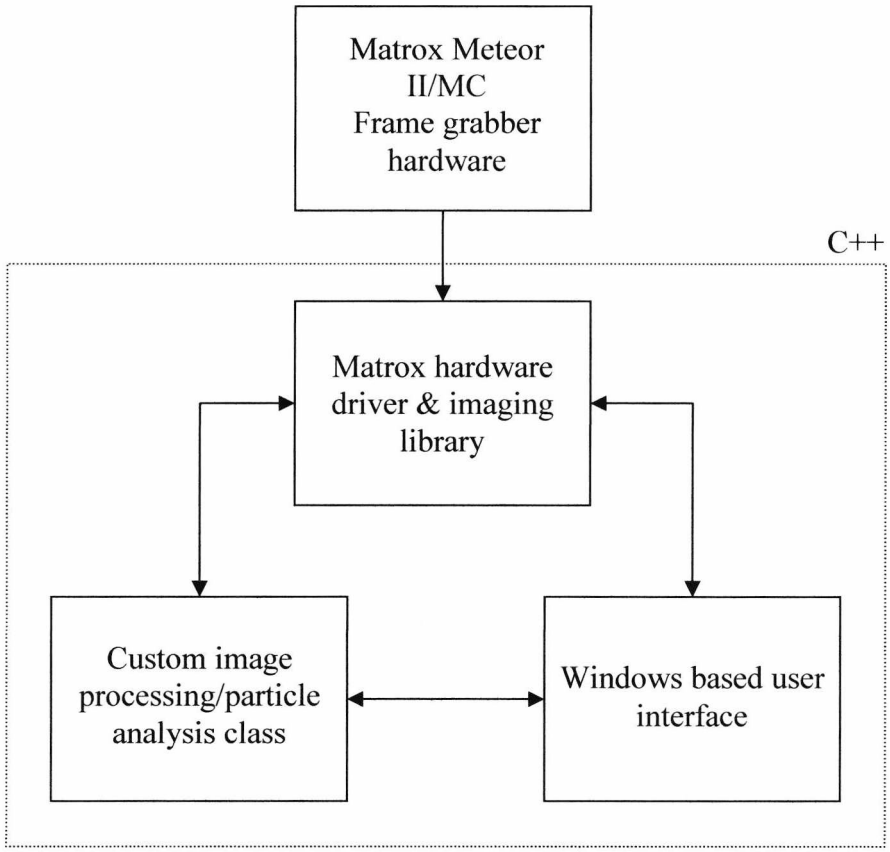

Figure 4.11 General software arrangement

4.4.1 General Processing Class Strategies

In order that the software would be quick to execute and easy to maintain, the image processing and particle analysis functions were separated from interface code and housed in their own class. This class, upon first use, sets up two image buffers of the required size and uses these for processing operations. These two buffers can be described as a primary image buffer and a secondary 'back' buffer. Two are required since several processing operations require the original image to remain intact throughout generation of the new 'processed' image. After a processing operation the current software exchanges the address pointers of the two buffers. This effectively swaps their purpose: the primary buffer becomes the back buffer and vice-versa. This prepares the system to perform the next operation without having to copy the entire processed image after each task, thus conserving memory bandwidth; often a limiting factor in PC based image processing. The primary buffer may be accessed, for initial loading and final image removal, through access functions.

Some operations within the software require that look up tables be produced. Once these have been created they may be used by processing operation code. The processing class manages their creation and keeps track of all allocated memory so that it can be freed properly before program termination. A more detailed look at the software structure, with emphasis on the image processing class, is shown in Figure 4.12.

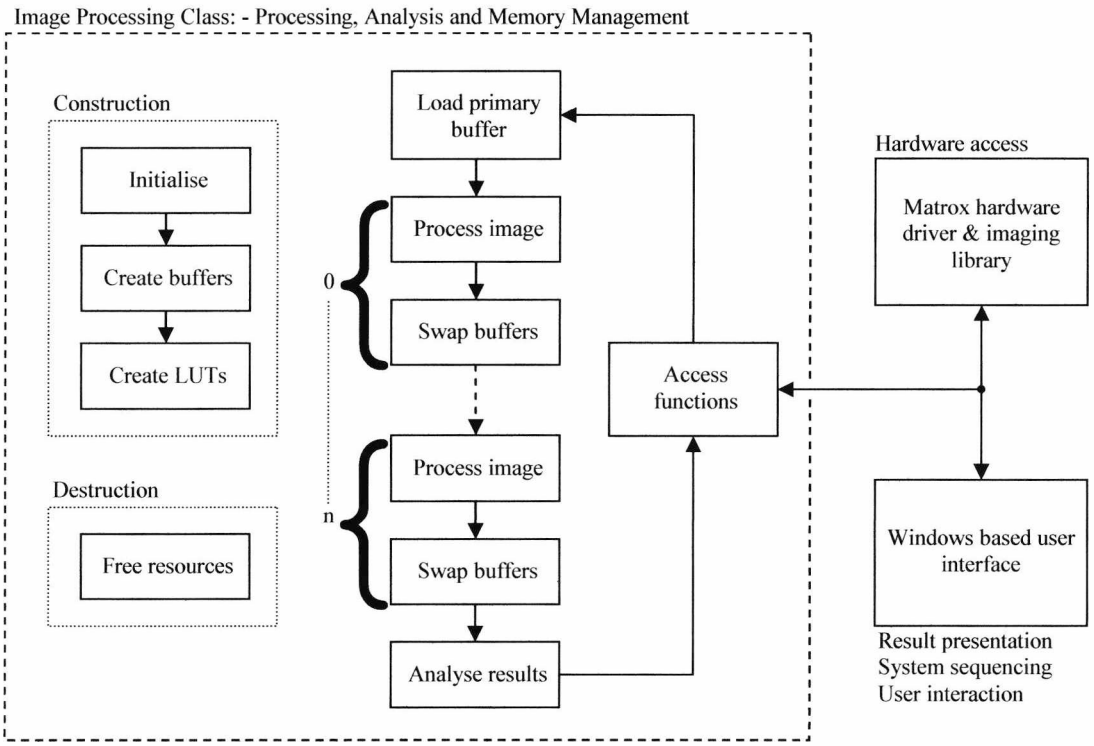

Figure 4.12 Internal software structures

4.4.2 Sequence of Processing Operations

In previous sections various algorithms have been presented that implement the software's processing capabilities. The basic structure of the software has now also been shown. In order that full and complete information is provided in respect to the system software it is necessary to detail the exact order in which processing operations are executed. Many operations are dependent on the results of those preceding them, as has been shown during descriptions of the operations themselves. Some ancillary operations and processing functions have yet to be described and others may still require some clarification, which will be dealt with in due course. The sequence of operations is shown in Figure 4.13.

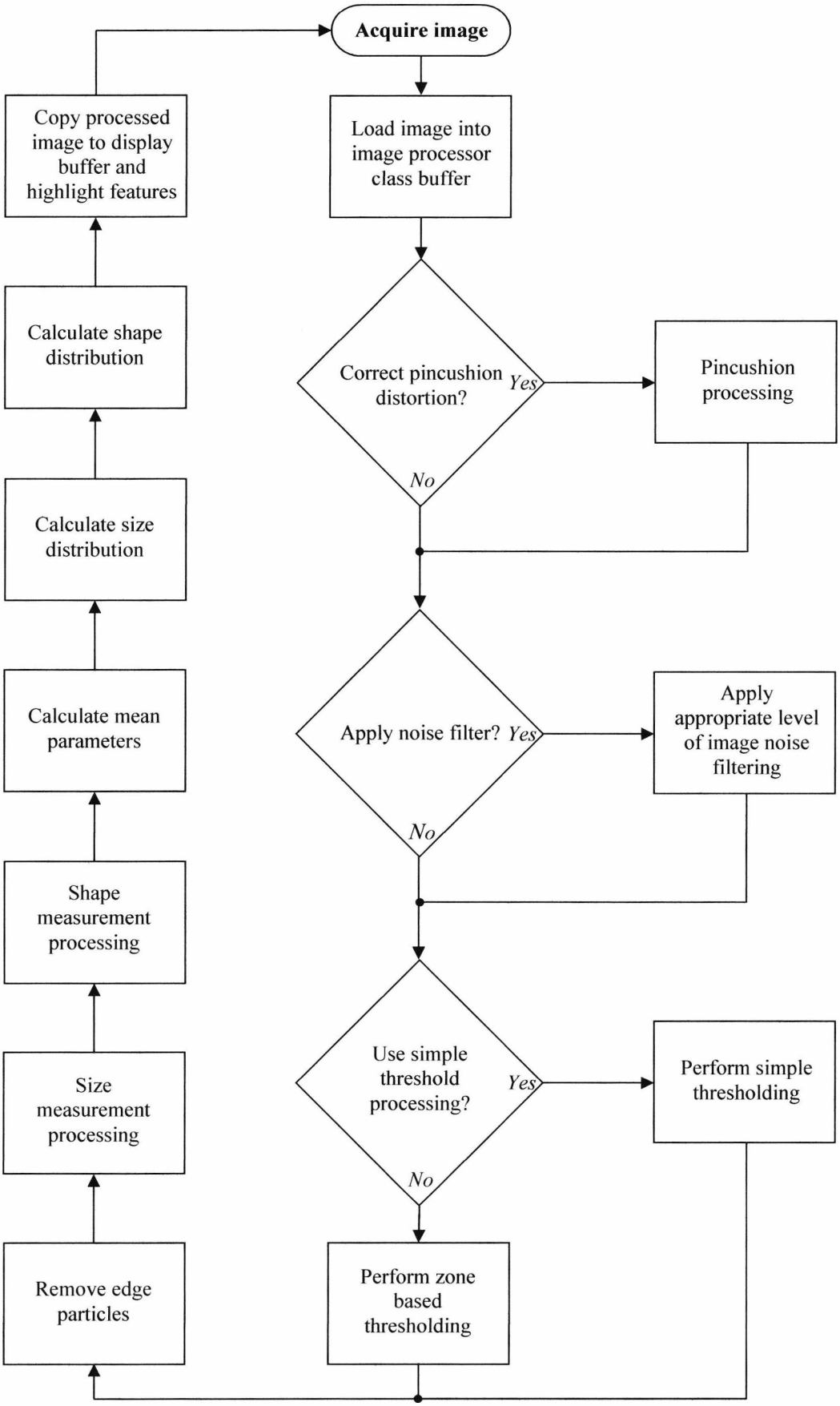

Figure 4.13 Sequence of operations

The first stage is to acquire an image and load it in to the image processing buffer (see figure 4.13). Now processing can commence. The first processing operation is a pincushion distortion reduction algorithm. Pincushion distortion may be introduced by the lens at small working distances and the algorithm used here to eliminate it will be covered in the next section. It is possible to choose not to use this functionality if no significant distortion exists.

The second processing option is provided to filter the image in order to reduce random noise. The filter used is a simple 3x3 neighbourhood low pass filter with all values set to unity and the divisor set to nine. This filtering may be applied between one and three times, depending on the magnitude of the noise, the number of iterations being selectable through the user interface. Heavy filtering should be avoided with small particles as it will decrease the accuracy of perimeter detection. No filtering was used during system performance tests.

The last option allows simple thresholding to be selected for analysis of difficult or synthetic images and those acquired from sources other than the hardware frame grabber (the software is provided with the option to load images from files rather than grab from the hardware). For normal images the zone based algorithm should be used.

The final image processing operation is always applied, there is no option to disable it. This processing removes edge particles from the images. This means that any particle that is in contact with the edge of the video frame is removed from the image before it is sized, counted or otherwise measured. This ensures that 'partial' particles do not cause errors in the mean parameter results. The method used will be discussed in the next section.

Now that a clean, thresholded, image is available the size and shape measurement algorithms may be applied (as described in Chapter 3). Once raw parameter data are available statistical analysis may be performed in order to find mean values, standard deviations and distributions.

The final step in the processing sequence is to display the processed image and draw/highlight any important features. Particle centroids etc. are shown. More details will be given in the next section.

4.4.3 Additional Algorithms

In this section processing algorithms and features that have been mentioned, but not explained, will be detailed. This includes pincushion distortion correction, edge particle removal and image feature highlighting.

4.4.3.1 Pincushion Distortion Correction

Pincushion distortion is a lens related phenomenon which is so named due to the resulting images' similarity to a small cushion that swells towards the centre. A lens is, by its very nature, a radial device: it is circular, focusing light to a focal point. This means that, when focussed on a flat subject (such as the imaging surface in the current work) objects at the centre of the interrogation area will appear closer to the camera than those at the edges. This problem is insignificant when a narrow angle lens is used, focused on a fairly distant subject as the resulting distortion is smaller than the dimensions of a singe pixel and so it may be ignored. When, however, a wider angle lens is used, and/or the subject is close at hand, the problem may become significant. In the present set-up a 50° lens is used at a small working distance, this combination results in a small, but significant, amount of pin cushioning that must be corrected. The general problem is illustrated in Figure 4.14 which shows; a) an image with pincushion distortion and b) the corrected image. Note that these images were taken using a wide angle lens (92°) in order that the problem would be visible clearly, also that the lens used was of the cheap plastic variety and some residual distortion due to general non-linearity in the lens is still visible in image b.

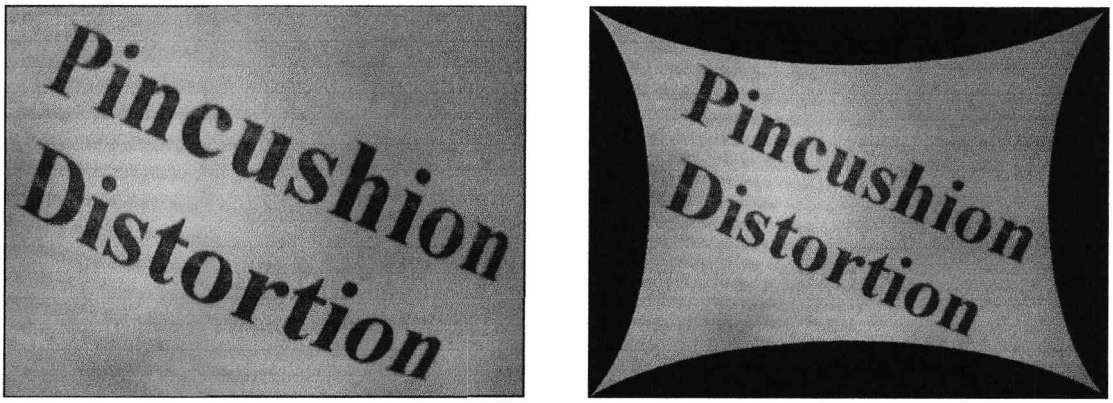

a) Original distorted image b) Corrected image

Figure 4.14 Pincushion distortion

In addition to the geometric distortion it is possible that there may be some reduction of brightness towards the edges of the images (similar to the effect caused by optical vignetting). This effect is just visible in figure 4.14 and must be dealt with in the processing algorithm.

The apparent nearness of objects in the centre of the frame is not actually an apparent problem but a real one. The distance from the focal point to the centre of a flat objective is less than that to its edge. In order for all distances to be the same, thus avoiding pincushion effects, the subject would have to be a concave surface or 'bowl'. Based upon this realisation, it is possible to correct the pincushion distortion as in figure 4.14b. It must be imagined that the distorted flat objective has been 'pushed backward' or 'projected' into a concave shape. In practice each pixel generated through interrogation of the flat objective must be 'mapped' to a new location based upon its relative position on an imaginary concave objective. Each 'ray' emerging from the camera (a 'ray' corresponds to the light path representing a single image pixel) must be allowed to pass through the flat objective and strike the concave one. The ray can now double back upon itself (remaining parallel to the central imaging axis) and when it strikes the flat objective again the new location is noted. Figure 4.15 shows this process diagrammatically.

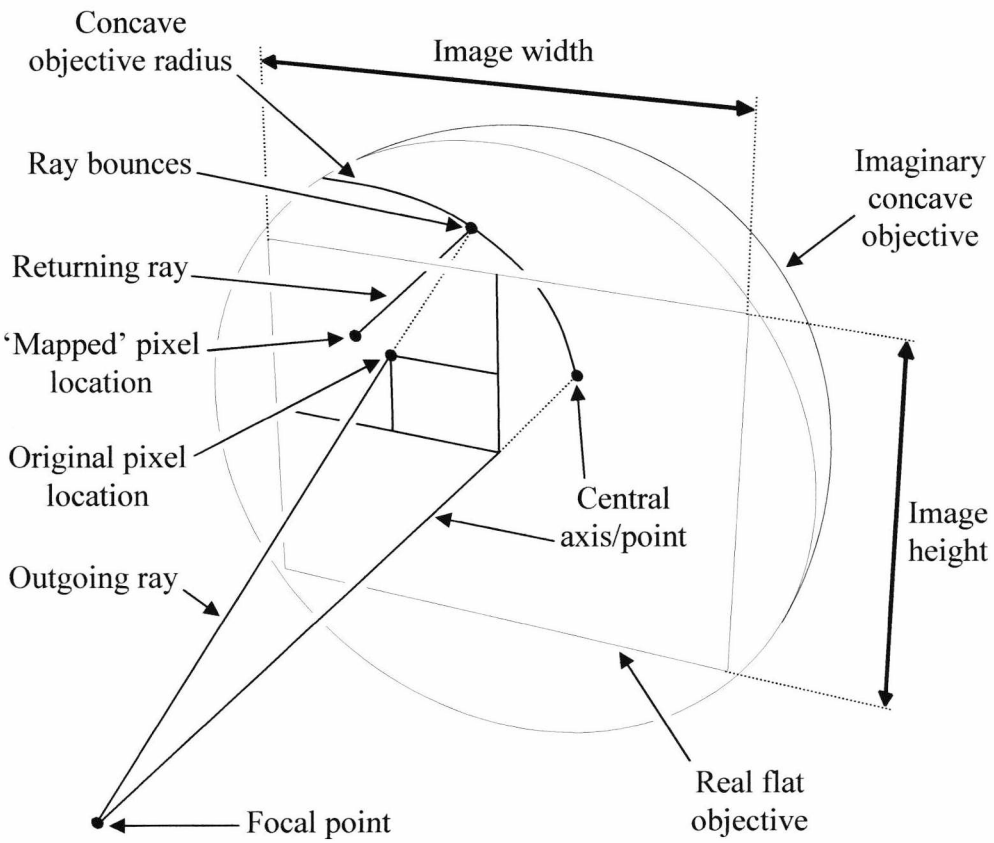

Figure 4.15 Mapping pixels to an imaginary concave objective

From figure 4.15 it can be seen that two pixel locations exist for every 'ray' that is processed. Consider two images: one is the original distorted image and the other is the corrected (or processed) version. In order to process the distorted image all pixels must be scanned through and re-mapped. In order to find the value of each pixel in the processed image the value must be taken from the 'mapped' location in the original image. The relative lengths of the 'rays' can be used in order to correct the mapped pixels for intensity distortion. In order to express the process mathematically various dimensions must be labelled. Figure 4.16 shows the amended diagram. This figure should be considered in conjunction with the following mathematical description covering the mapping process for one pixel (every pixel must be mapped in this way).

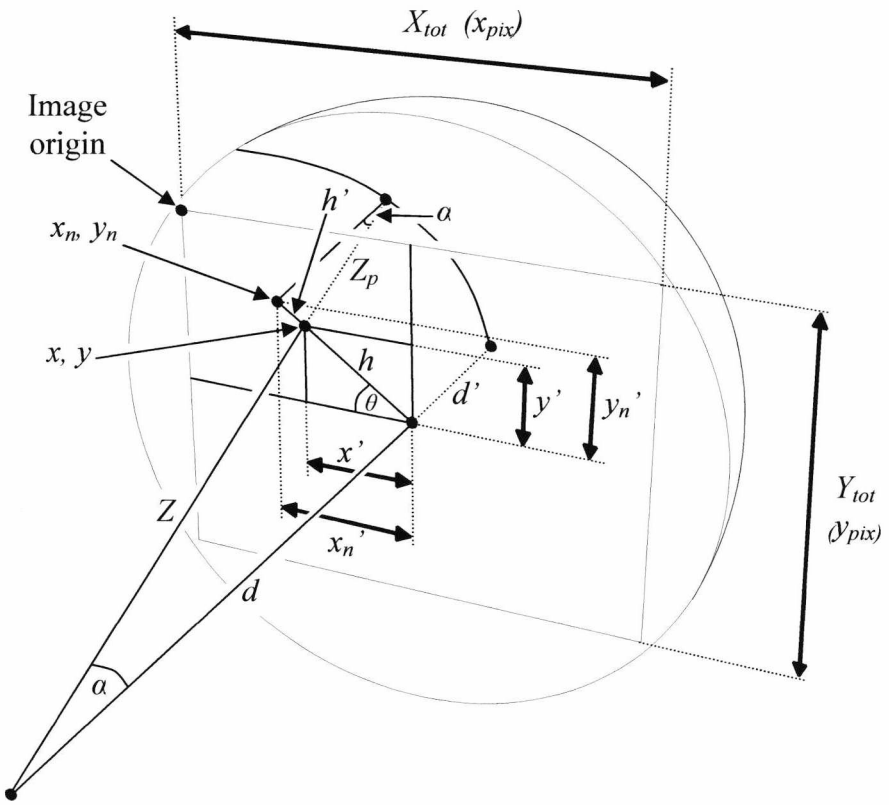

Figure 4.16 Pixel mapping diagram amended with dimensions

It should be noted that the distorted image has its origin in the top left hand corner and pixel locations in *(x, y)* coordinates are measured from this origin. Initially only two of the dimensions in figure 4.16 are known; the working distance, *d* in mm and the location in pixel coordinates of the pixel of interest, *(x, y)*. For the purposes of this algorithm it is necessary to work with the image centre as the origin and so the first step is to find the distances *x'* and *y'* as follows:

$$x' = \left(\frac{x_{pix}}{2}\right) - x \qquad [4.1]$$

and

$$y' = \left(\frac{y_{pix}}{2}\right) - y \qquad [4.2]$$

These quantities are integer pixel values and they must be converted into millimetre values in order to be used in future equations. Since the interrogated image size and

image resolution are known the size, in millimetres, represented by each image pixel is known. This is split into x and y values as x_{mmp} and y_{mmp} respectively. So:

$$x'_{mm} = x' \times x_{mmp} \quad [4.3]$$

and

$$y'_{mm} = y' \times y_{mmp} \quad [4.4]$$

Now the distance, h, from the image centre to the pixel of interest and the distance, Z, from the focal point to the pixel of interest can be found:

$$h = \sqrt{x'^{2}_{mm} + y'^{2}_{mm}} \quad [4.5]$$

$$Z = \sqrt{h^2 + d^2} \quad [4.6]$$

The distance from the focal point to the imaginary concave objective is not known currently but can be calculated. It should be noted that the flat objective intersects (or rather, meets or touches) the concave objective at its corners. This realisation allows the distance to the concave surface, which will be described as D, (d+d' on the diagram) to be found through the use of Pythagoras' theorem:

$$D = \sqrt{\left(\frac{Y_{tot}}{2}\right)^2 + \left(\frac{X_{tot}}{2}\right)^2 + d^2} \quad [4.7]$$

Now;

$$D = Z + Z_p \quad [4.8]$$

$$\therefore Z_p = D - Z \quad [4.9]$$

The angle, α, can now be calculated, allowing the extension to h, h', to be found:

$$\alpha = \cos^{-1}\left(\frac{d}{Z}\right) \quad [4.10]$$

and

$$h' = Z_p \tan\alpha \qquad [4.11]$$

The angle, θ, must now be calculated:

$$\theta = \tan^{-1}\left(\frac{y'_{mm}}{x'_{mm}}\right) \qquad [4.12]$$

The location of the new, mapped, pixel can now be found (in millimetres):

$$x_n{}'_{mm} = (h'+h)\cos\theta \qquad [4.13]$$

and

$$y_n{}'_{mm} = \sqrt{(h'+h)^2 + x_n{}'^2_{mm}} \qquad [4.14]$$

These dimensions must be converted to pixel values:

$$x_n' = \frac{x_n{}'_{mm}}{x_{mmp}} \qquad [4.15]$$

and

$$y_n' = \frac{y_n{}'_{mm}}{y_{mmp}} \qquad [4.16]$$

Finally they must be transformed into image origin space (with the origin at the top left):

$$x_n = \left(\frac{x_{pix}}{2}\right) - x_n' \qquad [4.17]$$

and

$$y_n = \left(\frac{y_{pix}}{2}\right) - y_n' \qquad [4.18]$$

Where x_{pix} and y_{pix} represent the size of the image as integer pixel values. Enough information is now known to calculate an intensity correction factor (to compensate for

the 'vignetting' type effect). This is a function of the distance to the flat objective from the focal point.

$$\varepsilon = \frac{d}{Z} \qquad [4.19]$$

Where ε is the intensity correction factor. The mapped pixel's intensity must be multiplied by this value in order to correct the intensity distortion.

In practice the pincushion correction algorithm is used to generate two look up tables: one for mapped pixel location and one for intensity correction. In this way the complex math routines only need to be run through once and during actual image processing high speed LUT access is all that is required.

One problem with this method is that the working distance, *d*, must be known. With the current board camera lens the exact focal point, and therefore working distance, is not known. The rough value must be entered and then fine tuned visually whilst observing a sheet of graph paper. Another point in respect to this algorithm is that some mapped pixels may lie outside the image boundary since a rectangular image cannot be mapped fully onto a circular one. There will be curved bands at the sides of the processed image where no pixel value is available and in these cases the current algorithm fills the 'dead' space with black (zero) as in figure 4.14b. Lastly, the algorithm, as presented, applies only to the first image quadrant, for other quadrants some values must be inverted etc. This is achieved easily during implementation.

4.4.3.2 Edge Particle Removal

Another processing feature that has yet to be described in detail is edge particle removal. It is possible when examining real particle images that some particles may intersect the edge of these images and only part of them will be visible. In this case these particles must be ignored. This is achieved through a simple flood fill process. After the image has been thresholded it exists in a binary state: particles are black (zero) and the background is white (255). In its basic form the edge particle removal algorithm draws a one pixel wide black border around the edge of the image and then performs a flood fill on this

border, replacing the black with an intermediate colour (in this case intensity 128 is used). During this process any particles that have intersected the border will also be overdrawn with the new colour. When the sizing and shape measurement algorithms are applied they only consider black (zero) pixels to represent particles and so the edge particles are automatically ignored.

Where significant pin cushioning was corrected in the image this simple method can no longer be used since the curved bars at the sides prevent edge particles from actually reaching the sides of the processed image. This is not difficult to compensate for as the bars are filled with black already and the boundary of the image and the bars can be outlined using information from the pincushion correction operation. To describe the exact process used would be to repeat much of the work already explained in respect of pincushion correction. It is the basic methodology that is important.

As a point of interest a custom flood fill algorithm was developed for this work; a recursive system is used that is optimised for speed and a software memory stack is set up and managed in order to avoid stack overflows. To describe the details of this algorithm would be beyond the scope of this document since the flood fill plays such a small part in the current work.

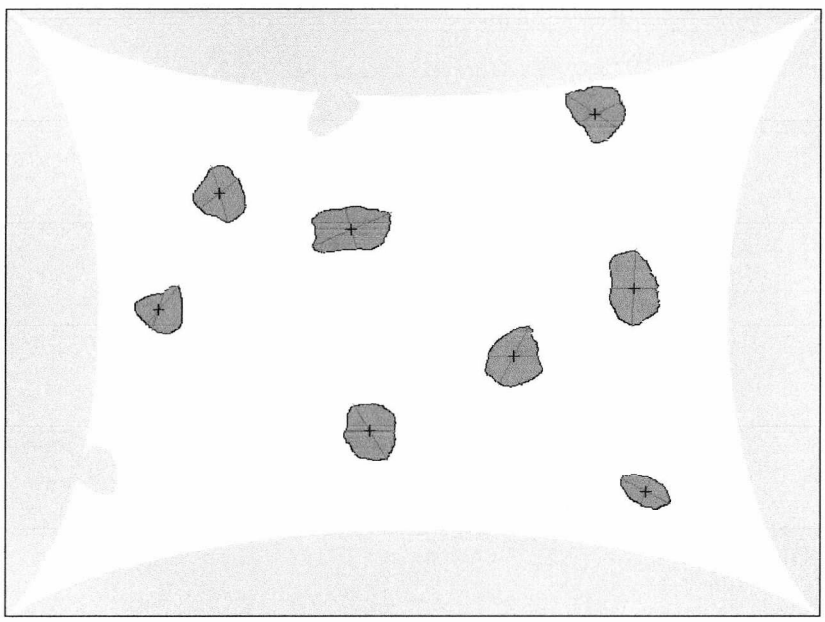

Figure 4.17 Processed image with edge particles removed

An example of a processed image with some edge particles removed is shown in Figure 4.17. Particles that have touched the edge can be clearly seen at the left and at the top. They have been shaded in as a light colour and were not taken into account during sizing. It should be noted that excessive pincushion correction was applied in order to exaggerate the effect for clarity.

4.4.3.3 Image Feature Highlighting

The last aspect of image processing to be discussed in this section is image feature highlighting. It can be seen in figure 4.17 that processed particles have three features highlighted: Their centroid is marked with a cross, their perimeter is shaded in a dark colour and the two radii used for aspect ratio determination are shown. Information regarding these features is stored during algorithm execution and as a last processing operation these details are drawn onto the image for user information. Any particle that does not have these features has not been recognised properly. It is also interesting to see the radii chosen for the aspect ratio calculation. The perimeter shading is not a continuous band but rather it shows all points at the ends of the radii that were scanned during shape factor determination.

4.4.4 Presentation of Results

An important feature of any piece of scientific software is its ability to present results to the user in a way that is both useful and easy to understand. Also the kind of results generated may be considered to be a useful indicator of the applicability of the current particle analysis technique. There are three aspects to the presentation of results: numerical presentation, graphical presentation and data logging for later analysis. The current software supports all three options. The best way in which to illustrate this is to simply show relevant screen captures and discuss points of interest. Figure 4.18 shows a screen capture from the on-line numerical results section of the software.

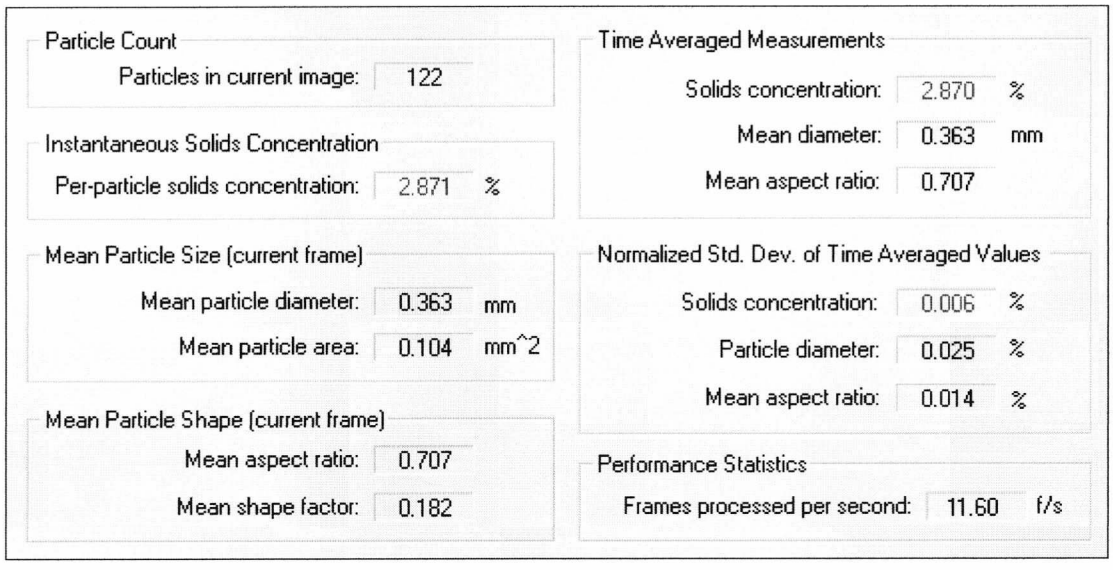

Figure 4.18 User interface showing numerical results

It can be seen that the basic results: mean size, shape and concentration are presented, together with some other quantities. The number of particles in the current image is presented as this may be important when determining the statistical validity of a set of results. The processing rate, in frames per second, is also shown for this reason. The software allows the mean values to be time averaged over a chosen number of frames at the push of a button and the results from this are shown at the top right of figure 4.18. During the time averaging procedure normalised standard deviation of measurements is calculated as this may be important when considering the reliability of the measurements. These results can also be seen in figure 4.18.

The mean size and mean aspect ratio are not the only useful results that can be derived from the image processing procedures. Distributions of these quantities are calculated and displayed in the form of real time histograms. Figure 4.19 shows a screen capture of these graphs.

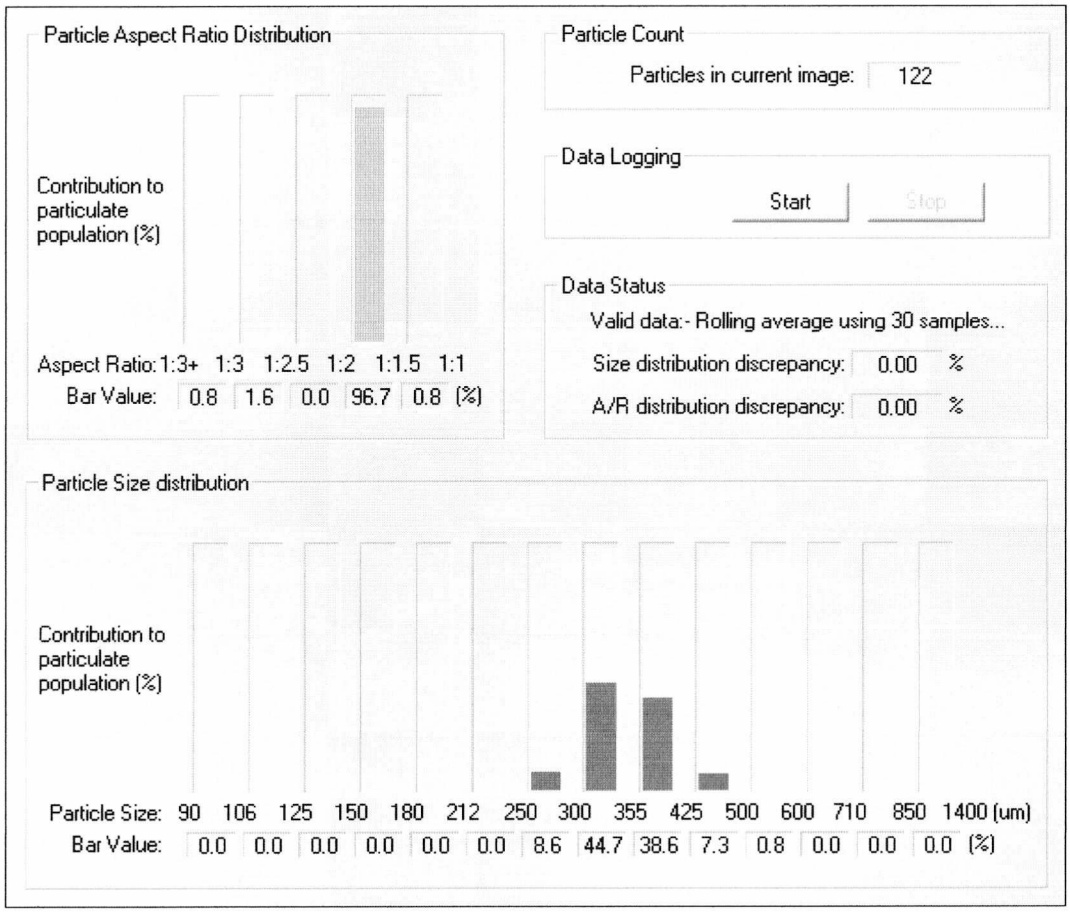

Figure 4.19 User interface showing graphical results

There are two histograms; one for particle size and one for aspect ratio. At the bottom of figure 4.19 the size histogram can be seen. The size ranges used for the bars are standard sieve sizes used in industry for particle sizing they can, however, be changed as required, for the size of material under interrogation. Above this, and to the left, is the aspect ratio distribution histogram. Fewer bars are used here as there are no accepted ranges for aspect ration measurement and less resolution is required. The bars represent actual ratios rather than the floating point representation used within the software which has a more intuitive meaning (aspect ratio distributions may be helpful if the system was used for scientific study but they are of no use in establishing measurement accuracy and so none will be presented here). As the distributions may be expected to change considerably from frame to frame some time averaging is important and it can be seen from the figure that 30 samples were used in this case. Another value shown is that of discrepancy, expressed as a percentage, for both graphs. This figure expresses the variability of the data (see chapter 6, section 6.3.2.4). The number of particles in the images is also relevant here and so it is shown again.

The last point shown in figure 4.19 is the option to log the data to a file. When file logging is selected all quantities shown in the on-line results are logged to a file in a comma separated values format. This includes histogram data for particle size and shape.

There is one final form of result presentation that has not yet been shown. Under some circumstances it may be of interest to observe the properties of individual particles within an image. This functionality is provided in the current software. It is possible to draw certain important information onto the processed particle image so that each particle is individually labelled, as shown in Figure 4.20.

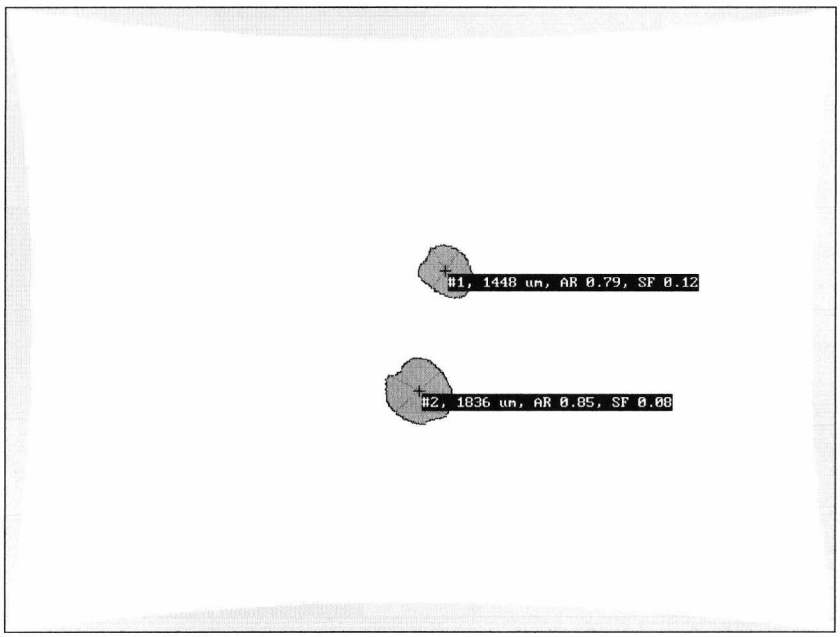

Figure 4.20 User interface showing labelling of individual particles

The particle number (particles are numbered based upon the order in which they were detected during scanning), size, aspect ratio and shape factor can be shown and it is possible to select which, if any, of these quantities should be displayed. The facility to label particles in this way may only be used when very few particles are present in each image but it remains a useful feature especially during performance testing using synthetic test images.

An important point when presenting results is that of displayed significant figures. The software makes all its internal calculations to many decimal places but the usable accuracy of the system is not this high. To display all decimal places in results would be

misleading. The number of decimal places used for the results shown in this section were decided upon so that they reflect the true precision that can be achieved. When file data logging is used a greater number of decimal places are logged in order that rounding errors etc. in further analyses are reduced.

4.5 Static Laboratory Tests

4.5.1 Material Selection

By far the most important capability of the imaging based particle analyser is its ability to produce particle size distribution results. These data are very useful in industry. So far the system's basic accuracy has been established through the use of synthetic test images but no real particles have been analysed. In this section various materials will be observed by the system and size distribution results will be produced. These results will be compared with the results obtained when passing the same materials through an industrially accepted commercial size analyser, in this case a laser scattering based system from Malvern Instruments. Differences between the results will be discussed and explained.

The materials used were limited in suitable size range by two factors. Firstly, the Malvern instrument was only capable of measuring particles of up to 1000μm in diameter, allowing the upper size limit to be set. Secondly, the lower limit was established by considering the limitations of the current system (see section on size analysis) and was fixed at approximately 100μm in this case. A summary of the materials chosen, their size ranges and industrial uses, is given in table 4.3. A wide range of materials was chosen in order that many industries were represented. Materials of varying shape (some rounded and some flaky etc) were chosen in order to assess possible effects.

The materials were tested using both systems. The commercial system requires a large sample of about 100g that is fed into it through a small hopper. Unfortunately it is a lost sample system (the sample cannot be retrieved after being tested) and so the same sample could not be used for the imaging system. In order to minimise possible problems the main source of material was well mixed before separating samples for testing. When

using the imaging based system five independent measurements were taken for each material each using a different, random, selection of particles from the sample. The use of a number of particulate samples ensured that the data were sufficiently representative (see chapter 2, section 2.2). Each of the five readings represented a rolling average over a period of 20 frames. In total therefore, 100 readings were used for each size distribution result. As each frame contained 100–200 particles, between 10000 and 20000 particle measurements were taken into account, leading to reduced statistical uncertainty of the size measurement (see chapter 2, section 2.2).

Table 4.3 Materials used for size distribution testing

Material	Approximate size range in sample (μm)	Typical use
Olivine sand (small)	80-600	Slag conditioner, sand blasting, moulding sand for metal foundries, production of mineral wool, ballast and covering material for underwater pipes and cables, high quality raw material for refractory products
Olivine sand (large)	100-700	
Maize grits	200-1000	Food
Lysine sewon	80-1000	Animal feed additive that boosts growth in poultry and pigs
Soda lime glass	80-600	Pharmaceutical, electronics, bearing, check balls for pump sprayers
Soda ash	80-1000	pH adjustment, acid neutralization, pulp and paper, chemical production, flue gas desulphurisation

4.5.2 Results

Figures 4.21 to 4.32 show the results of the tests ('commercial' referring to the Malvern instrument). Comparative size distribution histograms are shown along with detailed discrepancy results. It should be noted that the discrepancies cannot be considered to be errors, since there is no way of telling which system is 'more correct', but rather differences between instrumentation types.

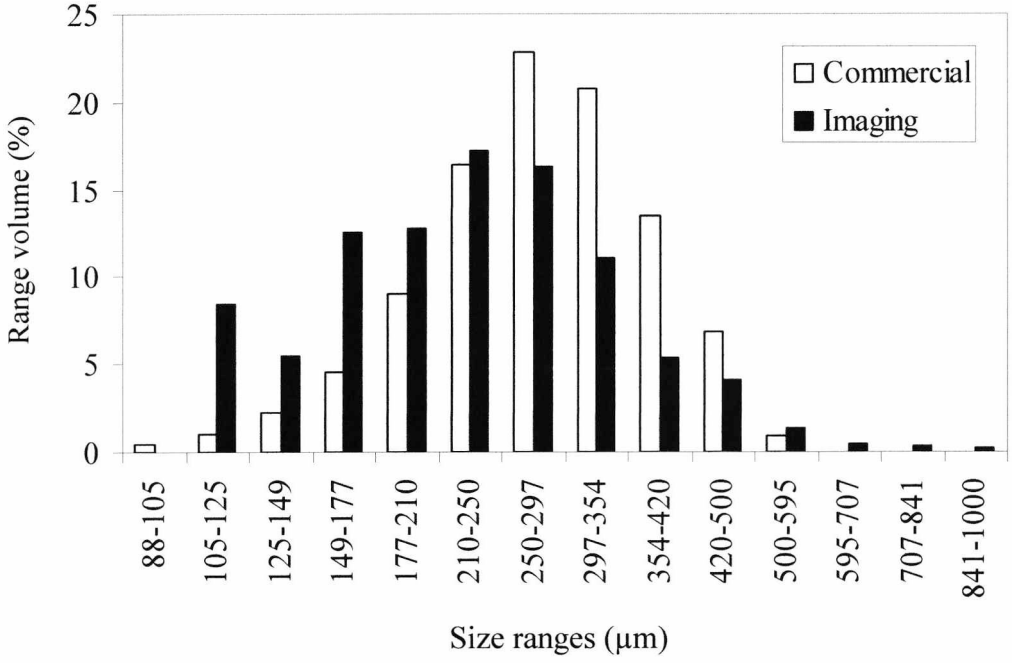

Figure 4.21 Small olivine sand size distribution

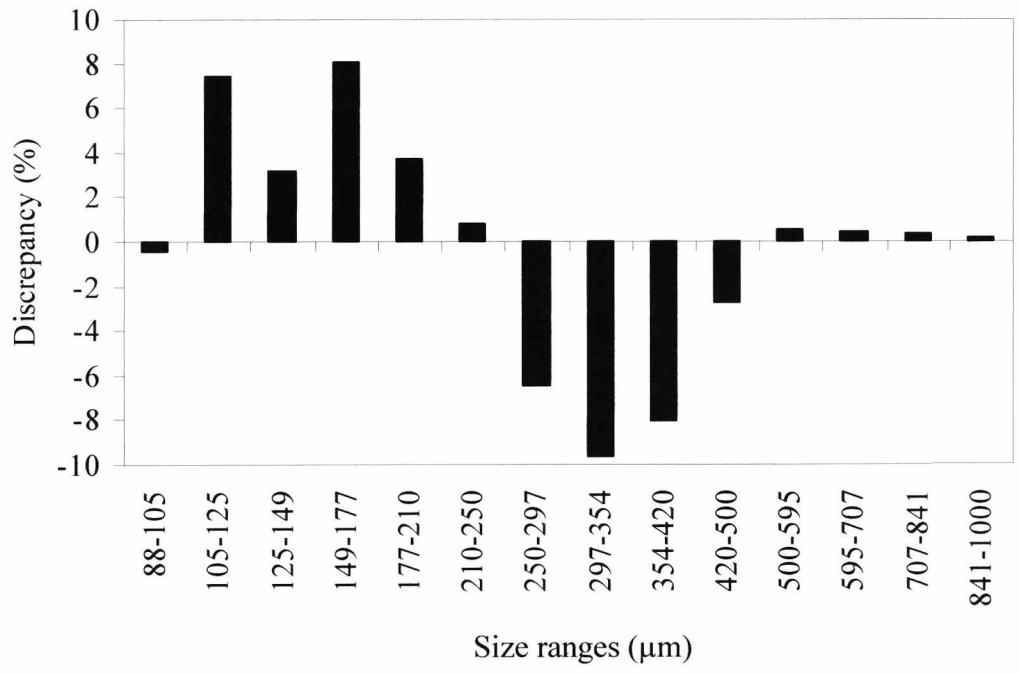

Figure 4.22 Small olivine sand discrepancies

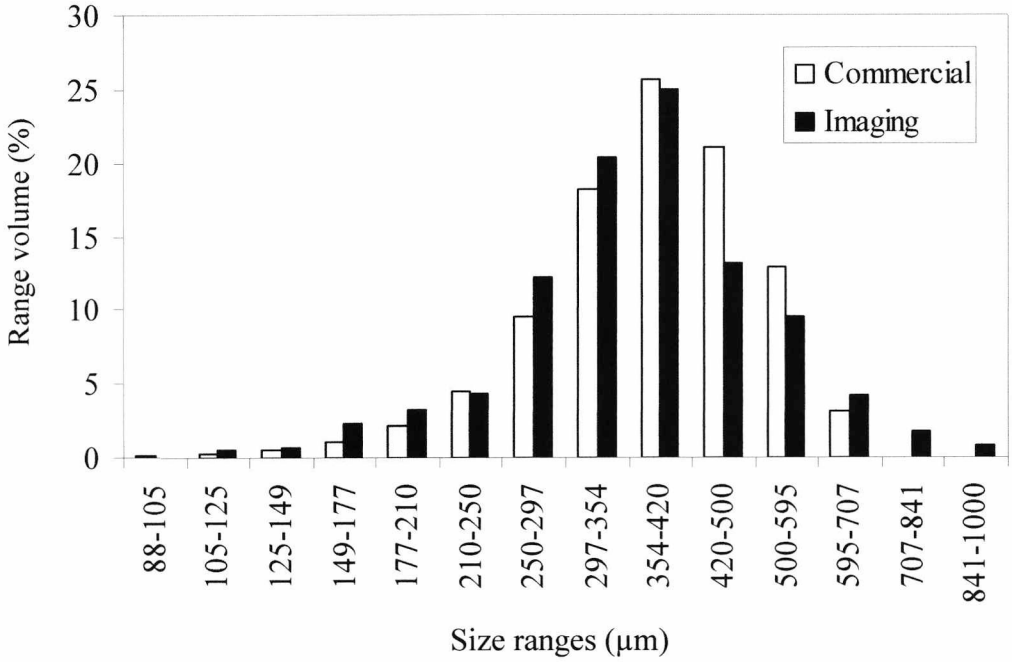

Figure 4.23 Large olivine sand size distribution

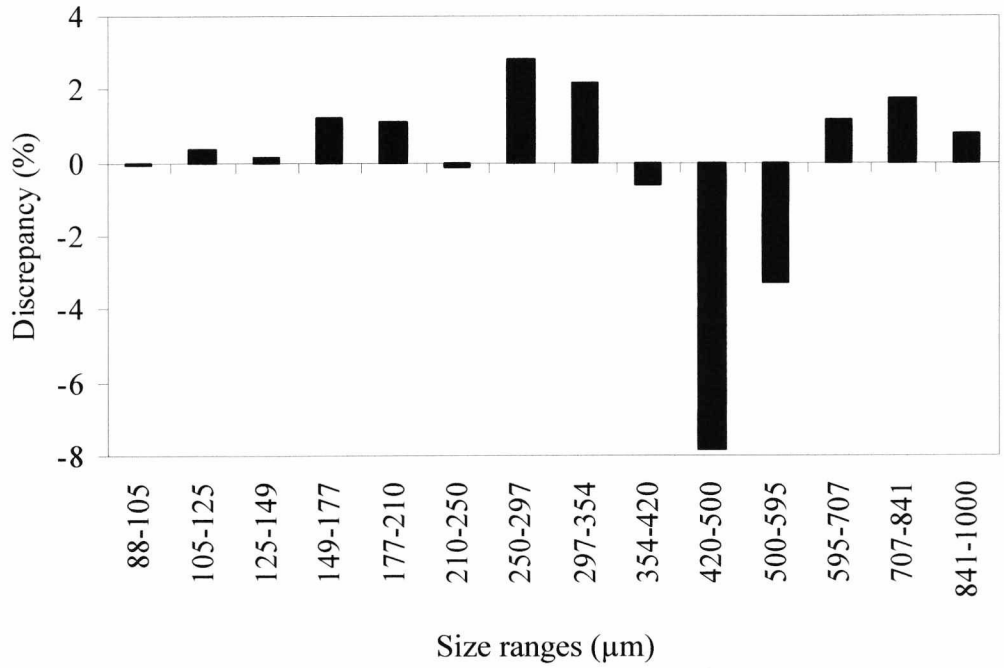

Figure 4.24 Large olivine sand discrepancies

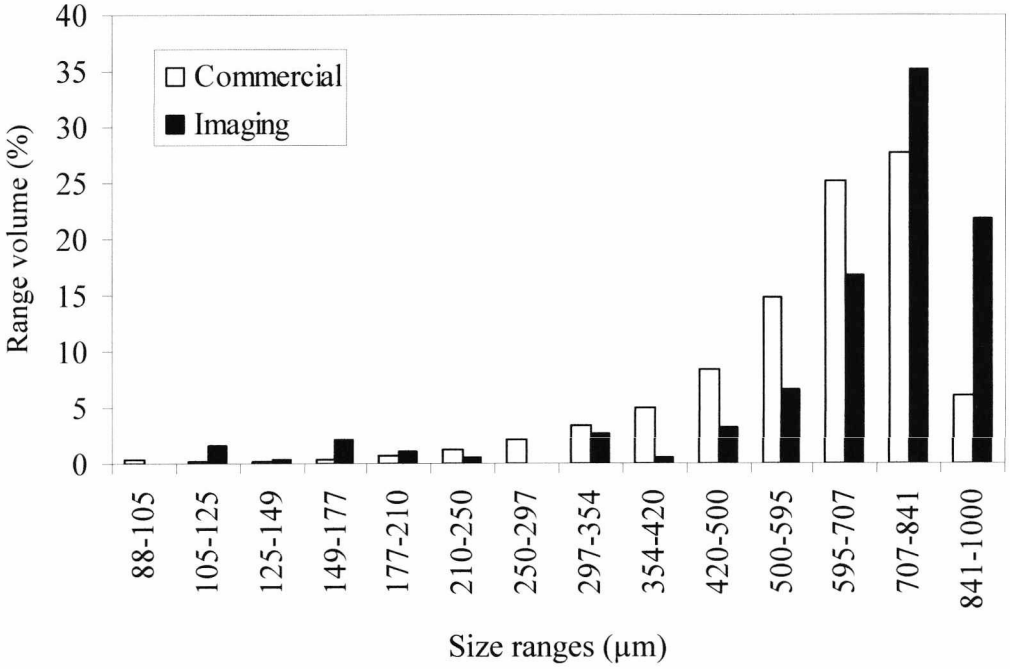

Figure 4.25 Maize grits size distribution

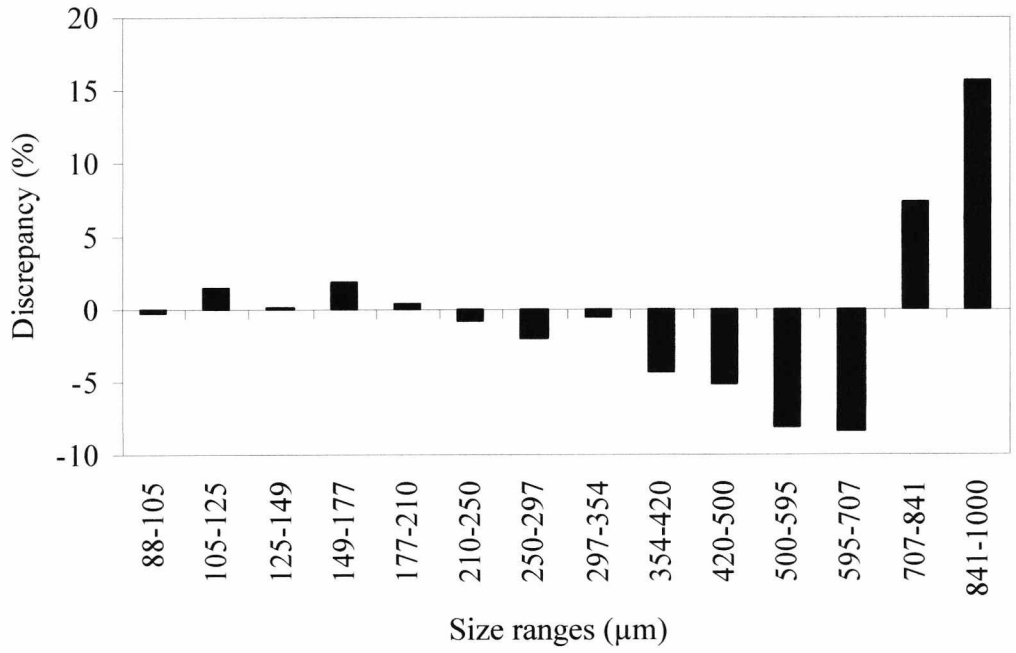

Figure 4.26 Maize grits discrepancies

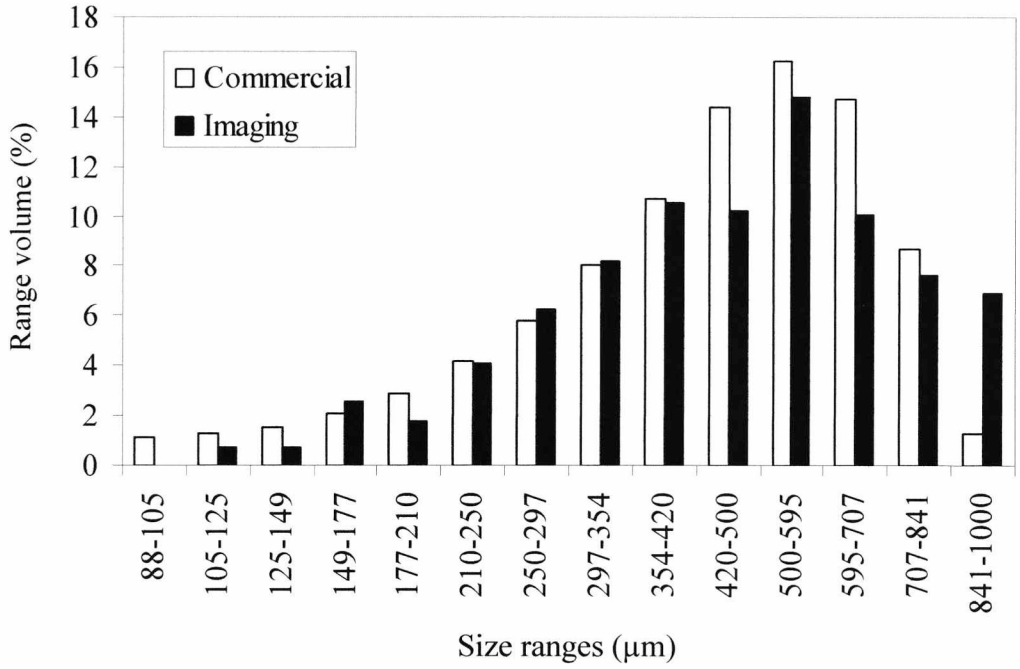

Figure 4.27 Lysine sewon size distribution

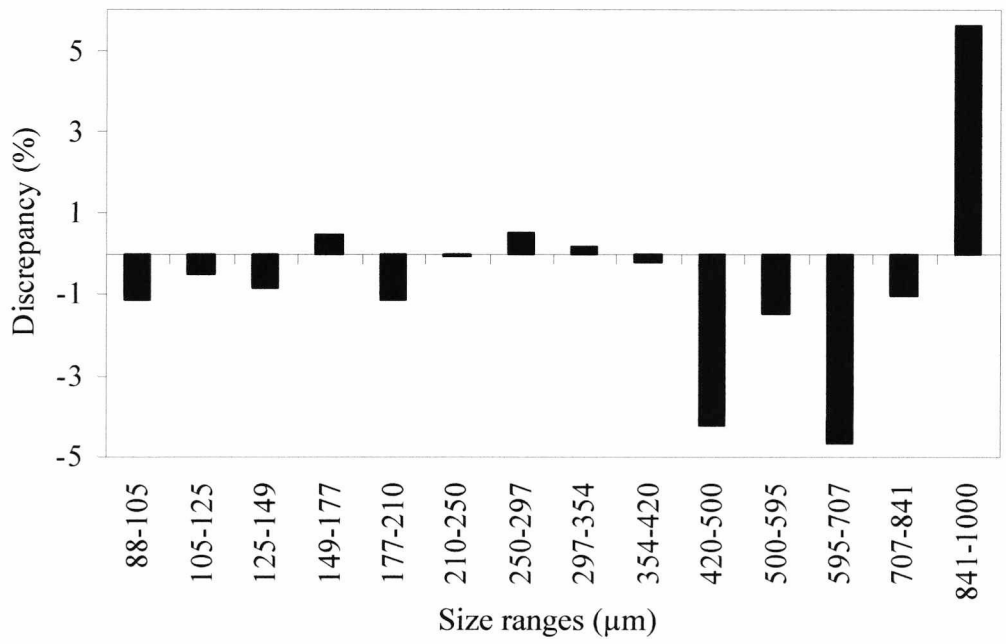

Figure 4.28 Lysine sewon discrepancies

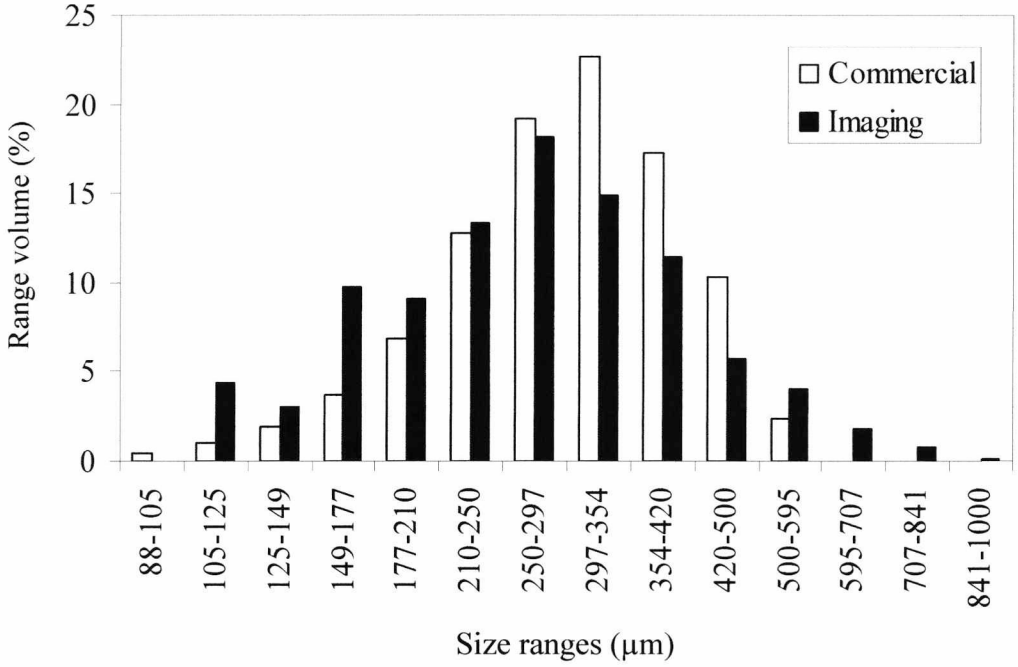

Figure 4.29 Soda lime glass size distribution

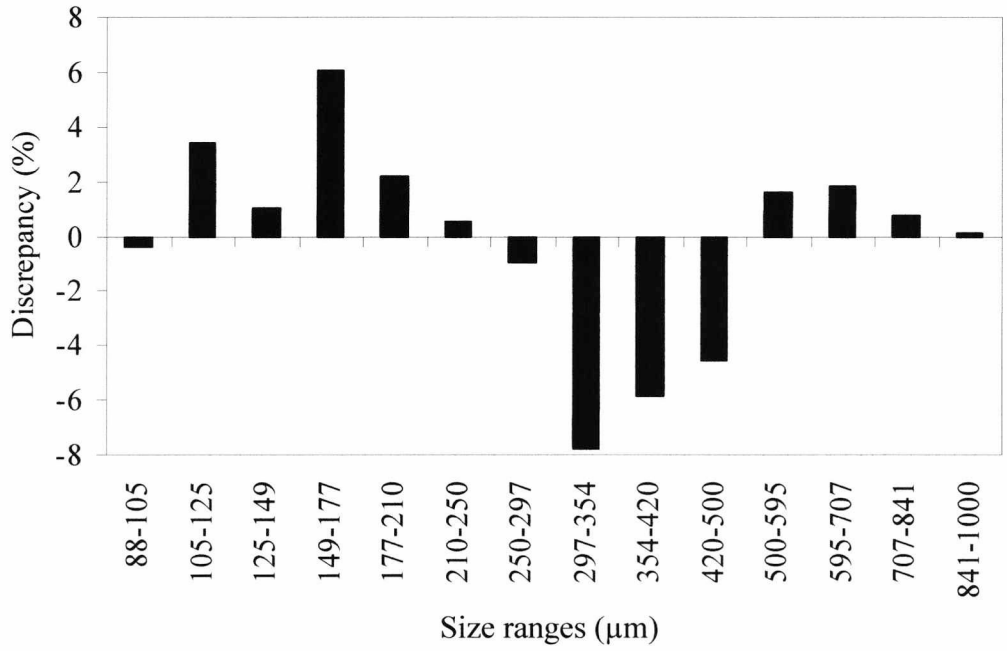

Figure 4.30 Soda lime glass discrepancies

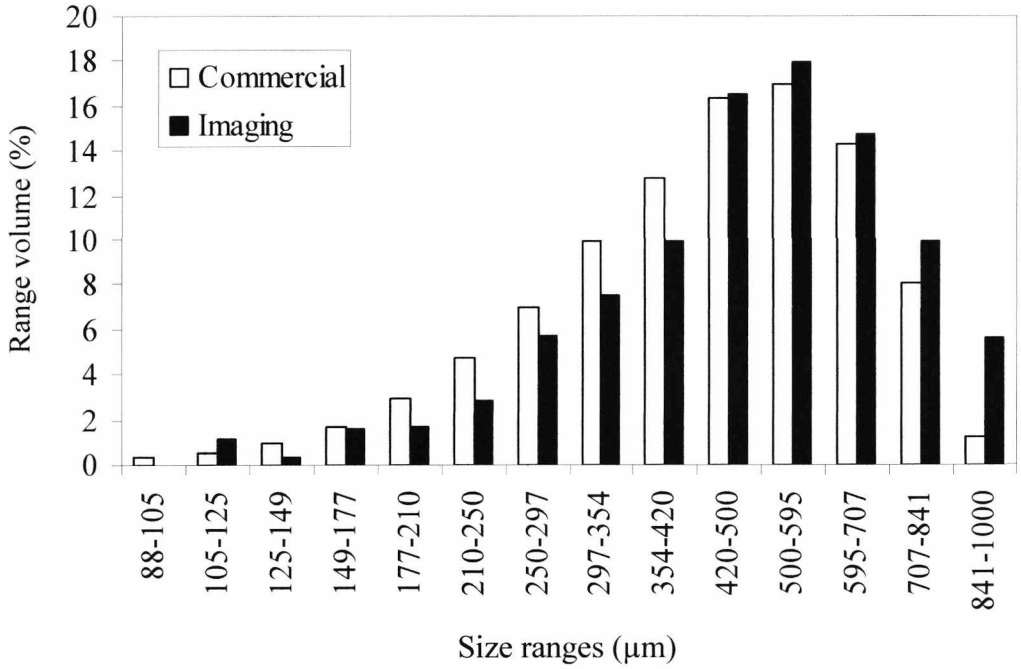

Figure 4.31 Soda ash size distribution

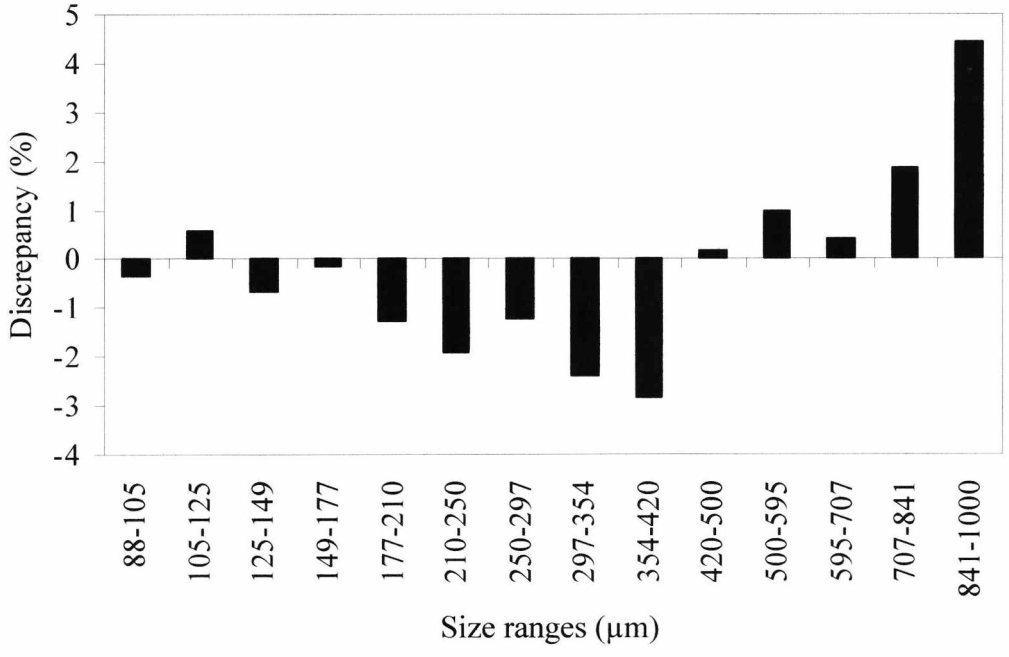

Figure 4.32 Soda ash discrepancies

4.5.3 Discussion

In general, the results show a relative discrepancy of less than ±10%. There are several issues that allow this degree of error to be accounted for. Firstly, the fundamental differences between the two kinds of instrumentation will cause some deviation of results. The Malvern instrument is a light scattering based system and therefore the results it generates are susceptible to variations in the materials' shape (the diffraction pattern of an irregular shaped particle is not circular) and refractive index (see chapter 2). These limitations are not shared by the present instrumentation and may therefore have contributed strongly to the discrepancies in the results. The commercial particle size analyser also uses a large (≈100g) sample, which is interrogated over a period of several seconds. There are such a vast number of particles in this sample that the result is very much a mean distribution. The imaging based system must, by its very nature, only interrogate a small section of the total sample, certainly less than 100g at a time. Although a rolling average is used and five different measurements made, the averaging is still far less severe than with the light scattering based instrument. Furthermore, since the commercial set-up is a lost sample system it was impossible to use the same sample for both reference and measured results, although the material did come from the same source (and was well mixed) it is possible that settling effects and other phenomena led to variations in the distributions.

Another issue affecting the results is the uncertainty that will always occur between size ranges. The differences in random error between the two instrumentation techniques may cause certain borderline particles to be placed in one range by one system and in the neighbouring range by the other. This effect can be seen clearly in several of the result graphs, for instance the 297-354μm and 354-420μm bars in the Lysine Sewon distribution graphs (Figures 4.27 and 4.28). The first bar has been slightly over estimated and the second slightly underestimated so that some of the particles that were judged by the scattering based system to be in the second range have been placed in the first range by the imaging technique.

The last issue is one of particle size. The lower size ranges cannot be expected to be as accurate as the higher ones since the imaging system is nearing its lower sizing limit.

Although the samples were chosen to be of largely applicable size range there may also have been some larger particles in the samples and the unfortunately low size limit of 1000μm imposed by the scattering based instrument may have produced discrepancies between the results (this limit is not shared by the current instrumentation and although no bar is shown on the histograms, the presence of >1000μm particles would be reflected in a reduction of the other values in the results).

4.5.4 Material Specific Issues

It is believed that errors of ±10% can be clearly accounted for by the issues already addressed. There are, however, some specific discrepancies or points of interest that should be discussed in respect of the results generated for each particulate material. When considering these points it may be useful to consult raw, unprocessed, images of the materials during sensing. Typical images are shown in Figure 4.33. The following discussions are assigned letters in accordance with the material lettering in this figure.

a) 'Small' olivine sand: This material is mainly shown in the smaller size ranges where the imaging system has lower accuracy. The general agreement is still useful and it can be seen that the overestimation in the lower size ranges has forced underestimation in the larger ones.

b) 'Large' olivine sand: This result shows very good general agreement between the two systems. The commercial instrument though, seems to be having difficulty with the larger sizes, simply ignoring the last two ranges, whereas the imaging based system is showing a gentle, believable, roll off at the high end. These extra percentage volumes must cause further differences in the results and it is believed that the large discrepancy in the 420-500μm size range can be accounted for in this way. It is interesting to note that the material *looks* bigger than the smaller sand in figure 4.33 despite the fairly small numerical size difference.

c) Maize grits: Whilst there is some random error in the small size ranges the main discrepancies here are in the larger sizes. In fact it appears as though the whole graph has been shifted to the right by the imaging based instrumentation.

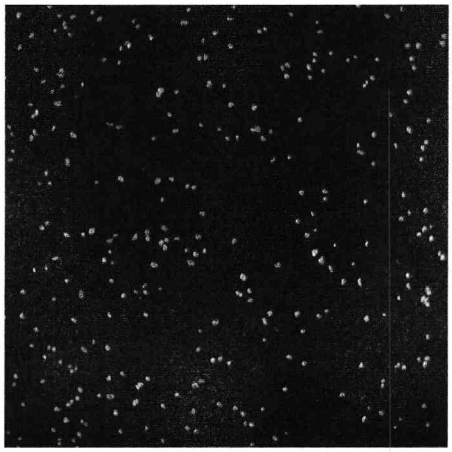

a) Small olivine sand

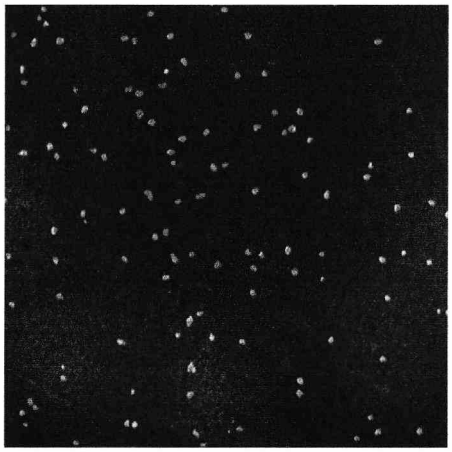

b) Large olivine sand

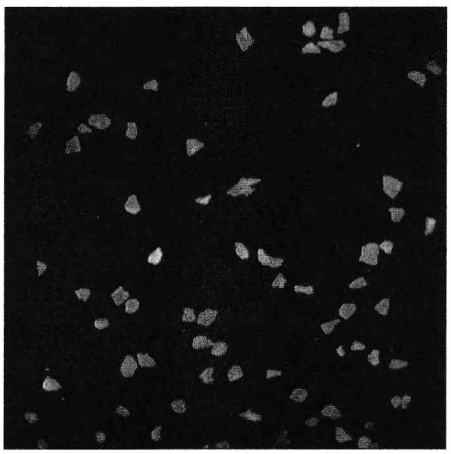

c) Maize grits

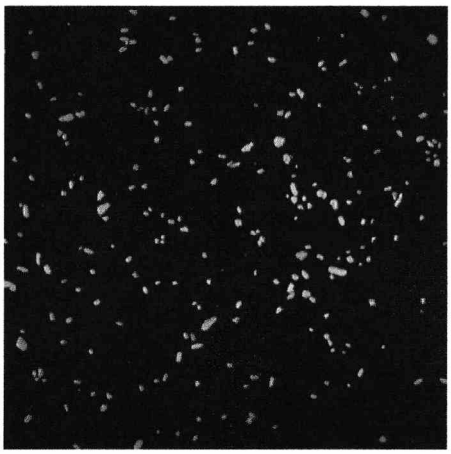

d) Lysine sewon

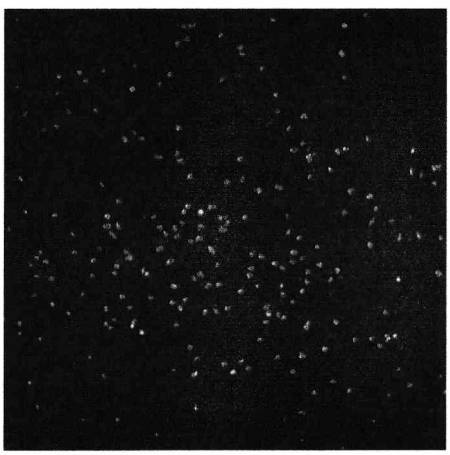

e) Soda lime glass

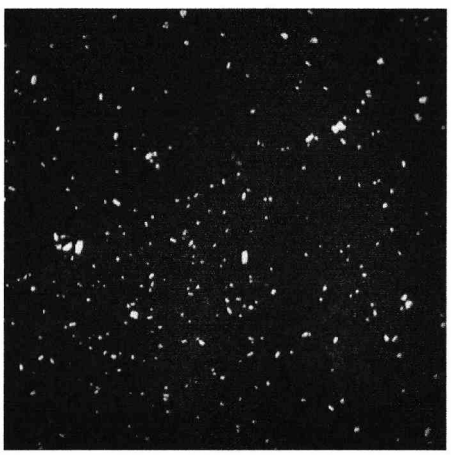

f) Soda ash

Figure 4.33 Unprocessed particle images

The reason for this is that maize grits are 'flaky' in shape. In the light scattering based commercial system, where an 'in-flight' measurement is made, the average size of the whole particle is found, but in the 2D imaging system the particles are laid flat on the interrogation surface and so they tend to appear larger than suggested by the reference data. This is not necessarily an error on the part of the imaging system but rather a different way of defining size. Clearly, in the case of flaky materials, the results from the two measurement methodologies will not be comparable (particle shape is clearly of importance, see chapter 3, section 3.4).

d) Lysine sewon: In the lower size ranges the agreement between results is excellent. It is thought that the discrepancies in the upper ranges can be attributed mainly to the differences between the two samples used. This material has a wide range of sizes and to select two small samples that represent all of them (especially the larger, less common ones) is difficult. This material also has some tendency to 'clump' forming larger conglomerated particles. This tendency will be reduced during in-flight measurements, which explains the higher final size bar generated by the imaging system.

e) Soda lime glass: The general agreement is good. The discrepancies are caused by a combination of the upper size range problem seen for 'large' olivine sand and the low range errors seen for 'small' olivine sand. This material has similar optical properties to olivine sand but represents a larger range of sizes than the sand samples used.

f) Soda ash: Again, the general agreement is good and any discrepancies can be accounted for with combinations of issues already described. Whilst this is not a 'flaky' material the particles are slightly 'flattened' and this may have contributed to the 'right shifting' effect apparent in the graph (similar to the issue observed with maize grits).

The images in figure 4.33 show typical concentration levels that were used during testing (less than 2% solids concentration). At these concentrations particle overlapping is not an issue as determined earlier in this chapter. This means that any tendency to oversize particles in the images cannot be attributed to particle overlapping but must be explained in the ways outlined above.

4.6 Summary

In this chapter practical considerations for static particular analysis have been considered. Specific hardware has been detailed and its limitations assessed in terms of both lighting consistency and parameter measurement limits. The limits of both solids concentration measurement and size measurement have been discussed. It has been established that solids concentrations of up to around 3% can be measured accurately and that, for reliable particle sizing, particles must occupy a minimum of nine image pixels in the form of a 3x3 array.

For a practical system processing software is required and this too has been discussed. The general software arrangement and operation strategy has been described and details of processing algorithms used to solve practical problems, such as pincushion distortion correction, have been given.

Finally practical static material analysis tests, using materials relevant to a wide range of industries, have been undertaken and the results have been compared favourably to those taken by an established off-line industrial solution.

This chapter has considered the basic practical transition to real static analysis of particles. The next chapter will build on this to show how pneumatically conveyed particles may be measured on an on-line, continuous basis.

Chapter 5

On-Line Continuous Flow Imaging and Parameter Measurement

5.1 Introduction

Chapter 4 covered the transition from the theory of Chapter 3 to a real physical test setup. This setup, however, was of a static nature and used strictly for establishing measurement accuracies and developing processing algorithms under static conditions. In this chapter the transition to a real on-line sensing arrangement will be discussed. The problems involved with imaging moving particles will be discussed and solutions detailed also the physical details of the on-line system will be given. Any additional processing algorithms, required in order to deal with the new conditions, will be explained. In addition further functions available during on-line operation will be discussed. These include the use of the instrument to detect flow ropes or other inhomogeneous flow regimes and the use of an independent velocity measurement in order to establish, inferentially, the instantaneous mass flow rate of material. Where appropriate, test results are given that show the accuracy of measurement when compared to the static system.

5.2 Continuous Imaging of Particulate Flow

Discussion so far has centred on processing images of particles under static conditions. This has enabled basic principles and accuracies to be established free from the complexities of on-line operation. Static images of particles are very clear and repeatable but when the particles are moving this is not the case and so further techniques are required, both physical and in processing software, in order to extract the necessary information from the particle images.

5.2.1 Acquiring Images of Moving Particles – Lighting

Before any processing may commence the best possible image must be acquired using an appropriate physical and optical set-up. In real terms the requirement for good images translates into the requirement for a good lighting set-up. Focusing the camera upon the illuminated particles is a relatively simple problem. For static analysis two options were available: front lighting or back lighting (shadow imaging). These two options are still applicable to on-line flow and in general the same discussions on their relative pros and cons still apply, see Chapters 2 and 3. The problems involved in shadow imaging become far worse with on-line operation and it should be remembered that one of the aims of the work was to develop a system that operates in a non-intrusive manner. In order for good shadow images to be produced the flow would have to be split up so that a small 'flat' section could be passed over the backlight, see figure 5.1. Clearly this approach requires intrusive modification of the duct and can be ruled out here.

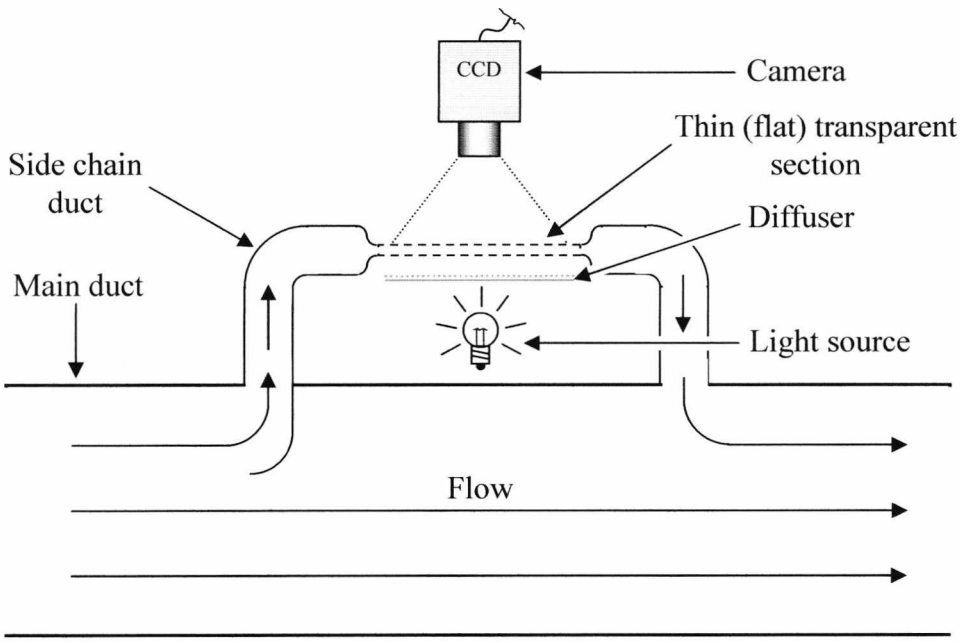

Figure 5.1 Possible intrusive back lighting based on-line sensing scheme

The only way in which the problems of intrusive installation can be avoided is if the duct is not modified to any significant degree and most importantly if there is nothing protruding into the duct. This suggests that all lighting and observation must be performed through some kind of viewing window that is let into the duct wall.

At first thought such a scheme might seem impractical as particles are present within the pipe at many different depths and in order for accurate sizing to be performed the depth of each particle must be known. This problem can be solved through the use of laser sheet illumination. Laser sheets have been used in the past for Particle Image Velocimetry (PIV) work and in this context they are widely accepted (see Chapter 2). In essence the light from a visible laser is passed through a barrel lens which spreads out the usual, circular cross sectioned, laser beam into a wide, thin, fan shaped sheet of light. For PIV this sheet is used lengthwise, along the duct, so that the movement of particles may be observed. For reliable sizing it has been decided that the opposite is necessary: the sheet must be perpendicular to the flow in order that the cross section of particles is highlighted as they pass through. The general concept is illustrated in figure 5.2 where the camera and laser are mounted on a corner in order that the camera and imaging plane remain at right angles to one another.

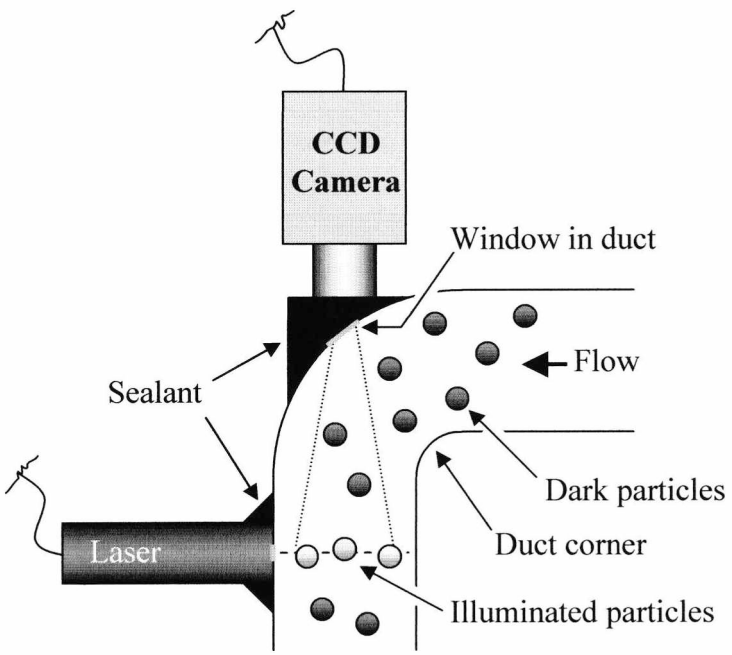

Figure 5.2 Non intrusive laser sheet based sensing scheme

It might seem at first glance that certain non-illuminated or 'dark' particles might obscure the camera's view. In practice this is not a problem if the concentration of particles is kept low (the particles in figure 5.2 are of greatly exaggerated size). This is very similar to the particle overlapping issue discussed in previous chapters and the upper concentration limits will be affected in a similar way, see the next chapter.

The usefulness of laser sheet illumination is limited with certain, highly refractive, materials such as glass beads but in general it is a widely used and well established technique. A practical implementation, and the accompanying problems, will be discussed in section 5.3.

5.2.2 Image Processing for Live Flows

Despite physical efforts to achieve the best possible flow images it cannot be expected that on-line images of moving particles will be as clear as images taken under static conditions. In order to counteract this it is necessary to use slightly different image processing algorithms from those developed for the static system described in previous chapters.

The main processing challenge, once images are available, is to separate the particles from the image background. It is necessary to locate particles in the images and determine reliably how many image pixels represent each particle, a process known as 'particle separation'. Once this information is known statistical processing will allow all useful parameters to be determined (see Chapter 3). With the static system it was found that thresholding was a suitable particle separation method so long as the threshold level could be determined reliably and a method of deciding upon a suitable threshold level was, therefore, detailed. With on-line images it has been found that thresholding alone is not suitable and it is necessary to perform some pre-processing of the images before the thresholding operation, detailed in Chapter 3, may commence.

There are two main differences between on-line and off-line images. Due to the laser sheet illumination the on-line images tend to exhibit lower contrast also the background is of a less consistent nature during on-line operation. These factors must be addressed in software.

5.2.2.1 Background Removal

When using the static particle sensing system the background is of a known and consistent nature (it will, in most cases, be a matte black surface) and will not present any

major variations of tone or intensity that may hamper particle separation efforts. When using the on-line imaging set-up, the concept of which was illustrated in figure 5.2, this is not the case. The particles are illuminated in the form of a sheet in mid air. Behind the illuminated particles there are other particles and the slanting surface of the duct wall. Particles that are not illuminated do not represent a problem but the duct wall does, since its surface nature cannot be controlled. It would of course be possible to paint the inside of the duct matte black but this would soon wear away, under the constant onslaught of fast moving particles, to leave the bare metal exposed. The bare metal duct wall causes two light related problems. Firstly, although the only source of light is the laser, there will be some ambient illumination in the duct due to reflections, refractions and diffusion of the laser beam as it interacts with the particles. This ambient light may be reflected from surface features of the duct wall to create static 'artefacts' in the particle images and will certainly increase the intensity of the background thus reducing the contrast in the images. Secondly as the laser beam does not cease to exist once its work is done, it will shine against the duct wall creating an intense line of light. This not only increases the ambient light level in the duct dramatically but also it may be possible to see this line in the images (depending on the particular optical geometry employed). An example image, taken without particles flowing and using an experimental system similar to that suggested in figure 5.2, is shown in figure 5.3. The ring of laser light, its accompanying 'glow' and the window through which the laser shines are visible clearly. Some means of removing static features from the images must be employed in order that further processing efforts may concentrate on the dynamic image elements i.e. the particles.

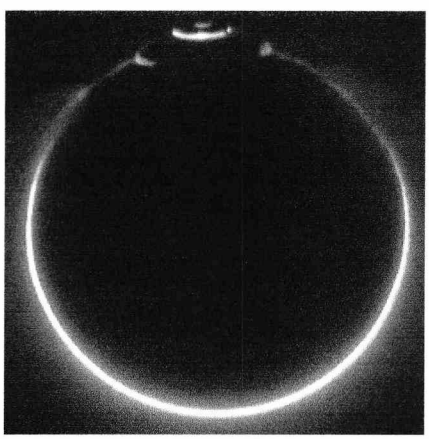

Figure 5.3 Duct background image

It can be seen from this image that, in this case, a circular mask routine could be employed to concentrate on the centre of the image and replace the offending static features with a dark background colour. This solution is not ideal since a) the central area would have to be small enough to avoid the 'glow' effect around the laser line thus limiting the sensing area and b) if the sensing geometry were not right angular, as used here, then a custom (hand drawn) non-circular mask would be required for each different geometry employed. A more elegant, automatic solution is, therefore, required.

In this instance the method employed in order to achieve background removal is an image subtraction based processing algorithm. A reference image is taken with no particles flowing and this is subtracted from all further flow images. This method has the advantages of simplicity and flexibility (varying imaging geometries are easily accommodated) but it is not perfect. Whilst this method will work all the time that the static aspects in the images remain absolutely constant it will be necessary to periodically re-establish the reference image if there is any drift in the static conditions. In a practical situation drift is inevitable and may be caused by vibration, temperature variation and ageing/wear of components. Depending upon the severity of static drift the re-referencing process will need to be performed more or less frequently, the necessary time scale must, therefore, be established for each individual scenario (when the time has come to re-reference the static image, anomalies between the old and new backgrounds will show up as particles in the processed images i.e. particles will appear to be present when no material is flowing). For research purposes, where test runs are short and re-referencing easy, this potential problem is greatly offset by the flexibility of the subtraction approach.

In an industrial situation, with much vibration, re-referencing may be required frequently and so it may be desirable to use the masking based approach in order to avoid re-referencing and simply accept a certain loss of interrogation area as a consequence. The flexibility of the subtraction approach would not be required in an industrial instrument since the sensing geometry would not change. The current software implements both subtraction based and circular mask routines that may be alternately selected by the user in order that possible vibration problems during industrial trials may be circumvented without having to 'return to base' to write new software routines.

5.2.2.2 Particle Contrast Enhancement

Static artefacts are not the only problem with on-line flow images. With the test set-up used in previous chapters the lighting and background were optimal resulting in relatively clear, high contrast, images. Laser sheet illumination, whist an accepted technique, does not produce such well defined images and in addition to this fundamental shortcoming the contrast is further reduced by the ambient light and non-ideal background effects discussed in the previous section. Figure 5.4 compares on-line and off-line images in order to illustrate this point.

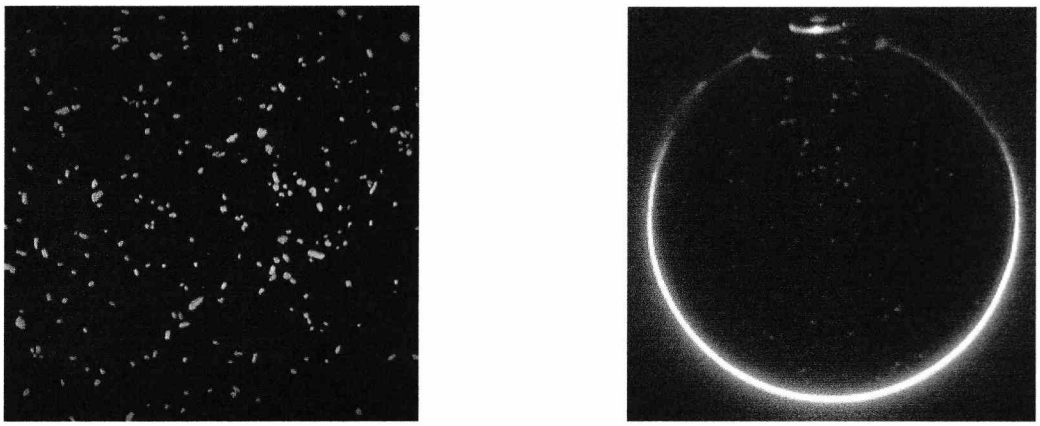

a) Off-line image b) On-line image

Figure 5.4 Comparison of on-line and off-line images

It is clear that, whilst particles are present in the on-line image, the contrast is very much lower than that of the off-line example. Conventional contrast adjustment may be applied to the image but it has been found that many of the particles are very close in colour to the background and their clarity is actually reduced by a conventional operation (a conventional contrast operation increases the gradient of intensity levels within the image thus producing an image that represents the clipped or limited intensity variation of an image with higher dynamic range, it is a form of signal compression). Some means of increasing the contrast of dynamic objects whilst ignoring the noise of the background is required and a method for achieving this has been identified. In order to explain this method it is necessary first to observe a close-up of some particles from the figure 5.4b image. This is shown in figure 5.5.

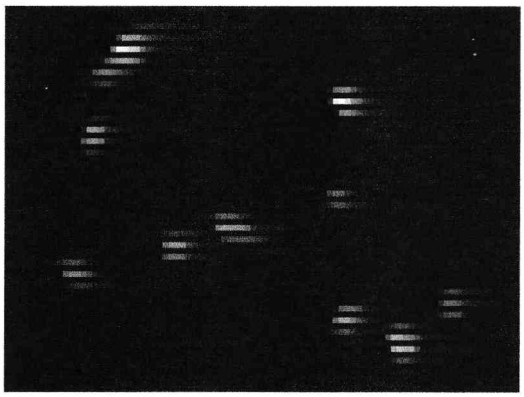

Figure 5.5 Close-up view of particles from figure 5.4b

The most striking feature of this image is the 'banding' within the particles. This is caused by the interlaced nature of the video images (see Chapter 4). The camera is capturing two images and transmitting them as one frame; one image is taken consisting of even lines and then, 20ms later, another is taken consisting of odd lines. This means that each image represents two 'snapshots' of the flow with approximately twice as many particles than are really present at any one time, causing concentration errors in the results. It is also possible for two temporally separated particles to overlap each other in the final composite image. For these reasons each sub frame (the odd lines or the even lines) must be dealt with separately. This means that, if in one instance the odd lines are discarded and the even lines used, the particles in the image will only be represented by every other image row, producing a 'banding' effect such as that seen in figure 5.5. The conventional method of de-interlacing a still image is to simply copy the lines that are to be kept over those which are to be discarded thus effectively halving the vertical resolution. Some algorithms take this a step further by applying some kind of interpolation filtering in an attempt to approximate the lost data. In the current work a method has been found of turning the 'banding' effect into an advantage. Initial de-interlacing is accomplished by overwriting the unwanted lines with the images mean intensity level so that all particles in the image now represent the same moment in time, thus eliminating concentration errors, but the banding still remains. The reason why this may be considered useful is more apparent once the realisation is made that only the particles will suffer from serious banding, (static artefacts were removed by the subtraction algorithm in the previous section leaving just the noisy background and particles) the background will not since it is itself close to the images mean intensity level for small particulate concentrations. The banding of the particles represents sudden

changes in intensity level (a high frequency component) around the particles, the background will only contain more gentle changes of intensity. If an edge enhancing or contour extraction filter (essentially high pass filters) is applied to the image then the particle intensity will be very much increased whilst the background will remain insignificant. The banding can now be removed with a suitable interpolation type de-interlacing filter (the filters used are standard zone based types and not being novel in any way will not be detailed here). The steps of the operation, as applied to the figure 5.5 image, are shown in figure 5.6 where the process is applied to a negative image in the interests of clarity.

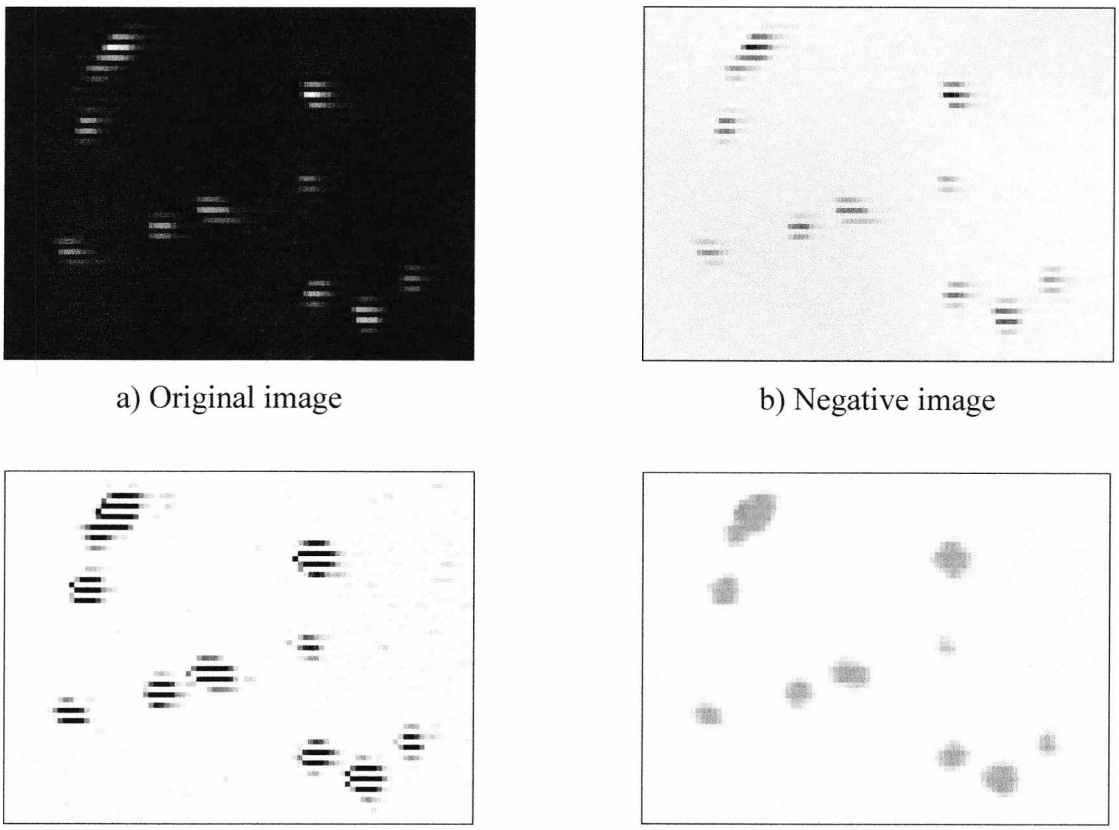

a) Original image

b) Negative image

c) Image with contours enhanced

d) Filtered version of (c)

Figure 5.6 Contrast improvement through edge enhancement (high pass filtering)

It can be seen that the particles are successfully enhanced through this sequence of operations. It is now possible to apply the adaptive thresholding algorithm that was introduced in Chapter 3 (in the example shown above it appears that the final image is already virtually in a binary form but in reality there is still noise present in the background allowing successful automatic threshold setting).

5.2.3 Sizing Limits and Accuracy for On-Line Measurements

In Chapter 4 the absolute size and concentration measurement limits for the static system were determined through experimentation. For the off-line system the upper concentration limit was set through observing the effects of particle overlapping and touching in the images. For the on-line version a similar issue is that of non-illuminated particles obstructing the camera's view of those illuminated in the laser beam. This issue (determining the upper concentration limit) will be investigated in the next chapter when the results of extensive laboratory trials will be detailed.

The other parameter of interest is size. Since the processing algorithms used for on-line work differ from those used off-line it is necessary to re-establish the small particle sizing limit. The most notable change in conditions is that imposed by the resolution reduction caused by the use of single interlaced sub-frames. In Chapter 4 the reduction in accuracy/minimum measurable size caused by the halving of resolution was discussed and it was shown that the effective minimum measurable size almost doubled. In this case the resolution has not been halved in both directions, only vertically and it is reasonable to expect that the effect of this reduction will not be as severe as the effect of both horizontal and vertical halving that was observed in Chapter 4. It should also be expected, however, that the errors of measurement will not simply be a multiple of those observed before due to the new edge based particle separation routines used here.

It is necessary to establish the effect of the resolution reduction through experimentation. For the off-line system this is easy and due to the nature of the imaging based approach the procedure is the same for the on-line set-up. It is possible to insert static test images into the duct, laser illumination cannot be used but similar low-contrast conditions are simply arranged, the contrast between particles and background in a real flow image is observed and lighting arranged so that similar conditions prevail during static image analysis. In Chapter 4 a series of tests was performed in order to establish the lower limit of sizing and a similar series of tests was performed here. Particles in the 25μm to 1mm range were employed (in reality 250μm to 10mm see Chapter 4). The results of these tests, together with those from the static system, are shown in figure 5.7.

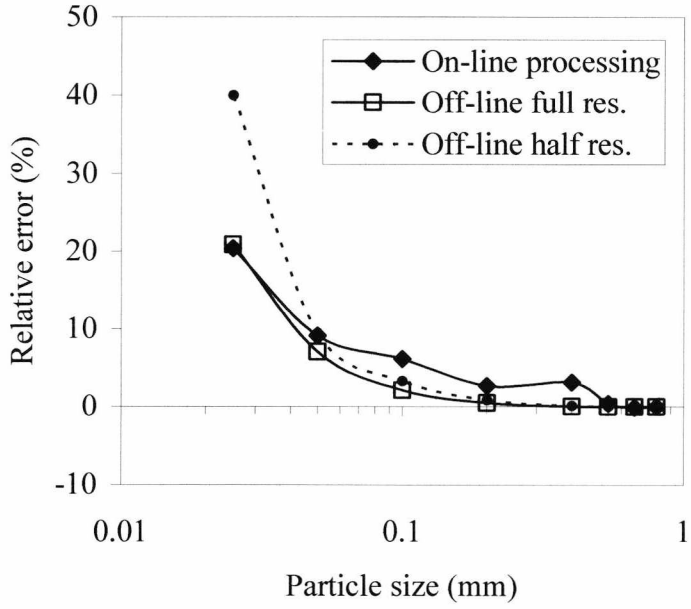

Figure 5.7 Relative error of particle size measurement for small particles

This figure shows interesting results, the maximum error being unchanged from the full resolution static arrangement, although in general the errors are higher. The first three data points, from right to left, exhibit very low errors (no more than 0.3%) but after this there is a sudden jump to around 3% error. It is believed that this is due to the effects of the alternate line image format as this issue becomes important once these sizes are reached. Beyond this the error rises as expected and falls in line with the off-line curve. It is to be expected that the smallest, single pixel, particles do not exhibit larger errors than under full resolution static conditions since the full resolution is still available but only on every other image line. In general, viewing the extremes is helpful in order to understand these results: for large particles the image banding is unimportant due to the sheer size of the particles, for very small particles the resolution is unaffected and for mid range particles the banding effect does lead to variations in measured particle size.

Under on-line processing conditions the errors will be higher than those experienced for ideal static conditions but this is to be expected. Clearly the edge based contrast enhancement method, in conjunction with the interlaced image banding, leads to less accurate results than straightforward thresholding under static conditions but the increase in errors is not prohibitive. It is thought that the minimum measurable particle size is not affected by the on-line processing methodologies employed, although a certain increase in errors must be accepted.

5.3 Physical Sensing Arrangement

The physical set-up used for on-line flows must overcome various difficulties if it is to operate successfully. In figure 5.2 the basic laser sheet based methodology was introduced. It was shown that the camera and laser were mounted on a duct corner in order that the camera could remain at right angles to the laser sheet. In practice this is not a particularly useful geometry as a suitable corner might not be available in a real situation. There may also be problems with turbulence and other effects at flow corners that could interfere with imaging. Another issue may be erosion caused by particles smashing into the camera lens. In short this is not a practical geometry and an alternative must be found that can be fitted to a straight section of duct. The solution employed here is shown in Figure 5.8. The laser is still at right angles to the duct but the camera is no longer at right angles to the laser sheet. It views the sheet from a shallow angle.

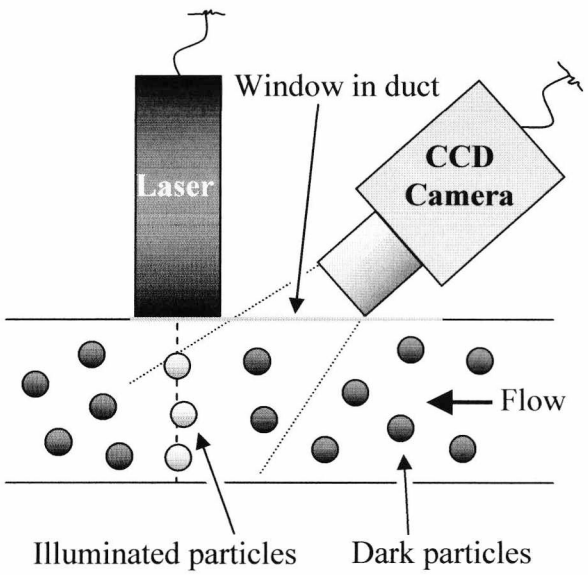

Figure 5.8 Practical 'straight duct' sensing geometry

It is clear that, whilst preferable from a physical viewpoint, this sensing geometry will lead to problems in respect to image processing. Specifically, there will be some trapezoid distortion introduced due to the camera angle (note that the camera angle is exaggerated in the above schematic figure and in reality the problem is not as severe as might at first be thought). Also there will be practical issues to consider such as how to

keep the window free of contamination so that clear images may be acquired through it. These issues will be addressed in this section.

5.3.1 Camera/Lens and Duct Coverage

A discussion on the actual camera and lens used would, at first, appear to be more at home in the sensing head description later in this chapter. Since, however, the preceding introduction on sensing geometry leaves some possible questions unanswered in respect to imaging coverage of the duct and since the next section on distortion correction assumes lens angles are known, these aspects will be discussed here.

In order to maintain comparability between static experiments detailed so far and on-line work to come, it was decided to use an optical set-up having the same properties as for the static system. In view of this the same camera was used. It may be remembered that this camera features automatic gain and shutter speed control which were not an issue for static measurement. Under dynamic flow conditions these automatic controls may cause problems for the system. It should be pointed out that one of the goals of the work was to investigate the usefulness of cost-effective components for on-line particle analysis and so an investigation into the effects of these automatic controls (invariably found on cost-effective cameras) is of relevance. It is believed that automatic gain control will not be an issue since the on-line images are so 'dim' the gain will probably saturate to its maximum value. Shutter speed, however, is more interesting. The effects of these automatic controls will be investigated in Chapter 6.

In order for the optical characteristics of the setup to remain constant camera, lens and working distance must remain the same. Any change in one of these parameters must be counteracted by an opposite change in another. When the final sensing head was designed (described in section 5.3.3) it was impossible, due to physical considerations, to use the same working distance that was employed in the static setup. Previously 35mm was used and for the on-line set-up this was increased to 73mm. It was mentioned in the previous chapter that a choice of two lenses was available and that the 50° type was used for the static set-up. For on-line work the other choice was employed and the specifications of this lens are given in table 5.1.

Table 5.1 Lens specifications

Type	Multi element ground glass with anti reflective coating
Aperture	Fixed – f2.5
Effective angular field of view (1/3" image sensor)	25°
Focal Length	12mm
Working distance	50mm – ∞

It can be seen that the lens angle is halved to 25° which compensates for the increase in working distance, yielding an identical sensing area. This area amounts to a rectangle of 26mm by 19.6mm (the slight change in aperture will not effect imaging geometry).

It will be readily appreciated that this rectangle does not cover the entire inside area of the duct. In fact the area covered is 38% of the 40mm internal diameter duct. It is not thought that this coverage will be an issue in tests since, for laboratory experiments, flow conditions will be set up that are steady and homogeneous i.e. the flow will be similar across the entire area of the duct. Even under inhomogeneous conditions this coverage is sufficient for the detection of such regimes. In addition, a rectangle having 38% of the area of the duct gives better coverage than might be thought intuitively. The sensing area, drawn to scale in relation to the duct, is shown in figure 5.9. It can be seen that the area is shifted slightly towards the top of the duct. This was due to practical considerations (the shallowest possible camera installation angle was employed in an attempt to minimise trapezoidal distortion, see section 5.3.2).

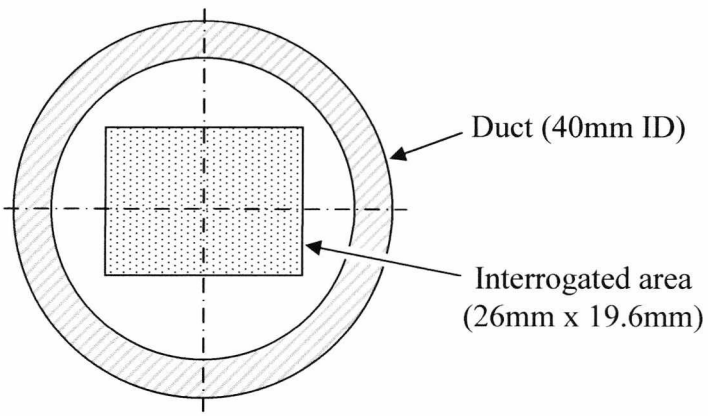

Figure 5.9 Area interrogated by the camera

5.3.2 Optical Considerations/Distortion Correction

There are two optical problems that must be considered with the straight duct sensing geometry. Firstly, the camera must observe the flow through a window which may lead to refraction, causing distortion of the images. In practice, it is not expected that there will be significant pressure in the duct and so a very thin window may be used, this minimises refraction issues so that they are swamped by the second problem: trapezoidal distortion, introduced due to the camera's viewing angle. The general problem is illustrated in figure 5.10 which shows; a) an image with trapezoid distortion and b) the corrected image – note that these images were taken using an extreme viewing angle in order that the problem be clearly visible and that due to this there is a little blurring top and bottom as a result of depth of field limitations.

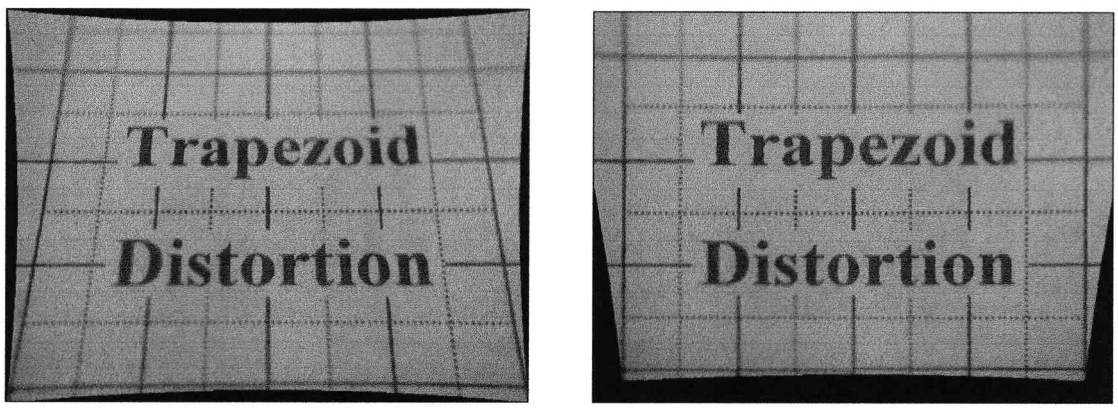

a b

Figure 5.10 Trapezoid distortion

There will also always be pincushion distortion in the images and it can be seen in figure 5.10(a) that the pin cushioning has already been eliminated as described in Chapter 4. The trapezoid distortion consists of two elements. Firstly, there is a 'perspective' effect with the image features converging towards the top of the image and secondly, but perhaps less obviously, there is also a foreshortening effect towards the top of the image. Put scientifically, the size of objects in both their horizontal and vertical aspects is related to their vertical position in the image. The 'perspective' type element requires that the image lines be compressed or expanded as necessary, without affecting the vertical spacing and the foreshortening requires the same treatment in respect to the image columns, this time

leaving the lines untouched. The procedure is understood more readily once the source of the distortion is understood and this is explained diagrammatically in figure 5.11.

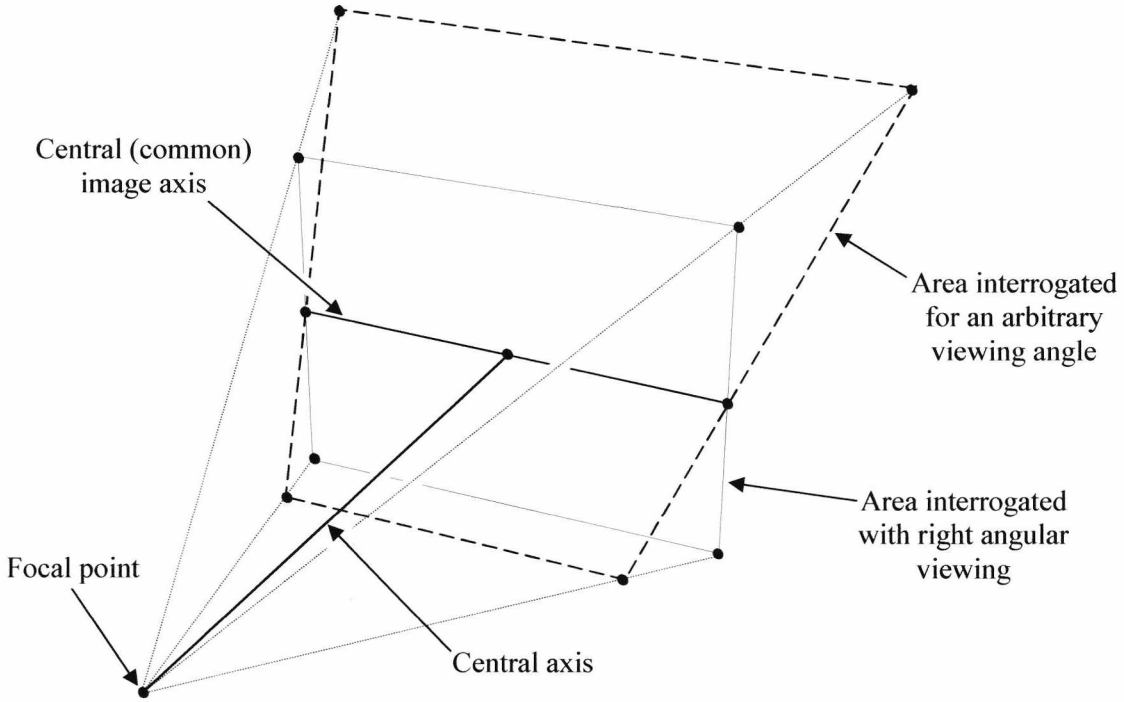

Figure 5.11 Explanation of trapezoid distortion

In this diagram the rectangular area that would normally be interrogated, when the camera is right angular with respect to the imaging plane, is shown along with the trapezoid shaped area that results when the imaging plane is at a different angle with respect to the camera. It can be seen that the top part of the trapezoidal image covers a wider area than the normal rectangular area and that the bottom half covers a smaller area. Similarly the top half of the trapezoid area is higher (vertically) than its rectangular counterpart and (although hard to see on this 3D diagram) the lower half is shorter. These two geometric facts explain the source of the two effects which constitute trapezoid distortion.

In order to correct this distortion it is necessary to know the angle of interrogation and the central distance to the imaging plane. It is then possible to calculate the widths and heights of the trapezoidal image in relation to the rectangular image and produce linear 'correction factors'. These factors allow each individual image line or column (depending upon which aspect of distortion is being tackled) to be expanded or contracted as necessary. In all cases the common central image axis (at right angles to the central distance to the imaging plane) is unchanged as it is used as a reference point. It can be

seen from figure 5.10(b) that during the correction process some of the lower half of the image is not utilised (by equal token some of the upper part of the image is lost). This is because the lower half of the trapezoidal objective represents less area than the lower half of the rectangular one.

Exact details of the processing mathematics employed for trapezoid distortion correction will now be given. The two different aspects of the distortion, perspective and foreshortening, will be dealt with separately.

The most obvious error in a trapezoid distorted image is the perspective effect and so this will be dealt with first. In order to correct this error it is necessary to compress lines lying toward the bottom of the image and expand those towards the top (see figure 5.10). In order to do this it is necessary to know three things: the widths represented by the image at the bottom, the middle (at the reference axis) and the top ('the widths represented by the image' refers to the actual physical distances interrogated, referring to the graph paper seen in figure 5.10 it can be seen that the width represented by the top of the image is larger than the bottom – the central axis is used as a reference). In order to work out these widths it is necessary to know the depths of the near field and far field imaging extents (the bottom and top of the image respectively). When the camera lens angle and central imaging distance are known these quantities can be calculated. Necessary dimensions are detailed in figure 5.12 which represents the figure of 5.11 viewed from the side and in only two dimensions.

The first dimension of interest is the far field distance, D_{ff}. The first step in determining this dimension is to list known, relevant, relationships:

$$\tan\gamma = \frac{e_{ff}}{Z_{ff}'} \qquad [5.1]$$

and

$$Z_{ff} = \frac{Y_{tot}}{2} + Z_{ff}' \qquad [5.2]$$

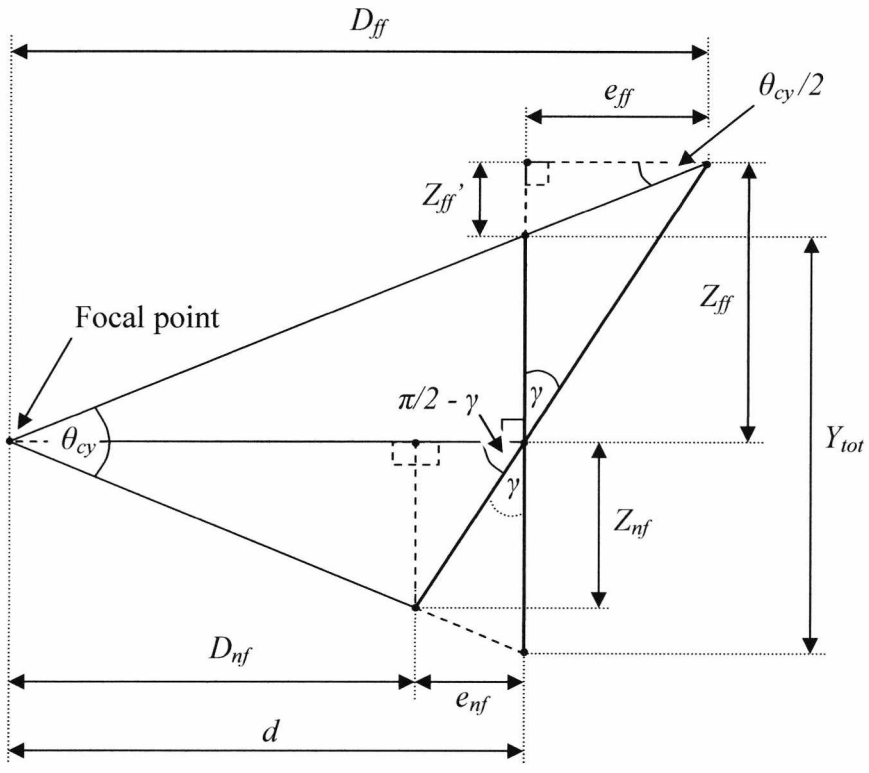

Figure 5.12 Dimensions required for near and far field depth calculation

also

$$\tan\left(\frac{\theta_{cy}}{2}\right) = \frac{Z_{ff}'}{e_{ff}} \qquad [5.3]$$

Where γ is the camera viewing angle (deviation from perpendicular with respect to the interrogation surface), e_{ff} is the depth difference between the angular and perpendicular image intercepts, Z_{ff} is the height from the central image reference axis to the far field angular intercept, Z_{ff}' is the difference between Z_{ff} and the vertical perpendicular image dimension, Y_{tot} is the total vertical size of the perpendicular image and θ_{cy} is the camera's vertical viewing angle.

From these equations it can be seen that two different expressions are available which yield the value of Z_{ff}' :

$$Z_{ff}' = e_{ff} \tan\left(\frac{\theta_{cy}}{2}\right) \qquad [5.4]$$

and

$$Z_{ff}' = Z_{ff} - \frac{Y_{tot}}{2} \quad [5.5]$$

These may be equated in order to find an expression representing the value of Z_{ff} :

$$Z_{ff} - \frac{Y_{tot}}{2} = e_{ff} \tan\left(\frac{\theta_{cy}}{2}\right) \quad [5.6]$$

$$\therefore Z_{ff} = e_{ff} \tan\left(\frac{\theta_{cy}}{2}\right) + \frac{Y_{tot}}{2} \quad [5.7]$$

By rearranging equation 5.1 we find another definition of Z_{ff} :

$$Z_{ff} = \frac{e_{ff}}{\tan\gamma} \quad [5.8]$$

Equations 5.7 and 5.8 may be equated and simplified in order to find an expression representing e_{ff} :

$$\frac{e_{ff}}{\tan\gamma} = e_{ff} \tan\left(\frac{\theta_{cy}}{2}\right) + \frac{Y_{tot}}{2} \quad [5.9]$$

$$\therefore \frac{1}{\tan\gamma} = \tan\left(\frac{\theta_{cy}}{2}\right) + \frac{Y_{tot}}{2e_{ff}} \quad [5.10]$$

$$\therefore e_{ff} = \frac{Y_{tot}}{2\left(\frac{1}{\tan\gamma} - \tan\left(\frac{\theta_{cy}}{2}\right)\right)} \quad [5.11]$$

Now, since, by inspection;

$$D_{ff} = d + e_{ff} \quad [5.12]$$

where D_{ff} is the far field objective depth and d is the known reference distance from the camera to the objective, it is possible to define a calculable expression representing D_{ff} :

$$D_{ff} = \frac{Y_{tot}}{2\left(\frac{1}{\tan\gamma} - \tan\left(\frac{\theta_{cy}}{2}\right)\right)} + d \qquad [5.13]$$

It is now necessary to find the near field objective depth. The first step, as before, is to define known, relevant, relationships:

$$\tan\left(\frac{\theta_{cy}}{2}\right) = \frac{Z_{nf}}{D_{nf}} \qquad [5.14]$$

and

$$\tan\left(\pi/2 - \gamma\right) = \frac{Z_{nf}}{e_{nf}} \qquad [5.15]$$

and

$$d = D_{nf} + e_{nf} \qquad [5.16]$$

$$\therefore \tan\left(\frac{\theta_{cy}}{2}\right) = \frac{Z_{nf}}{d - e_{nf}} \qquad [5.17]$$

Where Z_{nf} is the height from the central image reference axis to the near field angular intercept, D_{nf} is the near field depth and e_{nf} is the difference between the near field depth and the reference central axis depth, d.

It is now possible to define two expressions for Z_{nf}:

$$Z_{nf} = e_{nf}\tan\left(\pi/2 - \gamma\right) \qquad [5.18]$$

and

$$Z_{nf} = \left(d - e_{nf}\right)\tan\left(\frac{\theta_{cy}}{2}\right) \qquad [5.19]$$

These may be equated and simplified in order to find an expression representing e_{nf} :

$$e_{nf}\tan\left(\pi/2 - \gamma\right) = \left(d - e_{nf}\right)\tan\left(\frac{\theta_{cy}}{2}\right) \qquad [5.20]$$

$$\therefore e_{nf}\tan\left(\pi/2-\gamma\right)=d\tan\left(\frac{\theta_{cy}}{2}\right)-e_{nf}\tan\left(\frac{\theta_{cy}}{2}\right) \quad [5.21]$$

$$\therefore \tan\left(\pi/2-\gamma\right)=\frac{d\tan\left(\frac{\theta_{cy}}{2}\right)}{e_{nf}}-\tan\left(\frac{\theta_{cy}}{2}\right) \quad [5.22]$$

$$\therefore e_{nf}=\frac{d\tan\left(\frac{\theta_{cy}}{2}\right)}{\tan\left(\pi/2-\gamma\right)+\tan\left(\frac{\theta_{cy}}{2}\right)} \quad [5.23]$$

Now, since by inspection;

$$D_{nf}=d-e_{nf} \quad [5.24]$$

where D_{nf} is the near field objective depth, it is possible to define a calculable expression representing D_{nf} :

$$D_{nf}=d-\frac{d\tan\left(\frac{\theta_{cy}}{2}\right)}{\tan\left(\pi/2-\gamma\right)+\tan\left(\frac{\theta_{cy}}{2}\right)} \quad [5.25]$$

Now that both near and far field depths are known it is possible to calculate the width represented by the image at each of these extremes. These quantities are easily calculated if the camera's horizontal viewing angle is known:

$$X_{nf}=2D_{nf}\tan\left(\frac{\theta_{cx}}{2}\right) \quad [5.26]$$

and

$$X_{ff}=2D_{ff}\tan\left(\frac{\theta_{cx}}{2}\right) \quad [5.27]$$

Where X_{nf} and X_{ff} are the image widths at the near field and far field respectively and θ_{cx} is the camera's horizontal viewing angle.

Now that the widths represented by the image at near, far and central (X_{tot}) locations it is possible to process the image in order to remove the 'perspective' effect. This is achieved by compressing or expanding the lines of the image using a pixel mapping technique similar to that used for pincushion correction in Chapter 4 i.e. each pixel location within the processed image the pixel value is taken from an alternate location in the original image. For the present 'perspective' correction processing a simple compression or expansion that is linearly related to the vertical image location is required. The first step in establishing the compression or expansion factor is to define basic relationships:

$$y_{rat} = \frac{y}{y_{pix}} \qquad [5.28]$$

and

$$D_{diff} = X_{ff} - X_{nf} \qquad [5.29]$$

and

$$x_y = X_{ff} - \left(y_{rat} D_{diff}\right) \qquad [5.30]$$

Where y_{rat} is the ratio between the current vertical image location, y and the total height of the image in pixels, y_{pix}. D_{diff} is the difference between the near and far field widths and x_y is the width represented by the image as a function of the current vertical image location. The factor by which the current image line must be expanded or contracted (W_{rat}) may now be defined:

$$W_{rat} = \frac{x_{pix}}{x_y} \qquad [5.31]$$

It can be seen that this quantity is the ratio between the total image width, x_{pix}, and the vertical location related width.

It is now possible to apply this factor in order to process the image. This is achieved using a pixel mapping technique similar to that used for pincushion correction in Chapter 4. For every pixel location scanned during processing the actual pixel value in the final image is taken from a mapped location in the original image. The mapping function used must be

split in two in order that image lines are properly processed both left and right of image centre. The necessary operations are as follows:

$$x_n = \frac{x_{mm}}{2} - \left(W_{rat} \left(\frac{x_{mm}}{2} - x \right) \right) \quad [5.32]$$

and

$$x_n = \frac{x_{mm}}{2} + \left(W_{rat} \left(x - \frac{x_{mm}}{2} \right) \right) \quad [5.33]$$

Where x_n is the mapped pixel location and x is the original (note that this operation is performed for all Y coordinates and that W_{rat} changes with respect to image height location). Equation 5.32 is used to the left of image centre and 5.33 to the right.

This completes correction of the 'perspective' type effect and it is now necessary to correct for the 'foreshortening' effect that is also a part of trapezoid distortion. Fortunately much of the calculation already performed is useful for this operation also. In fact the two types of distortion that make up the trapezoidal effect are very similar to correct but in different image aspects – 'perspective' concerns horizontal distortion and 'foreshortening' vertical. When correcting the perspective effect it was necessary to know the widths represented by the image at both depth extremes, this could be referred to as dimension scaling since at the top of the image the distance represented by one pixel is different from at the bottom. When correcting the foreshortening effect it is necessary to know the magnitude of the vertical pixel scaling effect. The equivalent vertical image size represented by pixels at the top and bottom image extremes can be worked out quite simply once the image depths and vertical camera angle are known:

$$Y_{nf} = 2D_{nf} \tan\left(\frac{\theta_{cy}}{2} \right) \quad [5.34]$$

and

$$Y_{ff} = 2D_{ff} \tan\left(\frac{\theta_{cy}}{2} \right) \quad [5.35]$$

Where Y_{nf} and Y_{ff} are the image heights at the near field and far field respectively.

A correction factor based on linear scaling from the top to the bottom of the image can now be defined. The operation is similar to the width scaling ratio defined in equation 5.31.

$$H_{rat} = \frac{y_{pix}}{Y_{ff} - \left(\frac{y}{y_{pix}} \left(Y_{ff} - Y_{nf} \right) \right)} \qquad [5.36]$$

Where H_{rat} is the height ratio. It is now possible to apply this factor in order to process the image. This is achieved using the same pixel mapping technique applied to 'perspective' effect correction. This time new mapping functions are required that reflect the vertical nature of the 'foreshortening' effect. Two mapping functions are used, as before, in order that image lines are properly processed both above and below the image centre. The necessary operations are as follows:

$$y_n = \frac{y_{mm}}{2} - \left(H_{rat} \left(\frac{y_{mm}}{2} - y \right) \right) \qquad [5.37]$$

and

$$y_n = \frac{y_{mm}}{2} + \left(H_{rat} \left(y - \frac{y_{mm}}{2} \right) \right) \qquad [5.38]$$

Where y_n is the mapped pixel location and y is the original. This concludes trapezoid distortion correction.

In practice the preceding mathematics is not performed every time an image is processed but is used to create a look up table. The LUT is then consulted for each processed image in turn allowing high speed correction processing.

It is possible to combine the pincushion and trapezoid correction algorithms into a single LUT. In this way there is no impact on processing speed due to the additional distortion correction processing.

5.3.3 Sensing Head Design

The general imaging geometry has been discussed already leaving only details of the real, practical, sensing head to be described. This description will take the form of diagrams, pictures and brief descriptions covering any points of interest that have not yet been covered. The description of the sensing head falls naturally into three distinct areas and these will now be discussed in turn.

5.3.3.1 Spool Piece

The first consideration when designing the sensing head was that it must be removable from the rest of the flow rig pipe work, for reasons of portability and convenience during testing. Whilst, in theory, the imaging based system could simply be installed looking through a hole drilled into existing pipe work this approach would be suitable only for a permanent installation and not for a prototype. The solution to this problem is to use a 'spool piece' – a short section of pipe work with a flange at each end that can be bolted into a gap between two flanges in the flow rig. For the current work it was the intention to perform some tests under industrial conditions (see Chapter 6) and so the pipe work/spool piece used had to be compatible with the industrial flow setup. This requirement resulted in a spool piece having a length of 300mm between internal flange faces, built using 50mm outside diameter mild steel pipe (compatible with the 50mm PVC pipe used for the laboratory scale test rig, see section 5.6). Standard industrial flanges with 70mm fixing centres were used. This spool piece was machined to take the window mounting (described in the next section) also location pits were cut for fixing the outside enclosure around the spool piece firmly (see section 5.3.2.3). A full diagrammatic representation of the spool piece is shown in figure 5.13.

5.3.3.2 Viewing Window and Air Purging

In order that the camera and laser can 'see' into the duct it is necessary to fit a transparent window in the duct wall. In theory, in order to comply with the 'non-intrusive installation' requirement, this window should be curved to match the duct wall.

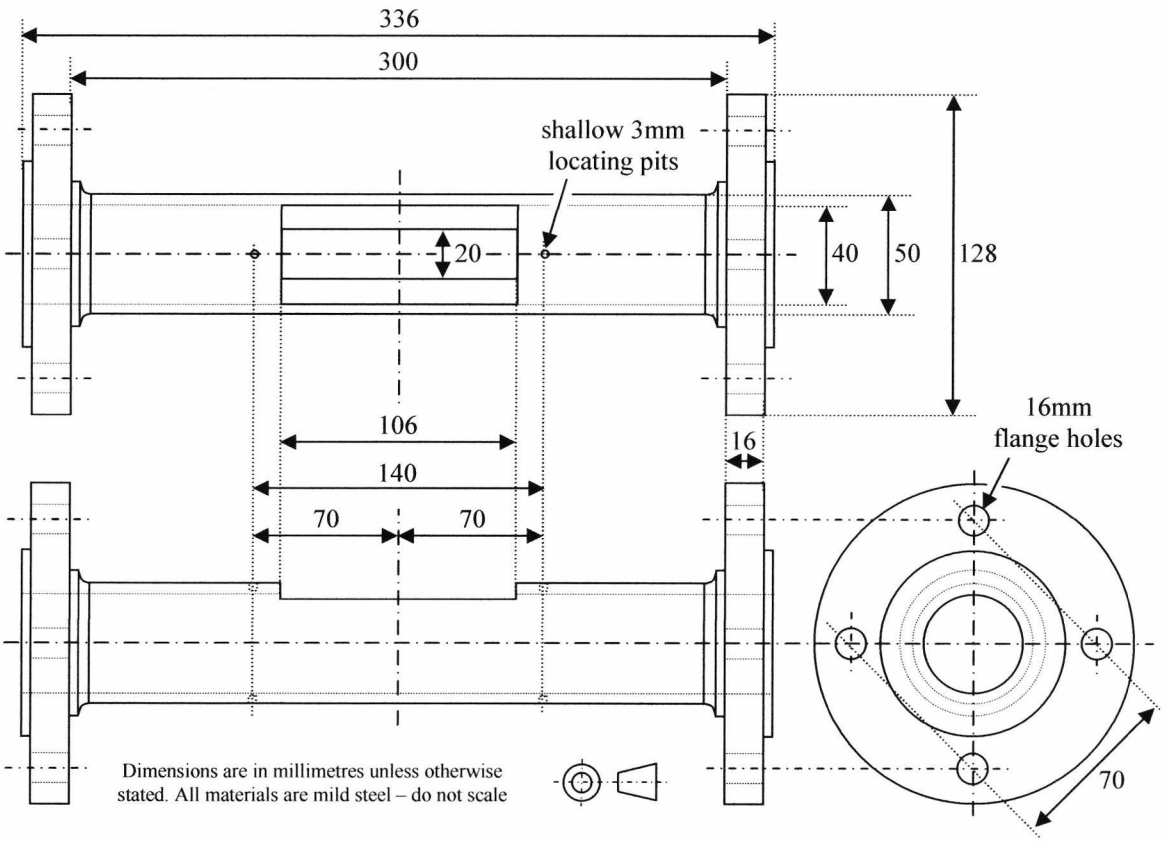

Figure 5.13 Spool piece design

In practice a curved window would be expensive, hard to produce accurately, difficult to seal and would produce complex optical distortions in the images, the removal of which would slow down processing speed dramatically. For these reasons a flat window is the best practical choice. A flat window, however, will protrude slightly into the duct suggesting that the installation is not entirely non-intrusive. This is not a significant problem in the present setup as the required window width is only 20mm, which is small compared to the 126mm internal circumference of the duct, and so the reduction in duct area as a result of installation is only 2.9% (a 36mm^2 infringement into a 1257mm^2 duct). This is illustrated in figure 5.14.

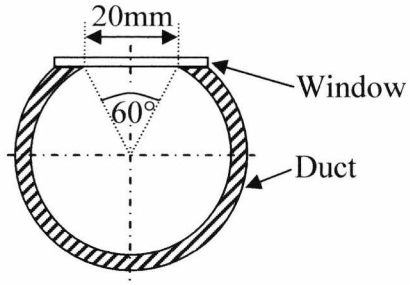

Figure 5.14 Window infringement into duct

The next choice to be made concerns the window material and thickness which are related parameters. The thickness of the window relates to both its strength and optical properties – a thick window will be strong but will cause major refraction problems at the viewing angles used in the current work and a thin window will not suffer from significant refraction but will be incapable of withstanding any pressure within the duct. Fortunately it is not usual for dilute phase pneumatic conveyers to operate at pressures that are significant when compared with the ambient environment. The industrial flow rig that the spool piece was designed to fit was quoted as operating at a maximum pressure, relative to ambient, of 100millibar (1.45psi) at up to 70°C. In the interest of convenience and low cost the use of a standard quartz microscope slide was considered for the window. In order to ensure operational safety it was decided that the window should be capable of withstanding static pressures of up to 1bar (14.5psi) at 25°C yielding a safety factor of ten, giving ample allowance for the slightly elevated operating temperature. Based upon the properties of quartz (G. E. Quartz 2005) a window with an unsupported width of 20mm would need to be 1.04mm thick in order to withstand this pressure. Standard microscope slides are 1-1.2mm thick and are therefore eminently suitable. In practice a window that is only 1-1.2mm thick is sufficiently thin that refraction distortion is not an issue, making this selection of window size and material ideal. Using quartz as a material also gives greater abrasion resistance than normal glass and this may be an advantage as particles flowing in the pipe may strike the surface of the window and cause scratching (abrasion resistance is one of the main reasons why a plastic material was not considered for the window, other reasons include problems with the 70°C operating temperature and optical distortion due to non-uniform material density and surface quality).

With the window material decided upon another issue must be addressed. The possibility of abrasion damage has already been introduced suggesting that material within the pipe may come into contact with the window. It has been explained that a quartz window should resist abrasion damage (and such has proven to be the case in experiments although the long term life of the window has not been investigated as experimental flow runs tend to be short) but there is a problem other than abrasion: contamination. Some materials, notably pulverised coal, are extremely 'dirty' tending to deposit a thin layer of tiny particles onto any surface that they interact with. If the window was to become contaminated in this way it would be impossible for high quality flow images to be acquired. For this reason an air purging system was designed into the sensing head.

Air purging is a technique whereby a tiny jet of compressed air is directed over the optics in a contamination prone system in order that they remain clean and transparent. In the present setup this was achieved by machining a tiny rebate in the window seat and supplying it with compressed air through a milled channel. The area of the resulting 'nozzle' is about $3mm^2$ which represents only about 0.2% of the duct's area and will not, therefore, affect the flow to any significant degree.

In general window mounting is achieved by milling a recess into a flat mild steel plate (3mm thick) into which the window may sit flush with the plate's surface. The centre of the recess is removed leaving a lip upon which the window may sit and seal against. A paper gasket is inserted under the window in order to improve the distribution of forces when the window is clamped into position. Clamping is achieved by bolting another metal plate onto the first (with a corresponding window hole) and a rubberised cork gasket (smeared with gasket sealing compound) is inserted between the two. The bottom plate is also milled to include the air purging nozzle as described above. The general arrangement is illustrated in figure 5.15 and details of the plates are given in figure 5.16.

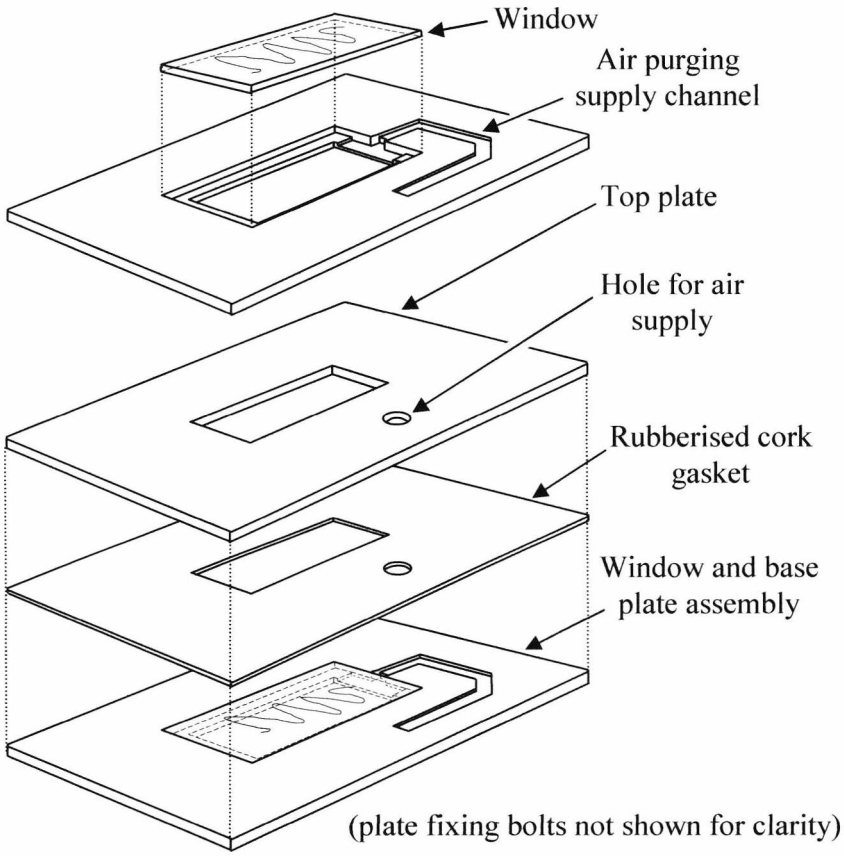

Figure 5.15 General arrangement of window mounting

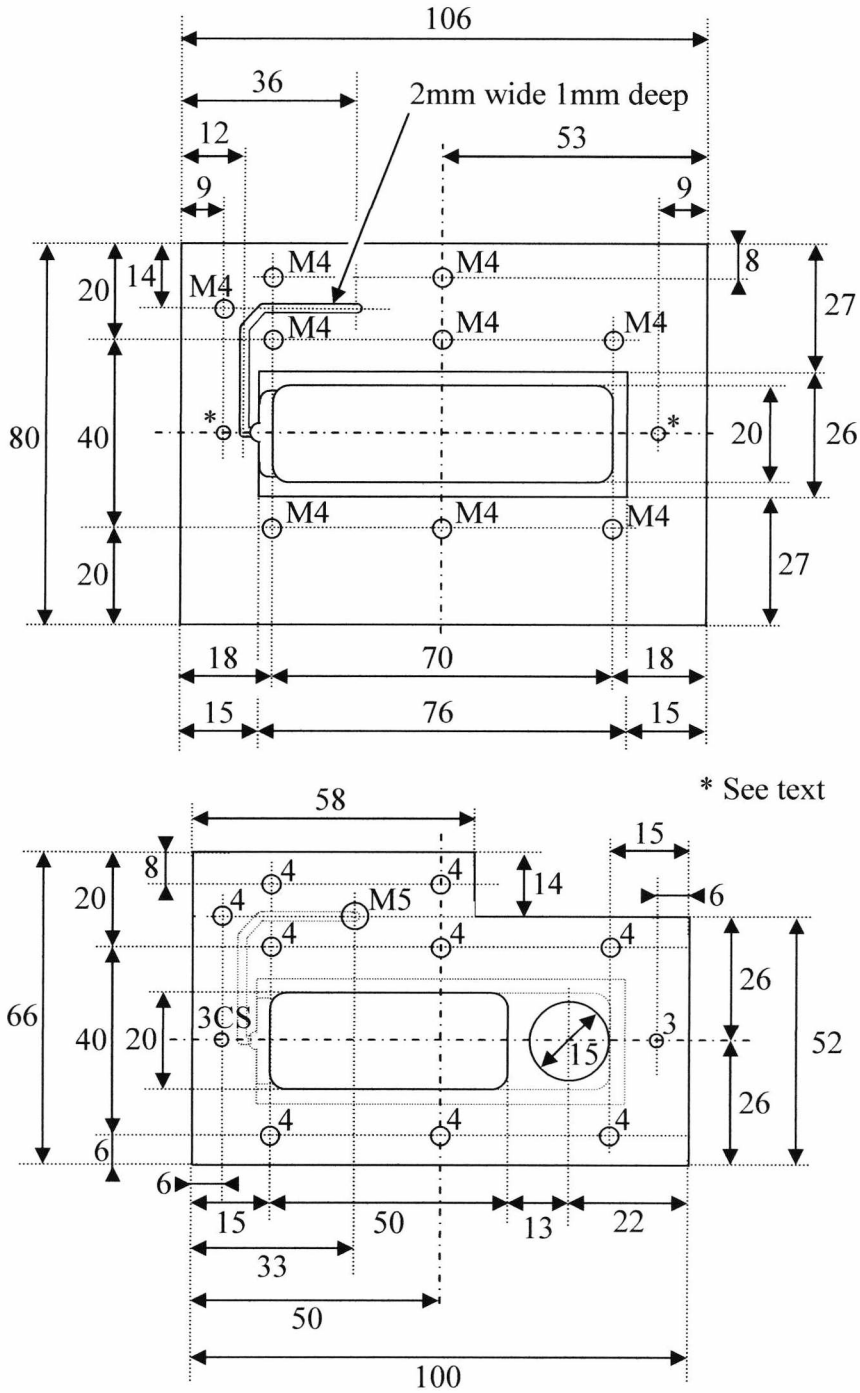

Figure 5.16 Details of window mounting plates

When the top and bottom plates are bolted together it is necessary, in the interests of good sealing and lateral support of the cork gasket, for there to be bolts at the ends of the plates as well as at the sides (marked on figure 5.16 with asterisks). The problem with this is that these bolt locations are over the duct and may lead to leaks or intrusion into the duct. This is avoided by fixing short threaded rods through holes in the bottom plate with epoxy resin and filing the underside smooth, thus sealing the joint and eliminating flow

modifying protrusions. In the top plate an end drill is used to mill a small recess into the plate at these locations in order that nuts may be sunken beneath the surface thus avoiding interference with the camera lens or laser mounting. The M5 tapped hole in the upper plate (as seen in figure 5.16) is used to mount a pressure fitting that introduces compressed air into the air purging supply channel and thence forth to the nozzle. The 15mm hole in the upper plate is used to locate the laser.

The lower plate of the window mounting assembly is fixed to the prepared recess in the spool piece using a high temperature steel loaded epoxy resin. This 'cold welding' approach avoids possible distortions of the window mounting seat as a result of the heat of a conventional welding or brazing process.

5.3.3.3 Enclosure – General Considerations and Overview

Once a spool piece fitted with a sealed and air purged window is available it is necessary to mount the camera and laser and also to fix the whole assembly inside a lightproof sealed enclosure.

The laser must be fixed at 90° to the flow and this is achieved easily using a small aluminium bracket bolted to the upper window mounting plate, the laser being held in place with a cable tie. The camera is a little more difficult as the angle must be known. The angle used is decided upon for practical reasons, the shallowest angle that can be achieved is used in order to minimise trapezoid distortion. The camera focuses as close to the geometric centre of the duct as the practical arrangement will allow (the actual focal point is about 5mm higher with the present setup) and in the present setup a viewing angle of 30° is achieved. The camera is fixed to a small aluminium plate that locates, with the aid of a peg, into one of the shallow locating pits in the spool piece and it is held in place with a cable tie allowing for easy adjustment. The fixing brackets for the laser and camera are extremely simple and could vary if different components were used. Exact details of their dimensions will not be given here but they are visible in the photographs and overview diagrams later in this section.

With camera and laser mounted the sensing head is functionally complete. It is not, however, possible to use it without some form of casing. There are three reasons for this:

firstly, all ambient light must be eliminated if consistent particle illumination is to be achieved. Secondly, the sensing head is a fairly delicate piece of equipment that must be physically protected and thirdly, in the unlikely event of the window breaking, it is necessary to ensure that any flow leak is contained.

These requirements are fulfilled through the simple expedient of fitting a sturdy wooden box around the sensing apparatus. The box is hinged and the spool piece passes through the box at the joint, the box closing onto the spool piece and locating firmly with the aid of location pegs that fit into the three remaining location pits in the spool piece. The box is painted matte black inside and out and sealing is achieved with the aid of adhesive foam tape. This is sufficient to exclude light from the box but the sealing will leak under pressure, it is, nevertheless, sufficiently good to stem all but a tiny fraction of the flow in the event of window breakage. The general arrangement and size of the protective casing is shown in figure 5.17 and the general internal arrangement is illustrated in figure 5.18.

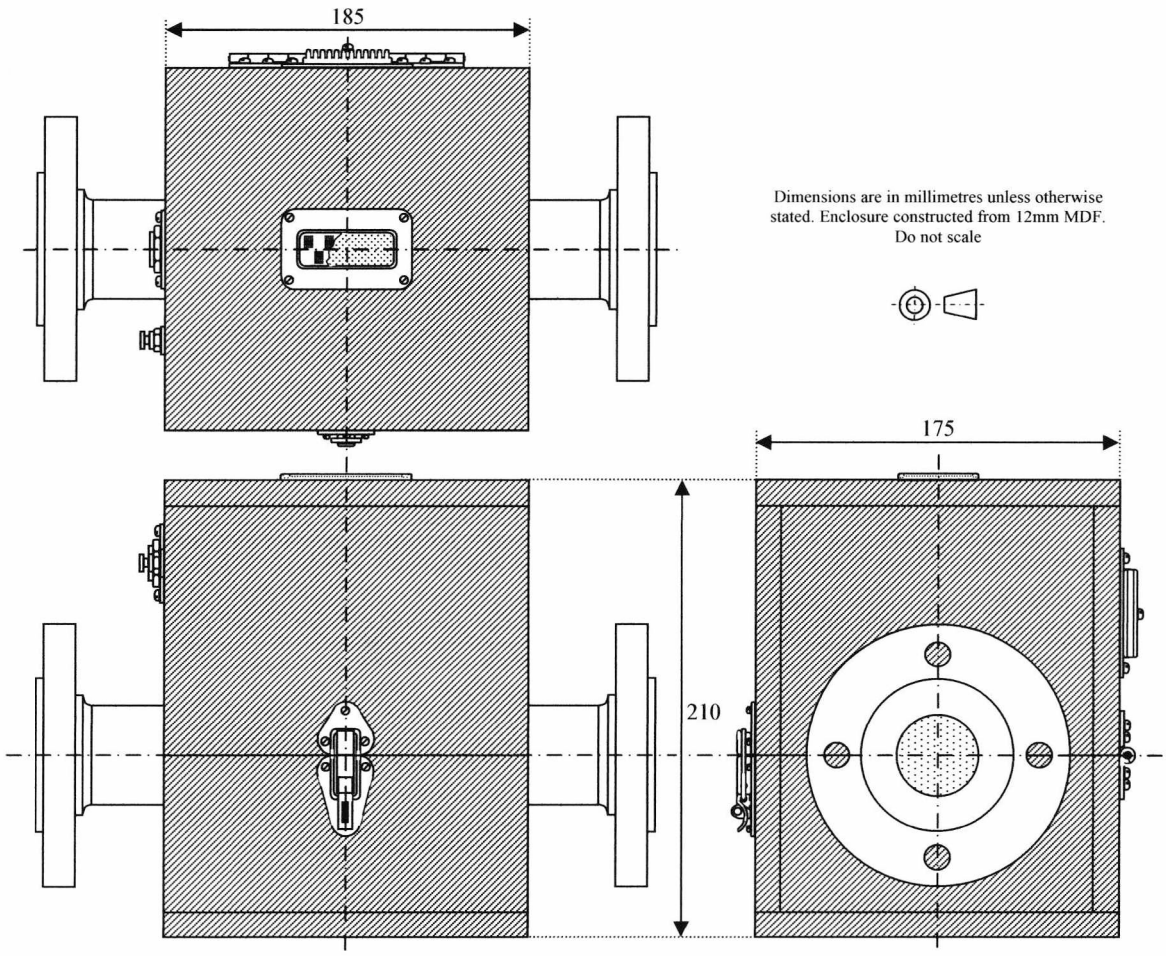

Figure 5.17 General arrangement of completed sensing head

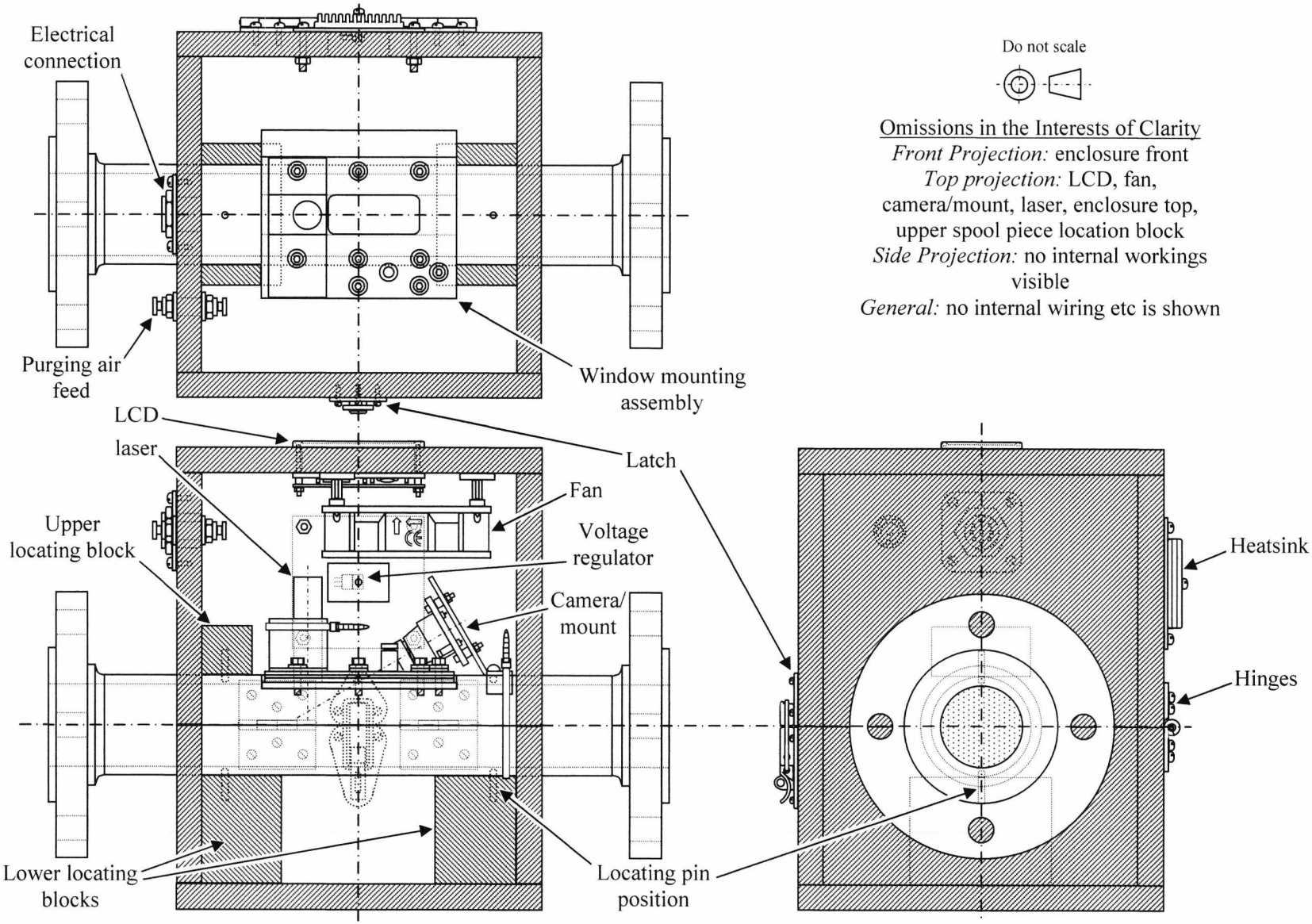

Figure 5.18 Internal arrangements of the sensing head

In figures 5.17 and 5.18 there are a number of minor features that have not yet been discussed and these will now be explained. Firstly, an LCD display is fixed into the top of the enclosure which is used to display useful data, such as particle size, concentration and system status and communicates with the host PC via an RS232 link.

Next, a heat sink is visible at the rear of the enclosure onto which an internal voltage regulator is fitted. In order that the camera and laser operate consistently it is necessary for them to be provided with a well regulated and noise free power supply. Because this cannot be guaranteed over the long cable run from the host PC the sensing head is supplied with a higher voltage (about 18V unregulated) and the necessary 5V and 12V rails are internally regulated.

The last point of interest is the fan. It can be readily appreciated that, with the electronics and hot spool piece fixed inside a sealed enclosure, the ambient temperature will be somewhat high inside the sensing head. It has been found that ambient temperatures of 60°C are the norm when operating on the industrial flow rig. It may appear that there is little point in fitting a fan inside a sealed enclosure as it will only move the hot air around rather than exhaust it to the external environment and draw in cool air. In reality, as hot air rises, without a fan the air at the top of the enclosure tends to be considerably hotter than that at the bottom, the fan ensures a uniform temperature distribution within the box irrespective of orientation and prevents damaging 'hot spots' from forming.

The following three figures show photographs of the finished sensing head. Figure 5.19 shows an overview of the whole closed unit from the front and figure 5.20 from the rear. Figure 5.21 shows the enclosure opened with fitments in the lid clearly visible. Figure 5.22 is a close up of the window mounting with camera and laser etc.

In these photographs it is interesting to note the cabling layouts etc., also that the camera has its own voltage regulator, fitted to the camera mounting plate, in the interests of noise immunity. The external heat sink is used for the regulator that the supplies the laser, fan and LCD.

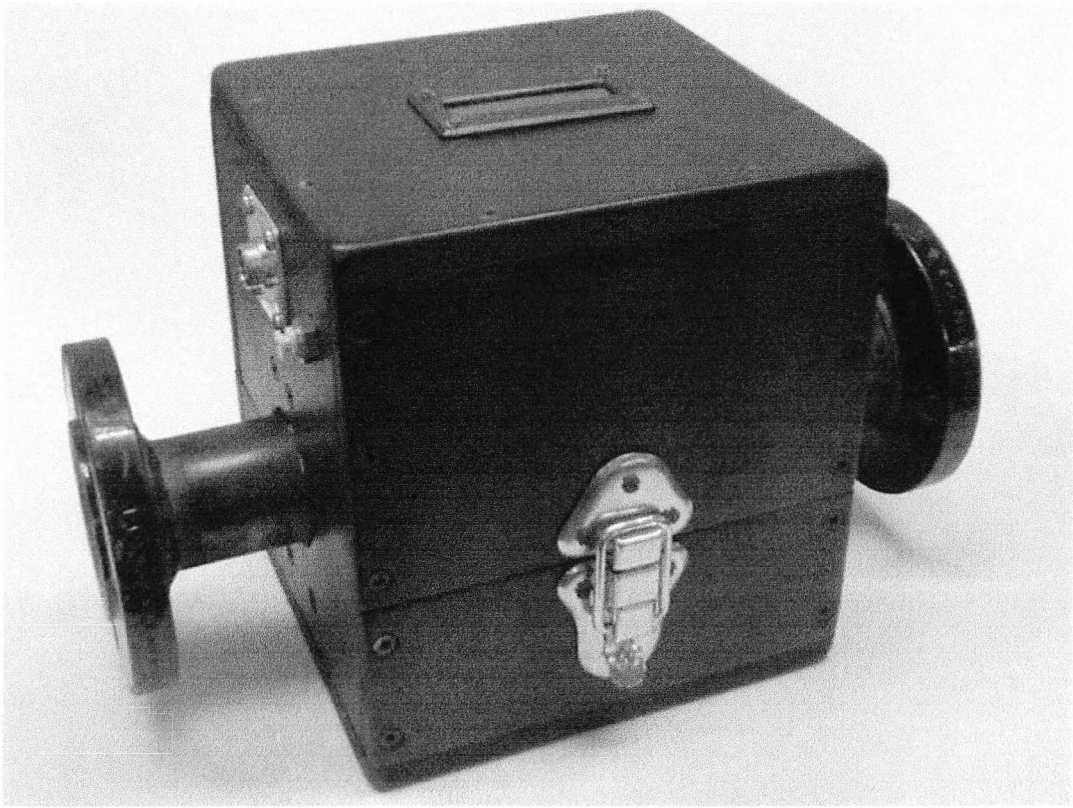

Figure 5.19 External front view of finished sensing head

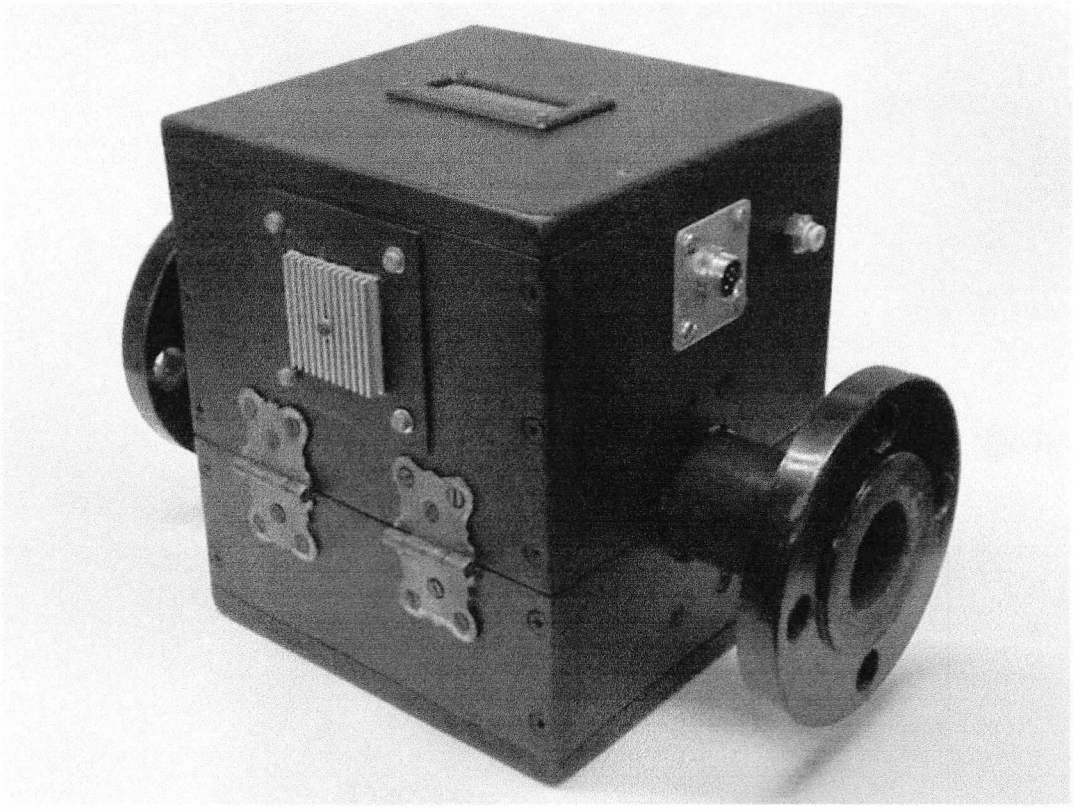

Figure 5.20 External rear view of finished sensing head

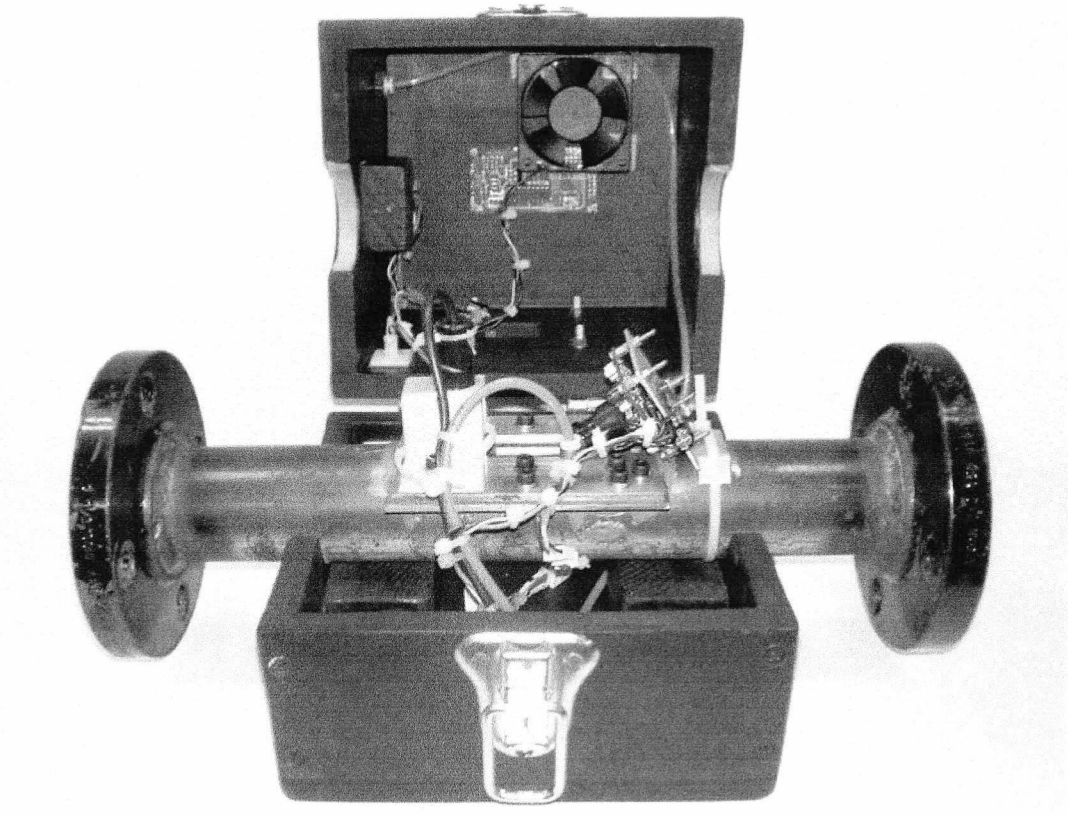

Figure 5.21 Internal overview of sensing head

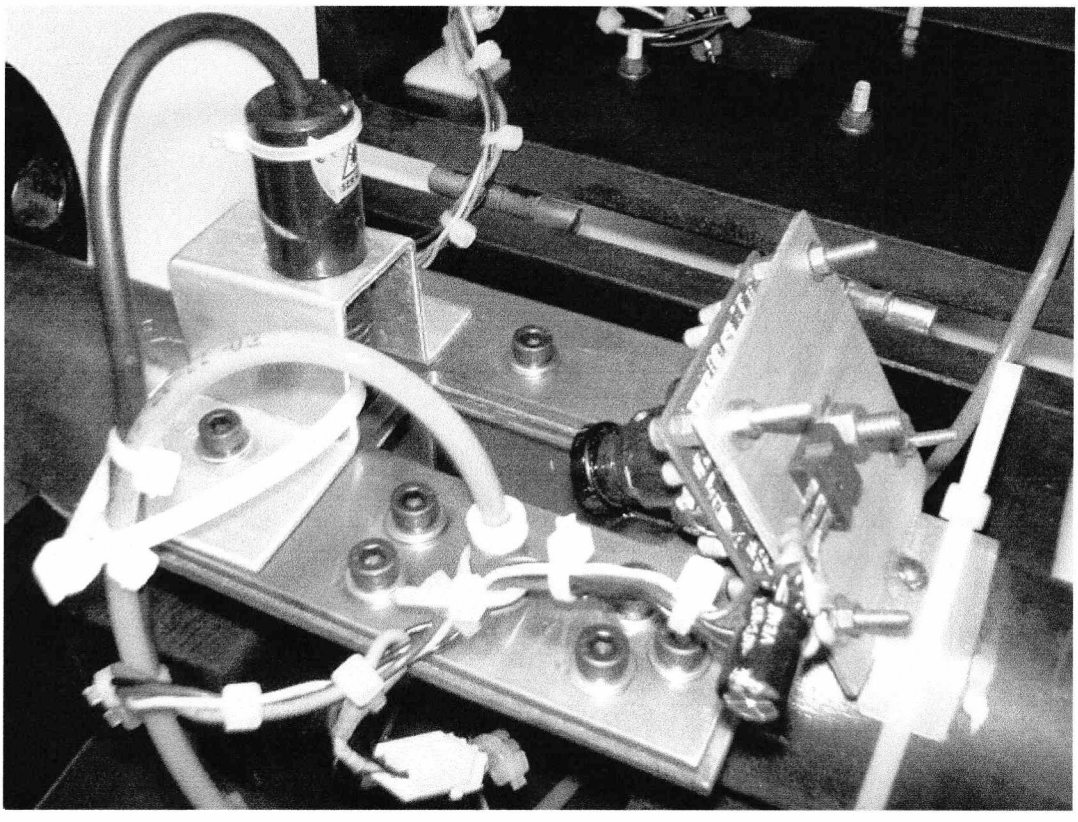

Figure 5.22 Close up of window mounting area

5.4 Inhomogeneous Flow Detection

An imaging based sensor has, as already intimated, many advantages over other sensing strategies. One of the main reasons for this is that the imaging approach measures flow parameters directly without using inferential techniques: it provides direct understanding of what is happening in the duct. In this way, with an imaging based approach, it is possible to detect possible problems with the flow such as inhomogeneity.

5.4.1 Homogeneity of Particulate Flows

The concept of homogeneity is a simple one: the particulate concentration will be not always exhibit uniform distribution across the whole area of the duct. It is easy to envisage, for example, that in a long horizontal run of duct the particles will have a tendency to sink to the bottom causing uneven distribution. This stratified flow is known as inhomogeneous. Some examples of different flow regimes are given in figure 5.23.

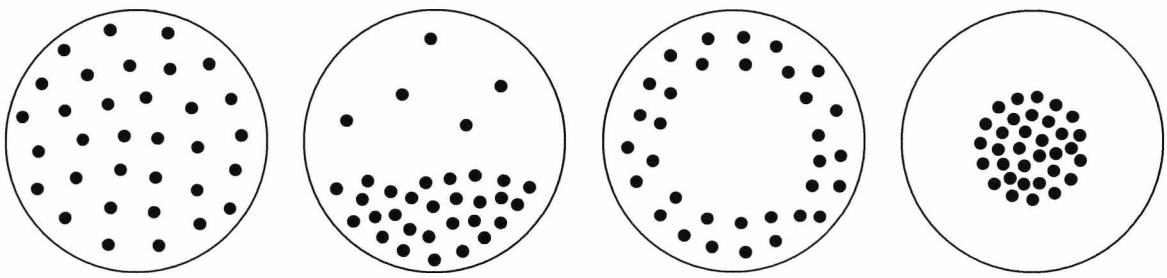

a) Homogenous b) Stratified c) Annular d) Roping

Figure 5.23 Flow regimes

In this figure a cross section through a duct is shown with the locations of particles within it. Homogenous flow is evenly distributed throughout the duct. Stratified flow (as in the previous example) shows the flow 'settling out' into layers of dense and rarefied concentration. Annular flow features a ring of particles around the outside of the duct with little flow in the centre whilst roping, the complete opposite, features a tight bundle (or 'rope' when considered in three dimensions) of particles occupying only a small area of the duct (not necessarily at the centre).

It is important that inhomogeneity is avoided – it can be seen from figure 5.23 that with such flow regimes the area of the duct is not used efficiently. This could lead to a variety of problems in industry such as product quality degradation through artificially high concentration at certain points in the flow, premature wear on conveying systems for the same reason or, simply, inefficient use of the equipment (e.g. Yan 2001 or Yilmaz and Levy 1998). It may even lead to blockages in extreme conditions and so it is important that these conditions be avoided. It is beyond the scope of the current work to suggest ways of preventing unwanted flow regimes but, as an imaging sensor 'sees' a cross section through the flow it is possible for it to detect these conditions allowing the necessary steps to be taken.

In industry, stratified flow is commonplace and usually not severe enough to be a problem also its causes are generally well known (such as gravity and centrifugal effects at bends). Annular flow is rare and usually not as severe as the example shown in figure 5.23. The main concern in industry is roping as this regime is particularly harmful to the operation of pneumatic conveyors. For this reason the detection of the roping regime will be discussed here.

5.4.2 Processing Algorithm

To detect a roping condition is not a straightforward task. It might at first appear that during roping flow all particles exist within a very small area of the duct and that such a condition could be defined easily. In reality this is not the case as ropes can be of varying densities and sizes and there will always be a low density flow of particles across the duct that is not part of the rope. There is no defined standard that allows roping flow to be explicitly identified which means that the detection of roping must always be a subjective procedure. For the current research a methodology and accompanying algorithm have been developed that allow for the detection of flow ropes – it is not possible to positively identify a rope as the final judgement must be left to a human operator but the software can decide if there is either a possible or probable rope in the flow (two levels of certainty) and if so where its centre lies.

The first step in the procedure is to make a record of where particles tend to exist within the images. This is achieved by setting up a special roping detector image buffer and drawing binary particle locations into it at each frame (after particle/background separation). The particle images are then decayed by a fixed amount between each frame. The effect resembles snow flakes falling onto a warm surface – they melt as they strike the surface but not immediately and evidence of past flakes is still visible as new ones fall (old flakes do disappear eventually). This technique results in a frame buffer that contains information about where particles currently are and where they have been in the past – any tendency to flow in a particular pattern, such as in a rope, will be clearly visible as the display gives temporal as well as spatial information. This 'roping detector image' allows a human operator to judge the presence of roping (and other inhomogeneous flow regimes) very easily but it is just the start of the automatic rope detecting procedure. The next step is to divide the image into zones so that the density of particles can be judged spatially and ropes can be identified. The general idea is illustrated in figure 5.24.

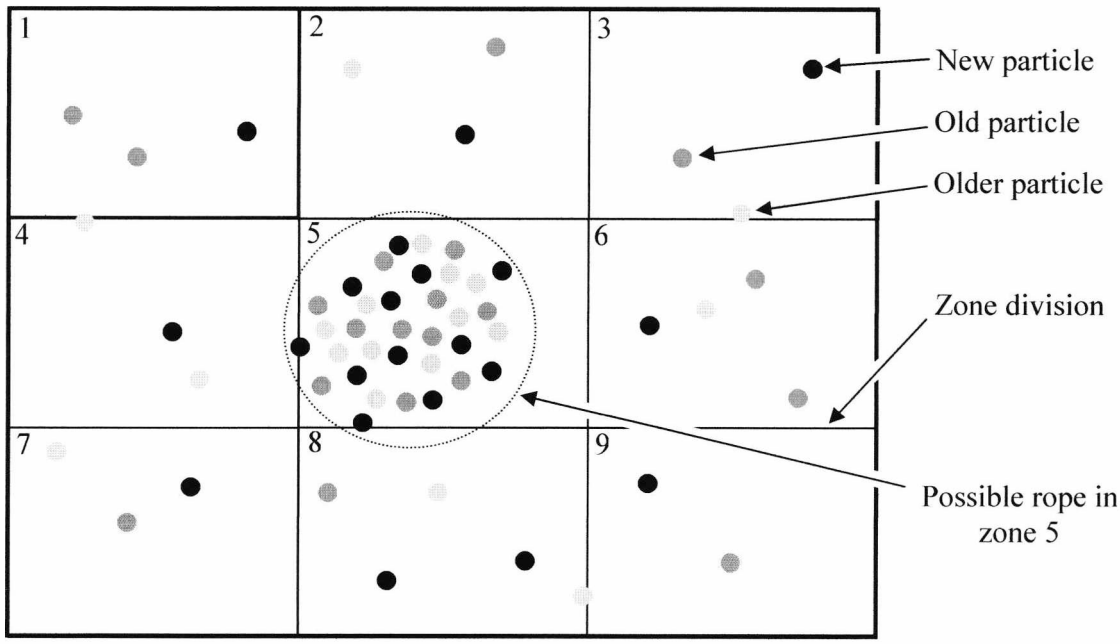

Figure 5.24 Concept of 'roping detector image'

The number of zones used here gives good differentiation between possible rope locations and sufficient sensitivity to localized particulate concentration. In practice ropes that are small enough to justify the added sensitivity of a larger number of smaller zones do not occur within the current test rig.

Once the zones have been defined the next step is to scan through them and find the arithmetic mean intensity of pixels in each. The following values can then be defined:

Z_{max}, the maximum mean zone intensity recorded

Z_{min}, the minimum mean zone intensity recorded

Z_{mean}, the arithmetic mean of all zone intensities

It is now possible to define two logic expressions that must be true in order for the system to suggest that a rope is present:

$$Z_{mean} < \left(Z_{\min} + \frac{Z_{\max} - Z_{\min}}{2} \right) \qquad [5.39]$$

AND

$$\frac{Z_{\max} - Z_{\min}}{2} \geq Z_{\min} \qquad [5.40]$$

The functionality of these expressions, which perform an arbitrary determinative function, is best explained empirically. The first inequality (equation 5.39) is the most straightforward conceptually. It suggests that, in order for there to be a rope present, the mean zone intensity should be lower than the halfway point between the minimum and maximum zone intensities. This can be readily understood: if the flow is homogenous there will still be small changes in intensity from zone to zone but they will not be dramatic and so the arithmetic mean value will lie at the halfway point – if one of the zones exhibits a higher concentration than the rest (possibly indicating the presence of a rope) then the maximum value will increase out of proportion to the increase in the mean value, placing the mean below the halfway point. It is possible for a rope to span zones and in this case the disproportionate change in mean and maximum intensities will be smaller reducing the sensitivity of the system to larger ropes – this is a good thing since, when the high intensity spans several zones, the certainty of it being a rope must be lower.

This first inequality is not enough to reliably detect roping conditions since it suffers from a flaw: its dynamic range is directly related to the range of values between minimum and maximum intensity. If there is little difference between these values – a condition suggesting homogenous flow – it is quite possible for the first inequality to be met sporadically due to a lack of range in intensity values. It is therefore necessary to establish that there is a large range of values present AND that the requirement defined by the first, 'roping detection', inequality is met. This requirement is fulfilled by the second inequality (equation 5.40). This ensures that the range of values present is at least twice the minimum value. This has proven to be an effective method in practice.

There is still one aspect of the detection system that has not been explained – the current system can distinguish between a possible rope and a probable rope. This is achieved through the simple expedient of examining the minimum zone intensity value after the first two inequalities have been met. If the minimum value is zero then there are no particles present in at least one zone, suggesting strongly that the flow is inhomogeneous and, therefore, the system declares a 'probable' rope. If the minimum value is greater than zero there are particles present across the whole sensing area and so the certainty that a rope is present is lower – a 'possible' rope is declared.

In summary, the rope determination sequence can be split into three steps:

1) Use equation 5.39 to establish that there is uneven particle concentration distribution in the image.

2) If (1) was successful then use equation 5.40 to establish if there is a high enough range of zone mean values available for the result to be trusted.

3) Determine the certainty of a roping condition by examining the minimum mean value.

The full rope detection sequence is shown diagrammatically in figure 5.25.

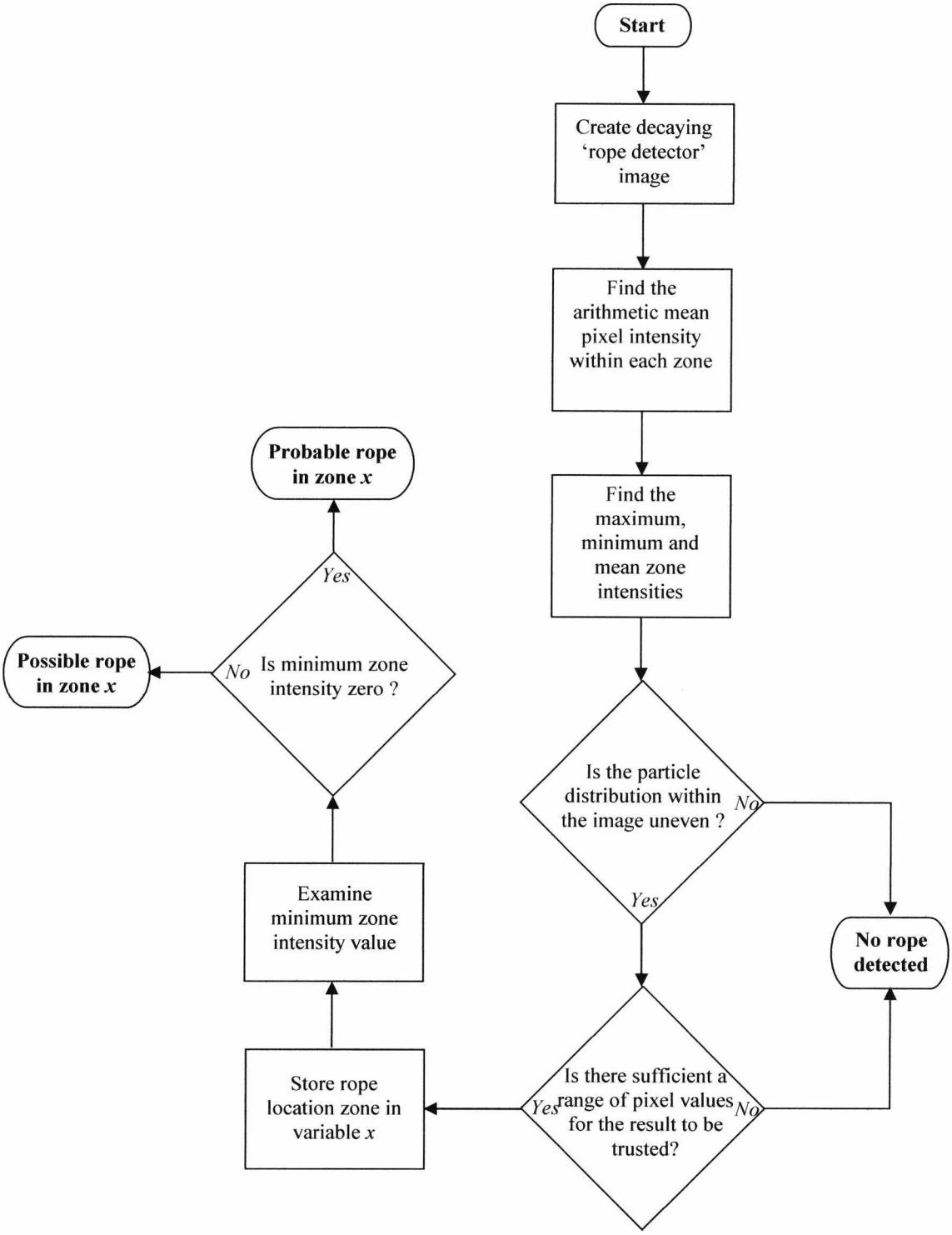

Figure 5.25 Rope detection sequence

The preceding method for rope detection was designed to be simple and straightforward to implement – in line with the other algorithms in this work it was designed for high performance on-line operation. The inequalities used avoid arbitrarily defined threshold values that would cause system performance to vary from flow system to flow system and provide a simple, consistent and unchanging framework for the detection of ropes.

5.4.3 Testing

Since the roping detection function is achieved through a clearly defined sequence of operations that are performed on binary images it is not considered appropriate to perform any testing using synthetic 2D images. It is possible to exactly predict the result when using such images and so test results would merely confirm correct coding of the algorithm. The effectiveness of the roping detection feature will be tested, as far as the current flow rig allows, with real on-line flows. The results of such testing will be detailed in Chapter 6.

5.5 Mass Flow Rate Measurement

It has already been shown that an imaging based system can measure particulate concentration in terms of volumetric concentration. This quantity is of use in its own right but a parameter of more widely accepted usefulness is mass flow rate. This quantity defines the absolute amount of material flowing in relation to time i.e. in kilograms per second. The imaging system cannot measure mass flow rate directly but, if the absolute density of the material and the flow velocity are known it is possible to derive this quantity. This section discusses the addition of an electrostatic velocity meter to the test setup in order to test the accuracy of this inferential approach. The availability of real mass flow rate data from the test rig (see section 5.6) also allows the solids concentration measurement accuracy of the imaging system to be assessed through a process of reverse calculation.

5.5.1 Electrostatic Velocity Measurement

The use of passive electrostatic sensors and cross correlation techniques to determine the velocity of particulate flows is an established and widely documented technique (e.g. Ma and Yan 2000) and so exact details of the methodology will not be given here but in the interests of convenience the basic principle is as follows: the movement of particles in a pneumatic pipeline generates a certain level of net electrostatic charge due to particle-particle interactions, particle-wall collisions and particle-air friction. Although the amount

of charge carried on particles is usually unpredictable, the dynamic variation of this charge can be detected by an insulated electrode in conjunction with a suitable signal processing circuit. As the charged particles move past the electrode, a constantly changing electrical signal is generated. If two signals are acquired from a pair of axially spaced circular electrodes that are a known distance apart, then the velocity of particles can be derived through cross correlation between the two signals. Such systems exhibit high repeatability, good linearity and fast response time. The general idea is illustrated in figure 5.26.

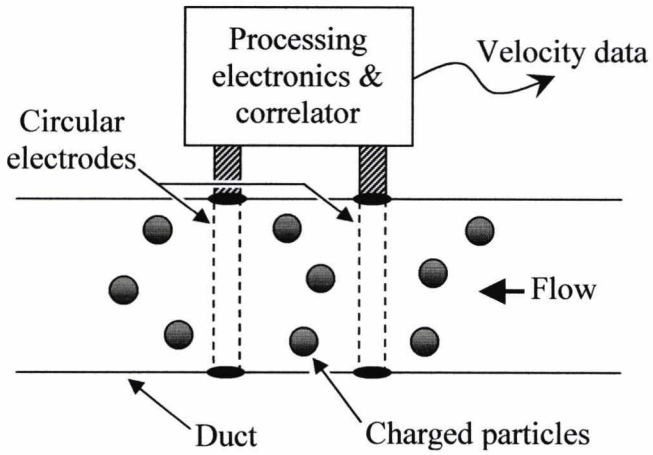

Figure 5.26 General arrangement of electrostatic velocity meter

It should be noted that the electrostatic approach measures the velocity of particles and not the conveying gas. This is a desirable characteristic for mass flow measurement – other velocity measurement systems based on differential pressures measure the gas and not the particles and would not, therefore, be suited to this application.

One interesting point in relation to the electrostatic meter used here is that, in addition to velocity information, it provides raw signal strength data. Whilst, as already stated, the absolute value of charge is not considered a reliable indicator of mass flow rate (Ma and Yan 2000) it is nonetheless interesting to observe the correlation between this and the real mass flow information. In view of this, some of the raw intensity data recorded during test runs will be presented and discussed briefly in the next chapter.

5.5.2 Inferential Mass Flow Rate Measurement

The imaging sensor provides information on volumetric concentration within the duct. Once this has been combined with velocity data it is possible to define the volumetric flow rate of material. This, in turn, may be combined with the absolute material density (the theoretical mass of solidly packed material per unit volume) to determine mass flow rate. This operation is defined as follows:

$$q_m(t) = A\rho_t V(t)\beta(t) \qquad [5.41]$$

Where, q_m is the mass flow rate of particles in kg/s, ρ_t is the true density of particles in kg/m^3, V is the velocity of particles in m/s, β is the volumetric concentration of particles, A is the cross-sectional area of the duct in m^2, and t is time in seconds.

The ability to determine mass flow rate using this inferential approach is not only important in itself but, in the wider context of imaging system testing, can be used as a tool to investigate the accuracy of on-line solids concentration measurement. As shown in equation 5.41 there are four related quantities in question. From a practical standpoint it is possible to set up a known mass flow rate condition using the laboratory test rig (discussed in section 5.6) the velocity of the material is established through the use of the electrostatic sensor and the materials absolute density is known and constant. It is therefore possible to rearrange equation 5.41 to make solids concentration the subject therefore allowing the solids concentration measurement accuracy of the imaging sensor to be established through experiment:

$$\beta(t) = \frac{q_m(t)}{A\rho_t V(t)} \qquad [5.42]$$

In Chapter 6 full testing of the system under live flow conditions will be detailed and the results of mass flow rate measurements will be given. The main usefulness of the mass flow rate measurement lies in its ability to be used as a tool to check the accuracy of solids concentrating measurement and this aspect of the results will also be discussed in Chapter 6.

5.6 Lab-Scale Test Rig

In order that the sensing head could be tested under controlled conditions it was necessary to set up a laboratory scale flow rig designed in such a way that the required flow parameters could be controlled accurately. The flow parameters of interest are listed in table 5.2 where they are categorised into those controlled by choice of material and those related to the flow rig.

Table 5.2 Flow parameters of interest

Parameters determined by rig setup	Velocity
	Concentration
	Mass Flow Rate
	Roping
Parameters determined by material choice	Roping
	Particle Size

It can be seen that there are four parameters that relate to the rig and these will be discussed here (Material choice and related considerations will be discussed in the next chapter). The first parameter, velocity, is controlled by the amount of energy used to move the material through the rig. With more energy the material will move faster and vice versa. It is, therefore, necessary to control the power of the system. Velocity can be monitored through the use of an electrostatic sensor as detailed in section 5.5.1 and can be precisely set up and controlled in a closed loop manner.

Concentration is a measure of how much material is present in the duct at any one time. Though, in a theoretical sense, solids concentration is dependant on velocity, from a practical viewpoint concentration must be controlled through varying the rate at which material is introduced to the rig. Since there are no reliable concentration measurement systems available at present (one of the driving forces for the current research) this parameter must be controlled in an open loop manner, during rig operation, by using fixed throughput settings on the material feeder.

Mass flow rate is controlled, as with solids concentration, by the rate at which material is introduced to the rig. Whilst it is difficult to obtain the instantaneous mass flow rate it is possible to determine the time averaged value during a particular 'run'. This is achieved by measuring the time it takes for a known mass of material to flow through the rig. If the system is operated under steady state conditions then the instantaneous mass flow rate will be the same as the time averaged value. If the mass of the source hopper is monitored continuously, using load cells or some form of balance, then a shorter term time averaged mass flow rate can be found and this is the approach adopted for the current flow rig.

Certain inhomogeneous flow regimes may be created within the rig for experimental purposes. Through the simple expedient of using a very low flow velocity, for example, it is possible to cause the material to flow only towards the bottom of the duct. For the present work, however, roping is the main phenomenon of interest. This may be created in two ways:

a) Forced artificial roping: If particles are introduced into the flow by a small diameter inlet probe, just before the sensor rather than at the main inlet of the flow rig, the resulting low diameter particle 'cloud' will be perceived as a rope.

b) Induced genuine roping: If a vortex can be induced in the conveying air then the flow itself will tend to form a vortex, causing the particles to form a rope.

Of these two techniques the latter is preferred as it creates conditions that are most similar to a genuine unintentional flow rope. Forced roping requires intrusive modification of the rig and also presents practical difficulties with material delivery. It can be seen in table 5.2 that roping has been placed under both rig and material categories. This is due to the fact that, with induced roping the mass of individual particles will affect their tendency to follow vortices in the conveying air flow and form a rope – small particles are more likely to do this than larger ones. In the present rig it has been found that roping will occur when using very fine materials at fairly slow velocities, there being a slight ever present vortex in the airflow due to the design of the pump used. There is no roping tendency with larger materials and higher velocities. This characteristic is suitable for testing the ability of a rope detector – precise control of the position and 'tightness' of the ropes is not required.

The presence of a rope may also be subjectively judged through visual inspection of the raw images being received from the sensing head.

Once the parameters that require to be controlled have been established more practical concerns, such as rig size, can be considered. The diameter of the duct was determined in this case by using the same diameter as used in small industrial test set-ups thus allowing the sensing head to be tested under industrial conditions without modification (50mm outside diameter PVC pipe was used). The length of the duct was determined by the size of the laboratory – a folded loop of about six meters total length was used. Another consideration is that of power – how will the particles be driven around the rig? In industry it is very common to use compressed air to blow material through but this approach has its shortcomings. Firstly this arrangement requires a complex pressurised feed hopper, secondly, if there is a leak in the duct, material will tend to blow out through it causing difficulties in a clean laboratory environment and thirdly complex filters and catchments hoppers are required at the receiving end of the duct. If these points are to be accepted then the only alternative to blowing the material though the rig is to suck it. If the material is sucked then it may be introduced simply though using a vibratory feeder, leaks are not an issue and the complex catchment hopper is combined with the suction mechanism, taking the form of an industrial vacuum cleaner. This is the solution used in this case. There are two additional advantages with this arrangement. Firstly, it is a simple matter to vary the velocity of the flow as the power of an electrical suction fan is easily varied through the use of a variable auto-transformer. Such easy variation is not available when material is blown through with compressed air. Secondly, the radial nature of the centrifugal impellers used in suction fans causes a slight vortex in the flow. This is of a very small magnitude under normal conditions and does not affect the flow most of the time but, with careful selection of material and velocity, allows roping flow to be studied. The general arrangement of the laboratory scale test rig is shown, schematically, in figure 5.27.

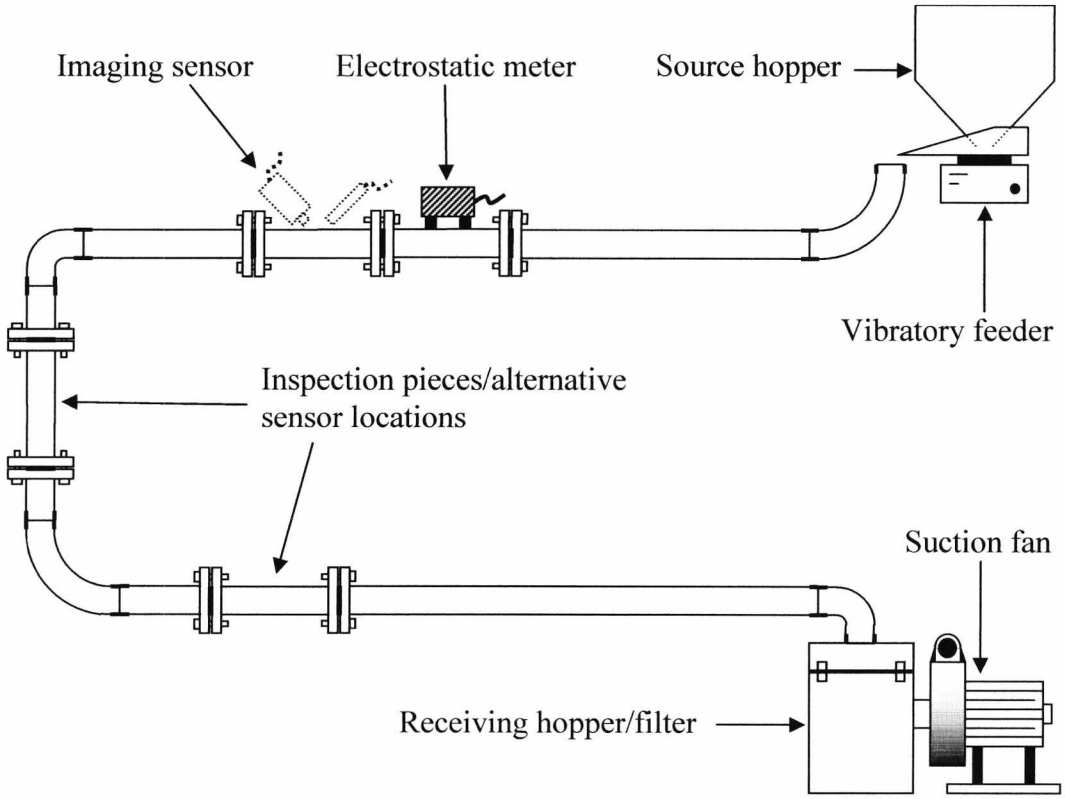

Figure 5.27 Schematic representation of lab scale test rig

The actual arrangement of the flow rig is shown in the photographs of figures 5.28 and 5.29. There are a few points of interest in relation to these figures that must be discussed. Firstly, a control panel can be seen at the top of the rig – this features controls for vibratory feeder power and power supplies for the sensing head and electrostatic meter. Next it can be seen that two suction fans (in reality industrial vacuum cleaners) are used. One of these is fitted with a variable autotransformer (visible next to the control panel) and one is not. With one fan switched off the other can be varied giving control over a 0 – 50% range of total rig power. With both switched on power can be varied from 50 – 100%. Lastly it is clearly noticeable that a network of thin wire has been wound around the PVC pipe work. This network of cable connects to the earthed rig framework and is necessary in order that large static electric potentials do not build up. Without this 'drain wire' potentially dangerous charges could build up under certain, heavy, flow conditions.

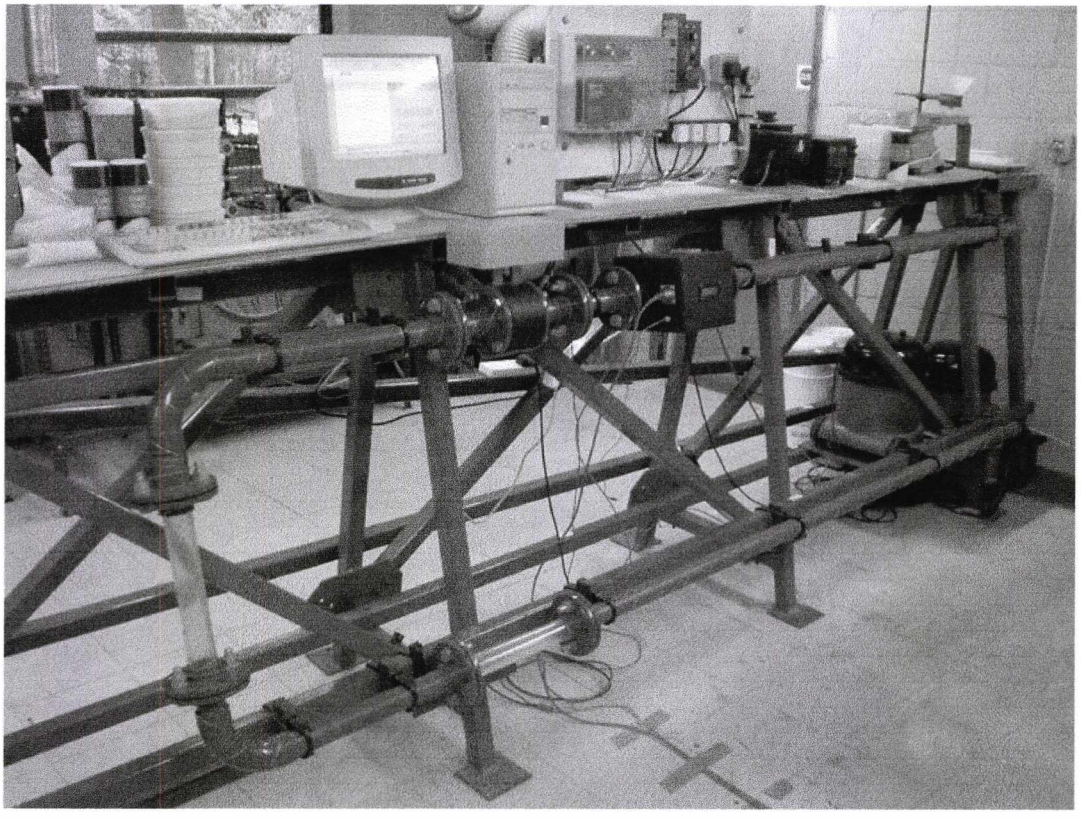

Figure 5.28 Overall view of flow rig

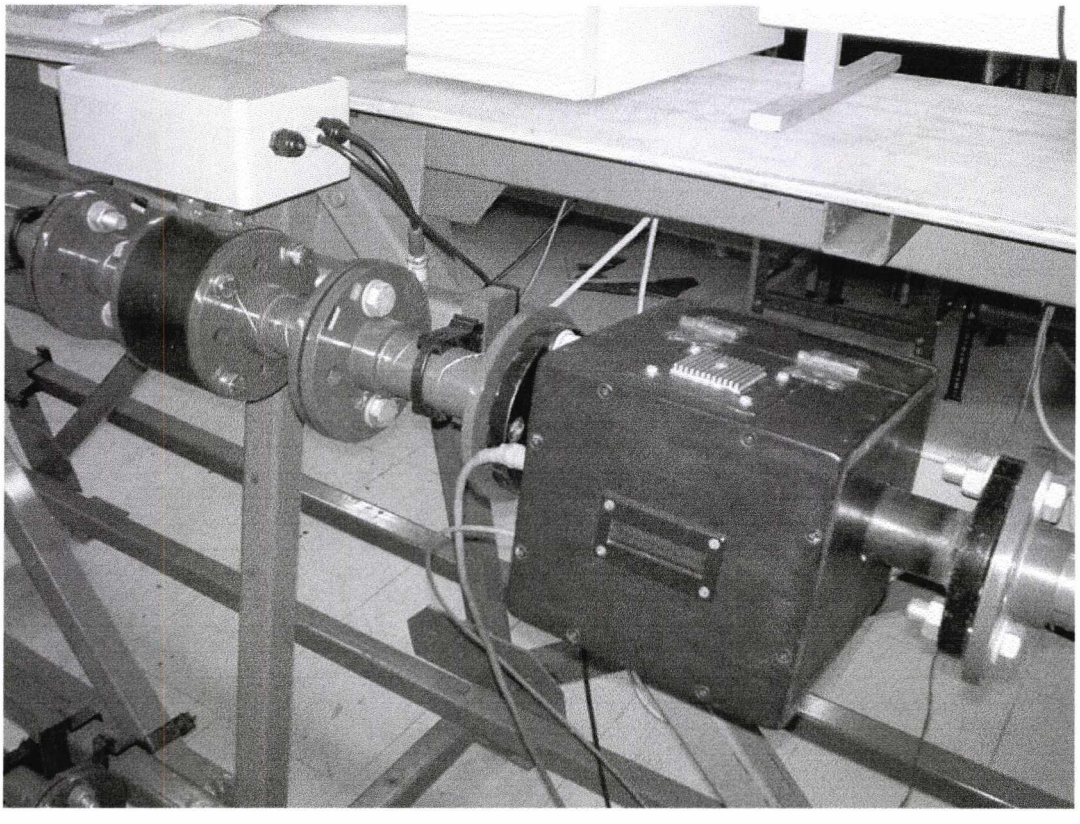

Figure 5.29 Close-up of imaging sensor and electrostatic meter

5.7 Summary

This chapter has covered the practical problems involved with imaging moving particles. The conceptual difficulties have been explained and image processing algorithms required to overcome these difficulties have been detailed. Any effects on system accuracy that these new algorithms may cause have been investigated and it has been shown that accuracy is not unduly affected when compared with operation under static conditions. The exact physical arrangement required for non-intrusive flow imaging has been explained in both schematic form and in the form of a final sensing head design. The optical issues introduced by a practical sensing head design have been discussed and new processing algorithms required in order to correct for these issues have been detailed.

An important part of this chapter has covered the ability of an imaging based system to detect inhomogeneous flow regimes – in particular roping flow. The concepts of roping and the difficulties in defining a quantity that is, by its very nature, subjective have been discussed and an algorithm for detecting flow ropes has been detailed.

Another new parameter that the system can measure, when a particle velocity measurement is available, is mass flow rate. It has been shown how an electrostatic sensor can be used to determine the velocity of particles in the duct and how this information can be combined with concentration data to produce mass flow rate information.

Finally, the laboratory scale test rig used for initial testing has been explained. The various choices made during development of this rig have been detailed.

In general this chapter has shown how the basic system, described in previous chapters, can be used in a real, practical, way. The problems involved with changing from an ideal to a real environment have been identified and solutions detailed. New uses for the imaging sensor have been identified and explained. All description of the imaging based particle measurement system has now been completed and in the next chapter the results of extensive tests, conducted using the test rig detailed in this chapter, will be presented. All flow parameters identified in this and previous chapters will be examined and the real usefulness of the system will be investigated.

Chapter 6

On-Line Experiments and Results

6.1 Introduction

Previous chapters have covered operating principals and have detailed the design and implementation of a practical testing set-up. Basic accuracy and limits of operation have been established under static conditions and so it falls to this chapter to detail the results of extensive tests performed on-line using the 'sensing head' and flow rig that have already been described. The results of industrial trials will also be covered here.

This chapter will discuss the materials chosen for on-line testing, explaining their preparation and use and experimental procedures will be detailed. The results themselves will cover all measurement parameters discussed so far, including particle size, shape, concentration and repeatability and a thorough discussion will be undertaken. Results, where necessary, are provided for two materials, exhibiting differing physical and optical characteristics. Static imaging, reference laser diffraction and on-line imaging results will be compared. The detection of inhomogeneous flow regimes is tested and discussed. Finally, experiments under real industrial conditions are presented. In general this chapter presents on-line test results and establishes the systems accuracy and repeatability.

6.2 Test Materials

6.2.1 Material Selection

The choice of materials used when performing on-line testing is important for a number of reasons. As discussed in the previous chapter (section 5.6) the choice of material will affect both the range of particle sizes flowing through the duct and the ability of the rig to achieve roping flow. Roping (and other inhomogeneous regimes such as stratification) can be assessed in separate tests from other parameters and so these two considerations do

not need to be addressed together (material for roping flow will be discussed in section 6.3.2.4). The size of particles is therefore the most important consideration for the majority of tests, although there are other factors which must be taken into account. It can be readily imagined that two materials can be found that demonstrate very similar particle size and yet represent differing particle shapes and optical properties. It is, therefore, necessary to test the system with at least two materials, nominally similar but varying in these ways, in order that the immunity or sensitivity of the system to these parameters can be established. It is also necessary that materials be used which are suitable for operation with the current rig in terms of safety and achievable mass flow rates and velocities. Suitable materials must comply with the following requirements:

- Since the rig is not sealed some material may escape into the laboratory and so harmful substances must not be used.
- The rig is constructed from plastic ducting and the occasional electrostatic discharge is not unknown – the material must therefore be non-flammable.
- In the interests of convenience the material should be 'clean' and not cause obscuration of the optical window.
- The size range of particles must be such that there are not significant numbers of particles that are too small for the present set-up to interrogate (about 100μm was established as a suitable lower limit in previous chapters although smaller particles can be interrogated with increased error).
- Although in theory (and under static conditions) the upper sizing limit is related only to the maximum size of particle that can fit into the camera's field of view it is necessary to establish a much lower maximum size limit when operating on-line. If particles are too large it may be difficult or even impossible to set up reliable flow conditions which exhibit acceptable solids concentrations.
- The present rig has a simple material feed system that is unable to cope with materials that are prone to caking - this suggests that only free flowing materials should be employed.
- The absolute density of the material must be known if accurate mass flow rate information is to be derived.

The first material chosen that meets these requirements is sand. Sand is defined for geological purposes as ground up rock with particle sizes in the range of 63μm to 2mm. This represents a good size range for the current system that can be further improved by careful grading (see the next section). Sand is available that consists mainly of silica (silicon dioxide) which has a known absolute density of 2600 kg/m^3 (Salt Institute 2005). It is true that this sand is not 100% pure and small quantities of other materials are present within it and so a more accurate absolute density was found through comparison with the second material: salt. Salt is readily available and, in the form of ordinary table salt, exhibits a very similar range of particle sizes to sand and is therefore suitable for the present tests. Whilst table salt does not consist of pure sodium chloride but contains anti caking agents such as magnesium carbonate and sodium hexacyanoferrate, these materials are only present in small quantities (typically less than 2%) and so the absolute density is largely unaffected (Salt Institute 2005) (the additives are of lower density than sodium chloride but do have significant density of their own and so the final absolute density of the table salt is affected by less than 0.5% typically). The absolute density of sodium chloride is 2163 kg/m^3 (Salt Institute 2005) and this value was used in the tests. This accurate value of density was used to achieve a more accurate value for the particular sand used here. A small container was filled to the brim with salt and weighed – this procedure was repeated with the sand and the ratio between weights was applied to the density of salt to achieve an absolute density figure of 2382 kg/m^3 for the sand. This procedure assumes similar packing density of the two materials (and equal air space) but since the two materials had been graded to similar size ranges this figure was considered to be an acceptable working value. Both sand and table salt are safe, clean and free flowing but represent different optical (colour) and physical (sodium chloride being crystalline and sand consisting of ground up material) properties – they are ideal for the present purpose.

6.2.2 Material Preparation

The materials chosen contain particles in the approximate size range of 63μm to 2mm. The optical analysis software was designed to give comparable results to a commercial laser diffraction based offline system, which was available, in the interests of result verification. This limited the upper size of particles to 1.4mm and a lower limit of 90μm

was decided upon based upon the limitations of the optical system in conjunction with the particular size ranges used in the bulk solids handling industry (where standard sieve meshes are used).

It would be possible to prepare the materials for testing by simply passing them through a 1.4mm sieve and using material that was captured by a 90μm mesh. In practice this would still result in large quantities of material of larger and smaller sizes than these limits as the sieving process is not perfect (for instance a relatively long and thin particle could slip through the mesh end-on but still be detected by the imaging or laser diffraction system as a larger particle – also small particles may be trapped amongst others and be unable to reach the lower size limit mesh). For this reason it was decided to sieve the materials through a smaller range of sizes and, after considerable experimentation in order to achieve the best yield of usable material, the range 150 to 355μm was selected. Both materials were sieved for 10 minutes each using the same sieve shaker settings.

6.3 Experimental Procedures

Establishing systematic and consistent experimental procedures is important for any scientific tests and in this case, in order to ensure consistency between materials it is extremely important. This section details the experimental procedures used to achieve the results that follow.

6.3.1 Off-Line Testing

6.3.1.1 Laser Diffraction Reference Data

A sample of each material (approximately 100g) was analysed using a Malvern Mastersizer – a laser diffraction based off-line system. The samples were taken from the main bulk of material after thorough stirring in order that material settling was minimised. Each sample was split into three parts (care again being taken to avoid settling) and fed through the analyser separately thus allowing the systems repeatability to be assessed. Results were recorded in the form of particulate size distribution histograms using

standard, internationally accepted, sieve mesh size ranges and a single distribution result was produced by finding the mean result for each size range from the three experiments.

6.3.1.2 Imaging System Static Testing

For static particle analysis the setup detailed in chapter 4 was used. Similar experimental procedures to those explained in chapter 4 (section 4.5) were adopted. In brief this consisted of using a carefully stirred sample of each material and randomly selecting a new sprinkling of particles for each test. The concentration of particles in each test was adjusted to be around 2% thus remaining below the particle overlapping limit whilst yielding the maximum number of analysed particles. As with the laser diffraction system three tests were performed in the interests of repeatability assessment. The mean of these three tests was again found and used as the final particle size distribution result. This distribution was compatible, in terms of the size ranges used, with the laser diffraction result. The imaging software was set to perform automatic threshold setting for the first experiment and the same values were used for the proceeding two. No system settings were changed between the experiments.

6.3.2 On-Line Testing

6.3.2.1 Size and Shape and Repeatability/Reproducibility Tests

The most important parameter measured by the imaging based particle analyser is the particle size. In order to assess the reliability of this measurement independently of other parameters it is necessary to test the system using the same material under varying flow concentrations and velocities. These varying conditions will also allow the consistency of particle shape measurement to be studied.

The flow rig, as described in the previous chapter, has been found through experimentation to be capable of achieving particle velocities of up to about 30m/s with light-weight materials at low concentrations. This velocity may be maintained only with significant fluctuation and a practical maximum, considering the materials and concentrations in use here, has been found to be 20m/s. The minimum speed of material

can be brought down as low as about 0.1m/s (as measured by the electrostatic meter) before flow ceases entirely but at such low speeds significant deposition of material occurs, leading to clogging of the duct and difficulties in achieving usable concentrations. Also stratification is an issue (see section 6.3.2.4). A practical minimum velocity, at which deposition and stratification are insignificant, has been found to be 5m/s and so this value was set as the minimum for basic size and shape testing.

Concentration control is dependant upon velocity and feed rate. The maximum measured concentration must be no higher than 2% if particle overlapping is to be avoided and so 2% was set as the upper concentration limit in this case (the rig was found to be capable of maintaining 2% concentration throughout the 5-20m/s velocity range). The lower practical concentration limit is determined by the size of the material as for reliable measurement there must be at least one particle per image frame otherwise rolling averages will be affected. It is desirable to have considerably more than one particle per frame if the results are to be truly representative and it has been found through experiment that a consistent flow with little fluctuation in the 5-20m/s range can be achieved at concentrations of down to 0.5% (giving an average of around 15 particles per frame). Below this level there may be difficulties maintaining a steady 5m/s as the rig is lightly loaded and so the minimum air velocity increases.

The practical capabilities of the rig and therefore the range of test conditions possible are summarised in table 6.1. It can be seen that the mass flow rate can be varied over two orders of magnitude with this range of flow settings.

Table 6.1 Summary of suitable test conditions

Particle velocity (m/s)	5-20
Measured solids concentration (%)	0.5-2.0
Approx. equivalent measured mass flow rate at 5m/s, 0.5%	2 g/min (33.3×10^{-6} kg/s)
Approx. equivalent measured mass flow rate at 20m/s, 2%	100 g/min (1666.7×10^{-6} kg/s)

Both the velocity and solids concentration ranges were divided up into four levels, yielding 16 combinations of velocity and concentration. This number of divisions was practical to set-up with the present rig – had greater division been used it may have become difficult to set up the resulting flow conditions with sufficient accuracy.

Experiments testing particle size, shape and size distribution were performed for each of the 16 flow conditions for each material. For each data point the rig was set in operation and the required flow condition established and allowed to stabilise. The software was then set to record all generated data in the form of a data file for approximately one minute. After this time the suction fan was turned off and a small container placed under the vibratory feeder to catch material and left for a carefully timed five minutes. This container was then removed and weighed (the feeder being disabled to avoid material wastage) and the mean mass flow rate during the run was calculated and recorded. During the run the software was set to generate data points using a rolling average over 20 frames. This, in combination with the achieved image processing rate of approximately five frames per second gave a software time constant of around four seconds which was roughly equal to the settling time of the rig. There is natural variation between the particles in each frame and so some time averaging is desirable if stable results are to be obtained – through making the averaging time constant equal to the mechanical time constant the maximum averaging that could be obtained without affecting the overall response time was achieved. Auto threshold setting was performed for each data point but no other system settings were altered.

The test matrix used is shown in table 6.2. In this table the tests are numbered from one to 16 and it should be noted that each of the 16 tests resulted in a large data file and a mean mass flow rate result.

Table 6.2 Numbered test matrix

Measured solids concentrations (%)	Velocities (m/s)			
	5	10	15	20
0.5	*1*	*2*	*3*	*4*
1	*5*	*6*	*7*	*8*
1.5	*9*	*10*	*11*	*12*
2	*13*	*14*	*15*	*16*

Results from this sequence of 16 tests were generated in the form of both time and spatially averaged mean values and also size distributions compatible with those from the static tests.

One aspect of testing that has not yet been covered is the repeatability of size measurement. In order to assess this parameter it was decided to run the rig for considerably longer than usual, determining the change in measured size distribution in relation to time. It was also decided to establish reproducibility by comparing the repeatability results to the particle size distribution measured using the same set-up on the previous day. For these tests a solids concentration of 1% was used this being a good compromise between high particle numbers and realistic material use rate. The test was run for 25 minutes (there was insufficient material available for a longer run) and results were recorded continuously during this time.

Presentation of repeatability results necessitated that a normalised standard deviation be found as this would be compatible with the repeatability measurements from the static systems. Such a parameter was straightforward to calculate. It was also decided that, in order to provide better immediate understanding and allow comparison with the previous day's results for the establishment of reproducibility, a direct presentation of size distribution change in respect to time should be given. In order to fulfil this requirement the 25 minute run data was split into four parts and the mean size distribution (i.e. the mean of each bar during the allotted time slice) found for each. These could then be compared with each other easily along with the reproducibility data.

6.3.2.2 Particle Brightness Variation

During testing it was decided (for reasons to be introduced later) that experiments must be performed in order that any correlation between particle brightness in the recorded images and velocity/parameter variation could be discovered. In order to reduce the amount of data produced it was decided to perform these experiments at one concentration only there being (as will be seen later) no suspected correlation between the brightness of particles and changes in concentration. These experiments were performed in the following manner: A concentration of 1% was used since at this level the rig could sustain a reliable 25m/s thus giving an extra data point in the series. The five resulting

flow conditions were each set-up (5, 10, 15, 20 and 25m/s each at 1% measured solids concentration) in turn and, once stable flow was achieved a raw, unprocessed, image was saved for each. These images were analysed by hand in order to establish the mean particle intensity value at each velocity. Each image was examined using a photo editing package and the maximum brightness at the centre of twenty evenly distributed particles in each image was found. The mean (maximum) particle brightness was thus established and it was possible to plot this quantity against velocity and other parameters as required.

6.3.2.3 Mass Flow Rate

The mass flow rate of material in the duct can be derived from concentration data in combination with velocity and material density as discussed in previous chapters. This information was calculated by the software and recorded in the experimental data files. Since a reference mass flow rate was available for each experiment (in the series of 16 experiments initially performed – see section 6.3.2.1, above) it was a simple matter to compare the calculated and reference data.

In addition to the series of 16 measurements, in order to confirm certain dependencies within the results, it was thought necessary to test mass flow rate measurement under slightly different conditions and so a further experiment was set up. This took the form of establishing a fixed mass flow rate and varying the velocity (and hence the concentration). In order to achieve this a steady flow at 2% concentration with a velocity of 5m/s was established and then the velocity was increased as far as possible. As the velocity increased the concentration decreased and so, due to the light loading at higher speeds, it was possible to increase the velocity as high as 30m/s in this case.

6.3.2.4 Lower Concentration Limit

In order that the lower limit of concentration that is suitable for use with the present set-up could be established a suitable experiment was performed. A fixed 10m/s flow was established and the concentration was increased from zero to 10%. Variation in measured particle size with respect to solids concentration was studied also another system parameter, as yet unmentioned, was found to be useful. This parameter shall be known here as sizing uncertainty and is calculated by the system on-line and recorded as part of

the results data files. When the size distribution of particles is calculated it is displayed as the percentage contribution of each size range to the whole. Clearly, if all the size distribution bars are added up the result should equal 100%. During the experimental runs however (as in any practical situation) it was necessary to use a rolling average to stabilise the results – the time averaged value of each bar is displayed (in this case over twenty frames or samples). Under these conditions all bars will not necessarily add up to 100%. If the flow conditions were entirely stable and unchanging the result would be correct but, as conditions vary there will be an increasing divergence from a 100% result as the magnitude of the variation increases. This divergence, or sizing uncertainty, is expressed mathematically in equation 6.1.

$$S_u = 100 - \sum_{i=1}^{n} S_b(i) \qquad [6.1]$$

Where S_u is the sizing uncertainty and $S_b(i)$ represents a particular size range volume. Once the solids concentration is so low that there are insufficient particles present for consistent sizing results this parameter will demonstrate a dramatic increase in value and can therefore be used to examine minimum concentration limits.

6.3.2.5 Inhomogeneous Flow

The present rig is capable of generating two inhomogeneous flow regimes: roping and stratified flow. Since the detection of these conditions is fundamentally insensitive to material variations these conditions were studied using one material only: salt.

Stratification is easily achieved by reducing the velocity of the flow until the phenomenon is observed. An experiment designed to achieve this consisted of setting up a steady flow at 5m/s 0.5% and slowly reducing the velocity to zero whilst recording results. The software generates inhomogeneous flow detection information in the form of a suggestion as to which area, or zone, of the image the possible undesirable flow regime is centred on (i.e. the regime does not necessarily exist solely within the indicated zone).

Roping is a more difficult regime to achieve. In the case of the present rig it was found that a continuous and reliable rope could not be established but that short pulses of flow

could be made to form ropes. In order to create these short ropes it was necessary to use very small particles travelling at very high speeds (material below 90μm in size was used, inaccuracy in particle sizing being unimportant in this test – many of the particles were too small to be detected singly, instead appearing as small 'clouds'). The experimental procedure employed consisted of setting up a very high air velocity (about 35-40m/s, being the maximum setting available with the suction fan used) and introducing small quantities of material as sudden 'pulses' of flow. With this method roping was often observed. It should be noted that the rope detector works independently of other software averaging procedures and so is unaffected by the short 'pulsed' nature of the ropes. Results take the same form as those for stratified flow. By the use of a special 'triggered grab' mode that is built into the software it was possible to record an image of one of these flow ropes which is presented in the results section.

6.3.3 Environmental and Operating Conditions

It is possible that changes in environmental conditions such as temperature and relative humidity may affect the properties and behaviour of materials and flow conditions used in this work. The electrostatic meter is particularly vulnerable to such variations (Ma and Yan 2000). Whilst a controlled environment was not available for testing the laboratory is of sturdy concrete construction and provides fairly constant conditions. Temperature and humidity were recorded at regular intervals during the tests (which took several weeks) and the range of these quantities is recorded in table 6.3. The internal conditions of the sensing head are also shown in this table. Experiments were not performed until the sensing head had reached its operating temperature (around 27°C).

Table 6.3 Environmental conditions

Location	Temperature (°C)		Relative humidity (%)	
	Min	Max	Min	Max
Laboratory	20	24	48	52
Sensing head	26	28	49	50

6.4 Results and Discussion

This section presents the results achieved when adopting the experimental procedures that have been discussed in previous sections. Results are discussed and explained and the logical process of one experiment leading to another is detailed. Similar sections are used to those in section 6.3 thus allowing easy cross referencing between experimental procedures and results. Due to the large quantity of results generated and in the interest of brevity, complete results are given only for table salt. Key data, highlighting similarities or differences between the materials, are presented for sand. In view of this it should be assumed that results shown are for table salt unless otherwise stated.

6.4.1 Size and Shape

Figure 6.1 shows the variation in measured particle size against solids concentration at the four velocities used. It should be remembered that the particle size data produced by the software represents the equivalent diameter of a circle having the same area as the particle in question. The results shown in figure 6.1 (and 6.2) represent the mean equivalent diameter during the run having been both spatially (within each image) and time averaged. It can be seen that there is little variation in relation to solids concentration (the 5m/s 0.5% point is believed to be spurious in this respect and will be discussed in section 6.4.5) but that there is a definite offset generated with respect to changing velocity. Since the material was not changed between tests this trend must indicate a shortcoming in the present system which will be discussed later. The trend can be seen more clearly in Figure 6.2, showing measured particle size against velocity, where the insensitivity to changes in concentration can be readily appreciated. Although the result is by no means identical at the different concentrations the variation is random and small enough to be accounted for in the natural variation in material experienced from experiment to experiment.

Figures 6.3 and 6.4 show measured particle size against solids concentration and velocity for sand (i.e. comparable to figures 6.1 and 6.2). It can be seen that similar velocity dependence is apparent. The only difference here is that the 0.5%, 5m/s data point is in line with the others, backing up the supposition that the offset seen before was spurious.

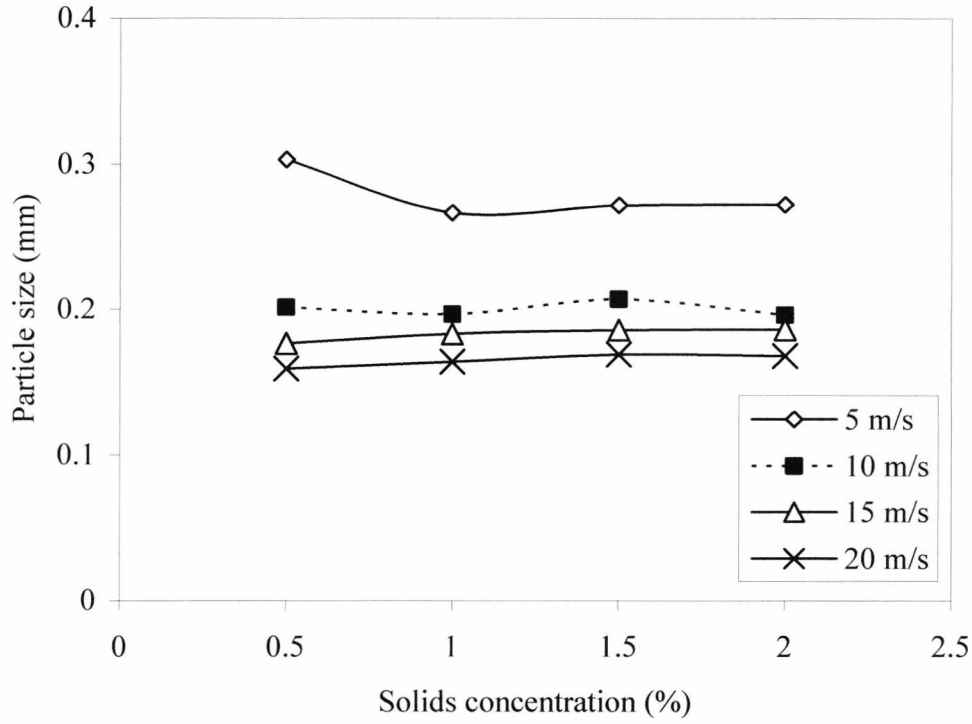

Figure 6.1 Measured mean equivalent diameter against solids concentration

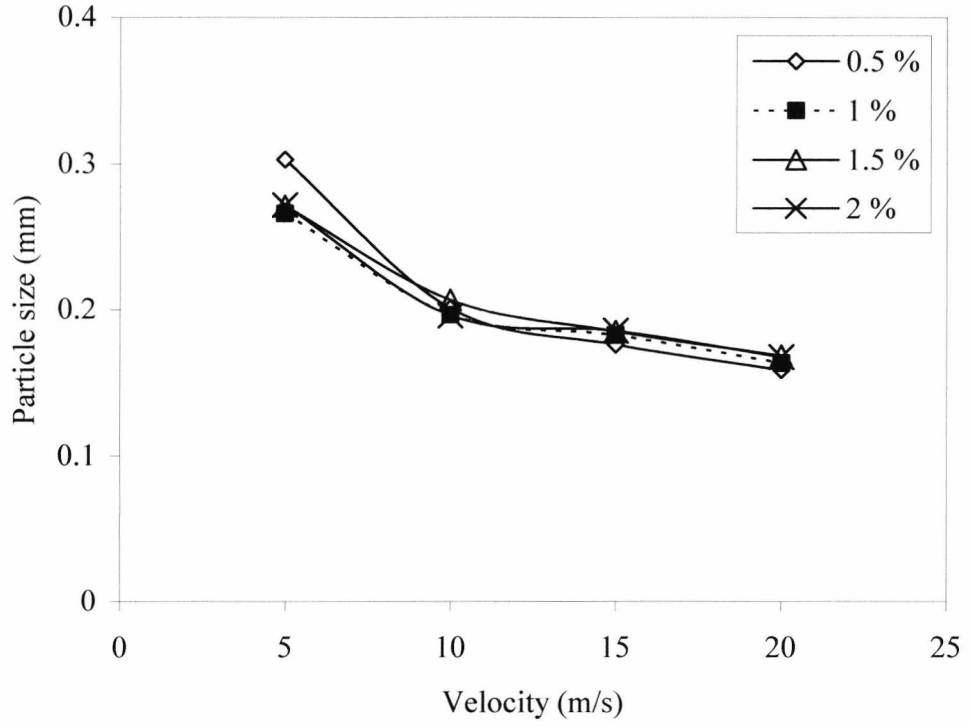

Figure 6.2 Measured mean equivalent diameter against velocity

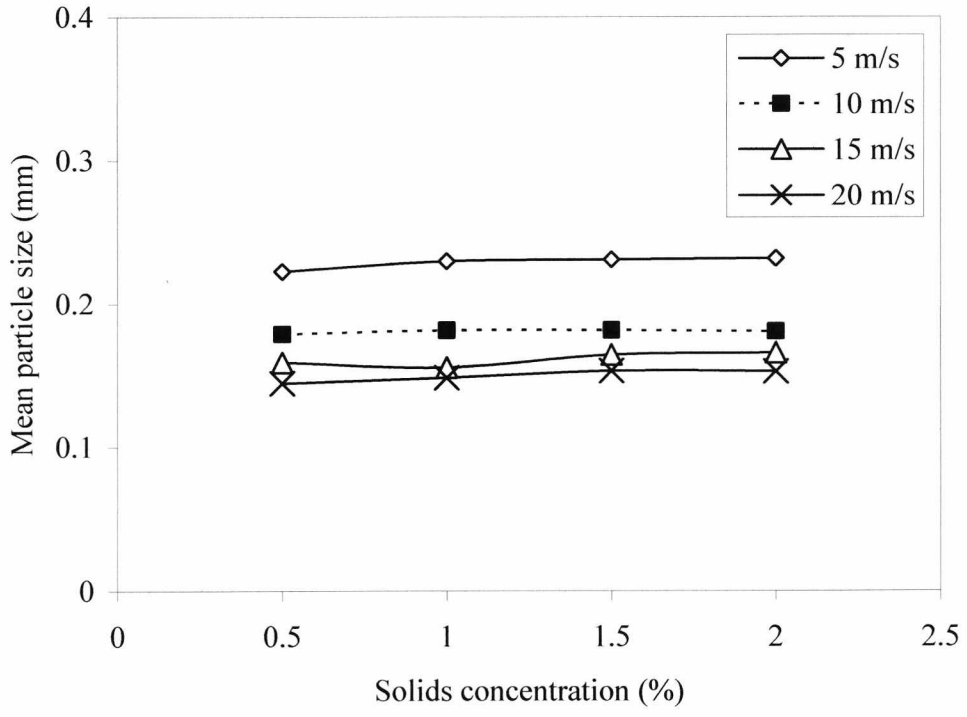

Figure 6.3 Measured mean equivalent diameter against solids concentration for sand

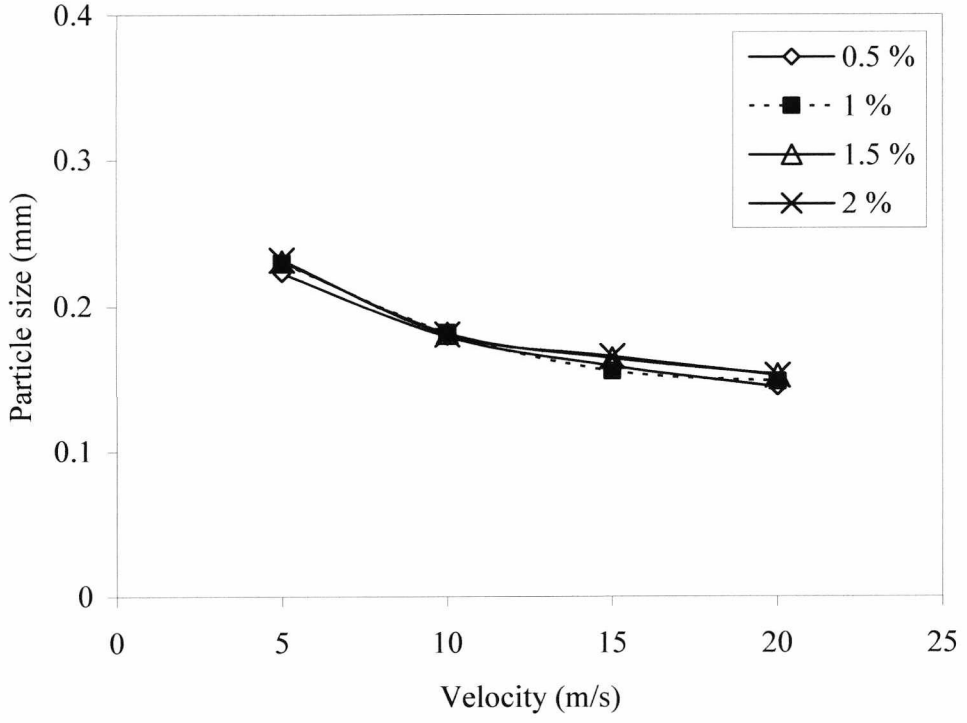

Figure 6.4 Measured mean equivalent diameter against velocity for sand

Figures 6.5 and 6.6 show the measured aspect ratio and shape factor of particles against concentration at each velocity. These results, in the same way as the sizing data, represent the mean value of each quantity and are both spatially and temporally averaged. The aspect ratio result is excellent with no significant change for any of the flow conditions.

A lack of change in the results is to be expected since the characteristics of the particles in the flow do not change. Shape factor measurement is also extremely consistent with no correlation between parameters. There is an apparent increase in shape factor with concentration upon initial inspection but this impression is given mainly by the spurious 5m/s 0.5% data point and is false. There is a certain random variation in both quantities but this can be readily explained in natural variation between experiments.

Results for sand are virtually identical and will not be shown here. The slight increase in the 5m/s 0.5% point is not apparent in sand but this has already been demonstrated in figures 6.3 and 6.4.

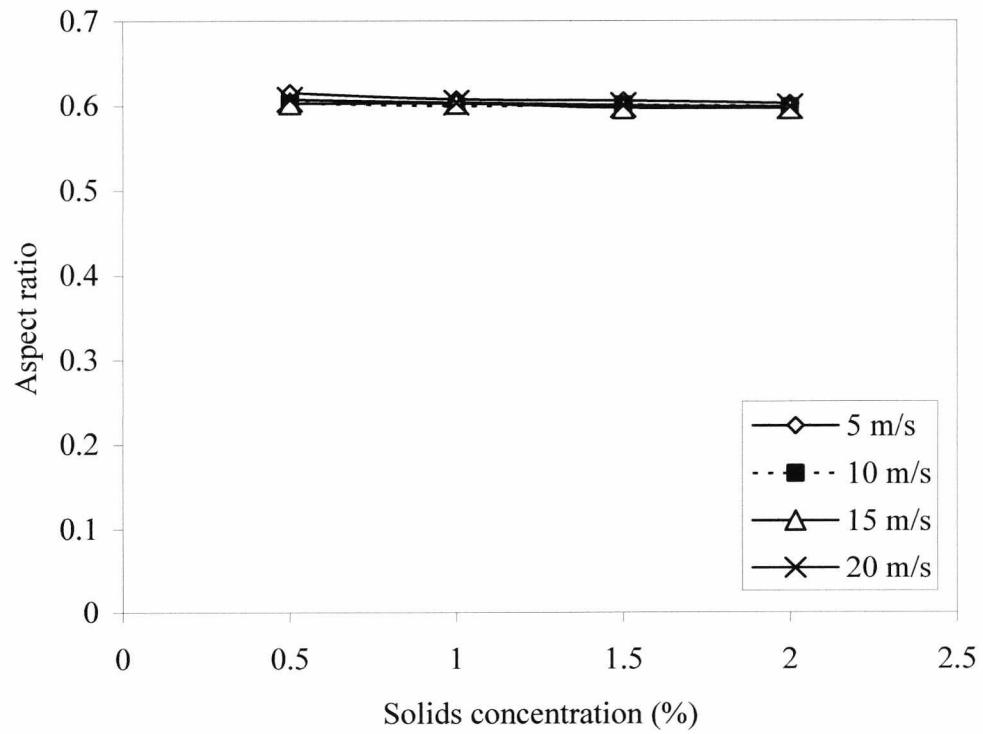

Figure 6.5 Aspect ratio against concentration

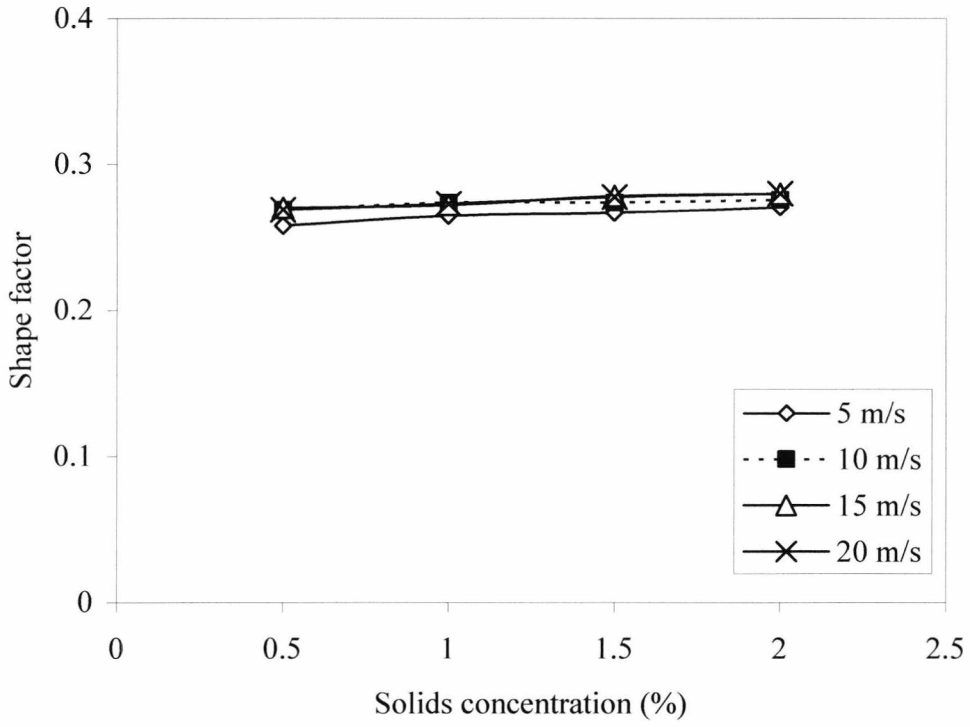

Figure 6.6 Shape factor against concentration

The only correlation demonstrated in the mean results is the tendency for measured particle size to decrease as velocity increases (e.g. figure 6.2). This decrease must be uniform around the particle since the measured aspect ratio and shape factor remain constant. A closer study of size measurement is required and this is presented in figures 6.7 through 6.10. These figures compare the measured size distributions for each concentration setting at each of the velocities starting at 5m/s and working up.

It can be seen, from figures 6.7 to 6.10, that the size distribution is very consistent with no significant variation between concentrations but that the distribution appears to be shifted downward with increasing velocity. This is the same trend as was shown for the mean results. The steady reduction in bar height is a result of the fact that an ever increasing proportion of the particles are too small to register within the range of sizes shown here.

Distributions for sand demonstrate an equal insensitivity to solids concentration and similar velocity dependence. The main difference between materials lies in a slight variation in actual size distribution. Representative (sand) results at 5m/s and 20m/s are shown in figures 6.11 and 6.12.

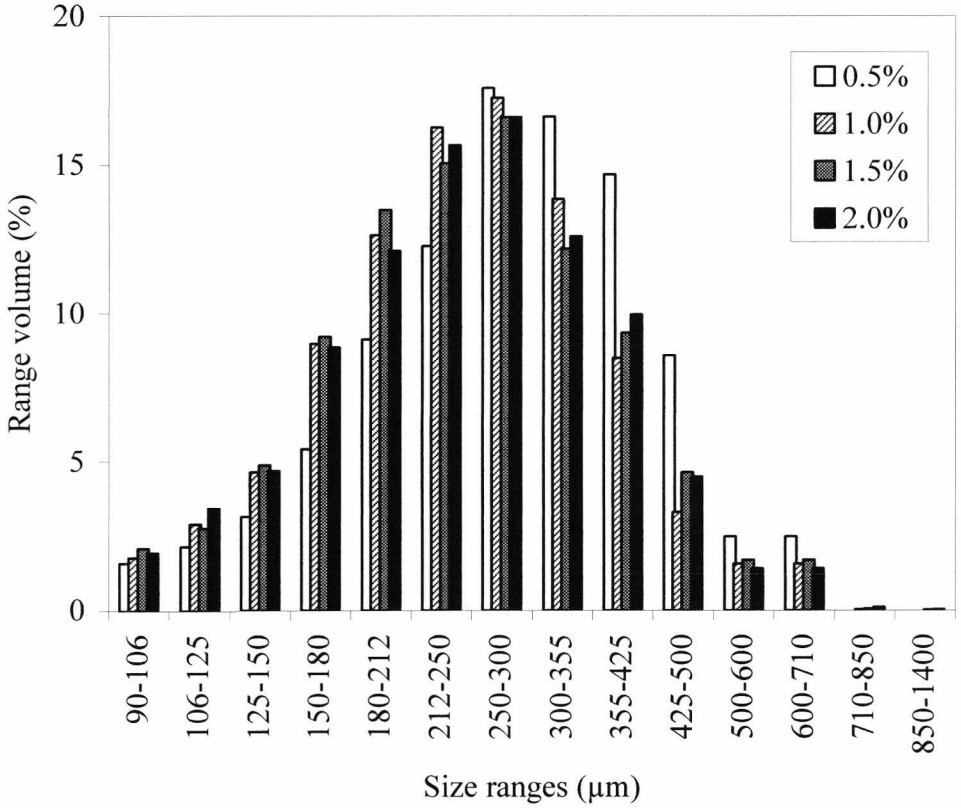

Figure 6.7 Size distributions at 5m/s

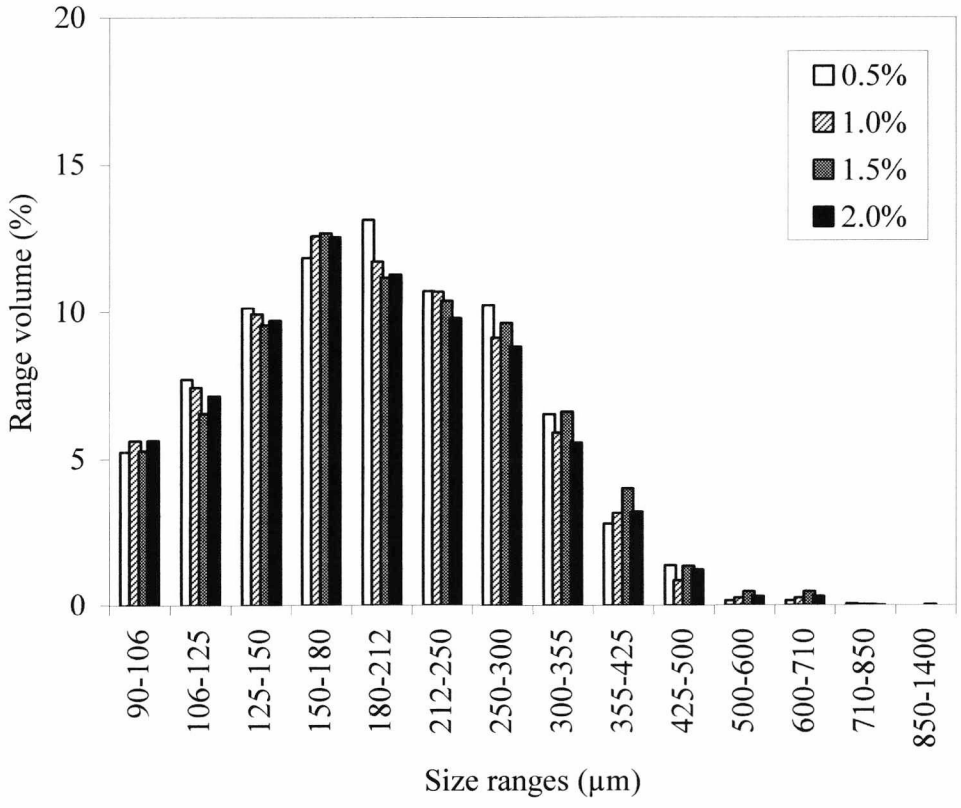

Figure 6.8 Size distributions at 10m/s

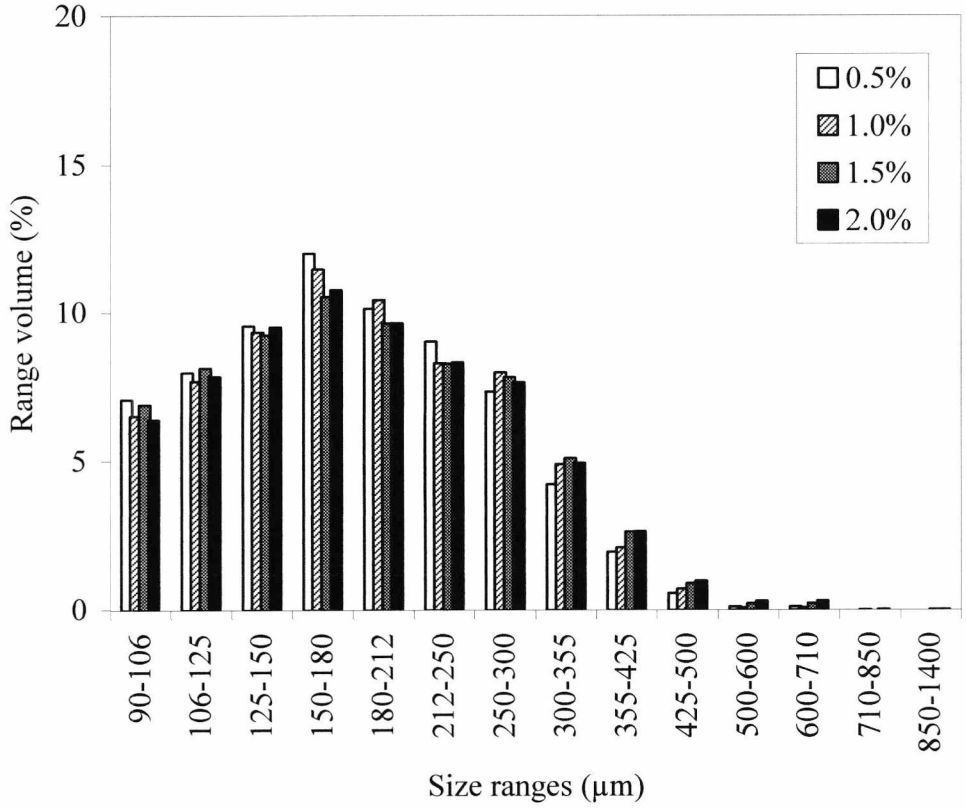

Figure 6.9 Size distributions at 15m/s

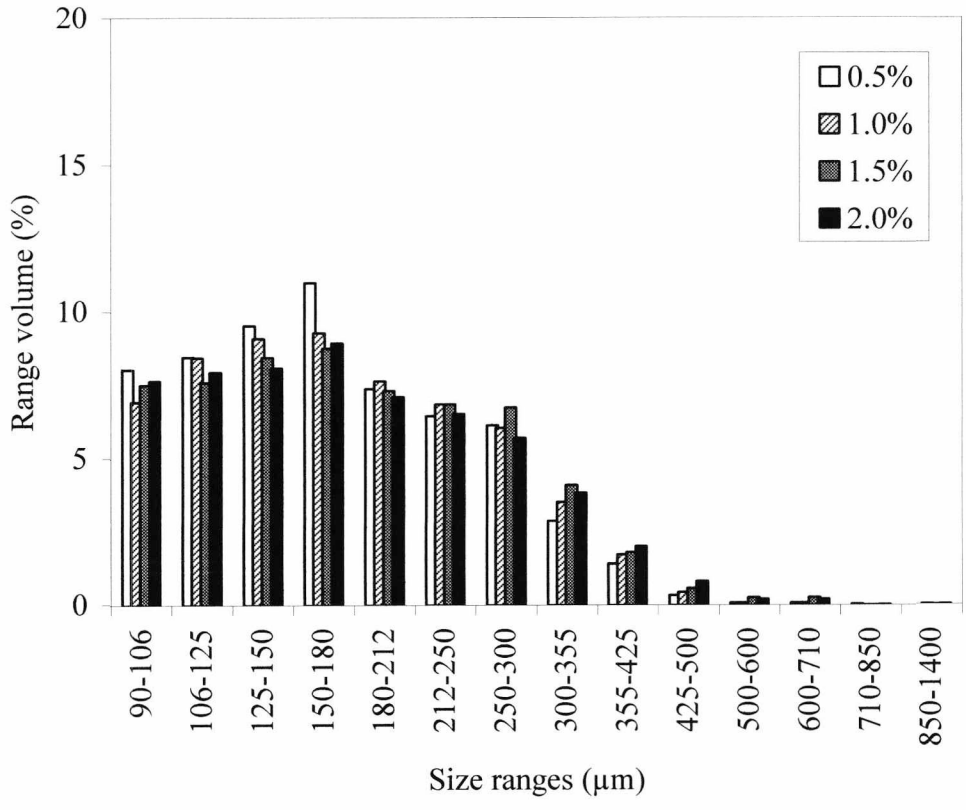

Figure 6.10 Size distributions at 20m/s

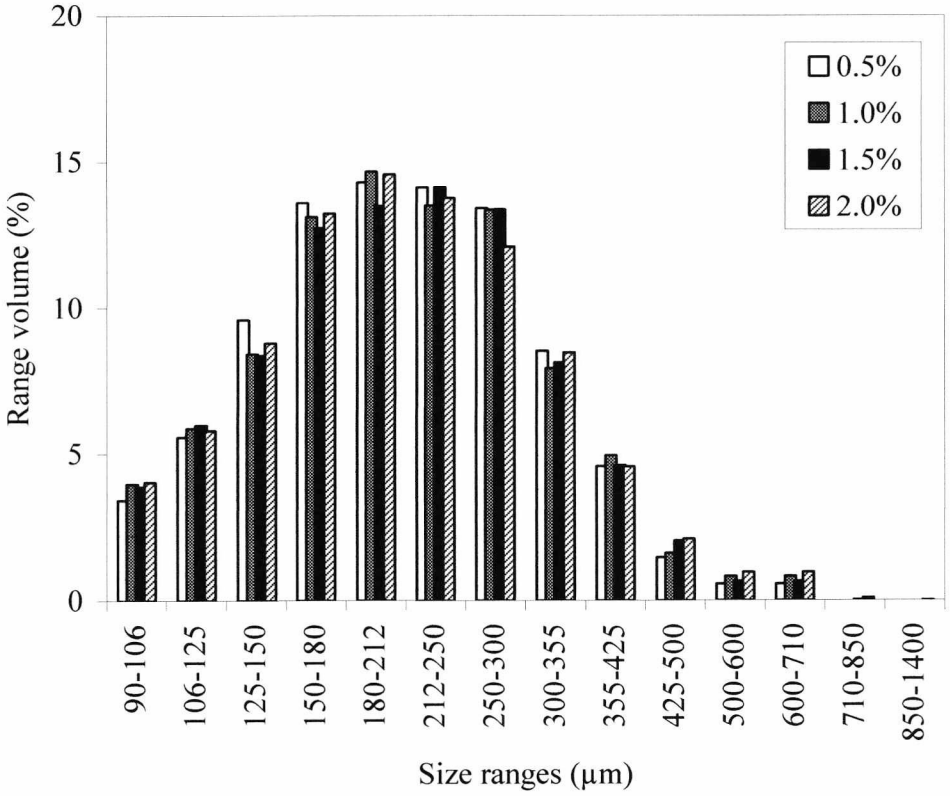

Figure 6.11 Size distributions for sand at 5m/s

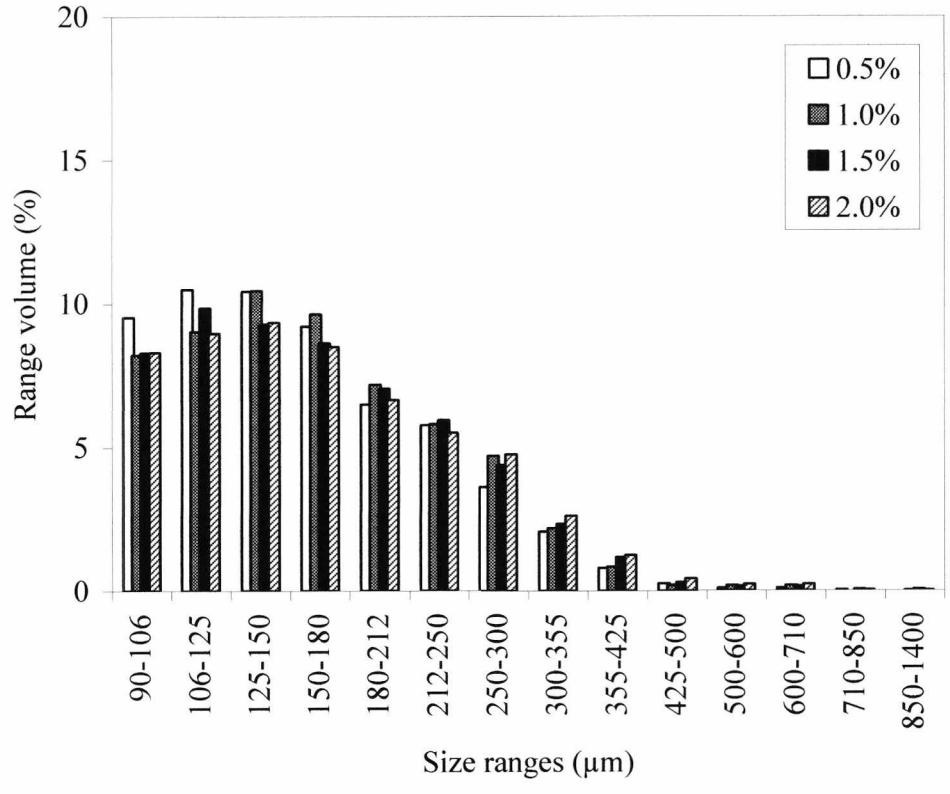

Figure 6.12 Size distributions for sand at 20m/s

6.4.2 Particle Brightness Variation

Clearly the size/velocity dependency is a problem that must be investigated further and, since the imaging software is fundamentally insensitive to velocity change (being unaware of the third dimension, though see section 6.4.5) the problem must arise in the physical or optical arrangement. The images being fed to the system appear to vary with changing velocity. Empirical inspection of raw flow images revealed that the particles appear 'dimmer' at higher velocities. Initially this would seem reasonable since the particles will remain in the laser sheet for less time at high speeds thus causing fewer photons to fall onto the CCD sensor. The camera in use, however, features automatic shutter speed and gain control and it was hoped that these functions would compensate for such changes in flow conditions. It would appear that there is insufficient automatic control, but one of the aims of the present work was to investigate the limitations of a low cost, automatically controlled, camera and experimental work has revealed a possible shortcoming of such a system.

If, however, there is a direct and predictable correlation between particle brightness and perceived particle size then this problem may be safely calibrated out. In order to test for such a correlation an experiment was conducted: The mean particle brightness was found at five different velocities (at similar concentration) and the result was normalised to the initial value and compared to the normalised mean particle size. The results are plotted in figure 6.13.

A direct and clear relationship can be seen to exist between these two quantities. This not only suggests that this variation may be successfully calibrated out (the inverse of figure 6.13 being used as a calibration curve) but also proves that brightness variation is the only source of this error and that no other factors are involved.

Figure 6.14 shows normalised brightness variation compared to normalised mean particle size for sand. Whilst the shapes of the curves are different to those seen in figure 6.13 they are similar to each other and calibration can be performed here also. It should be noted that calibration would be different for the two materials, reflecting their different optical properties.

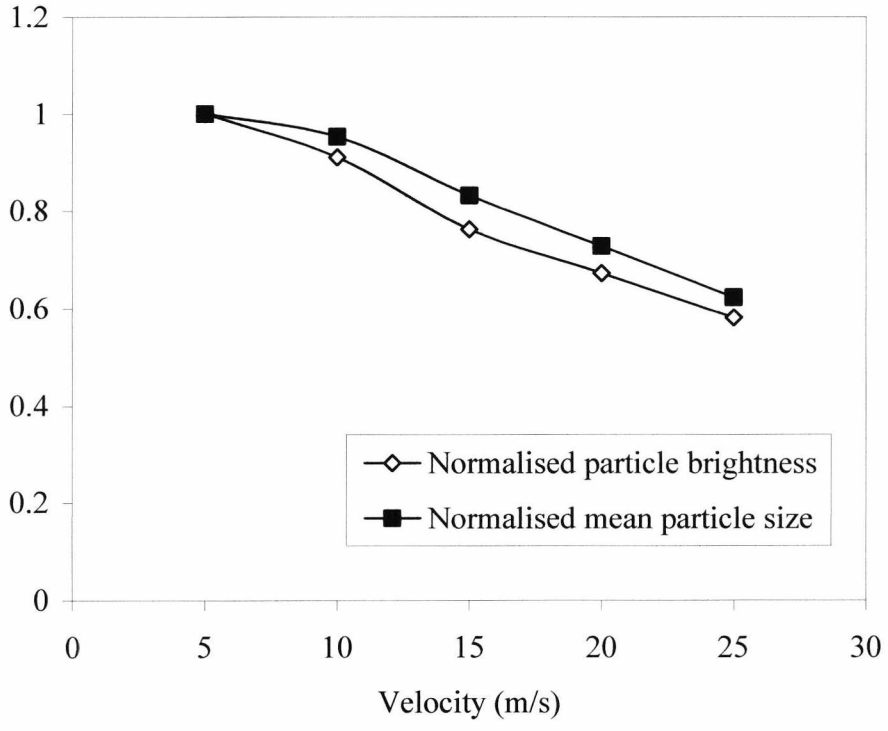

Figure 6.13 Particle brightness/size comparison as a function of velocity

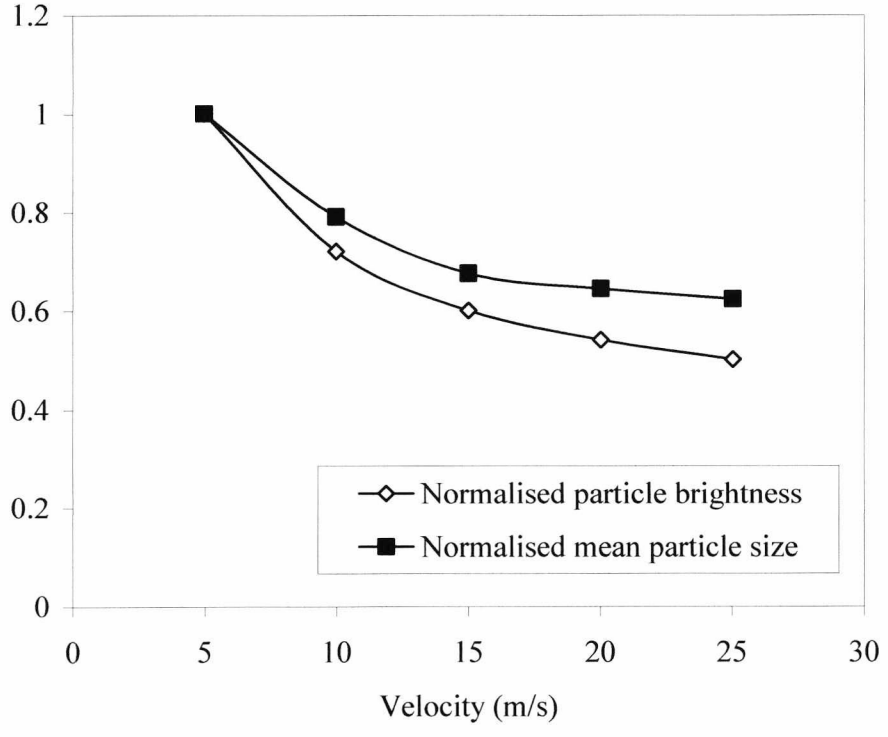

Figure 6.14 Particle brightness/size comparison, as a function of velocity, for sand

As discussed in previous chapters the automatic camera control was not the only system designed to cope with variations in the particle images. Automatic threshold adjustment was also intended to reduce immunity to such changes but it would appear that this is not capable of adjusting for changes of such magnitude (possibly due to the limited dynamic range afforded to it due to only eight bits of resolution per pixel). Despite this, automatic threshold adjustment has shown itself to be an invaluable tool for consistently and systematically defining realistic threshold values in the first instance, allowing simplified and consistent experimental set-up.

6.4.3 Comparison between Static and On-line Results

Whilst the fundamental accuracy of the imaging system under static conditions has been assessed already in previous chapters the on-line comparability of results to those generated by other systems and indeed the comparability between on-line and static operation have yet to be assessed. Figure 6.15 gives a comparison of the results recorded by the off-line laser diffraction based system and the on-line imaging system. The on-line results shown here represent the mean result from all four 5m/s experiments, these being the slowest available and therefore closest to the low speeds at which particles move through the laser diffraction system.

It can be seen that there is a very good general agreement between these results. Any discrepancies are shown more clearly, in the form of absolute discrepancies, in figure 6.16. These discrepancies cannot be described as errors since neither of the systems can be considered as 100% accurate thus they are simply variations between the results generated by different instrumentation systems each using a different sample of the same material. It should be noted here that both of these systems make 'in-flight' particle measurements and are therefore expected to generate comparable results. Discrepancies here can be seen to be within ±2.5% for each size group.

Figures 6.17 and 6.18 show the results for sand. Again, the general agreement is good. There is a larger peak variation here, approaching -4.5%. This is thought to be related to the fact that the range of sizes in the material extends below the range detectable by either system and it is uncertain how the laser diffraction results reflect this.

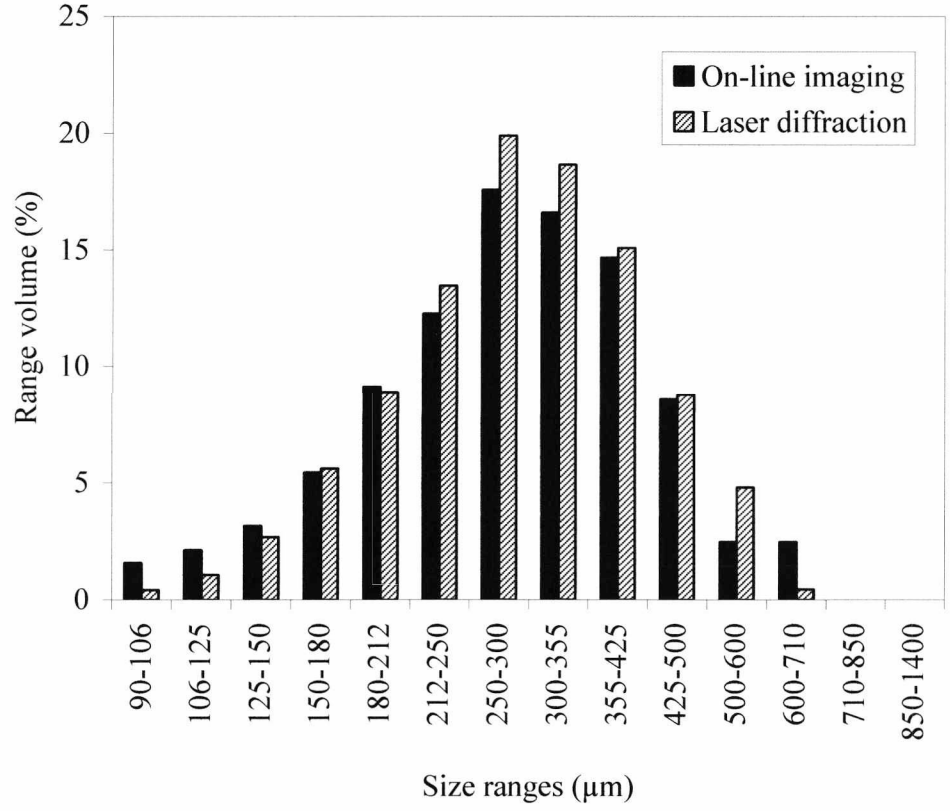

Figure 6.15 Comparison between on-line imaging and off-line laser diffraction results

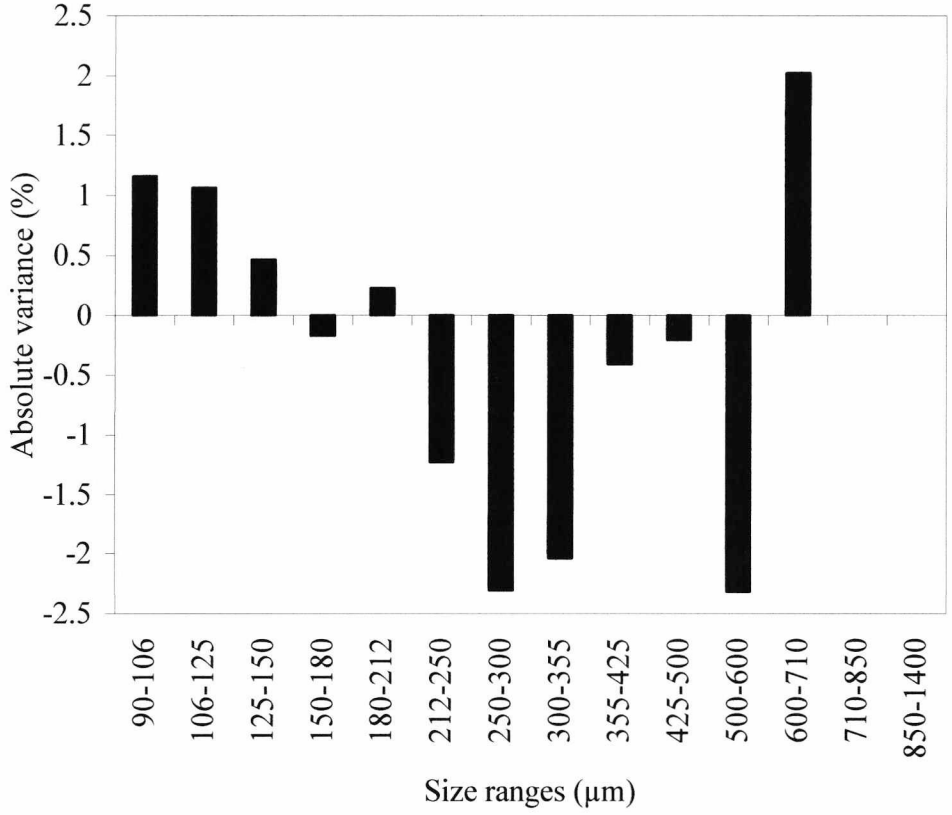

Figure 6.16 Discrepancies from figure 6.15

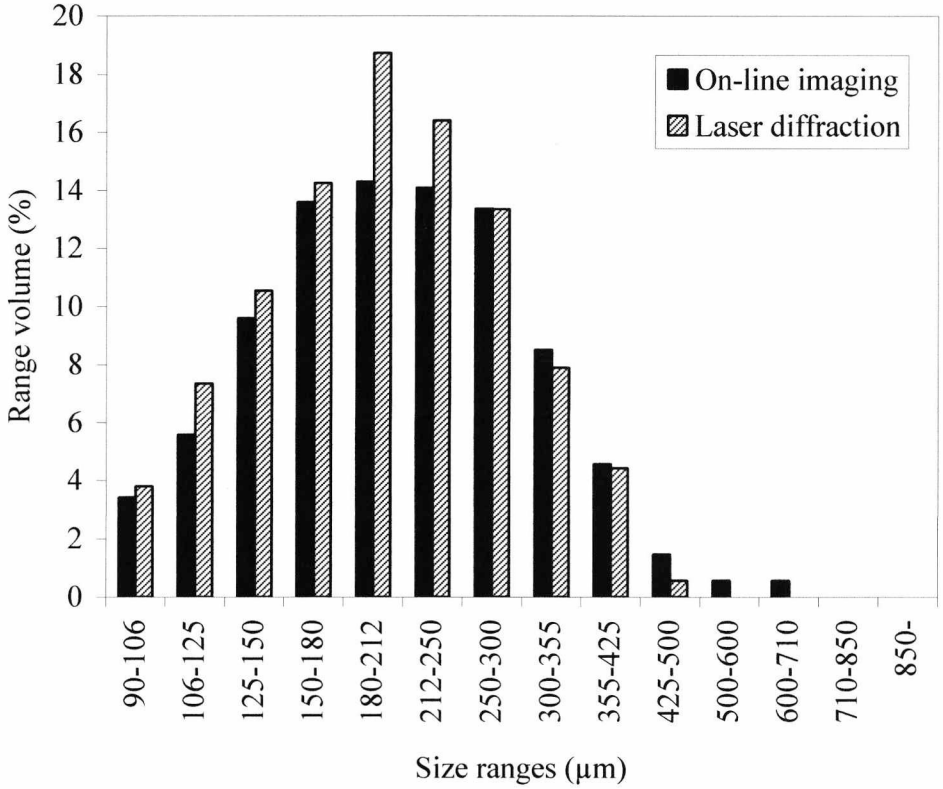

Figure 6.17 Comparison between on-line imaging and off-line laser diffraction results for sand

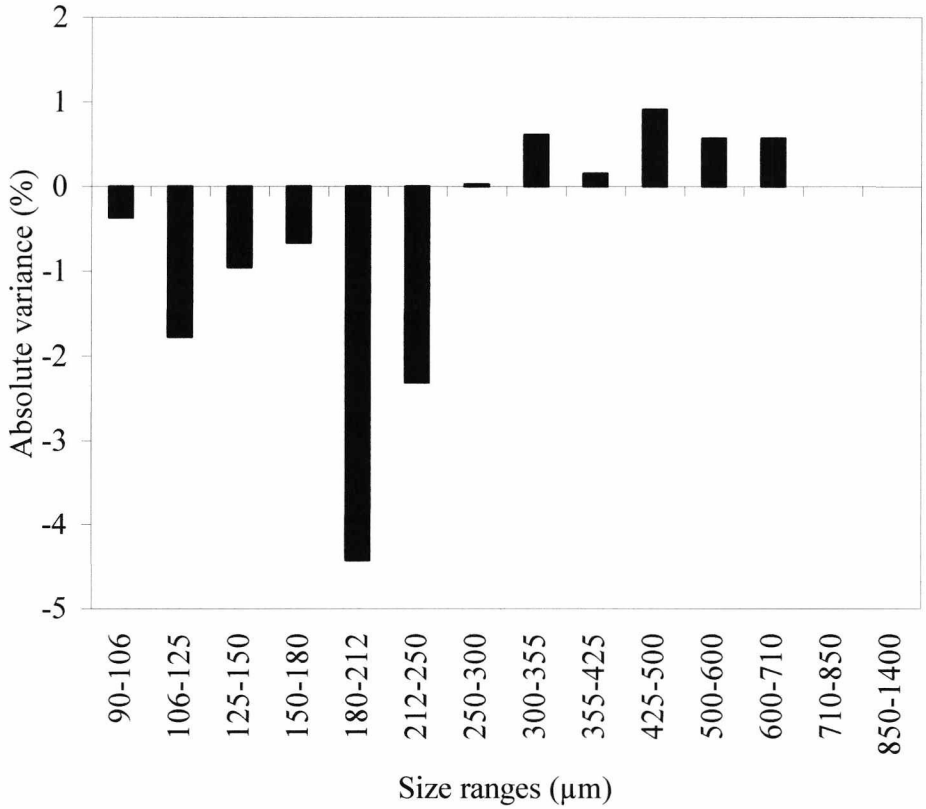

Figure 6.18 Discrepancies from figure 6.17

Since the 5m/s imaging results used here are evidently similar to those generated by the laser diffraction system it is reasonable to assume that this velocity yields correct results. The shift towards smaller perceived particle size experienced for higher velocities should not, in this case, produce the opposite effect for lower speeds. This suggests that the automatic camera adjustment must have reached its limit of control at 5m/s and be incapable of producing brighter particle images at lower velocities. This hypothesis will be investigated later (section 6.4.5).

The next comparison to be made is between on-line and off-line (static) imaging based measurements. This measurement is not expected to be comparable since the on-line measurement observes 'in-flight' particles and the static arrangement does not. These results are presented in figure 6.19.

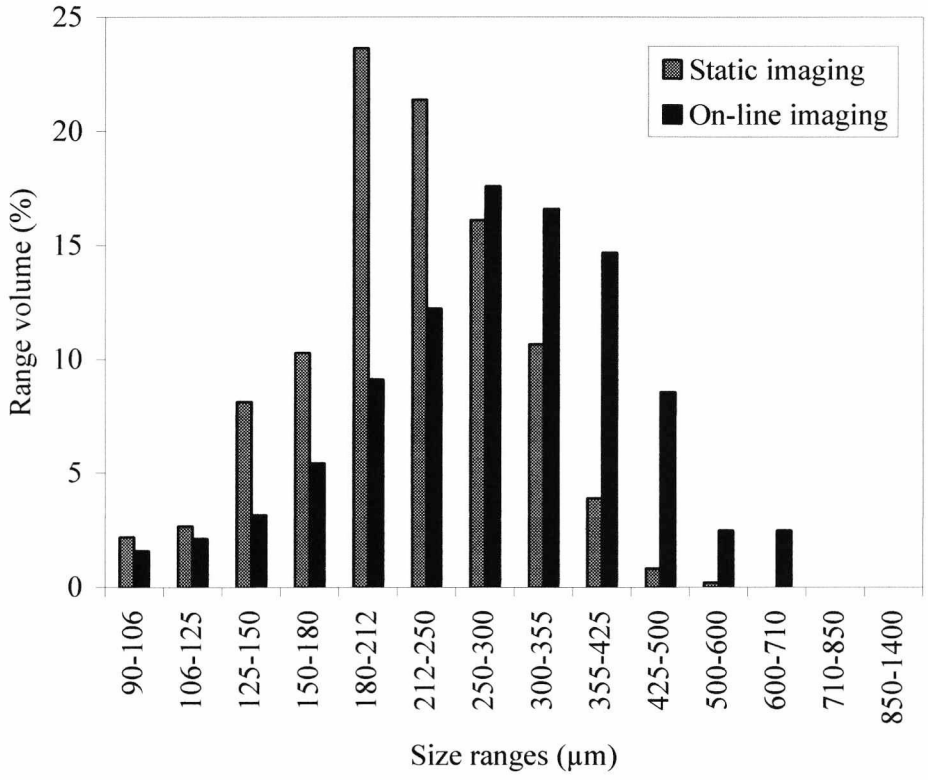

Figure 6.19 Comparison between on-line and static measurements

As predicted these measurements are not directly comparable. At first glance these results would seem to be the opposite of what is to be expected: under static conditions particles might be expected to lie flat thus presenting their largest side to the camera but in figure 6.19 the static particles appear smaller. It is believed that, whilst in the case of 'flake

shaped' particles this would always be the case, for the salt particles used here (which are crystalline and almost square) there is an equal chance that they will stand on end thus presenting their smallest side to the camera. The presence of such upright particles will cancel out the effect of those which lie flat. During the in-flight measurements it is unlikely that particles will travel lengthwise on (or broad side on) but rather will constantly spin about their centre of mass due to rotational energy gained during collisions with the duct wall and between each other. This will lead to an averaging effect in particle size making it impossible for the smallest face of a particle to be viewed on its own. Measured particle size will thus represent the mean size during rotation and, in general, particles will appear larger during in-flight measurements. This phenomenon can account for the results shown in figure 6.19 and is interesting in that it proves that there is particle shape dependence in both forms of measurement. It can be readily imagined that perfectly spherical particles will not be susceptible to this effect.

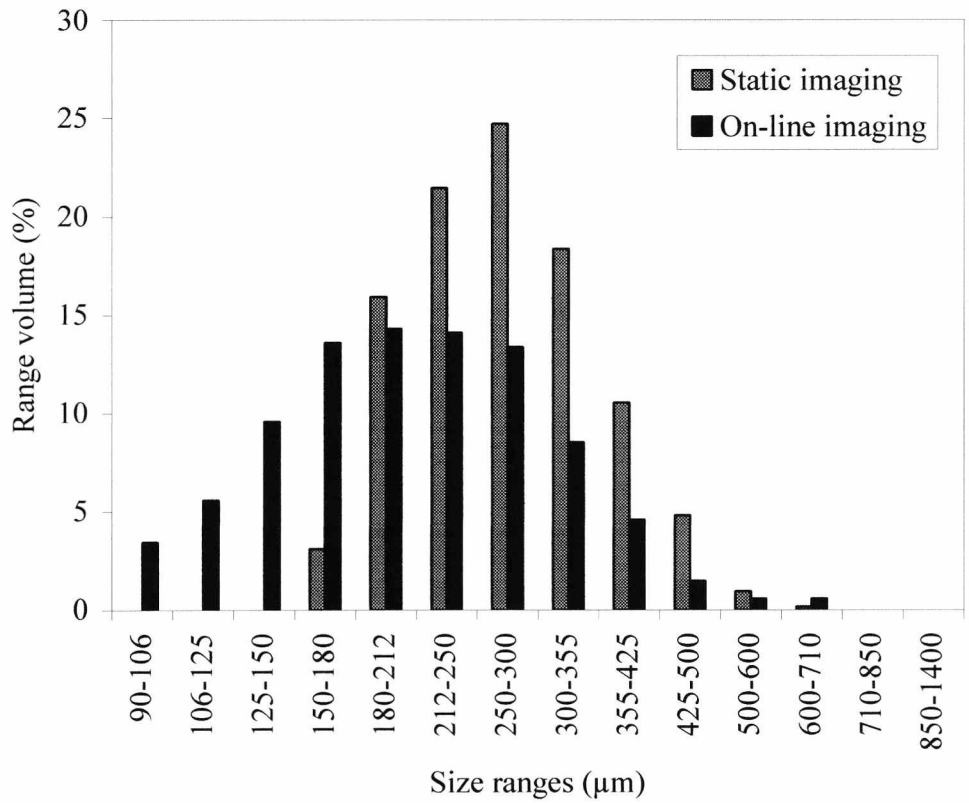

Figure 6.20 Comparison between on-line and static measurements for sand

Figure 6.20 shows a similar comparison for sand. It should be noted that for particles having a greater tendency to lie on their largest side they would indeed appear larger when stationary as initially assumed and this appears to be the case here as the static

result is showing larger numbers of larger particle sizes. In section 6.4.1 it was stated that shape measurements yielded identical results for the two materials and as both materials were very similar and graded to similar sizes this was understandable. The results shown here, however, suggest that the two materials are of different shapes thus allowing some particles to stand on end for salt but all the particles to lie flat for sand. In reality this is easily understood since through practical experience the salt is known to be a crystalline material that is very 'squared' in shape whereas for the sand this is less pronounced resulting from the square corners being softened from wear. This is illustrated in figure 6.21, showing particle images taken from the experiments resulting in figures 6.19 and 6.20.

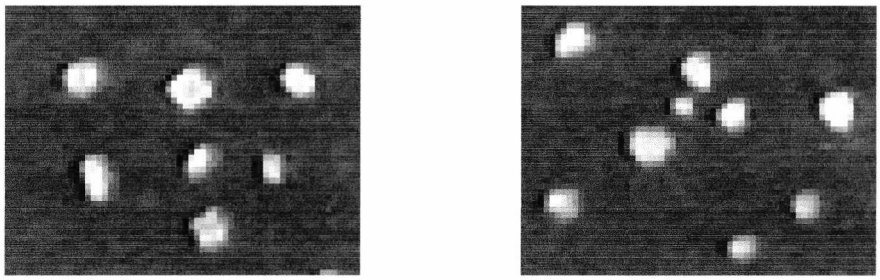

(a) Salt (b) Sand

Figure 6.21 Static material images

It is apparent that the tendency for corners to be softened for the sand is very slight and this, coupled with the small number of pixels representing each particle, explains why no differences were recorded in shape measurement (this function being designed to highlight more fundamental differences in shape. Such minor variations would be swamped by image quantisation effects – see chapter 3, section 3.4.4). It is interesting to note here that such a small change in particle shape can affect the results so dramatically. This interrelation of parameters is only found in static measurements, being irrelevant when particles are in-flight. This could lead to the argument that in-flight measurements are more valid than static results since they find the spatially averaged particle size but it could also be said that the static measurement gives a truer representation of the range of sizes within the material sample. Looking again at figures 6.19 and 6.20, despite the large variation between recorded distributions, it cannot be said that either measurement is wrong but simply that on-line and static approaches view the particles in different ways, each excelling in a particular way. In some situations the rotationally averaged in-flight

measurement might be more appropriate and in others the more accurate representation of actual physical sizes present in the sample provided by static interrogation might be preferred. In general it is interesting to observe and study this behaviour in the systems and it should be noted that this observation and direct comparison between in-flight and static measurement is only made possible by the imaging based approach.

6.4.4 Repeatability/Reproducibility

So far various size distribution results have been presented in which there are slight variations between measurements. The shift in particle size with changing velocity was clearly erroneous and the source of this error has been identified and explained (section 6.4.2). The variations between measurements taken at different concentrations are smaller, however, and may be simply due to accuracy limitations imposed by the fundamental repeatability of the measurements. Such limitations are not necessarily related to the instrumentation system itself but may be the result of natural variation in the material sample as the material used for the tests cannot be expected to consist of exactly the same size distribution throughout a series of experimental runs.

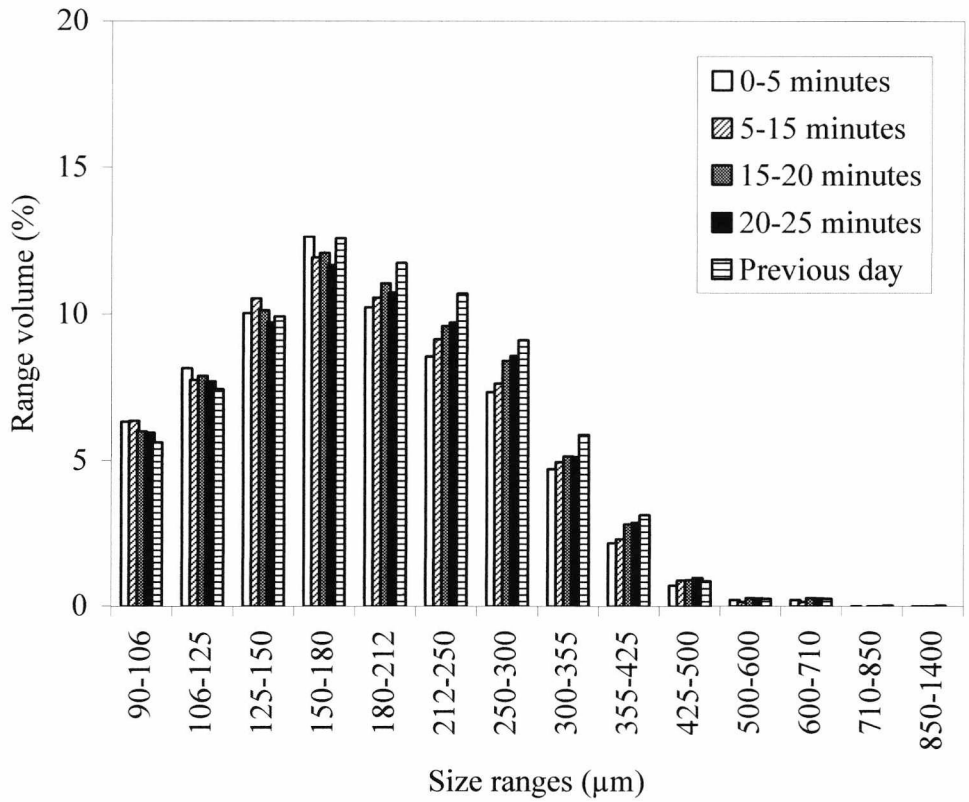

Figure 6.22 Long time run distribution variation and reproducibility

In order to assess the repeatability of measurement a long run of 25 minutes was performed at fixed concentration and velocity settings (1% 10m/s) and the mean size distribution recorded every five minutes. These results are shown in figure 6.22 where the previously recorded 1% 10m/s result (from the previous day) is also shown in the interests of establishing reproducibility. It should be noted that the fact that at 10m/s the result is shifted towards small particle size is of no importance here since it is relative changes between results taken under unvarying conditions that are under examination.

It can be seen in figure 6.22 that the agreement between results is good and that the variations here are of similar magnitude to those observed between distributions taken at varying solids concentration levels. This provides confirmation that the system is insensitive to changes in solids concentration, any variation lying within the natural levels imposed by fundamental system repeatability. Reproducibility is also good showing little variation from one day to the next. Particle sizes do seem to be slightly higher for the previous days result, however, and in fact there may be a very slight trend toward apparent particle size increase during the 25 minute run. It is believed that this can be attributed to an actual increase in particle size due to settling affects in the hopper during the run. As salt is extremely free flowing it is fair to assume that it would be susceptible to such effects. Further confirmation can be derived from the fact that the previous days result was achieved at the end of a series of runs using material left in the hopper but for the 25 minute run the hopper was freshly charged. The previous day's result was thus taken with the largest sizes of material that had settled out during the day and represents the ultimate result of the trend that was observed in the 25 minute run. It should be noted that the apparent particle settling trend is very slight and despite this the repeatability and reproducibility appear good.

During similar testing sand produced very similar results to those for salt and so will not be presented here. General agreement was good and slight evidence of material settling from one day to the next was seen (as before – see above).

It is more usual to assess repeatability by calculating the normalised standard deviation of results and this is presented, for the on-line and static imaging systems as well as the laser diffraction system, in figure 6.23.

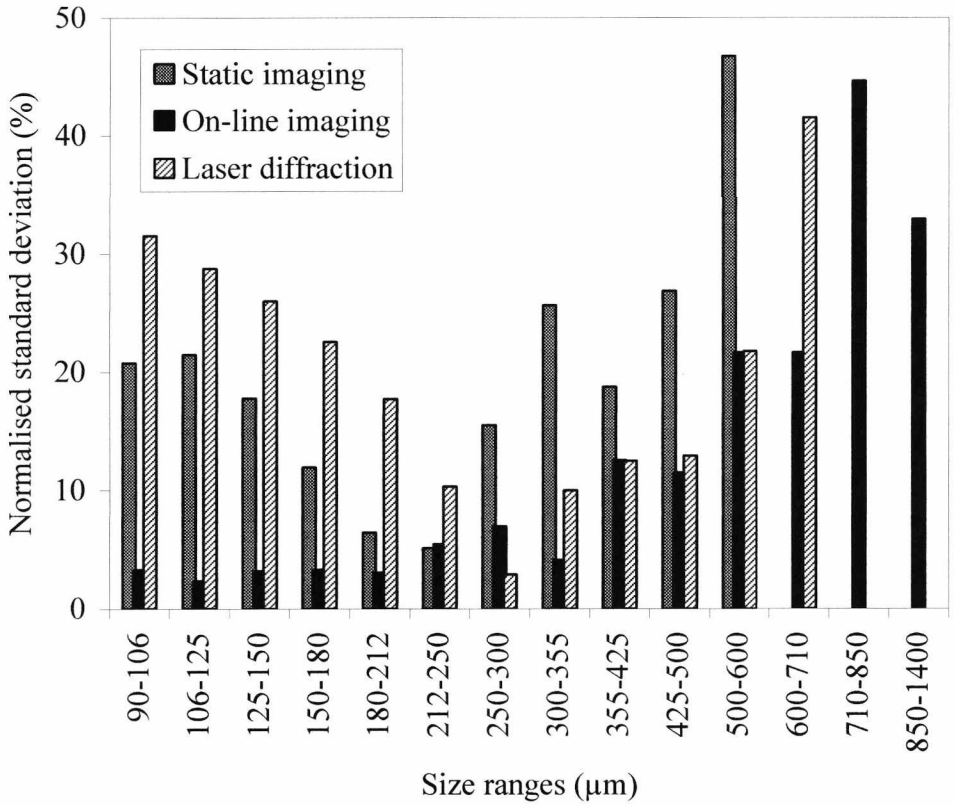

Figure 6.23 Repeatability

The first point to be made is that, in general, the normalised standard deviations appear high. This is to be expected since material will vary slightly from test to test and identical results cannot be expected. Both the static imaging and laser diffraction system show a similar tendency towards deviations that take the form of the inverse of the particulate size distribution (remembering that the static result is shifted to the left slightly). This can be explained by the fact that at the extremes of measurement (i.e. where the distribution curve is trailing off) there are less particles being interrogated than for the peak size ranges. This causes the results to be less averaged at the extremes implying that there will naturally be greater variation. In general the static imaging system and laser diffraction approach seem to give similar magnitudes of deviation. Of greater interest here is the on-line system result. At first glance it would appear to show a different trend to the others since there is no increase in deviation at the low end. In reality this is caused by the fact that the size distribution used was taken at 10m/s and hence shifted to the left so that the lower particle sizes do not show. This means that the 'trailing off' in distribution is not visible here. In figure 6.22, where the source distribution is shown, it can be seen that the lowest bar, 90-106μm, is roughly equivalent in size to the 300-355μm bar and that the

increase in standard deviation at the high end does not begin until the 355-425μm bar. This confirms the empirical observation that the lack of 'low end trail-off' is responsible for the seemingly anomalous deviation result. The use of the 10m/s result, with a broader distribution, is actually fortuitous in that it provides a wider range of distribution bars representing significant numbers of particles – from 90-106μm to 300-355μm. Within this range there is a peak in size, the 150-180μm bar being of nearly twice the size of the outer two, but this peaking in distribution is not mirrored by a trough in the standard deviation result. It is believed that this is an indication that for bars larger or equal to the size of the 90-106μm and 300-355μm ranges the deviation generated is the result of fundamental system repeatability whereas the other bars are swamped by the effects of distribution 'trail-off' (the absolute bar magnitude cannot be applied to the other systems since relative magnitudes vary with changes in distribution). Thus the use of the wide 10m/s distribution allows the actual repeatability limits to be studied, in this case indicating a mean normalised standard deviation of around 4% within this range. This is roughly equal to the minimum deviations generated by the other two approaches. It is probable that these variations of around 4% are the result of natural variation in the materials used. The in-flight nature of two of the approaches cannot be blamed since the static system shows variations of similar magnitude. When using controlled test images (see chapter 3) the static system yielded standard deviations in the fractions of a percent range and so it is reasonable to suggest that the higher deviations here are due to variation in the material. Despite this effect the study of normalised standard distribution has shown that, under realistic conditions, deviations of around 4% may be expected.

When testing with sand the results observed were very similar to those above (figure 6.23), supporting the observed mean normalised standard deviation result of around 4%. The distribution 'trail-off' effect was also present as both materials were graded to similar size ranges.

6.4.5 Mass Flow Measurement

The mass flow rate measurement technique employed by the current system is inferential in nature and limited in performance by two main factors. Firstly, the fundamental limitations of the spatially averaged cross-correlation based velocity information,

provided by the electrostatic sensor, will affect results. Whilst highly repeatable, cross correlation velocity is not necessarily representative of true spatially averaged velocity and may be susceptible to non-linearity, especially at higher velocities (Ma and Yan 2000). The second issue, leading to low confidence in the inferential technique employed here, is the automatic control, over shutter speed and gain, used by the present camera. It has already been seen that this automatic control has affected the results (see section 6.4.2) and so it is reasonable to expect that it will continue to do so here – if the shutter speed is being set to low then some form of volumetric averaging of the solids concentration data may be achieved, (see later in this section) leading to large offsets in the mass flow data. In view of these issues extreme accuracy in this measurement was not expected, the likelihood of offsets and non-linearity being high. Despite this it is still important to investigate inferential mass flow rate measurement here, not least because the study of this parameter allows the accuracy of solids concentration measurement to be assessed through a process of reverse calculation. Offsets may also be calibrated out and, if non-linearity is small, useful measurements may still be made despite the limitations of the low cost camera. A direct comparison between measured and actual mass flow rate is shown in figure 6.24. This result is raw and uncalibrated and so the issues discussed above must be remembered.

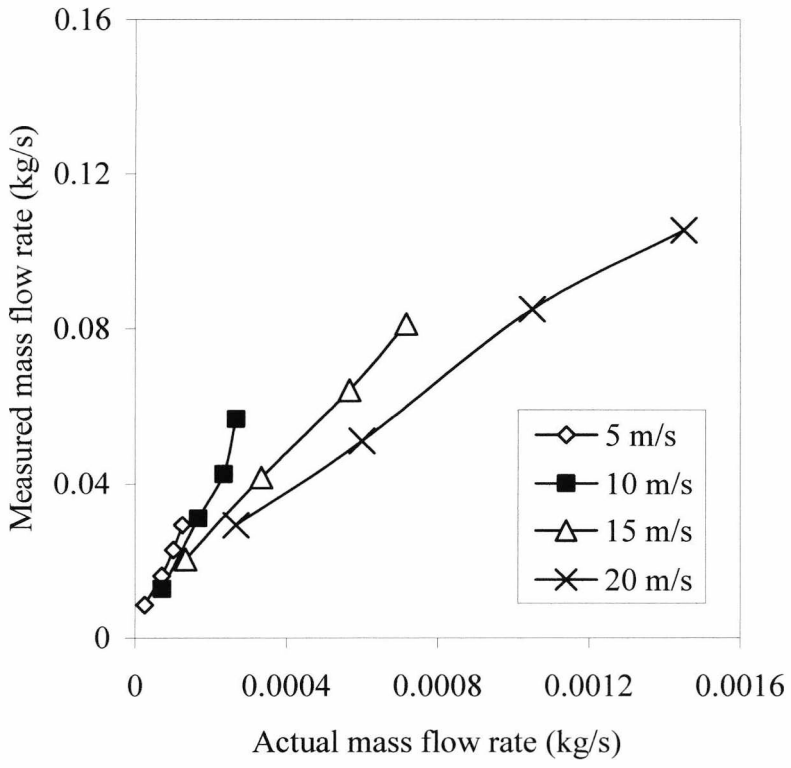

Figure 6.24 Direct comparison between measured and actual mass flow rate (raw)

It is clear that mass flow results are far from ideal. As predicted there is a large offset in the measured result and also a certain non-linearity. These problems will now be dealt with in turn.

The most striking error in the results is the large offset. Mass flow rate information is derived from the combination of solids concentration, velocity and absolute material density. Density is a known and constant value and so cannot be responsible for the offset whilst velocity measurement, though known to be a spatially averaged mean value, cannot possibly be inaccurate enough to account for an error of this magnitude (Ma and Yan 2000). This leaves solids concentration, where the source of the problem must lie. The system is measuring solids concentration as being much higher than it is. As already stated it is possible to work backwards using actual reference mass flow data to find accurate solids concentration information. This result is shown in figure 6.25 where actual (derived from actual mass flow data) and measured (as measured by the imaging system) solids concentration are compared at each of the velocities employed.

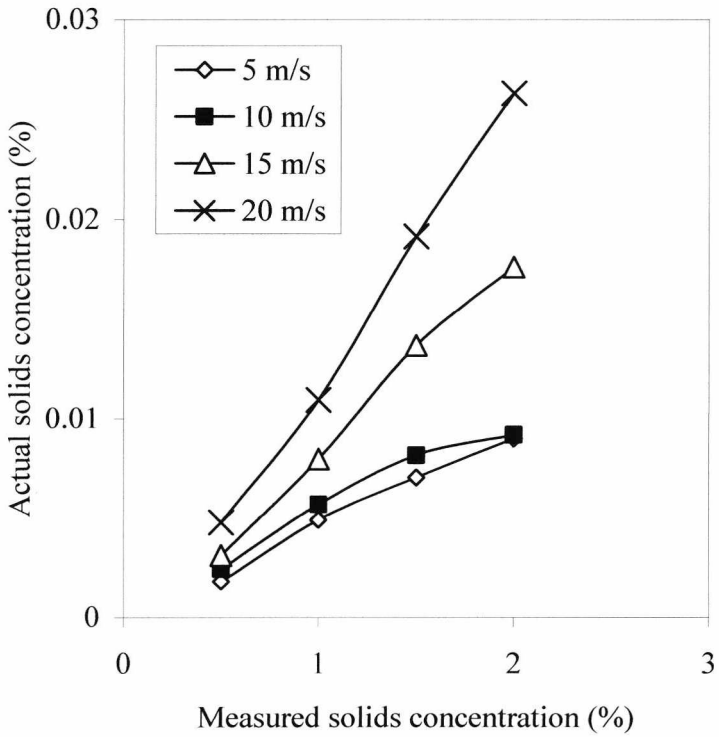

Figure 6.25 Measured against actual solids concentration (calculated)

The offset of approximately 100 times is accounted for here. It should be noted that the curves shown suffer from non-linearity and it must be remembered that the derived actual solids concentration relies upon cross correlated velocity data. It is believed that these nonlinearities are due to limitations inherent with cross correlated velocity instrumentation. These will be discussed later as it is the general trends and dependencies that are of interest here. It can be seen that each concentration suffers from both a large offset and a velocity dependant increase that is roughly logarithmic in nature. This can be better appreciated in the rearrangement of results shown in figure 6.26. Note that the 10m/s 2% point is low due to the irrelevant nonlinearities already discussed.

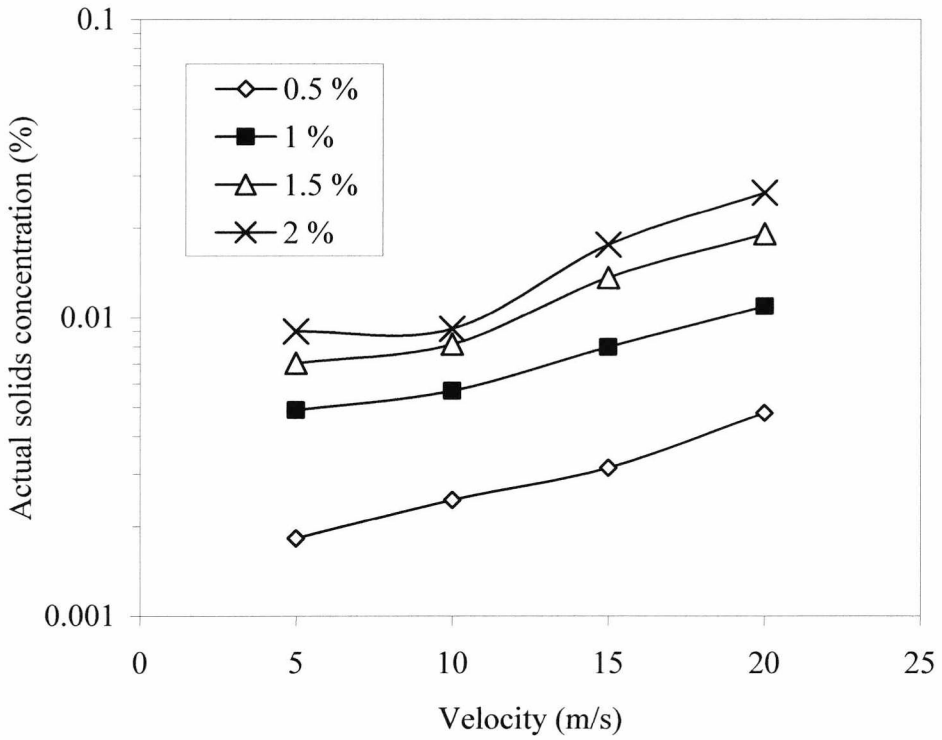

Figure 6.26 Rearrangement of figure 6.25 highlighting logarithmic velocity dependence

In summary, an explanation is required that not only sheds light on the fact that solids concentration is perceived, by the imaging system, to be considerably higher than it is but also on the velocity dependence that can be seen above. Such an explanation may be found readily, but first a short recap. on the method of solids concentration measurement employed here, is called for.

Generally, solids concentration is derived from volumetric data and is equal to the ratio of solids volume to empty space volume in a duct, expressed as a percentage (see chapter 1).

For the imaging system, operating in only two dimensions and having, in theory, no knowledge of depth and therefore volume, this definition is revised to the ratio of solids area to total area in each frame, expressed as a percentage. It can be shown mathematically that volumetric and area based solids concentration are comparable if the two dimensional image used for the area based method represents an infinitely thin slice through the flow. The time averaged area based concentration would then give the same result as the instantaneous volumetric method if the same volume were interrogated (this would take place in one measurement for a volumetric system and over a period of time for the area based system). In a practical situation it is impossible to illuminate infinitely thin slices within the flow and indeed to interrogate all of the possible slices, there being frame rate limitations imposed by the camera and processing equipment.

The concept of solids concentration may be applied to any vessel or volume containing some unknown quantity of material. Such material may consist of a single piece or body in which case infinitely thin slices would certainly be required in order to accurately calculate the solids concentration by the area method. In practice, as infinitely thin slices are impossible to measure, discreet steps could be treated with simple area processing and if a sufficient number of steps were used the error would be insignificant. In the case of particulate flow the material is already in the form of tiny discreet bundles and so it can be readily appreciated that accurate solids concentration information can be derived through the area method if the slices used are no thicker than one particle diameter. In the case of dilute phase flows this requirement should be able to be further relaxed as the spacing between particles is large (as the present system is suitable for concentrations by volume of up to two percent, which is considered dilute, there will be considerable space between particles). If the slice thickness is too large, however, there will be significant error in the solids concentration measurement. This flow slice size dependence, for particulate flows, is best illustrated diagrammatically – see figure 6.27.

The slices (marked 1 and 2) in figure 6.27 are the thickness of one particle diameter. If these slices are interrogated individually then the solids concentration result will be correct (note that in this case, as in a steady homogeneous flow, the solids concentration in each slice is representative of that at any point within the duct and therefore continuous interrogation of all possible slices is not required). If the interrogation system were only

capable of selecting slices of twice this thickness, i.e. slices one and two would be treated as a single slice, then the perceived solids concentration would be twice its actual value.

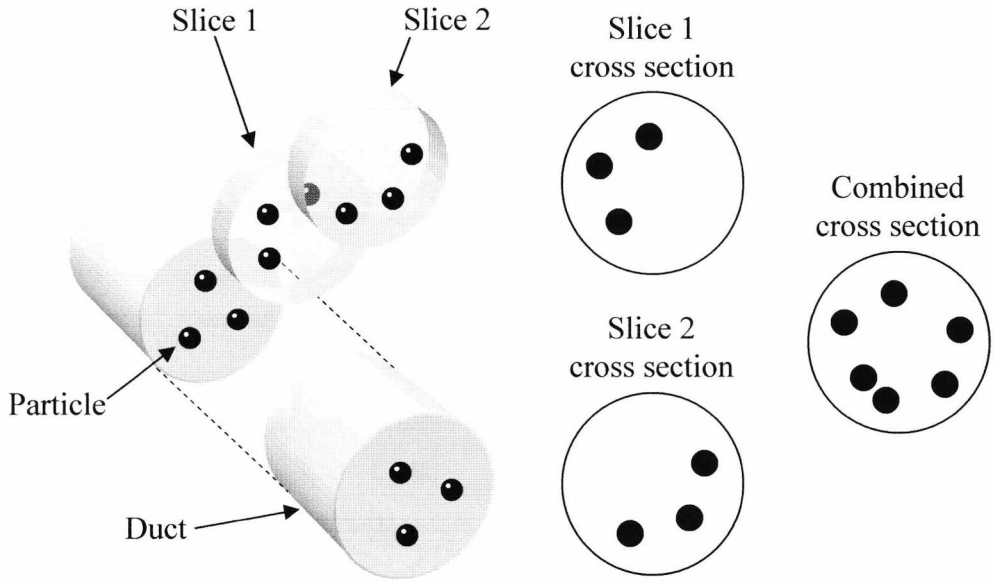

Figure 6.27 Flow slices

Although the area based method works from a two dimensional perspective the 2D particles in each image would represent two distinct depths within the flow and so the measurement would become volumetric. The error generated by excessive slice thickness will be constant if the thickness of the slice is constant and may be calibrated out. If the thickness of the slice is known then the solids concentration measurement may be treated as a volumetric one and so the error will not exist. In either case there is the possibility of closer particles obscuring deeper ones but, as with static measurements, this will not be a significant issue if sufficiently dilute concentrations are used.

The large offset in the solids concentration results generated by the imaging system is believed to be due to this slice thickness effect. More specifically it is due to the fact that a CCD camera (or any other camera) does not generate an instantaneous image, but rather allows an image to build up over a period of time known as the exposure period, the inverse of which is the shutter speed. In the present work a standard camera that adjusts its shutter speed automatically was employed (for reasons of establishing the limitations of imaging technology when used with cost-effective and readily available equipment) and so the time taken to generate each image, and therefore the depth of the image derived through combination with velocity data, is not known. When the camera was

selected this was known, but it was thought highly probable that, when operating with such dark images as those generated here, the automatic control would saturate selecting the slowest possible shutter speed for all images. Whilst this would result in thick slices it would also generate a constant error that could be calibrated out. The results presented here suggest that the error is not constant and so it can only be concluded that the shutter speed is variable. This hypothesis may be tested by employing the actual solids concentration information, derived through working backward from the reference mass flow data, to establish the error at each data point and thenceforth to enable calculation of the shutter speed required in order to generate this error. The results of this analysis (which assumes that the minimum possible slice thickness is equal to the mean particle diameter) are shown in figure 6.28.

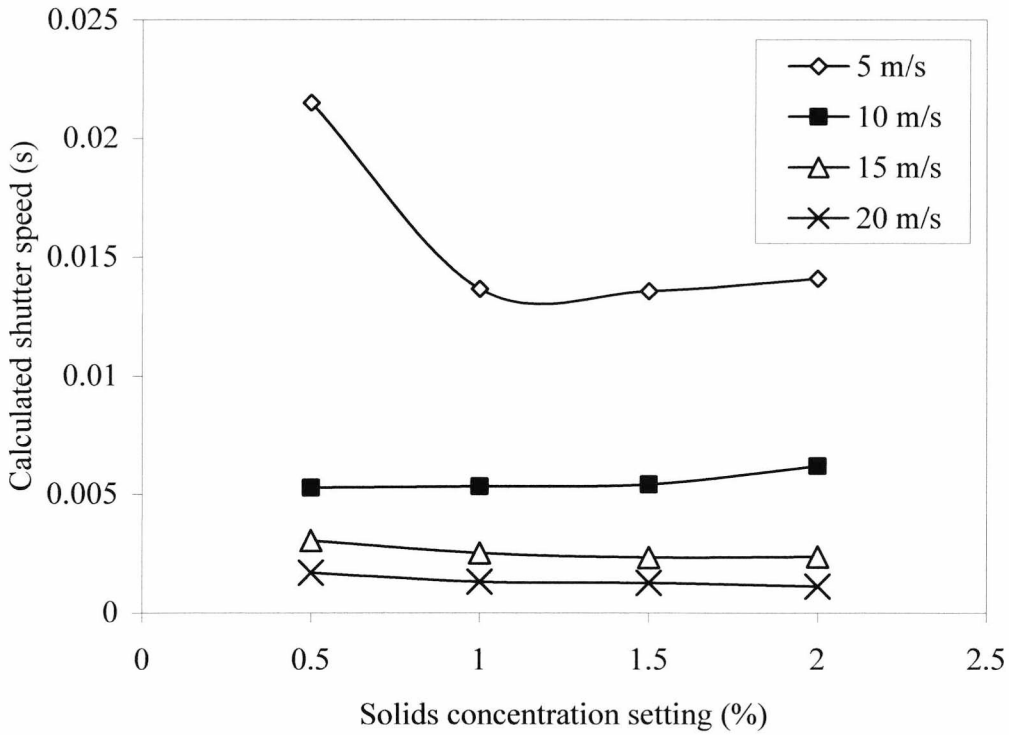

Figure 6.28 Calculated shutter speed against concentration at each velocity

The general trend here is that the shutter speed is dependant upon velocity and not concentration. The camera used here is capable of a minimum shutter speed of 1/50 seconds (0.02 s) and a maximum of 1/100000 s (10μs). The calculated shutter speed values are not only within this range but also lie towards the slower end of the scale as predicted. The 5m/s 0.5% point is spurious as suggested in an earlier part of this chapter – the fact that the calculated shutter speed for this point lies above the maximum exposure

time shows that its position is not correct. So far, in order to avoid confusion, sand results have not been presented in this section. It is, however, interesting to note here that sand mass flow results have shown very similar trends. Shutter speed calculation for sand generated similar results to those above, but without the spurious 5m/s data point. This is shown in figure 6.29.

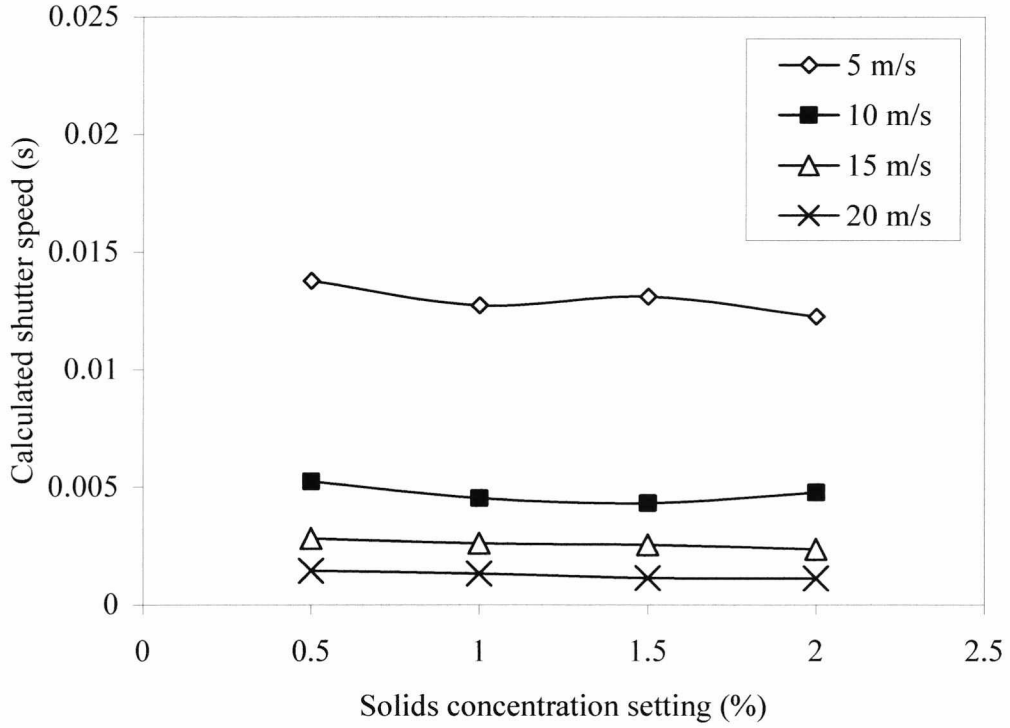

Figure 6.29 Calculated shutter speed for sand showing similarity with Figure 6.28

It is clear that the camera is selecting a different shutter speed for each velocity. This will cause the slice thickness effect, and therefore the solids concentration offset, to vary with velocity. Also this variation in shutter speed is likely to be the cause of the particle brightness variations that were found to lead to velocity dependence in the particle sizing data of section 6.4.1 – the study of mass flow rate has allowed confirmation of the error mechanisms discussed for particle sizing. It should be noted here that the statement made in section 6.4.2 to the effect that 'the imaging software is fundamentally insensitive to velocity change (being unaware of the third dimension)' is still valid despite the volumetric nature of the measurement in relation to shutter speed. This is because the volume interrogated by the system is not interrogated instantaneously but rather over a period of time (the exposure time), this volume being 'swept' by the laser sheet causing a 2D image to build up on the CCD sensor. There are, therefore, no 'depth of field' or

perspective effects, the volume being effectively parallel viewed and transformed into a 2D projection. Fundamental particle sizing conditions are only affected by shutter speed in that its variation causes brightness variation in the particle images (the camera's automatic controls may also be varying the gain which would contribute to this effect) so the slice thickness effect cannot cause errors in sizing information directly.

In general the flow slice thickness effect discussed here is not necessarily a problem once it is recognised and taken into account. In fact this phenomenon allows true volumetric solids concentration to be measured. It also presents the possibility of using an extremely slow shutter speed to enable very low solids concentrations to be accurately interrogated in terms of both concentration and sizing results (the larger number of particles collected in an image during a long exposure time would provide more representative particle sizing at extremely low concentrations). Clearly the automatic controls used by the low cost camera cause difficulties in measurement. Despite this, however, the suitability of the imaging system for solids concentration measurement has been proven so long as shutter speed is known.

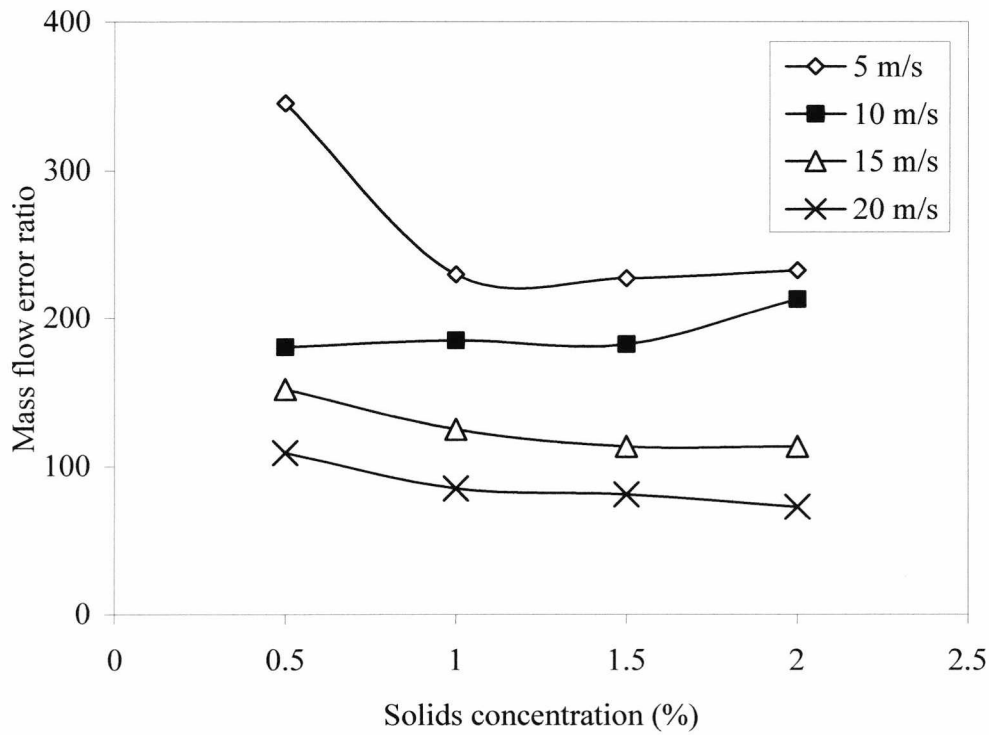

Figure 6.30 Mass flow ratio (measured/actual) against concentration at each velocity

The fact that these shutter speed effects and variations are the sole cause of the large offset in mass flow results can be more readily appreciated when the errors in mass flow rate are presented in terms of a ratio, of measured to actual, against concentration at each velocity. This is shown in figure 6.30 where clear similarity with the shutter speed results of figure 6.28 is apparent.

The source of the solids concentration offset is now clear. Also the variations in mass flow gradient shown in figure 6.24 have been explained as being related to the velocity dependence of sizing measurement that was discussed earlier in the chapter (if particle size measurement is incorrect then similar errors will be created in solids concentration and hence in mass flow rate data). Once the sources of these errors are understood they may be safely calibrated out. This is achieved in the case of the offset by subtracting the mean offset from the data set for each velocity and, in the case of the compounding error arising from velocity sensitivity in sizing data, the sizing error is trimmed out (based on the use of a mean particle size derived from the 5m/s value) and new solids concentration and hence mass flow data calculated (a possible real time calibration procedure). The result is shown in figure 6.31 and relative errors are presented in figure 6.32.

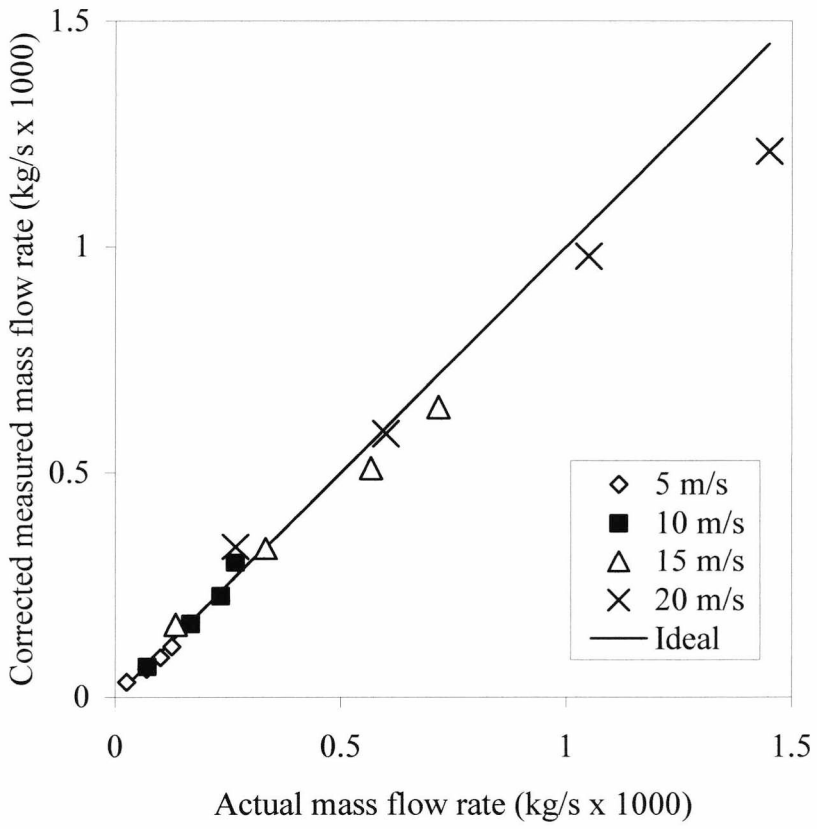

Figure 6.31 Measured mass flow rate with offset and velocity sensitivity calibrated out

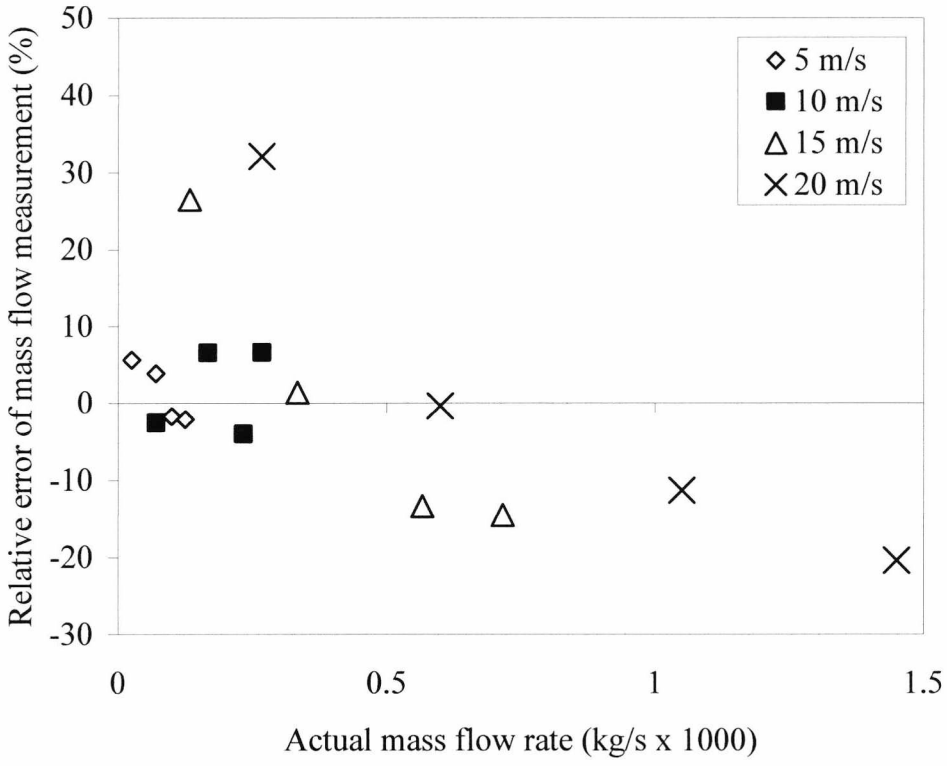

Figure 6.32 Relative errors of calibrated mass flow measurement

It is interesting to note in these results, calculated using a mean size value, that the spurious data points have fallen back into believable positions. This is indicative that the original supposition of the spurious nature of these points, arising from spikes in the original recorded data, was correct. It can be seen that for the 5m/s and 10m/s data, errors are now randomly distributed and lie within about ±5%. This is a fairly high error but is considered acceptable since the mass flow data is a derived value relying on information from two different sources, the errors from which will compound. The higher velocities show more considerable error and it is believed that this is due to inconsistency in the correlation velocity data (Ma and Yan 2000). Since the electrostatic cross-correlation meter is the only source of velocity data it is hard to find evidence to support the supposition that the data is unreliable at higher velocities. It is possible, however, to prove that the electrostatic meter is operating under increasingly variable conditions as velocity increases through studying the 'dust concentration' data recorded by the instrument. These data represent the mean electrostatic field intensity recorded by the instrument and, whilst of little use for concentration measurement (as suggested by the name) due to the variable nature of the charge in the duct (Yan 2001), are representative of the fluctuation in recorded data in relation to velocity. These results are shown in figure 6.33.

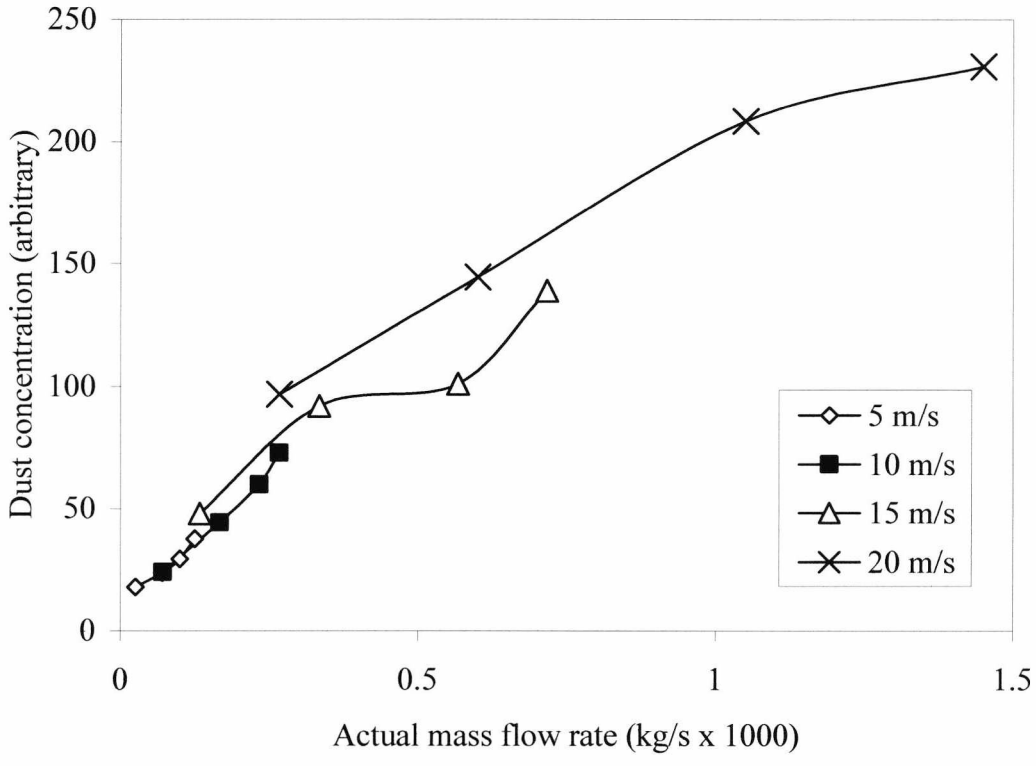

Figure 6.33 Electrostatic 'dust concentration' against actual mass flow rate

It can be seen that there is increasing fluctuation in the data as velocity and concentration increase. There is also some correlation between the discrepancies in the figure 6.31 data and the fluctuations shown here. This provides some confirmation that the electrostatic meter is the source of the remaining errors in figures 6.31 and 6.32.

Mass flow performance with sand as the test material was similar to that demonstrated above and, in view of space limitations, no further data will be presented here. No significant variation between materials was recorded during mass flow measurement apart from the lack of the spurious data point for sand as illustrated in figures 6.28 and 6.29.

The discussion on mass flow rate measurement has introduced a number of dependencies and correlations within the data. So far, however, these data have been taken from a single set of experiments. In view of this it was thought necessary to briefly confirm these trends and dependencies using an independent experiment. Such confirmation will be presented only using salt, due to space constraints, as sand did not generate significantly different results.

The source of the large offset in mass flow rate has been discussed extensively already and so the dependencies of interest here are: the decrease in measured mass flow rate with velocity, the correlation between the decrease in mass flow rate and the decrease in measured particle size and the increasing fluctuation in data at high velocities leading from increasing unreliability in correlation velocity data.

In order to test these dependencies an experiment was performed during which the mass flow rate was kept constant (the material feeder was not adjusted throughout the experiment) and velocity steadily increased. The change in velocity and resulting change in solids concentration is shown in figure 6.34. The concentration was varied from 2% down to about 0.1% during the run and velocity increased from 5m/s to just over 30m/s. The resulting measured mass flow rate, normalised to the highest value (since the offset is of no interest here), is shown along with velocity change in figure 6.35.

It can be seen that measured mass flow rate is, as before, decreasing with velocity, ultimately reaching only a quarter of its initial value. In order to confirm the correlation between mass flow rate and particle size these quantities are plotted in figure 6.36.

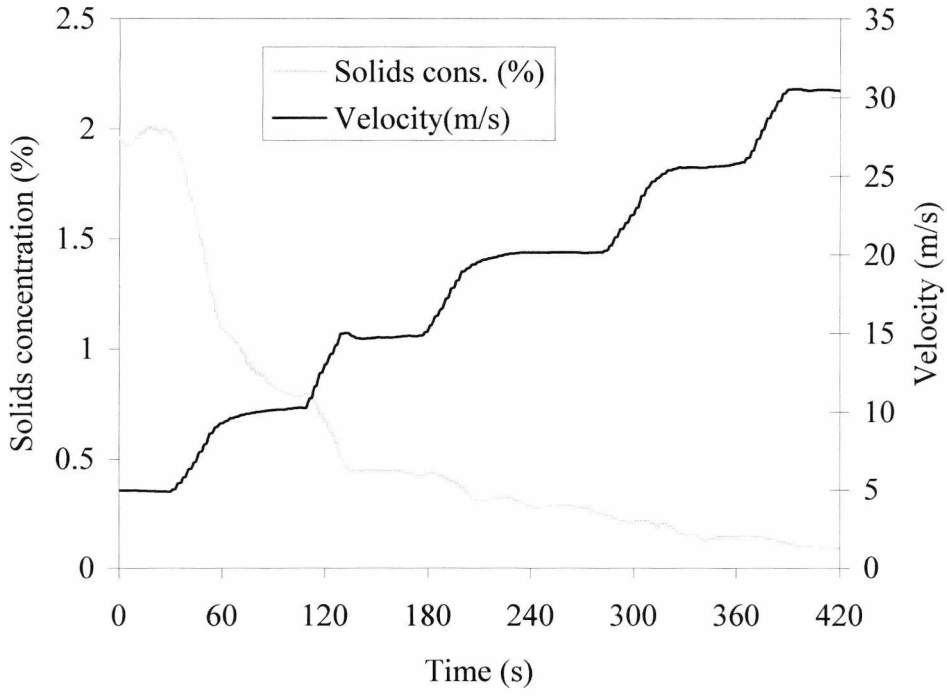

Figure 6.34 Variation of velocity and concentration for a fixed mass flow rate

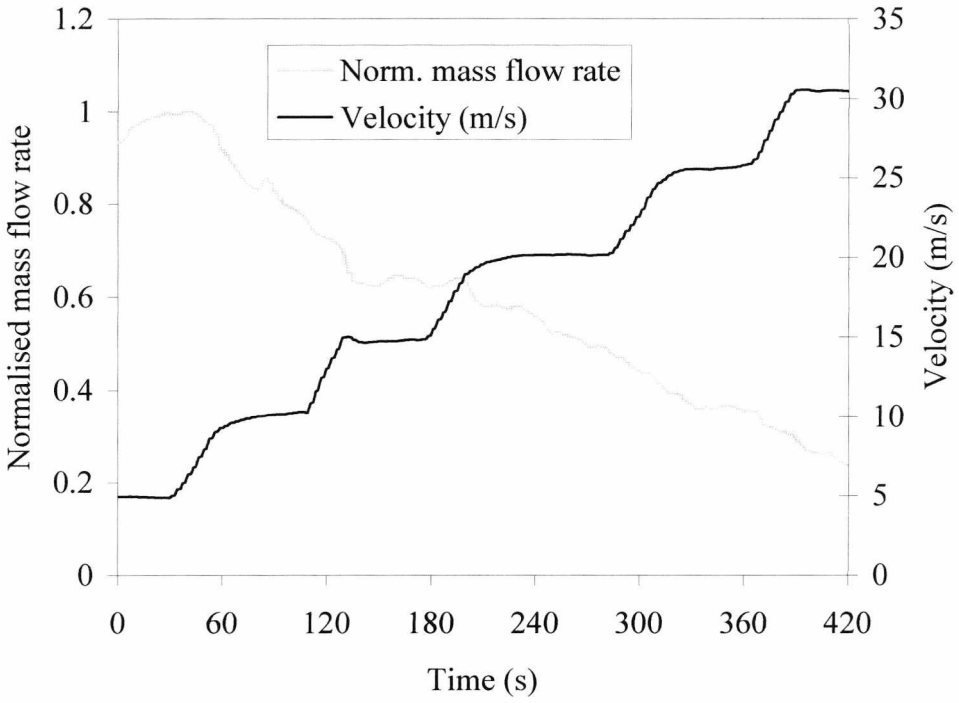

Figure 6.35 Variation of measured (normalised) mass flow rate and velocity

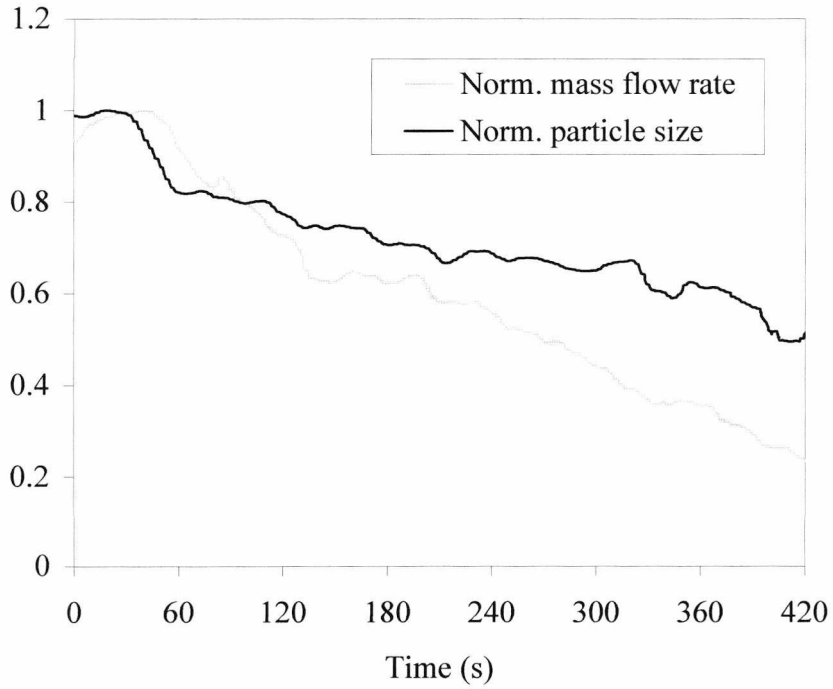

Figure 6.36 Measured (normalised) mass flow rate and particle size

In this graph both quantities have been normalised to their maximum value in order to simplify comparison. It can be seen that there is a good correlation between these quantities, confirming this dependency independently of previous results. The correlation however is not perfect as the mass flow result 'breaks away' from particle size at around 180 to 240 seconds and increases its downward gradient (ignoring variations at the start of the run when the system was still stabilising and considering the gradient and shape of the curve rather than the absolute values). It is believed that this is due to the effects of increasing velocity upon the cross correlation based electrostatic meter. This time frame (referring to figure 6.35) corresponds to a velocity of around 13 to 20 m/s which corresponds with the velocity range at which the cross correlation result became troublesome previously thus confirming this aspect of the previous discussion.

The results discussed here have shown that mass flow derivation has been an invaluable tool for assessing the performance of the imaging system, in particular the variations in data imposed by automatic camera adjustment. However, the reliance of mass flow measurement upon correlation velocity data, limits its usefulness as a measured parameter.

6.4.6 Minimum Measurable Concentration

An important factor when operating on-line is the minimum concentration conditions under which the system will give reliable results. In theory the imaging system will operate at extremely low concentrations where there is only the occasional particle passing the sensor. In practice such conditions would cause difficulties with averaging and it would take an unrealistic amount of time to build up a representative size distribution result. Averaging difficulties at extremely low concentrations would manifest themselves as an erroneously low particle size result due to the large number of image frames containing no particles. If the concentration were to be slowly increased the measured size would increase until a point was reached where sufficient particles were present and the sizing result levelled off to its correct value. If the concentration continued to increase another point would be reached where the size result would begin to increase again, due to particle overlapping, as discussed in previous chapters. In order to experimentally confirm this concentration related behaviour and establish the lower

concentration limit for the present set-up, an experiment was performed. The experiment consisted of establishing a velocity of 10m/s and steadily increasing the concentration from 0 to 10% thus fully covering the range of values expected to be suitable for the present system. The changes in concentration and particle size are shown in figure 6.37.

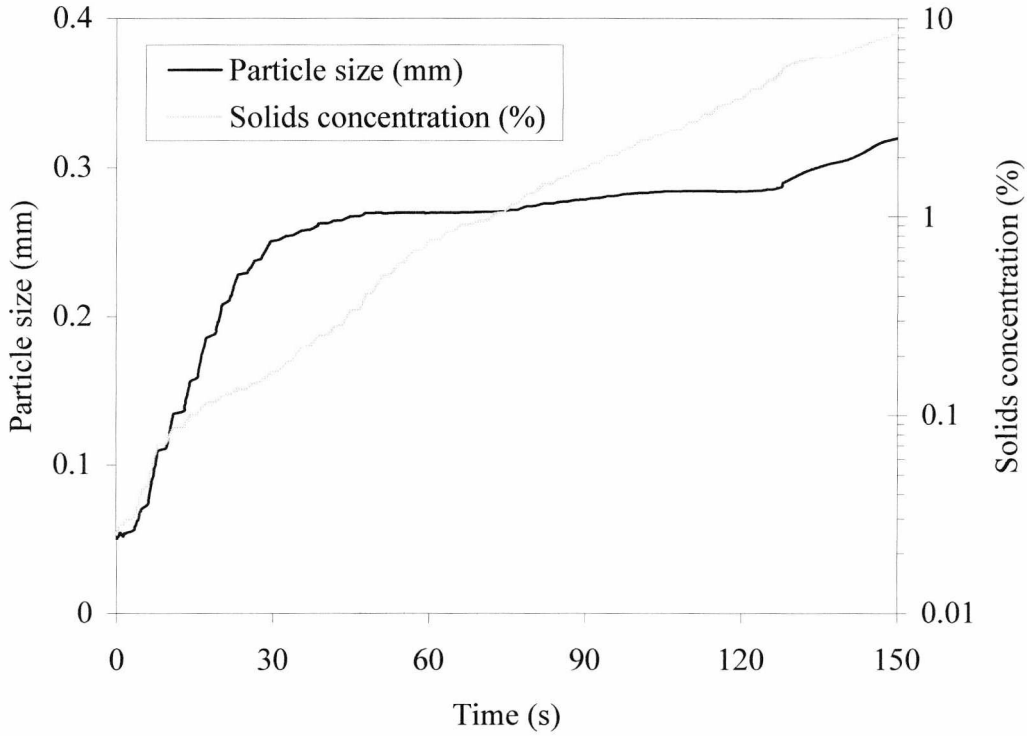

Figure 6.37 Measured size change with extreme concentration variations

It can be seen that the predicted behaviour is confirmed. At extremely low concentrations the particle size is very low as there are sufficient frames containing no particles to affect the rolling average. As the concentration increases this effect is reduced until about 0.3% is reached at which point the size curve levels off indicating that there are sufficient particles for consistent sizing. At the high end the particle size begins to increase again at around 1.5% concentration and at 2%, the maximum limit set previously, the particle size has increased by only 3%: an acceptable error. Figure 6.38 shows size and size uncertainty against time. It can be seen that the size uncertainty parameter gives a good indication of the reliability of size results. This parameter levels off at the same point that size levels off and may therefore be used as an on-line indicator of size data reliability. At the higher concentration limit uncertainty cannot be used as an indicator of result reliability since there are more than enough particles to provide consistent sizing – the

upper limit is imposed due to overlapping effects in the processed images as discussed previously.

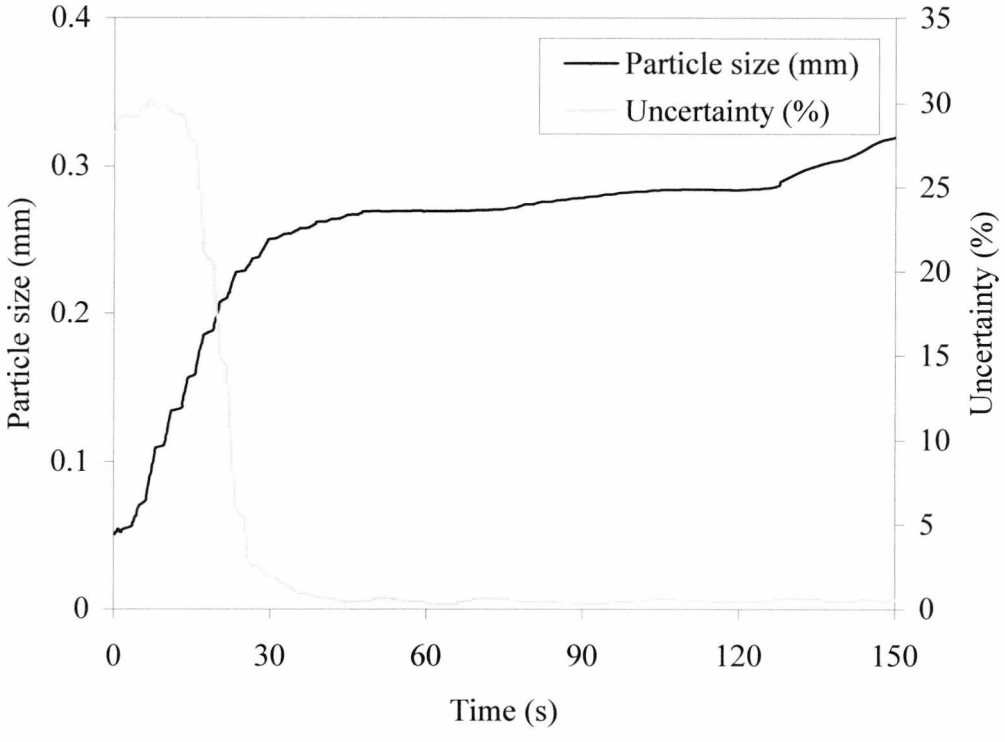

Figure 6.38 Size and size uncertainty against time

These data suggest a minimum concentration of 0.3% and a maximum of 2% giving a turndown ratio of ten. In reality, however, it must be remembered that, due to the slice thickness effect, the lower limit is actually much lower than this giving a much higher turndown ratio. The exact figure for minimum concentration cannot be given here since the shutter speed is not known but, based on the previous shutter speed results (at the lowest concentration and 10m/s), it is probably in the order of 0.015% with the current camera. The use of a superior camera featuring adjustable shutter speed would facilitate the tailoring of minimum measurable concentration to a particular application with a slower shutter speed giving a lower minimum concentration. It should be pointed out that the upper concentration limit demonstrated here will be affected by the slice thickness effect also and so a true 2% upper limit could only be obtained with a camera which could be set to high shutter speeds. Despite the complications imposed by the automatic camera these results demonstrate that the system is capable of a useful turndown ratio and is certainly capable of interrogating industrial lean phase flows which consist typically of concentrations in the 0.1-1% range.

6.4.7 Consistency of Test Conditions

Throughout the results thus far each data set has been presented with velocity constant and varying concentration or vice versa. Data have, for example, been plotted at four different concentrations at four different velocities. Since each data point has required a separate experimental run it is important to provide information on the consistency of parameter setting between runs. In other words, how accurately was the rig set to deliver each particular concentration and with what consistency was each velocity set up? For each of the nominally 5m/s runs, for example, what was the actual velocity? Figures 6.39 and 6.40 present, respectively, the consistency of velocity and solids concentration settings during the runs. It can be seen that there is some variation but it is random, of a small magnitude and does not, in general, correlate with any of the fluctuations observed in the preceding results. The only slight correlation here can be seen in the 5m/s 0.5% point which has been troublesome throughout. It is believed that some abnormally large particles passed through the duct during this run causing the higher than expected concentration and sizing results. Consistency for sand experiments was similar and will not be shown here.

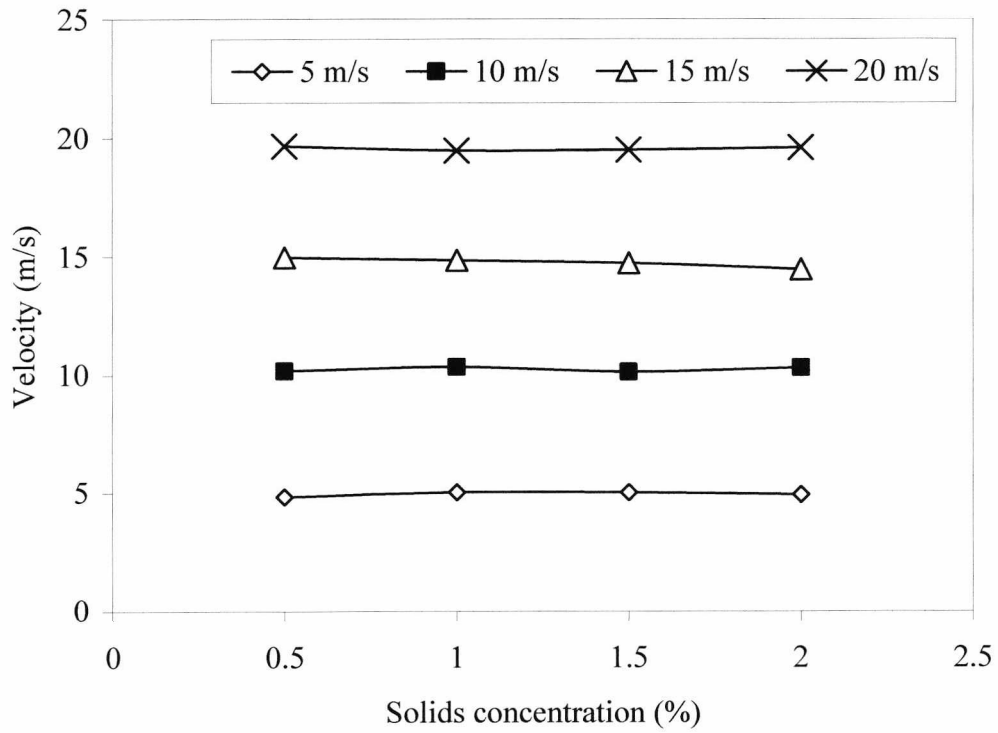

Figure 6.39 Velocity consistency during experiments

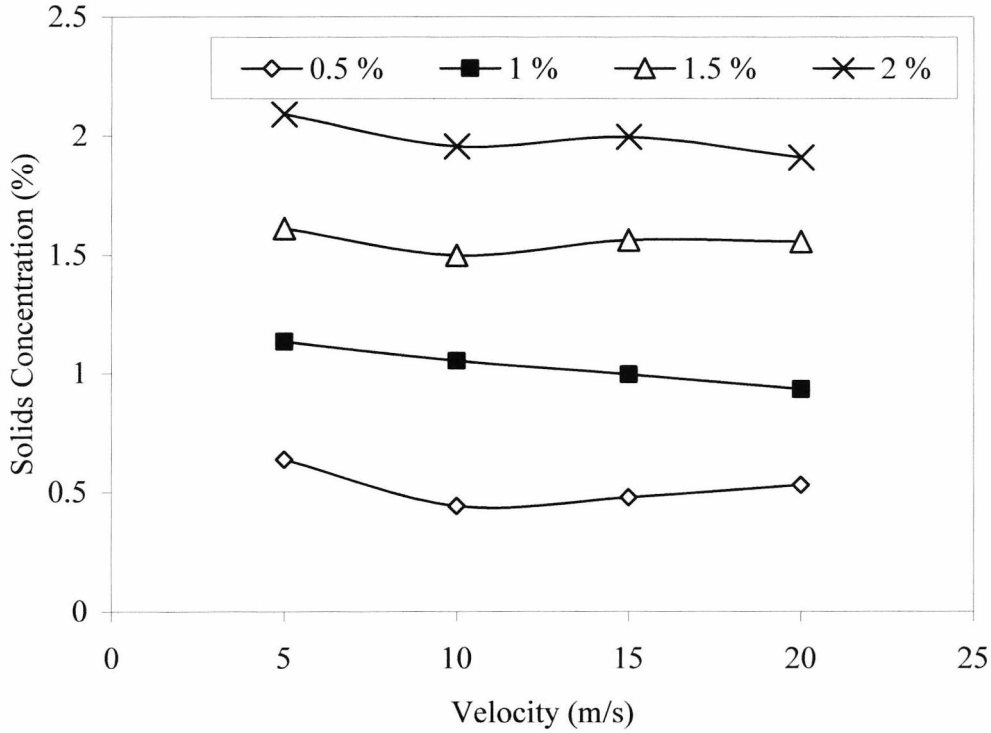

Figure 6.40 Solids concentration consistency during experiments

6.4.8 Inhomogeneous Flow Detection

The importance of inhomogeneous flow detection and the theoretical capabilities of the imaging system in this regard, have been discussed already. The performance of this detection will now be demonstrated.

Stratification is extremely common in industrial flows and such conditions are easily created in the laboratory through the steady reduction of material velocity until the phenomenon is observed. Figure 6.41 shows the results of such an experiment, presenting the output of the roping flow detection routine (note that stratification is detected through the use of routines developed for rope detection and therefore the term 'rope detector' is used throughout this discussion) and velocity, both against time.

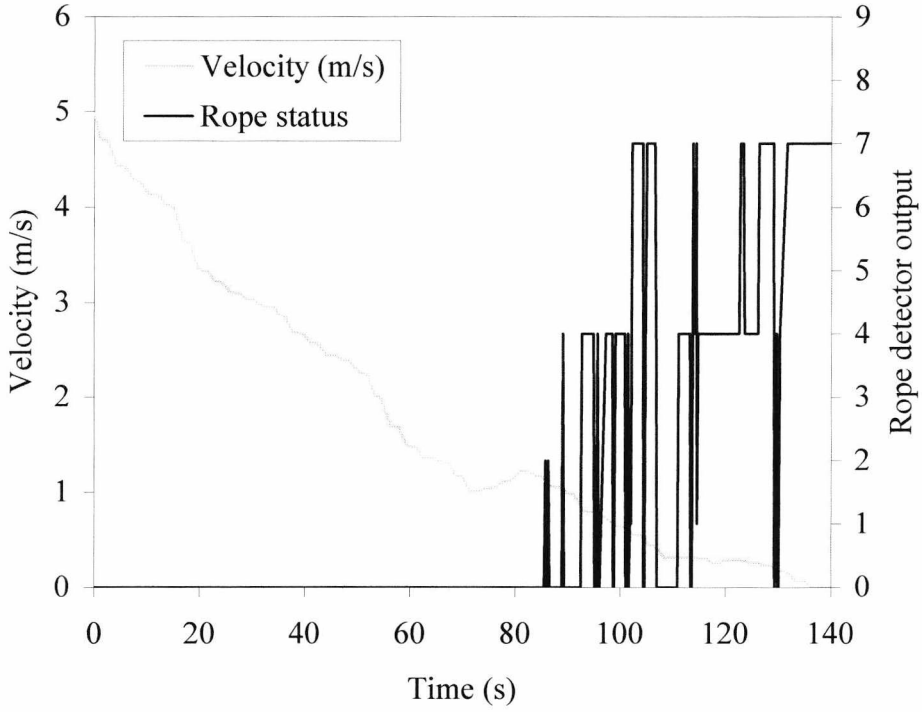

Figure 6.41 Stratification test results

It is clear that some form of inhomogeneous flow is detected once the velocity has been reduced to less than about 1m/s. The output of the rope detector indicates the image zone in which a problem is detected and so, in order to fully understand these results, it is necessary to know the layout of these zones (this was presented in chapter 5 but, due to installation details, will be covered here also). This layout is presented in Figure 6.42.

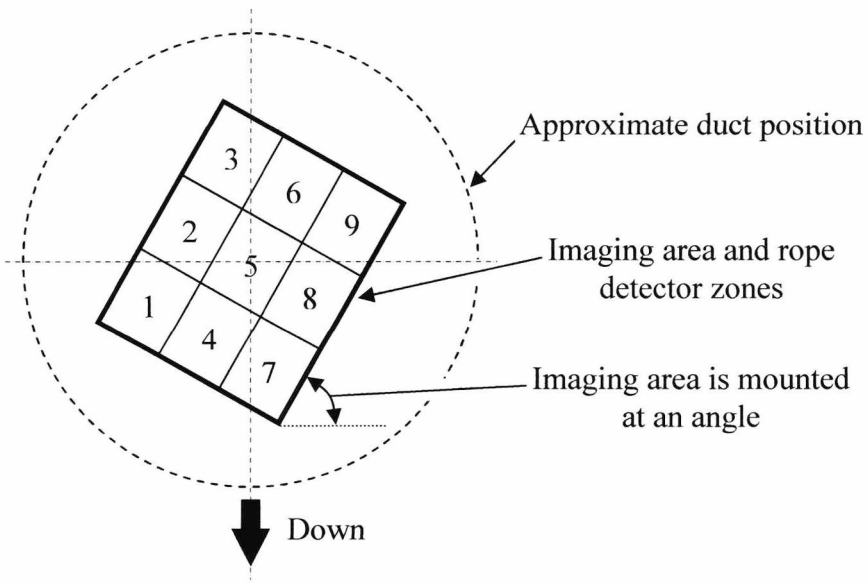

Figure 6.42 Rope detector zones

The most important things to notice here are the layout of the zones and the fact that the whole sensor is mounted at an angle thus making zone seven the lowest. The angular mounting was necessitated by practical considerations when attaching the sensing head to the rig and the particular angle is purely arbitrary. Referring back to the results of figure 6.41 and comparing them to the zone configuration in figure 6.42 it can be seen that a convincing detection of stratified flow has been performed. Initially the detector highlighted zone two indicating that the flow had fallen away from the upper zones. The stratified flow then proceeded to sink further in the duct, being detected mainly in zones four and seven. Clearly stratified flow can be detected successfully. It is interesting to note here that no detections centre on the zones to the right hand side of the duct. This suggests that the flow tends towards the left hand side, thus, though unquestionably inhomogeneous, the flow regime here is not pure stratification.

Roping flow is more difficult to induce than stratification and the exact methods employed were described earlier in this chapter. Sufficient is it to say, here, that short roped pulses of flow were created using extremely fine material. The results generated by the roping detector, together with solids concentration to indicate the pulsed nature of the flow, are shown in figure 6.43.

It can be seen that ropes have been detected in two out of three material pulses. These ropes centre on zones five and nine. It should be noted that with the pulsed flow technique ropes are not always generated and so the failure to detect a rope for the third pulse of material is not necessarily an error but may indicate that no rope was formed.

Since zones five and nine are close to the centre of the flow it can be readily appreciated that detection in these zones represents the presence of a flow rope. However, since the same routines are used for the detection of both roping and stratification is it certain that these detections represent ropes and not other inhomogeneous flow regimes? Figure 6.44 shows an image taken of the flow during one of these material flow pulses (some pre-processing has been performed on this image) and Figure 6.45 shows the corresponding rope detection window (a rope centred on, but not necessarily limited to, zone five was detected in this instance).

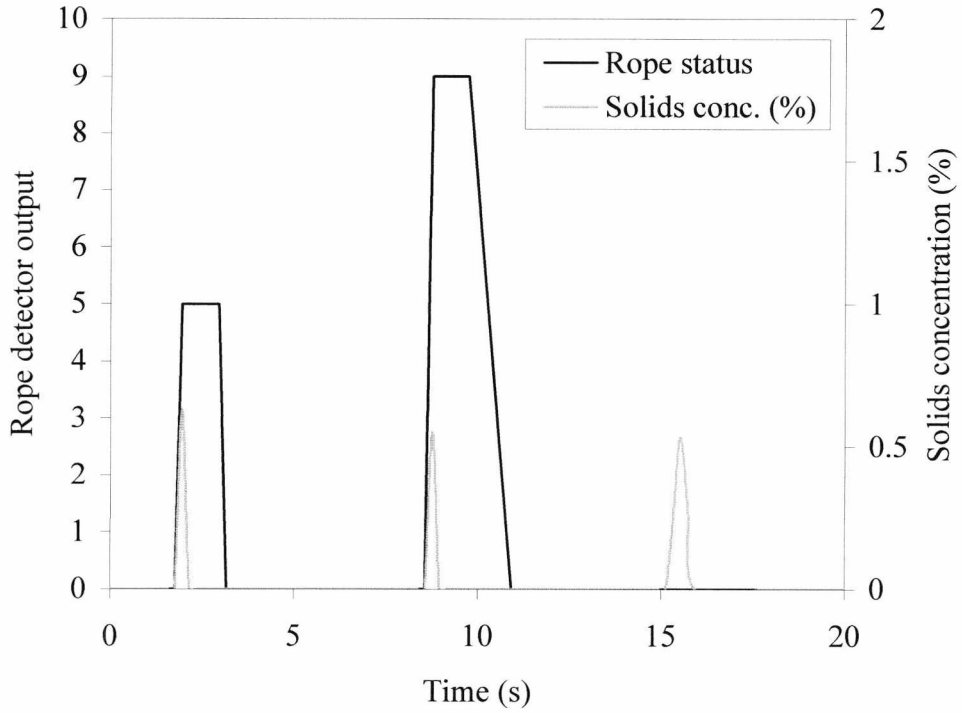

Figure 6.43 Roping test results

It can be seen that the flow is in the form of a circular localised concentration that may be considered to be a loose rope. It is interesting to note that though the overall concentration of the pulses is only around 0.5% it is high enough within the rope to cause visible particle overlapping effects (irrelevant in the case of inhomogeneous flow detection). Despite the limited range of test conditions provided by the present rig it is clear that the imaging system is capable of detecting inhomogeneous flow successfully. Both stratification and roping flow have been identified as expected. In a real situation it would only be necessary to identify the presence of such flows, which could then be investigated as required.

The detection of inhomogeneous flow is fundamentally independent of material properties. For this reason only salt has been used here.

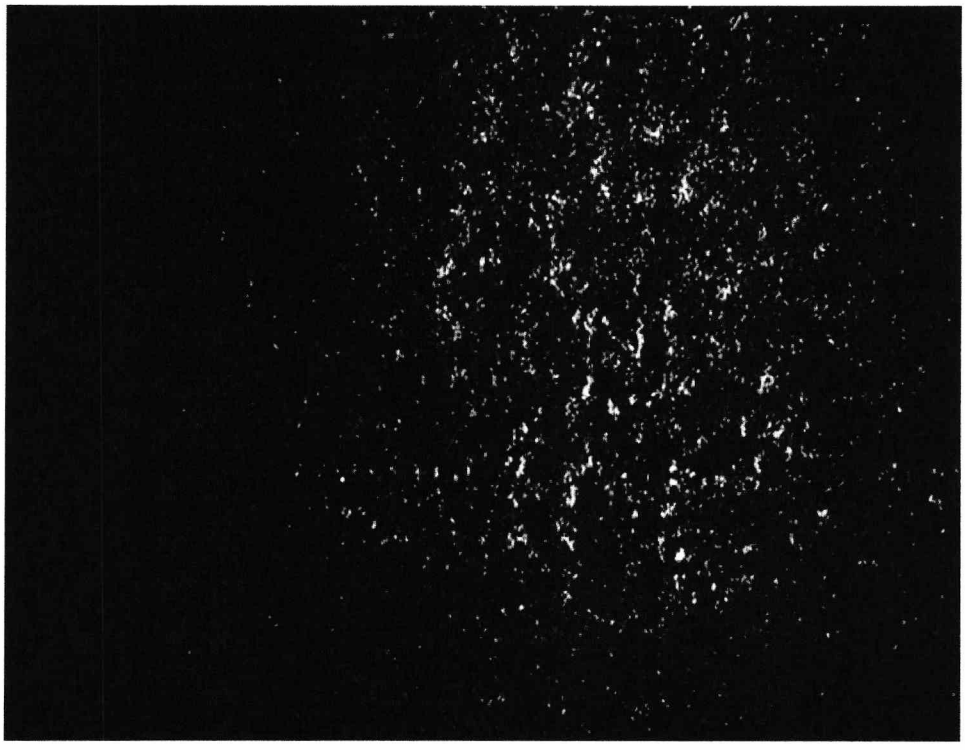

Figure 6.44 Roping flow image

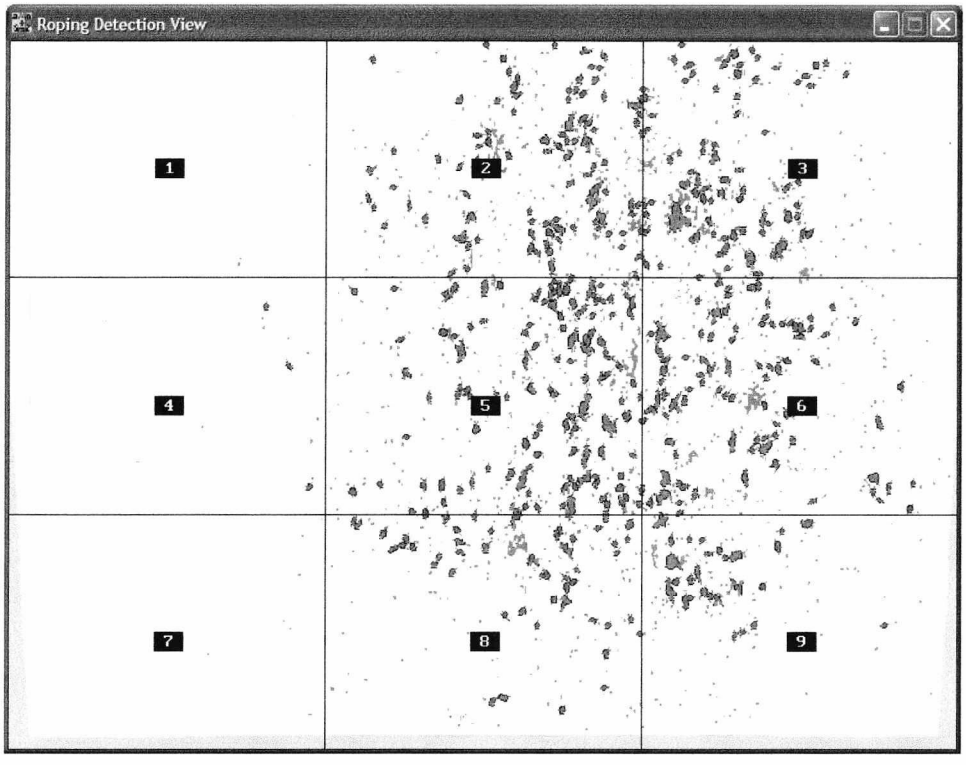

Figure 6.45 Rope detector window result for figure 6.34

6.5 Industrial Trials

One of the objectives of the work was to test the imaging system under real industrial conditions. This section details the facility used for and the results achieved by such testing.

6.5.1 Combustion Test Facility

Industrial testing was carried out using the $0.5MW_{th}$ Combustion Test Facility (CTF) that is owned and operated by RWE npower at Didcot in Oxfordshire (UK). This facility consists of a test furnace that is an exact but scaled down replica of those found in full size power stations, thus allowing representative testing to be performed at reasonable cost. Pulverised coal and coal/biomass mixtures are the main fuels of interest.

Air is supplied to the burner in two ways: Primary air constitutes around 20% of the air supply and conveys the PF. Secondary air represents the remainder and may be varied to provide differing fuel to air ratios. PF and primary air are supplied through a pipe that is compatible in size with the on-line sensing head (see the next section). The test furnace is fitted with a range of sensors that are designed to monitor temperatures and emissions. These are of little interest here. As far as the PF feed is concerned (the only part that affects the conditions that will be experienced by the present instrument) the only values that can be controlled are the mass flow rate of PF (a time averaged value measured by load cells on the hopper) and, to an extent, the air to fuel ratio. It is usual, during operation, to keep the PF feed rate and primary air volume constant and vary the secondary air supply in order to set up the combustion conditions required for a given test. No facility is provided for velocity measurement of the fuel particles and so inferential mass flow measurement could not be attempted (there was not space for the electrostatic meter used in lab trials to be installed). In practice, the only variation in conditions that was possible during trials was a gradual reduction in PF feed rate, within a narrow range of values. This will be explained more in section 6.5.3.

6.5.2 Sensing Head Installation

The sensing head was installed in the PF pipe work close to the burner and shortly after a gentle bend. This was the only possible installation location. A general overview of the installation is shown in figure 6.46, the sensing head is circled in white. Figures 6.47 and 6.48 show more details, featuring the furnace face/burner and sensing head respectively. In both cases points of interest are labelled.

Whilst actual testing only lasted for approximately eight hours (see section 6.5.3) the sensing head was installed on the rig for a 48 hour period. During this time the air purging system was in operation and no problems were experienced with window fouling. It was found that the compressed air pressure used for air purging was not critical – a flow rate of around one litre per second was found to be sufficient.

Under industrial conditions the sensing head operated well from a physical viewpoint. There were no leaks and no problems with the elevated temperatures and vibration that were experienced. A possible shortcoming was identified with the enclosure fixing method. The clamshell approach used here made it difficult (but not impossible) to open the sensing head for inspection when installed on vertical pipe work.

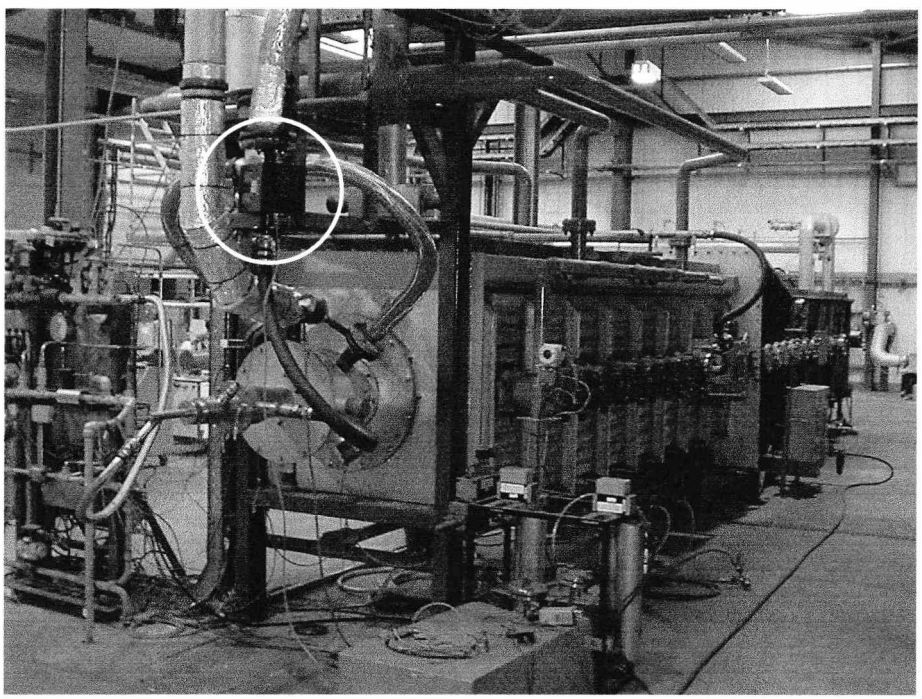

Figure 6.46 Sensing head installation overview

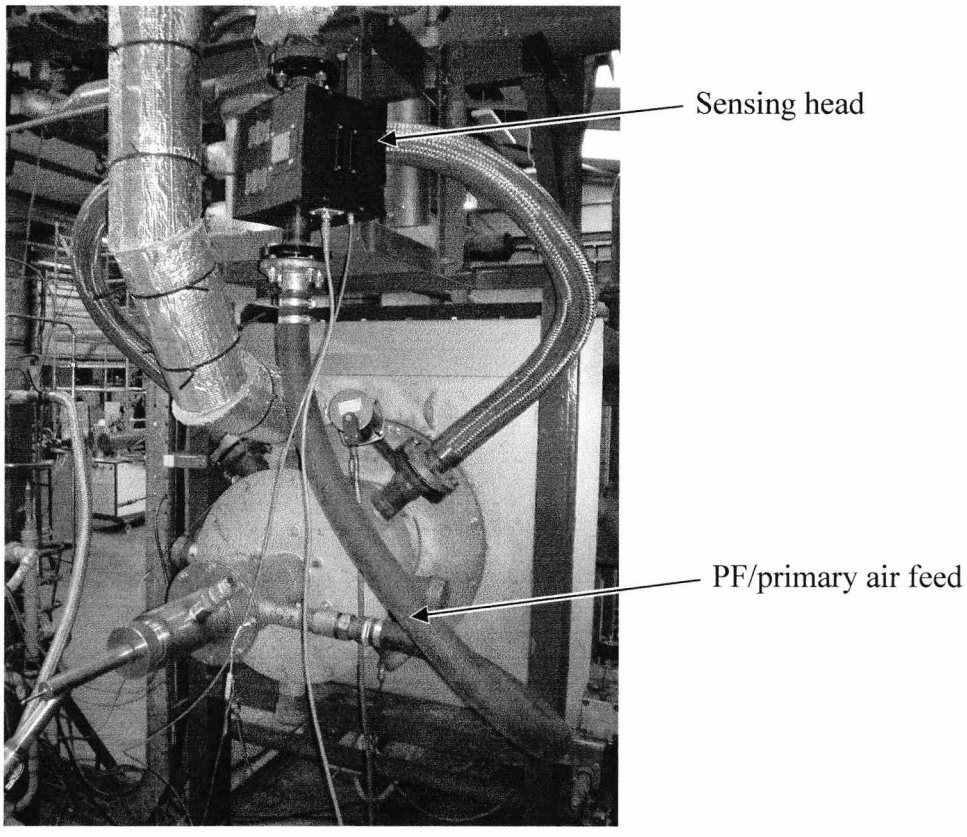

Figure 6.47 Furnace face detail

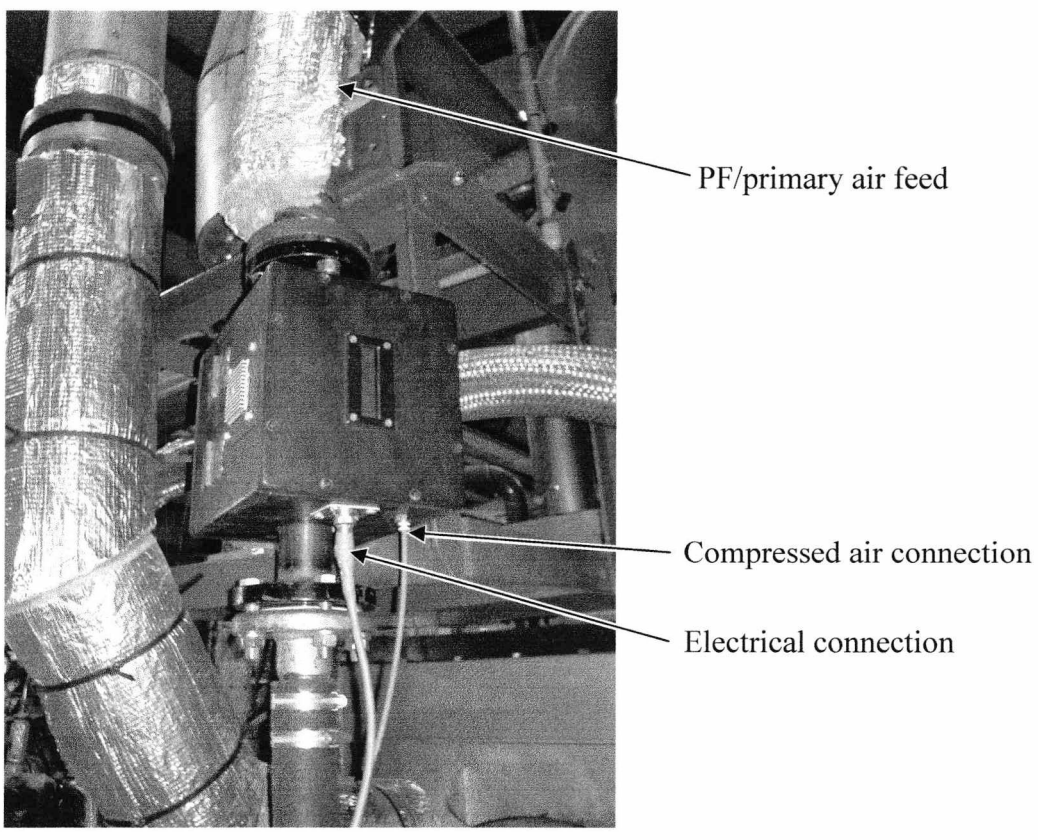

Figure 6.48 Sensing head close-up

6.5.3 Results and Discussion

Experimental conditions during testing were extremely limited. In essence the tests that were conducted consisted of establishing a fixed mass flow rate of PF at a constant fuel to primary air ratio. This imposed a single test condition during which PF was fed at a rate of 71kg/hr. No on-line velocity data were available but the rig operators suggested that 25m/s was a reasonable assumption based upon experience of tests in the past. This allowed a crude estimation of the solids concentration in the duct to be made, the result being around 0.05% (Yan 2002). This is clearly within the range of applicable values that was established during lab testing.

Despite appropriate concentration levels, problems were experienced. It was found that images were of very low contrast, so much so that detection of particles was erratic and useful results were not generated. Visual inspection of the window revealed that air purging was operating and that no fouling was occurring. During rig shutdown at the end of testing the PF flow rate was reduced gradually whilst leaving primary air constant and in this way lower concentrations were observed. It was found that image quality improved as concentration was reduced until, at around 25kg/hr, reliable results were obtained.

Since the solids concentration shown above was only approximate it was not possible to perform any meaningful concentration measurements. The assessment of roping flow was also impossible due to the fixed conditions within the duct. The only possible result was a particle size distribution. This is shown in figure 6.49 where the result of testing the same material under static conditions is also shown.

It can be seen in figure 6.49 that the general agreement is good but before this can be discussed in detail some information about the material used here must be presented. The material consisted of a 90:10 coal/biomass mixture. The particular biomass used was sawdust with very irregularly shaped particles. During on-line work the laser sheet illumination was suitable for both coal and biomass but for static testing different, contrasting, backgrounds had to be used for each material. This meant that the materials had to be sized separately under static conditions and the results combined in the correct proportion. Representative images of the materials are shown in figure 6.50.

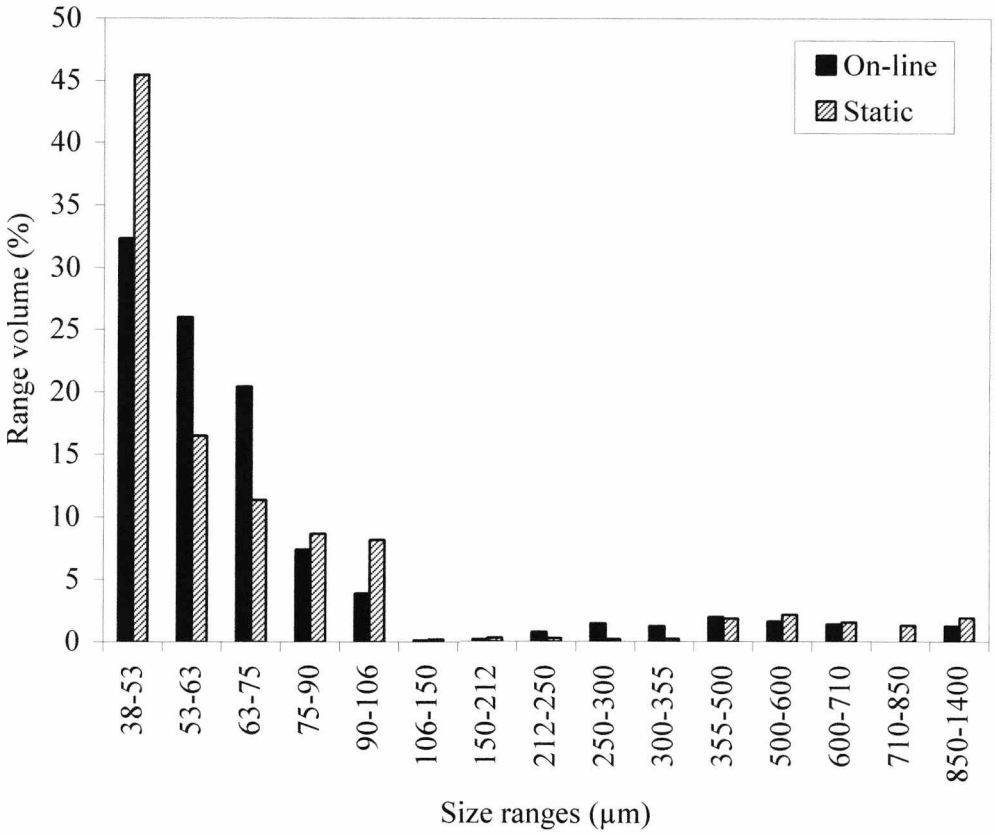

Figure 6.49 Industrial size distribution results

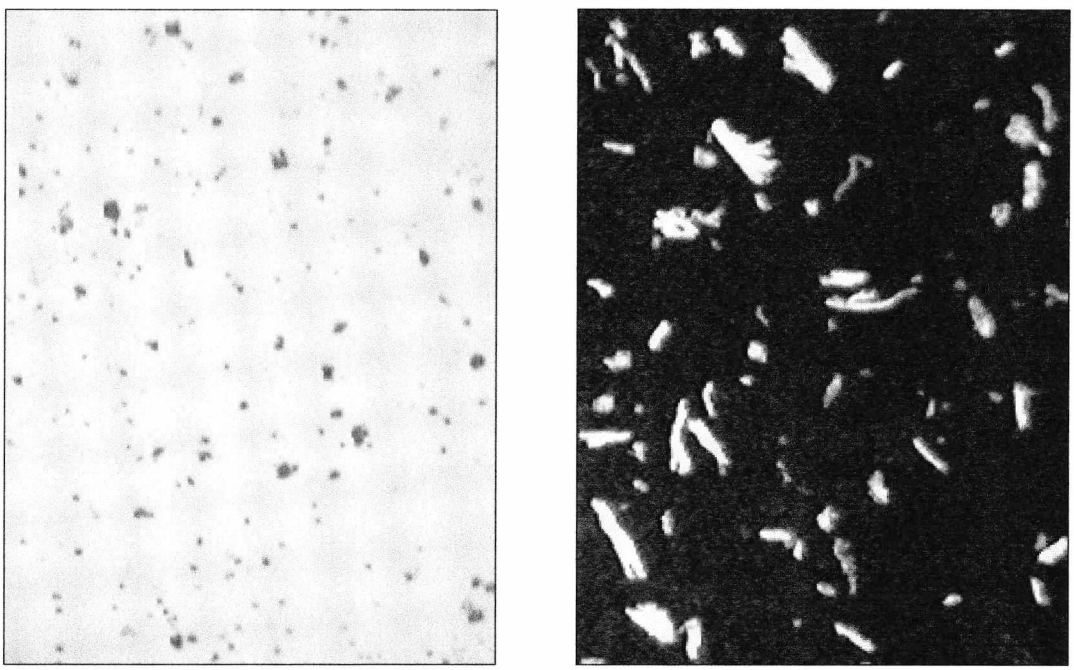

a) Pulverised coal

b) Biomass (sawdust)

Figure 6.50 Materials used in industrial testing (shown at the same scale)

It is clear that the biomass particles are of extremely varied shape. Many of them are in the form of flakes and this will lead to a reduction in perceived size during 'in-flight' conditions. This is confirmed in figure 6.49 where distribution is clearly bimodal in nature. It can be seen that the small upper peak, representing the biomass, tends towards larger sizes under static conditions. The lower peak, representing the PF, shows good but not exact agreement between methods. There is some tendency for this material to clump under static conditions and this could explain the variation here. Most importantly it is clear that the PF distribution must extend well below the range of particle sizes currently detectable by the imaging system. It is believed that the presence of vast numbers of very tiny particles was responsible for the initial difficulties in imaging the flow. Such tiny particles will create significant light scattering and extinction. Clearly with such a fine material the existence of particles between the camera and illuminated section of flow is a significant issue.

In general useful results were obtained at the lowered flow rate although it is clear that the scattering of tiny particles must be taken into account in some way if full flow rate tests are to be successful. Despite this issue the initial results shown here are promising and it has been shown that the present technique can be used under industrial conditions.

6.6 Summary

In this chapter the practicality of the on-line system has been demonstrated. It has been shown that the physical designs of the sensing head function as intended. The automatic controls of the low-cost camera have been shown to affect the results suggesting that a camera with fixed (though adjustable) settings would be preferable. Despite this, good results have been achieved for particle characterisation; in particular repeatability is good being similar to off line techniques such as laser diffraction.

Inferential mass flow measurement has been shown to be problematic with the present setup the main difficulty being due to non-linearity in the correlation velocity data. The automatic camera controls were also a hindrance here.

The only significant difference between the two test materials was seen under static test conditions. Very slight changes in material shape were found to cause significant changes in the recorded size distributions due to the way in which particles lay on the test surface. Such changes were not present in in-flight results but could affect certain industrial processes. The comparison between in-flight and static measurement is only possible with the present technique.

Inhomogeneous flow detection was successful with both stratification and roping flow detected. It was interesting to note that under roping conditions localised solids concentration was increased dramatically despite a low overall value.

Under industrial conditions the air purging kept the sensing head operational for the whole 48 hour installation period though the effects of large numbers of tiny particles limited the maximum permissible concentration to lower than expected levels.

In general the system performed well when operating on-line and the results recorded here have allowed future improvement of the methodology to be identified. Details of such future work, along with a more detailed summary of accuracies achieved will be presented in the next chapter.

Chapter 7

Conclusions and Recommendations for Future Work

7.1 Introduction

This thesis reports on the design, implementation and experimental evaluation of a prototype imaging based instrumentation system for use with dilute phase solids-in-air pneumatic flows. The system operates on-line and is non-intrusive. The primary parameters measured are particle size and solids concentration though particle shape measurement, inferential mass flow metering and the detection of roping and stratification are also discussed. The system is based upon 2D imaging using an unusual perpendicular laser sheet illumination scheme and novel image processing algorithms. It has been proposed that this scheme may eliminate vertical particle movement problems experienced with other (PTV type) laser sheet based experiments whilst avoiding depth of field issues that have plagued diffuse, back-light, illumination arrangements. Throughout the work low cost hardware has been employed in order that practically achievable results may be recorded and also so that, in principle, the system may be applicable to large scale industrial use.

The initial stages of the work consisted of development of image processing algorithms using a static front-lit imaging arrangement. During this phase extensive tests were carried out with precision calibration images so that the limits of measurement and repeatability for such a system could be reliably established. In addition a number of real particulate materials, representing a broad range of industrial applications, were analysed with the system and these results were compared to results achieved with an accepted laser diffraction based analyser.

The next phase of work consisted of the design and construction of a 40mm ID sensing head for full on-line operation. Such operation necessitated further work on the image processing algorithms and required that a number of practical issues be addressed. A

systematic experimental programme was conducted which evaluated the system under real on-line conditions using a small flow loop that was set up in the laboratory, using pneumatically conveyed table salt and sand as test materials.

The final stage of the project was to test the system under industrial conditions using RWE npower's Combustion Test Facility at Didcot, Oxfordshire, UK. A mixture of 90% pulverised coal and 10% biomass (sawdust) was observed whilst the rig was operating normally. On-line results were compared with static test results using the same material.

This chapter presents the conclusions that have been drawn from the research programme presented here. Also recommendations are given for future research work in this field.

7.2 Conclusions

7.2.1 Research Strategy and Image Processing Software

The research strategy used in this case was to separate fundamental imaging issues from on-line operation problems by conducting initial development work with the use of a simple static imaging system. This strategy was successful, not only simplifying early work but also allowing the fundamental limits of measurement to be established. When the time came for on-line development work the existing static system provided a solid foundation of concepts and methodologies upon which to build. Whilst low contrast images were observed image processing allowed this shortcoming to be dealt with in software. The laser sheet illumination provided adequate images of on-line particles and no inconsistencies in the results which may have been caused by particle movement in the beam were recorded. This confirmed the suitability of the sensing arrangement used here.

Image processing software has been developed that allows raw particle images to be processed reliably. The main challenge was to provide some means of separating particles from image background consistently (i.e. determining particle boundaries). This challenge was met with the development of a novel image analysis algorithm that allows simple threshold processing to be used consistently. The methodology was further enhanced

through the use of a novel zone based threshold level variation simulating a 'natural-algorithm' approach. For the on-line system a method of enhancing poor quality images was created so that the image analysis (threshold setting) algorithm would work with these also. Other key processing tasks included lens distortion correction, particle size determination through pixel counting, particle counting, determination of particle centroids, measurement of aspect ratio, determination of shape factor through the study of particle radii, background removal, elimination of invalid particles that cross the outer image boundaries and statistical analysis of the recorded data. In addition, many minor tasks were required in order to bring the key elements together. Throughout development emphasis was placed on high performance processing in order that cost-effective hardware could achieve real-time operation. A standard desktop PC (AMD Athlon XP 2500 with 512 Mb of dual channel 333 MHz memory) was capable of achieving five frames per second, with the final software, which was more than adequate to provide real-time operation for the test loop in question (the test loop was found to demonstrate a time constant of around four seconds when flow conditions were changed). The software was developed using portable ANSI standard C++ where possible and object orientated techniques were employed. In use the software was robust and reliable, operating consistently and without crashing for long periods (during industrial trials the software operated for around eight hours without mishap). In general the suitability of the algorithms employed in the software has been confirmed by results achieved and conclusions arising from these results will be dealt with in the proceeding sections.

7.2.2 Off-Line Measurement of Size Concentration and Shape

Extensive tests of the static system were performed using accurate calibration images featuring particles in the 250-2000μm size range. In all testing enough particles were analysed to ensure the representative nature of results. Fundamental errors in sizing were found to be within ±0.15% and system linearity was excellent. Maximum normalised standard deviation of measurements was 0.3% this quantity dropping off as expected for larger particles. This confirmed excellent repeatability of measurement.

A change in the optical arrangement was used to simulate particles down to 25μm and these smaller particles were used to establish lower limits of measurement. It was found

consistently that the smallest particle that may be measured with confidence must occupy an area of around nine pixels. At this level the sizing error was found to be around 2%. Smaller particles could be measured with increasing errors – a particle occupying a single pixel was sized with approximately 15% error. The effects of these limitations would be reduced with measurement averaging in a real situation where large numbers of particles are used. Since the maximum particle size is limited only by the size of the imaging plane very large particles may be imaged with ease. For the present set-up this results in a turndown ratio of approximately 1000:1.

Calibration images were also used to assess the spatial sensitivity of the sensing arrangement and it was found that small variations did exist when particles of nominally the same size were measured at different places on the focal plane. These variations were not found to correlate with variations in lighting intensity and must be attributed to slight imperfections in the lens leading to image distortions that cannot be corrected. Peak deviations from the mean value (as distinguished from absolute errors) were in the order of ±2% across the focal plane though if the very edges of the image are avoided much lower values can be expected (it should be remembered that the processing software ignores particles that intersect the image boundary and so this requirement will be met in most cases). It should be noted here that this source of error manifests itself as a variation (overestimation or underestimation) in measured particle size with respect to position and will probably be swamped by the effects of particles presenting different sides to the camera. In a real situation large numbers of particles will be interrogated and mean results of one form or another will be calculated. This means that these small spatial variations are not significant if the requirements of representative sampling are met.

Calibration images provided solids concentrations of up to around 3.5% and the accuracy of measurement was found to lie within ±1.5% in all cases. This was considerably higher than the sizing error since sizing and concentration measurement are linked and sizing errors affect concentration values in a cumulative manner. Linearity was excellent and good repeatability was demonstrated by a normalised standard deviation of less than 0.6%. An investigation was carried out into the upper limit of measurable concentration after which particle overlapping would become an issue. This was achieved by measuring the mean measured particle size as solids concentration was increased – serious overlapping issues would manifest themselves as increasing mean particle size. It was

found that at around 2-3% solids concentration this phenomenon occurred. At 4% concentration the sizing error had risen to 10%. This upper limit of around 2-3% was found to be consistent throughout testing (also for on-line work – see the next section) indicating that the phenomenon of particle overlapping may be ignored at concentrations below this level. As the system is intended for use with dilute phase flows (up to around 1% concentration) this is not an issue. The turndown ratio achieved for concentration measurement during static testing was around 700:1.

The measurement of particle aspect ratio and shape factor was achieved successfully. It has been assumed in the past that imaging based methods can operate irrespective of the shape and orientation of particles. Tests were performed here in order to assess the effects of rotating a range of shapes and recording the changes in measured aspect ratio and shape factor. A range of shapes of varying complexity were used. It was interesting to note that the absolute accuracy of aspect ratio measurement was found to be only 3% for a circle and 0.3% for a square. This was attributed to the quantised nature of digital images and the resulting limitations and proved that insensitivity to shape should not be taken for granted. It was impossible to define the absolute error of shape factor measurement since no error free reference value could be calculated easily. Despite this the shape factor increased in line with increasing shape complexity and was proven to be a valid quantification.

Both measured aspect ratio and shape factor were found to vary with shape size. For realistic 'particle like' shapes these variations lay within ±1%. Less practical shapes, such as crosses and 'explosions', demonstrated higher variation of around ±3% and ±5% for aspect ratio and shape factor respectively. Again, this was attributed to quantisation effects. Similar variations, attributed to the same cause, were recorded when rotating the shapes through 45°. Practical shapes showed less than ±1% of change and the less practical ones much greater variation, in this case within ±8% for both quantities. These results showed that whilst the affects of image quantisation in relation to particle shape and orientation are not insignificant for all shapes, they can be ignored for most practical particle shapes that may be found in pneumatic conveyors. It should be noted here that these shape and orientation sensitivities are taken into account automatically in particle size and concentration results and contribute to the errors found there, which themselves must be due to the same cause i.e. image quantisation. If a camera with infinite resolution

was used with perfect optics the static analysis of particles would be error free. The errors and variations reported here stem from practical considerations imposed by finite resolution and real world optics.

When testing the static arrangement with real materials and comparing size distribution results with those recorded by the laser diffraction based Malvern Mastersizer, it was found that discrepancies were within ±10%. These discrepancies varied from one material to another being much lower in some cases. Individual materials are discussed in chapter 4 but, in general, it was found that the discrepancies could be blamed on the variations of particle shape (and to an extent on unavoidable variations in material samples). The laser system is fundamentally sensitive to shape whereas the imaging set-up is not. Despite this the imaging results were affected by changes in shape under static conditions as 'flaky' particles tended to lie flat, presenting their largest side to the camera. This phenomenon must be considered in all static measurement work.

7.2.3 On-line Measurements

For on-line work the cameras interlaced video format was an issue and its effect on particle sizing accuracy was investigated. It was found that for large particles the image banding caused by interlacing is unimportant due to the sheer size of the particles, for very small particles the resolution is unaffected and for mid range particles the banding effect does lead to variations in measured particle size. In summary, errors were increased slightly for mid sized particles but it is thought that the minimum measurable particle size is not affected by the on-line processing methodologies employed, although a certain increase in errors, in comparison to static work, must be accepted.

The flow rig set up for this work has proven to be suitable for all tests, providing a wide range of stable flow conditions. The size of duct used was identical with small scale industrial test rigs allowing testing of the same sensing head under industrial conditions. One possible shortcoming of the rig is its limited run-time which is related to material feed and collection arrangements. Another is the unsuitability of the rig to operate with pulverised coal, which is in part due to safety and environmental issues in the laboratory but also related to the unsuitability of feed and collection arrangements. The sensing head

proved to operate reliably and the air purging arrangements kept the duct window clean under all test conditions.

Thorough on-line tests focused mainly on establishing if there are any dependencies on velocity or concentration in the results. It was found that shape measurement was completely consistent but that sizing showed a slight dependency on velocity. This trend was seen in both mean data and size distribution results and was successfully correlated with an observed decrease in particle brightness as velocity increased. This direct correlation would allow the problem to be calibrated out. In general this problem is believed to be caused in part by the inability of the automatic threshold setting algorithm to deal with brightness changes of this magnitude and partly due to the limited dynamic range of the camera. The automatic camera gain control may also have been a contributory factor as this is a shortcoming of the low-cost camera employed.

On-line imaging has shown an excellent agreement with laser diffraction results, variations lying within ±2%. This improvement over static conditions is attributed to the fact that now both systems are making in-flight measurements. Under static conditions the same materials have shown greater variations.

Repeatability studies have shown that the repeatability of the on-line imaging system is excellent and is better than the laser diffraction system, giving normalised standard deviations of around 4%. With practical materials the static system showed slightly lower repeatability than this, being similar to the laser diffraction instrument.

Mass flow rate measurement was found to be problematic. The automatic shutter speed setting of the low cost camera was found to generate a form of volumetric sampling. Since there is no means of knowing what shutter speed the camera has set itself to under real conditions (in the laboratory this can be arrived at through reverse calculation of reference data) this effect was of importance not only for mass flow measurement but also for on-line solids concentration. To an extent the problem can be calibrated out but avoidance through the use of a camera with known shutter speed would be a preferable solution. The particle size errors due to velocity dependence also affected mass flow measurement, highlighting dependencies between measured parameters. Another problem lay in a certain non-linearity, particularly at high velocities – the electrostatic velocity

sensor gives a correlation velocity which cannot be trusted to represent the averaged cross sectional velocity (Ma and Yan 2000). Attempts to calibrate out the problems listed above resulted in mass flow accuracy of around ±10% for lower velocities but these values rose to about ±20% for higher, problematic, particle speeds.

The lower limit of measurable concentration was found to be around 0.015% where it was found that the volumetric measurement imposed by the inexpensive camera could be considered to be an advantage. It is the uncontrolled nature of the shutter speed variation that must be avoided. The use of the automatic camera has shown that the volumetric technique may be a useful tool if applied in a controlled manner. Upper concentration limits were found to be consistent with static conditions there being problems with particle obscuration beginning at around 1.5-2% concentration.

The capability of the test rig to generate inhomogeneous flows was proven and the usefulness of the imaging system in detecting these flows was demonstrated. Both roping and stratification were detected. Quantification of the reliability of this aspect of performance is difficult, but during operation the system appeared consistent and this capability is certainly a useful tool for flow analysis and optimisation.

In general, most difficulties and shortcomings could be traced to the inexpensive camera. Despite this, particle sizing was practical and reliable with this set-up demonstrating that the technique is viable for on-line flow analysis.

7.2.4 Industrial Trials

During industrial tests the sensing head operated successfully, showing no ill effects despite conditions of elevated temperature and vibration (other than a certain softening of the foam sealing tape and a general coating of grime upon removal). The air purging kept the window clear successfully and no fouling issues manifested themselves during the 48 hour installation. The presence of very large numbers of very tiny particles was found to reduce the contrast of images considerably, due to increased light scattering and diffraction, which lead to unreliable detection under heavier flow conditions. Despite this

the general results were encouraging with a convincing bimodal distribution generated. This distribution was compared favourably with a static result using the same material.

7.3 Future Work

It is believed that the outcome of the research programme is both useful and promising. The limits of performance for a basic imaging based particle size analyser have been investigated and successful on-line non-intrusive operation has been achieved under both laboratory and industrial conditions. A future system may be the solution to a long standing industrial flow monitoring problem. In order to achieve this, a number of areas have been identified which require further research.

Firstly, the limitations of the low cost camera used in the current work have been reflected in the results achieved. Whilst this was not an issue in static testing, or indeed for particle size measurement it is important that the use of a more expensive scientific camera be investigated. Such a camera should certainly offer manual shutter speed and gain control, progressive image scanning may also be of use. It is possible that the improvements in performance achieved may outweigh the increase in cost.

Another area of interest is the processing software. One area of improvement lies in overlapping particle detection. The overlapping particle phenomenon limits the upper value of solids concentration that can be measured and if this limitation were removed the instrument would find application in fields other than dilute flows. It is believed that a system capable of detecting and ignoring overlapping particles may be preferable to one which attempts to separate such particles since a 2D image cannot provide information on how much of each particle is obscured by the other. Separation may be possible in situations where particles are all of similar, known, shapes (e.g. spherical particles).

Another possible software improvement lies in improved low-contrast image processing. Images recorded under industrial conditions were seen to demonstrate very low contrast due to the presence of many extremely small particles. This issue may be dealt with partly in software but also improvements to the sensing geometry may help here. More powerful

illumination may help but more reliable improvements may be achieved through reducing the distance that both illuminating light and scattered (image) light must travel through the flow.

Certainly further testing under industrial conditions using the Combustion Test Facility at Didcot is required. This will allow the improvements listed above to be tested. The use of this facility to generate a wider range of flow conditions than have been experienced previously should also be investigated. Following CTF testing the system should be adapted for tests in a working power station. The main difficulty here will lie in achieving good flow coverage in ducts that may be up to 20" in diameter. High resolution cameras and/or optical 'zooming' techniques should be investigated.

An important point to note is that the system presented here represents a means of extracting many useful parameters from images of particulate materials. The use of such a system is not limited to particle sizing in on-line flows for power generation but may be applied to many situations. There are, for instance, many large granular materials used in the food industry that would benefit from on-line monitoring (rice grains, coffee beans etc). Other possible areas of application lie in pharmaceuticals and geology. Parameters measured by the system should not only be used directly but may be used as input data to fuzzy logic or neural network type analysis in order that the material under observation may be identified. It may be possible, for instance, to differentiate between different kinds of rice through analysis of recorded parameters. This may be useful in product verification, the study of product quality, or the detection of adulterated material supplies.

Finally, the work reported in this thesis offers a foundation for future on-line imaging based particle measurement and demonstrates the potential of the technique. The basic methodology is sound but further research is required, as described above. With such studies complete it is envisaged that this research may lead to a robust and practical industrial instrumentation system.

References

1. 'A Mobile On-Line Particle Size Analyser', Editorial, Powder Handling and Processing, vol. 15, pp335, 2003

2. 'A Vision for Clean Fossil Power Generation', UK Advanced Power Generation Technology Forum, May 2004, downloadable from: www.apgtf-uk.com

3. 'A Review of the Case for Government Support for Cleaner Coal Technology Demonstration Plant - final report', DTI, December 2001, downloadable from: www.dti.gov.uk/cct/cctdemohome.htm

4. Adamczyk A. A., Rimai L., '2-Dimensional Particle Tracking Velocimetry (PTV): Technique and Image Processing Algorithms', Experiments in Fluids, vol. 6, pp373-380, 1988a

5. Adamczyk A. A., Rimai L., 'Reconstruction of a 3-Dimensional Flow Field From Orthogonal Views of Seed Track Video Images', Experiments in Fluids, vol. 6, pp380-386, 1988b

6. Alexander D. R., Wiles K. J., Schaub S. A., Seeman M. P., 'Effects of Non-spherical Drops on a Phase Doppler System', Particle Sizing and Analysis, Proc. SPIE 573, pp67-72, 1985

7. Allen T., 'Particle Size Measurement', Chapman & Hall, 4th edition, ISBN 04123570, 1992

8. Azzazy M., Hess C., F., 'Characterisation of Suspended Particulates on Multicomponent Systems using Polarization Intensity Ratio and Pointer Beam Techniques', Proc. SPIE 573, 1985

9. Barber P. W., Hill S. C., 'Light Scattering by Particles: Computational Methods', World Scientific, Singapore, 1990

10. Barratt I. R., 'Radiometric Determination of the True Mass Flow Rate of Solids in a Pneumatic Suspension', PhD, University of Greenwich, 2000

11. Barratt I. R., Yan Y., Byrne B., 'A Parallel-Beam Radiometric Instrumentation System for the Mass Flow Measurement of Pneumatically Conveyed Solids', Measurement Science and Technology, vol. 12, pp1515-1528, 2001

12. Barrett P. J., 'The Shape of Rock Particles, a Critical Review', Sedimentology, vol.27, pp291-303, 1980

13. Baxter L. L., 'Char Fragmentation and Fly Ash Formation during Pulverised Coal Combustion', Combustion Flames, vol. 90, pp174-184, 1992

14. Bayvel L. P., Jones A. R., 'Electromagnetic Scattering and its Applications', Applied Science, London, 1981

15. Beck M. S., Lee K. T., Stanley-Wood N. G., 'A New Method for Evaluating the Size of Solid Particles Flowing in a Turbulent Fluid', Powder Technology, vol. 8, pp85-90, 1973

16. Bertollini G. P., Oberdier L. M., Lee Y. H., 'Image Processing System to Analyse Droplet Distributions in Sprays', Optical Engineering, vol. 24, pp464-469, 1985

17. Black D. L., Mardson Q. M., Bonin M. P., 'Laser-Based Techniques for Particle-Size Measurement: A Review of Sizing Methods and Their Industrial Applications', Energy Combustion Science, vol. 22, pp267-306, 1996

18. Bonin M. P., 'Optical Measurement of Particle Size Velocity and Number Density in Two-Phase, Isothermal and Reacting Flows', PhD, Brigham Young University, 1992

19. Bonin M. P., Queiroz M., 'A Parametric Evaluation of Particle Phase Dynamics in an Industrial Pulverised, Coal-fired Boiler', Fuel, vol. 75, pp195-206, 1996

20. Bonin M. P., Queiroz M., 'An Analysis of Single Stream Droplet Combustion Through Size and Velocity Measurements', Heat Transfer in Combustion Systems, pp3-8, The American Society of Mechanical Engineers, HTD vol. 142, 1990

21. Bonin M. P., Queiroz M., 'Local Particle Size Velocity and Concentration Measurements in an Industrial Scale Pulverised Coal Boiler', Combustion Flames, vol. 85, pp121-133, 1991

22. Borhen C. F., Huffman D. R., 'Absorption and Scattering of Light by Small Particles', Wiley, New York, 1983

23. Boron S., Waldie B., 'Particle Sizing by Forward Lobe Scattering Intensity-ratio Technique: Errors Introduced by Applying Diffraction Theory in the Mie Regime', Applied Optics, vol. 17, pp1644-1648, 1978

24. Bowman E. T., Soga K., Drummond T. W., 'Particle Shape Characterisation using Fourier Analysis', CUED/D-Soils/TR315, 2000

25. Boyko C. M., Le T. H., Henein H., 'Ensemble and Single Particle Laser Probe Sizing Results for Gas Atomized Zinc Powders', Part. Part. Syst. Charact., vol. 10, pp266-270, 1993

26. Bracewell R. N., Journal of Applied Physics, vol. 9, pp198-217, 1956

27. Cao Z. M., Nishino K., Torii K., 'Measurement of Size and velocity of Water Spray Particles using Laser Induced Fluorescence Method', Proceedings 2nd Pacific Symposium on Flow Visualisation and Image Processing (PSFVIP-2), paper: PF039, 1999

28. Chang T. P., Watson A. T., Tatterson G B., 'Image Processing of Tracer Particle Motions as Applied to Mixing and Turbulent Flow – I. The Technique', Chemical Engineering Science, vol. 40, pp-269-275, 1985a

29. Chang T. P., Watson A. T., Tatterson G B., 'Image Processing of Tracer Particle Motions as Applied to Mixing and Turbulent Flow – II. Results and Discussion', Chemical Engineering Science, vol. 40, pp-277-285, 1985b

30. Chang T. P., Wilcox N. A., Tatterson G B., 'Application of Image Processing to the Analysis of Three-Dimensional Flow Fields', Optical Engineering, vol. 23, pp283-287, 1983

31. Chigier N., 'Optical Imaging of Sprays', Progress in Energy Combustion Science, vol. 17, pp211-262, 1991

32. Clark M. W., 'Quantitative Shape Analysis: a Review', Mathematical Geology, vol. 13, pp303-320, 1981

33. Crawley G., 'On-Line Particle Sizing in Mill Optimisation', Powder Handling and Processing, vol. 15, pp246-247, 2003

34. Davies R., 'A Simple Feature-Space Representation of Particle Shape', Powder Technology, vol. 12, pp111-124, 1975

35. Durst F., Naqwi A., 'Phase Doppler Anemometry and Spray Measurements', Advanced Combustion Science, Springer, Berlin, pp80-85, 1993

36. G. E. Quartz website – ww.gequartz.com

37. Goodwin D. G., Mitchner M., 'Flyash Radiative Properties and Effects on Radiative Heat Transfer in Coal Fired Systems', International Journal of Heat and Mass Transfer, vol. 32, pp627-638, 1989

38. Gouesbet G., 'Generalised Lorenz-Mie Theory and Applications', Part. Part. Syst. Charact., vol. 11, pp22-34, 1994

39. Gouesbet G., Grehan G., Maheu B., 'Generalised Lorenz-Mie Theory and Applications to Optical Sizing', Combustion Measurements, pp339-382, Hemisphere, Washington DC, 1991

40. Green R. G., Thorn R., 'Sensor Systems for Lightly Loaded Pneumatic Conveyors', Powder Technology, vol. 95, pp 79-92, 1998

41. Grehan G., Maheu B., Gouesbet G., 'Scattering of Laser Beams by Mie Scatter Centres: Numerical Results Using a Localize Approximation', Applied Optics, vol. 25, pp3539-3548, 1986

42. Herpfer D. C., Jeng S., Jeng M., 'Planar Measurement of Droplet Velocities and Sizes within a Simplex Analyser', AIAA J., vol. 35, pp127-132, 1997

43. Herpfer D. C., Jeng S., Jeng M., 'Streaked Particle Imaging Velocimetry and Sizing in a Spray', Atomisation Sprays, vol. 5, pp403-416, 1995

44. Hess W. F., Pankewitz A., Steigerwald S., 'In-Line Particle Size Measurement by Means of Ultrasonic Extinction for Control of a Stirrer-Ball-Mill Process', Powder Handling and Processing, vol. 15, pp238-245, 2003

45. Heywood H., 'Particle Shape Coefficients', Journal of the Imperial College Chemical Society, vol. 8, pp15-33, 1954

46. Hirleman E. D., 'Laser Based Single Particle Counters for in-situ Particulate Diagnostics', Optical Engineering, vol. 19, pp854-860, 1988

47. Hirleman E. D., Bohren C. F., 'Optical Particle Sizing', Applied Optics, vol. 30, pp4685-4687, 1991

48. Hodkinson J. R., 'Particle Sizing by Means of the Forward Scattering Lobe', Applied Optics, vol. 5, pp839-844, 1966

49. Holve D. J., Annen K. D., 'Optical Particle Counting, Sizing and Velocimetry using Intensity Deconvolution', Optical Engineering, vol. 23, pp591-603, 1984

50. Holve D. J., Davis G. W., 'Sample Volume and Alignment Analysis for an Optical Particle Counter Sizer and Other Applications', Applied Optics, vol. 24, pp998-1005, 1985

51. Holve D. J., Harvill T. L., Bonin M. P., 'Applications of an Optical Probe for In-Line Continuous Measurement of Particle Volume Concentration', Air Waste Management Assoc., 85th Annual Meeting, Paper no. 92-74-02, 1992

52. Holve D. J., Meyer P. L., 'In Situ Particle Measurement in Combustion Environments', Combustion Measurements, pp279-299, Hemisphere, Washington DC, 1991

53. Holve D. J., Self S. A., 'Optical Particle Sizing for In Situ Measurements Part 1', Applied Optics, vol. 18, pp1632-1645, 1979

54. Holve D. J., Self S. A., 'Optical Particle Sizing for In Situ Measurements Part 2', Applied Optics, vol. 18, pp1646-1652, 1979

55. Hounsfield A. V., 'Reconstructive Tomography in Diagnostic Radiology and Nuclear Medicine', Br. Journal Radiography, vol. 46, pp1016-1022, 1973

56. Human C., 'Time Dependent Property Changes of Freshly Deposited or Densified Sands', PhD, University of California, Berkley, 1992

57. ISO13320-1, 'Particle Size Analysis – laser diffraction methods', 1999

58. ISO9931, 'Coal Sampling of Pulverised Coal Conveyed by Gases in Direct Fired Coal Systems', 1991

59. Kadambi J. R., Martin W. T., Amirthaganesh S., Wernet M. P., 'Particle Sizing Using Particle Imaging Velocimetry for Two-Phase Flows', Powder Technology, vol. 100, pp251-259, 1998

60. Kanerva H., Kiesvaara J., Muttonen E., Yliruusi J., 'Use of Laser Light Diffraction in Determining the Size Distributions of Different Shaped Particles', Pharm. Ind., vol. 55, pp849-853, 1993

61. Kerker M., 'The Scattering of Light and Other Electromagnetic Radiation', Academic Press, New York, 1969

62. Kim I. G., Lee S. Y., 'A Simple Technique for Counting and Sizing Spray Drops Using Digital Image Processing', Experiments in Thermal Fluid Science, vol. 3, pp214-221, 1990

63. Knight J. C., Ball D., Robertson G. N., 'Analytical Inversion for Laser Diffraction Spectrometry Giving Improved Resolution and Accuracy in Size Distribution', Applied Optics, vol. 30, pp4795-4799, 1991

64. Krumbein W. C., 'Measurement and Geological Significance of Shape and Roundness of Sedimentary Particles', Journal of Sedimentary Petrology, vol. 11, pp64-72, 1941

65. Kumar R., Kannan S., 'Drop Size Measurement in a Two-Phase Swirling Flow Using Image Processing Techniques', Int. J. Heat Mass Transfer, vol. 37, pp559-570, 1994

66. Kuo K. K., 'Principles of Combustion', Wiley, New York, 1986

67. Lackermeier U., Rudnick C., Werther J., Bredebusch A., Burkhardt H., 'Visualisation of Flow Structures Inside a Circulating Fluidised Bed by Means of Laser Sheet and Image Processing', Powder Technology, vol. 114, pp71-83, 2001

68. Laux S., Grusha J., McCarthy K., Rosin T., 'Real Time Coal Flow and Particle Size Measurement for Improved Boiler Operation', Power-Gen 1999, New Orleans, Los Angeles

69. Laux S., Grusha J., Rosin T., 'Benefits of Real Time Coal Flow and Particle Size Measurement for Pulverised Coal Boilers', Foster Wheeler Energy Corporation, 2001

70. Lefebvre A. H., Proceedings of 'Atomisation and Sprays', Hemisphere, Washington DC, 1989

71. Leung C. F., Lee F. H., Yet N. S., 'The Role of Particle Breakage in Pile Creep in Sand', Canadian Geotechnical Journal, vol. 33, pp888-898, 1996

72. Lohmander S., Rigdahl M., 'Influence of a Shape Factor of Pigment Particles on the Rheological Properties of Coating Colours', Nordic Pulp Paper Research, 2001

73. Ma J., Yan Y., 'Design and Evaluation of Electrostatic Sensors for the Measurement of Velocity of Pneumatically Conveyed Solids', Flow Measurement and Instrumentation, vol. 11, pp195-204, 2000

74. Malvern FPIA-2100 Brochure, Malvern Instruments, 2005

75. Malvern Instruments website – www.malvern.co.uk

76. Masuda H., Gotoh K., 'Study on the Sample Size Required for the Estimation of Mean Particle Diameter', Advanced Powder Technology, vol. 10, pp159-173, 1999

77. Masuda H., Iinoya K., 'Mean Particle Diameter in an Analysis of a Particulate Process', Mem. Faculty Eng., Kyoto University, vol. 34, pp344-358, 1972

78. Masuda H., Iinoya K., 'Theoretical Study of the Scatter of experimental Data Due to Particle Size Distribution', Journal of Chemical Engineering, vol. 4, pp60-67, 1971

79. Milstein N., 'Image Segmentation by Adaptive Thresholding', Technion – Israel Institute of Technology, www.cs.technion.ac.il, 1998

80. Murai S., Nakamura H., Suzuki Y., 'Analytical Orientation for non-Metric Camera in the Application to Terrestrial Photogrammetry', International Arch. Photogrammetry XXIII, Commission V, pp516-525, 1980.

81. Naithier-Dufour N., Bougeard L., Devaux M., Bertrand D L., Deschault F., 'Comparison of Sieving and Laser Diffraction for the Particle Size Measurements of Raw Materials Used in Foodstuff', Powder Technology, vol. 76, pp191-200, 1993

82. Nakemajema Y., Ind. Eng. Chem. Fundamentals, vol. 6, pp587, 1967

83. Nishino K., Hiroyuki K., Kahoru T., 'Stereo Imaging for Simultaneous Measurement of Size and Velocity of Particles in Dispersed Two-Phase Flow', Measurement Science and Technology, vol. 11, pp633-645, 2000

84. Nishino K., Kasagi N., Hirata M., 'Three-Dimensional Particle Tracking Velocimetry Based on Automated Digital Image Processing', Transactions of the ASME, vol. 111, pp384-391, 1989

85. Nukiyama S., Tanasawa Y., 'Experiments on the Atomisation of Liquids in an Air Stream, Report 3', Trans. SME Japan, vol. 5, pp62-67, 1939

86. Oberdier L. M., 'An Instrumentation System to Automate the Analysis of Fuel-Spray Images using Computer Vision', ASTM, vol. 848, pp 123-136, 1984

87. Odreitz W., Behrens C., 'Seamless quality Management by On-Line Particle Size Analysis using Laser Diffraction Spectrometry', Powder Handling and Processing, vol. 16, pp38-45, 2004

88. Ow C. S., Crane R. I., 'A Simple Off-Line Automatic Image Analysis System with Application to Drop Sizing in Two-Phase Flows', International Journal of Heat and Fluid Flow, vol. 2, pp47-53, 1980

89. Ow C. S., Crane R. I., 'Pattern Recognition Procedures for a Television-Minicomputer Spray Droplet Sizing System', Journal Inst. Energy, vol. 9, pp119-123, 1981

90. Oxford Lasers website – www.oxford-lasers.co.uk

91. Padilla-Sosa P., Moreno D., Guerrero J. A., Funes-Gallanzi M., 'Low-Magnification Particle Positioning for 3D Velocimetry Applications ', Optics and Laser Technology, vol. 34, pp59-68, 2002

92. Pan X. H., Luo R., Yang X. Y., Yang H. J., 'Three-Dimensional Particle Image Tracking for Dilute Particle-Liquid Flows in a Pipe', Measurement Science and Technology, vol.13, pp1206-1216, 2002

93. PharmaVision830 Brochure, Malvern Instruments, 2005

94. Poczeck F., 'A Shape Factor to Assess the Shape of Particles Using Image Analysis', Powder Technology, vol. 93, pp47-53, 1997

95. Pohl M., 'Particle Sizing Moves Form the Lab to the Process', PBE International, pp25-30, May 2001

96. Putorti A. D. (Jr), Everest D., Atreya A., 'Simultaneous Measurements of Drop Size and Velocity in Large-Scale Sprinkler Flows Using Particle Tracking and Laser-Induced Fluorescence', Building and Fire Research Laboratory, U.S. Department of Commerce US National Institute of Standards and Technology, Document: NIST GCR 03-852 (61 pages), 2003

97. Rawle A., 'Basic Principles of Particle Size Analysis', Malvern Instruments Limited, 2001

98. Ricci R. J., Juels R. J., Henley E. J., Cooper H. R., 'A Real Time Particle Size Analyser', 64th national meeting, American Institute of Chemical Engineers, March 1969

99. Rittenhouse G., 'A Visual Method of Estimating Two-Dimensional Sphericity', Journal of Sedimentary Petrology, vol. 13, pp79-81, 1943

100. Sankar S. V., and Bachalo W. D., 'Performance Analysis of Various Phase-Doppler Systems', 4th Int. Congress on optical Particle Sizing, Nuremberg, Germany, 1995

101. Sankur B., Sezgin M., 'Image Thresholding Techniques: A Survey Over Categories', Bogazici University, Istanbul, Turkey, 2002

102. Savakis A. E., 'Adaptive Document Image Thresholding using Foreground and Background Clustering', International Conference on Image Processing 1998 (ICIP98)

103. Shen L., Song X., Murai Y., Iguchi M., Yamamoto F., 'Velocity and Size Measurement of Falling Particles with Fuzzy PTV', Flow Measurement and Instrumentation, vol. 12, pp191-199, 2001

104. Siegel R., Howell J. R., 'Thermal Radiation Heat Transfer', Hemisphere, Washington DC, 1992

105. Sommerfeld M., Ando A., Wennerberg D., 'Swirling Particle Laden Flows Through a Pipe Expansion', Journal of Fluids Engineering, vol. 114, pp648-656, 1992

106. Sommerfeld M., Qiu H. H., 'Characterisation of Particle Laden Confined Swirling Flows by a Phase Doppler Anemometry and Numerical Calculation', International Journal of Multiphase Flow, vol. 19, pp1093-1127, 1993

107. Sommerfeld M., Qiu H. H., 'Detailed Measurements in a Swirling Particulate Two Phase Flow by a Phase Doppler Anemometer', International Journal of Heat and Fluid Flow, vol. 12, pp20-28, 1991

108. Song X., Yamamoto F., Iguchi M., Kato H., Murai Y., Ishii K., Sasaki Y., 'PIV Measurement of Particle Number Rate and Velocity for Falling Particles', ISIJ International, vol. 39, pp471-476, 1999

109. Swithenbank J., Beer J. M., Taylor M., Abbot D., McCreath G. C., 'Laser Diagnostic Technique for the Measurement of Droplet and Particle Size Distributions', Progress in Astronautics and Aeronautics, vol. 53, pp421-447, 1977

110. Tate R. W., 'Some Problems Associated With the Accurate Representation of Droplet Size Distributions', Proceeding of the 1st International Conference on Liquid Atomisation and Spray Systems (ICLASS), pp341-351, 1982

111. The Salt Institute website – http://www.saltinstitute.org/

112. Thomas M. C., Wiltshire R. J., Williams A. T., 'The Use of Fourier Descriptors in the Classification of Particle Shape', Sedimentology, vol. 42, pp635-645, 1995

113. Vallejo L. E., 'Fractal Analysis of Granular Materials', Geotechnique, vol. 45, pp159-163, 1995

114. van de Hulst H. C., 'Light Scattering by Small Particles', Wiley, New York, 1957

115. Wadell H., 'Volume, Shape and Roundness of Rock Particles', Journal of Geology, vol. 40, pp443-451, 1932

116. Wang X., Chang Z., Zhang D., He S., 'Primary Investifgation on Particle Image Velocimetry in Solid-Liquid Two-Phase Flow', Tsinghua University, Beijing, China, 1995

117. Washington C., 'Particle Size Analysis in Pharmaceutics and Other Industries: Theory and Practice', Ellis Horwood, London, 1992

118. Wedd M. W., 'Particle Sizing (on-line) in Crystalization', Analyt. Proc., vol. 30, pp447-449, 1993

119. Weiner B. B., Fairhurst D., 'How to Choose a Particle Size Analyser: Considering Quantitative and Qualitative Needs', Powder Bulk Engineering, vol. 6, pp22-26, 1992

120. Weiss B. A., Derov P., DeBiase D., Simmons H. C., 'Fluid Particle Sizing Using a Fully Automate Optical Imaging System', Optical Engineering, vol. 23, pp561-566, 1984

121. Yan Y., 'Guide to the Flow Measurement of Particulate Solids in Pipelines Part 1: Fundamentals and Principles', Powder Handling and Processing, vol. 13, pp343-352, 2001

122. Yan Y., 'Guide to the Flow Measurement of Particulate Solids in Pipelines Part 2: Utilisation in Pneumatic Conveying and Emission Monitoring', Powder Handling and Processing, vol. 14, pp12-21, 2002

123. Yan Y., 'Mass Flow Measurement of Bulk Solids in Pneumatic Pipelines', Measurement Science and Technology, vol. 7, pp1687-1706, 1996

124. Yan Y., 'Mass Flow Measurement of Pneumatically Conveyed Solids', PhD, University of Teesside, 1992

125. Yang W. Q., Liu S., 'Role of Tomography in Gas/Solids Flow Measurement', Flow Measurement and Instrumentation, vol. 11, pp237-244, 2000

126. Yilmaz A., and Levy E. K., 'Roping Phenomena in Pulverised Coal Conveying Lines', Powder Technology, vol. 95, pp43-48, 1998

127. York J. L., Stubbs H. E., 'Photographic Analysis of Sprays', Trans. ASME, vol. 74, pp1157-1162, 1952

128. Zhang J. Q., Yan Y., 'On-Line Continuous Measurement of Particle Size Using Electrostatic Sensors', Powder Technology, vol.135, pp164-168, 2003

129. Zhang J., Coulthard J., Cheng R., Keech R., 'On-Line Flow Measurement and Control of Pulverised Fuel', Measurement + Control, vol. 37, pp273-275, 2004

Nomenclature

A	Area of the pipe or duct
A_p	Area of a particle
A_{pix}	Area of a particle in pixels
A_{px}	Area of each pixel
A_s	Area occupied by solids
α	Angle used during pincushion correction
$\beta(x,y,t)$	Local solids concentration
$\overline{\beta_s}$	Time averaged solids concentration
$\beta_s(t)$	Volumetric Concentration of Solids
C_{pix}	Circumference of particle in pixels
d	Optical working distance
d'	Distance between flat and imaginary concave objectives during pincushion correction
D	Distance to imaginary concave surface during pincushion correction
D_{diff}	is the difference between the near and far field widths
D_{eq}	Particle equivalent diameter
D_{ff}	Far field objective distance for trapezoid correction
D_{nf}	Near field objective distance
e_{ff}	Depth difference between angular and perpendicular image intercepts
e_{nf}	Difference between D_{nf} and the reference central axis depth, d
ε	Intensity correction factor
γ	Camera viewing angle (deviation from perpendicular with respect to the interrogation surface)
h	Distance from the image centre to the pixel of interest during pincushion correction
h'	Extension to h from the pixel of interest to the new mapped location
I	Transmitted radiance
I_0	Incident radiance
M	Gradient data
n	Number of particles in an image
n_{pix}	Number of pixels in a particle

N_{rad} Number of radii to scanned

P_i Currently interrogated pixel

R_a Aspect ratio

r_{min} Minimum radius length

r_{mean} Mean radius length

r_{max} Maximum radius length

$r_{rms.d}$ RMS deviation of radii lengths

S_b Size distribution bar value, where i is the bar in question

S_F Shape factor

S_u Sizing uncertainty

τ Optical path length

θ Angle used during pincushion correction

θ_{cx} The camera's horizontal viewing angle

θ_{cy} The camera's vertical viewing angle

W Filter window width

W_{rat} The factor by which the current image line must be expanded or contracted for trapezoid correction

x_d Data value

$\overline{x_d}$ Averaged data value

x Horizontal Cartesian dimension

x_{mm} Horizontal size of interrogated area

x_{mmp} Horizontal pixel size in mm

x_{pix} Horizontal image size in pixels

x' Horizontal location referenced to the image centre

x'_{mm} Local x location used during pincushion correction in mm

x_n Mapped horizontal pixel location for distortion correction

x_n' Horizontal new mapped pixel location referenced to the image centre

$x_n'_{mm}$ Horizontal new mapped pixel location in mm

x_y The width represented by the image at a particular vertical location

X_{ff} Far field image width

X_{nf} Near field image width

X_{tot} Horizontal image size in mm

y Vertical Cartesian dimension

y_{mm} Vertical size of interrogated area

y_{mmp} Vertical pixel size in mm

y_{pix} Vertical image size in pixels

y' Vertical location referenced to the image centre

y'_{mm} Local y location used during pincushion correction in mm

y_n Mapped vertical pixel location for distortion correction

y_n' Vertical new mapped pixel location referenced to the image centre

$y_n'_{mm}$ Vertical new mapped pixel location in mm

y_{rat} is the ratio between the current vertical image location

Y_{ff} Far field image height

Y_{nf} Near field image height

Y_{tot} Vertical image size in mm

Z Distance from the focal point to the pixel of interest during pincushion correction

Z_{ff} Height from the central image reference axis to the far field angular intercept Z_{ff}'
Difference between Z_{ff} and the vertical perpendicular image dimension

Z_{nf} Height from the central image reference axis to the near field angular intercept

Z_p Distance from point of interest to imaginary concave surface, in the plane of Z, during pincushion correction

Appendix A

The Definition of Particle Size

A1 Defining the Size of Individual Particles

A particle is a three dimensional object. Such objects require at least three different measurements in order to specify their size (i.e. length, width and height) and even with three measurements a complex shape will not be accurately defined. When information on particle size is required in industry or the laboratory it is convenient to specify the size of particles with a single number. The representation of a complex three dimensional shape with a single number is difficult and there are many ways to achieve this. This topic is widely understood and has been presented many times in the past (good examples being Allen 1992, Black et al. 1996 and Rawle 2001) despite this it will be covered briefly here in the interests of convenience.

Methods for the definition of particle size may be related to a particular physical process, for example the minimum sized square aperture that a particle will pass through is used as the definition for sieve based sizing. In general, however, the realisation that a perfect sphere may be readily and accurately defined by a single number is used and the relationship between a given particle and some form of sphere definition is employed to generate an equivalence diameter. The various equivalent diameters that are commonly employed, along with their definitions, are shown in table A1.

It is clear that many of these definitions are related to a particular measurement technique such as sedimentation and drag diameter. Others, such as volume and area based definitions, are more general and their relevance is more readily understood. Any given definition is not necessarily the best to use in all circumstances as the requirements of the process engineer or scientist vary from application to application. The various definitions will each produce a different numerical result for a given particle (unless the particle is a

perfect sphere) and any one of these may be most relevant to the situation in question. The present work is not concerned with discussing or investigating the benefits of particular definitions of size but rather with the usefulness of a particular sensing strategy. For this reason only one definition is employed in this thesis – projected area – as this lends itself best to imaging based analysis.

Table A1 Various definitions of particle diameter

Symbol	Name	Definition
d_a	Projected area	Diameter of a circle having the same area as a projection of the particle
d_d	Drag diameter	Diameter of a sphere with the same viscous drag as a particle in the fluid with the same velocity
d_F	Feret's diameter	Mean value of the distance between pairs of parallel tangents to the projected outline of the particle
d_M	Martin's diameter	Mean chord length of the projected outline of the particle
d_{max}	-	Diameter of a sphere of the same maximum length
d_{min}	-	Diameter of a sphere of the same minimum length
d_s or d_{sieve}	Sieve diameter	Width of the minimum square aperture through which the particle will pass (or the diameter of the sphere which passes through the same sieve aperture)
d_{sa}	-	Diameter of a sphere of the same surface area
d_{sed}	Sedimentation Diameter	Diameter of a sphere having the same sedimentation rate
d_{St}	Stoke's diameter	Diameter of a sphere of similar density having the same freefall velocity as the particle
d_v	-	Diameter of a sphere of the same volume
d_w	-	Diameter of a sphere of the same weight (assuming similar density)

A2 Particle Size Distribution

When the sizes of all particles in a sample are known (as in the present work) the distribution of sizes may be plotted in the form of a histogram. This data is not always available, however, and in such cases size distribution functions must be employed. Size distribution functions relate mathematically the volume or concentration of particles with their size and represent an elegant and concise way of defining the distribution of particle sizes within a material sample. Such functions also allow the volume of particles outside the measured range to be extrapolated reliably and can provide insight into the process in which the particles are involved (Lefebvre 1989).

The concept behind the use of size distribution functions is that when a particulate material is created (ground etc) or prepared (sieved etc) for a particular use the aim will be to produce particles of a certain mean size (see the next section). Not all of the particles will be of this size but instead the volume of particles will tail off gently to either side of the mean value. The exact nature of this 'tailing off' can be defined mathematically: the simplest and most widely known distribution function is the normal distribution. Whilst the normal distribution is well known it has been found that most powders in industrial conditions, notably pulverised coal, that are produced by grinding, fit a modification of this known as the log-normal distribution (Goodwin and Mitchner 1989, Washington 1992).

The normal and log-normal are the most widely known distribution functions but there are others that have been defined to fit the distributions of other particulate systems. Notably, the Rosin-Rammler function fits fine powders and sprays whilst coarser sprays are better characterised by the Nukiyama-Tanasawa function (Nukiyama and Tanasawa 1939). The topic of distribution functions is covered in some depth, including all necessary equations, by Allen (1992) and details of a number other formulations can be found in Lefebvre (1989) and Kuo (1986).

Distribution functions are used mainly for analysis of data by process engineers and scientists and no discussion on particle size distribution would be complete without mentioning these methods. The present research concentrates on imaging based particle sizing and this method allows exact experimental distributions to be plotted. This means that size distribution functions are not used directly in the work but knowledge of these is essential. If the system generates results that seem to fall in line with a known distribution function for a given material (e.g. log-normal for pulverised coal) then a high degree of confidence in the result can be entertained.

A3 Mean Particle Size

It is often desirable to represent an entire size distribution as a single mean value. The mean is some form of arithmetic average of the data and there are a number of ways to calculate this. Table A2 shows the most common methods.

Table A2 Definitions of mean diameter

Symbol	j, k	Name	Description
d_{10}	1, 0	Arithmetic mean diameter	Normal average particle diameter of the size distribution
d_{20}	2, 0	Surface mean diameter	Diameter of a sphere with the average surface area of the particles in the size distribution
d_{30}	3, 0	Volume mean diameter	Diameter of a sphere with the average volume of the particles in the size distribution
d_{21}	2, 1	Surface diameter	Diameter of a sphere having the surface area of the average particle size in the distribution
d_{31}	3, 1	Volume diameter	Diameter of a sphere having the volume of the average particle size in the distribution
d_{32}	3, 2	Sauter mean diameter or surface area moment mean	Diameter of a sphere with the equivalent surface to volume ratio of all the particles in the size distribution
d_{43}	4, 3	De Brouckere mean, weight mean or volume or mass moment mean	Diameter of a sphere having the same average weight of all the particles in the size distribution

In this table j and k represent the order of terms in the numerator and denominator respectively. Any of the definitions may be of greater importance in a given situation but the choice of which to use is often related to the type of measurement system being employed. Laser diffraction systems, for instance, generally use d_{43} (Rawle 2001). For the present work a calculation of d_{10} is performed within the software, this lending itself best to the data available, but since the particle diameters are in the form of d_a (derived from particle area) the mean calculation may be considered closer to d_{20}.

The mean is not the only single figure representation of particle size distribution that is commonly used. The median value of the data can also be of importance, being the value of particle size that divides the population into two equal halves. The mode value is also often employed, being the highest point on the particulate distribution curve i.e. the most frequently occurring particle size. If a material sample exhibits a symmetrical size distribution function (e.g. a normal distribution) then the three values of mean, median and mode will be the same. This is illustrated in figure A1.

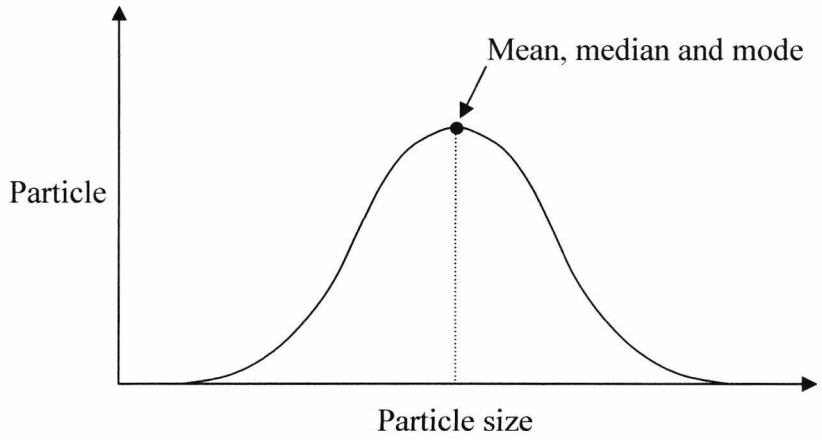

Figure A1 Average values of a normal distribution

It is clear in this case that the three values are interchangeable but this is not always true. In many particulate materials there will be a considerable number of large particles (the intended material size) and these will be accompanied by a certain amount of 'dust' i.e. material that has broken down into tiny particles through abrasion etc. In this case a bimodal distribution is produced, containing two distribution functions and this is where the different averaging techniques are useful – see figure A2.

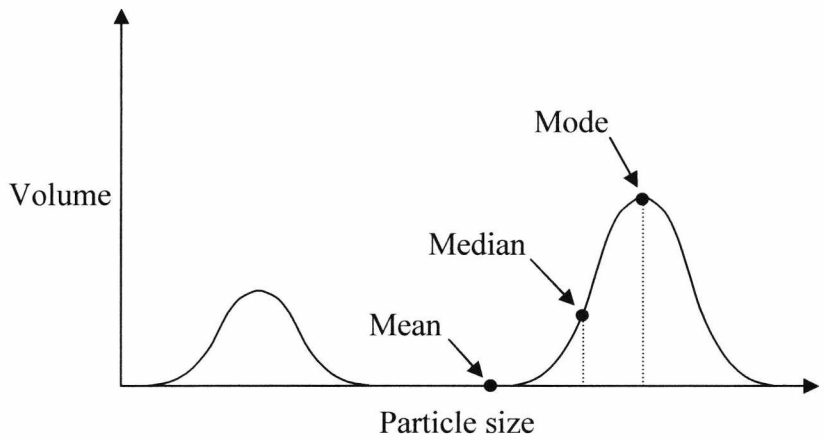

Figure A2 Average values of a bimodal distribution

It can be seen that the mean value indicates a size that is not represented in the particulate population and is therefore misleading. The mode shows the value that is probably of most interest in this case being the peak in the intended particle sizes and the median seems to indicate a useful mean volume value. Clearly these variables are only of interest in data analysis and since for the present work closely controlled materials are used and the emphasis is on the instrumentation a simple arithmetic mean is the only technique employed in this case.

Appendix B

Software Routines

The software written for the project is extensive and operates within the Microsoft Windows environment. To present the software in its entirety would take considerable space and so only key routines will be presented here. General organisation of the software, including the sequence in which processing is applied, has been explained in Chapter 4 and so only the implementation of the processing routines themselves will be presented here. It should be noted that the code below has been edited in order that parts which do not relate directly to the algorithms in question (mainly related to user interface and Windows code) are not shown.

B1 Auto Threshold Level Setting (Chapter 3, section 3.2.3)

```
if(PerformAutoThreshold==TRUE) // the auto thresholding loop - tries various levels
{
        double RawData[254]; // for storing raw input data
        for(int i=0;i<=253;i++) // initialise
                RawData[i]=NULL;

        char string[25]; // for user prompts

        // setup Matrox drawing colours (for graph)
        MgraColor(M_DEFAULT, M_RGB888(0,0,0));
        MgraBackColor(M_DEFAULT, M_RGB888(254,248,222));

        for(i=0;i<=253;i++) // collect the raw data
        {
                MbufGet(MilGrabBuffer,ImageProcessor.GetFrameBuffer()); // refresh the
                input buffer
                ImageProcessor.SetThresholdLevel(i+1);
                ImageProcessor.ThresholdHigher();
                ImageProcessor.FindParticleParameters();
                RawData[i]=double(ImageProcessor.GetTotalParticles());
                sprintf(string,"Collecting data...");
                SetWindowText(GetDlgItem(gTHprogDLG,IDT_THPTXT),string);
```

```
int before=NULL;
int after=NULL;
int FilterHalfWidth=10;
double SmoothedData[254]; // for storing filtered data
for(i=0;i<=253;i++) // initialise
        SmoothedData[i]=NULL;

for(i=0;i<=253;i++) // filter the data
{
        for(int ic=0;ic<FilterHalfWidth;ic++) // filtering loop
        {
                before=i-ic; // set up the range
                after=i+ic;
                if(before<0)(before=0); // limit the values
                if(after>253)(after=253);
                SmoothedData[i]=SmoothedData[i]+RawData[before]+RawData[afte
                r];
        }

        SmoothedData[i]=(SmoothedData[i]+RawData[i])/((FilterHalfWidth*2)+1
        );
        sprintf(string,"Filtering data...");
        SetWindowText(GetDlgItem(gTHprogDLG,IDT_THPTXT),string);
}
double Gradient[254]; // for storing gradient data
for(i=0;i<=253;i++) // initialise
        Gradient[i]=NULL;
before=NULL;
after=NULL;
for(i=0;i<=253;i++) // find the gradient
{
        before=i-3;
        after=i+3;
        if(before<0)(before=0); // limit the values
        if(after>253)(after=253);
        Gradient[i]=(SmoothedData[after]-SmoothedData[before]);
        sprintf(string,"Processing data...");
        SetWindowText(GetDlgItem(gTHprogDLG,IDT_THPTXT),string);
}

CreateAxes(); // a routine that draws the axes for graph display
int Xprev=NULL;
int Yprev=NULL;
MgraColor(M_DEFAULT, M_RGB888(0,0,255));
for(i=0;i<=253;i++) // plot the raw data on a LOG Y scale
{
        double temp=((log10(RawData[i]/1000))*67)+200;
        int temp2=int(temp);
        if (temp2<1)(temp2=1);
        temp2=200-temp2+20;
```

```
        MgraDot(M_DEFAULT,MilTGImage,(i+100),temp2); // draws dots…
}
Xprev=NULL;
Yprev=NULL;
MgraColor(M_DEFAULT, M_RGB888(0,128,0));
for(i=0;i<=253;i++) // plot the filtered data on a LOG Y scale
{
        double temp=((log10(SmoothedData[i]/1000))*67)+200;
        int temp2=int(temp);
        if (temp2<1)(temp2=1);
        temp2=200-temp2+20;
        if(Xprev==NULL){Xprev=(i+100); Yprev=temp2;}
        MgraLine(M_DEFAULT,MilTGImage,Xprev,Yprev,(i+100),temp2);
        Xprev=i+100;
        Yprev=temp2;
}

bool NegFound=FALSE;
bool PosFound=FALSE;
bool Point1Found=FALSE;
bool Point2Found=FALSE;
double TempGrad=NULL;
int point1=NULL;
int point2=NULL;
for(i=0;i<=253;i++) // find the points of interest (systematic search)
{
        if(PosFound==FALSE) // look for the first high peak
        {
                if(Gradient[i]>=5)
                {
                        PosFound=TRUE;
                }
        }
        else
        {
                if(NegFound==FALSE) //look for the first peak falling off
                {
                        if(Gradient[i]<-5)
                        {
                                NegFound=TRUE;
                        }
                }

                if((Point1Found==FALSE)&&(NegFound==TRUE)&&(Gradient[i]>-
                0.25)) // point 1
                {
                        point1=i;
                        Point1Found=TRUE;
                        TempGrad=Gradient[i];
                }
```

```
                        if((Point1Found==TRUE)&&(Point2Found==FALSE)&&(Gradient[i]>(
                        TempGrad+0.5))) // point 2
                        {
                                point2=i;
                                Point2Found=TRUE;
                        }
                }
        }
        if(Point2Found==FALSE)(point2=254);
        if(Point1Found==FALSE)(point1=254);
        MgraColor(M_DEFAULT, M_RGB888(255,0,0)); // plot the points
        double ntemp=((log10(SmoothedData[point1]/1000))*67)+200;
        int ntemp2=int(ntemp);
        ntemp2=200-ntemp2+20;
        MgraArc(M_DEFAULT,MilTGImage,(point1+100),ntemp2,5,5,0,360);
        ntemp=((log10(SmoothedData[point2]/1000))*67)+200;
        ntemp2=int(ntemp);
        ntemp2=200-ntemp2+20;
        MgraArc(M_DEFAULT,MilTGImage,(point2+100),ntemp2,5,5,0,360);

        if(point1==point2)
        {
                MessageBox(gTGWind,"Image unsuitable for auto
                thresholding","Failed!",MB_OK|MB_ICONWARNING);
        }
        else
        {
                sprintf(string,"Values chosen are %d and %d. \n Proceed using these
                values?",point1, point2);
                if(MessageBox(gTGWind,string,"Proceed?",MB_YESNO|MB_ICONQUESTION)
                ==IDYES)
                {
                        ThresholdLow=point1;
                        ThresholdHigh=point2;
                        sprintf(string,"%d",ThresholdLow);
                        SetWindowText(GetDlgItem(gProcessingDLG,IDED_THRESHOLDLOW),s
                        tring);
                        sprintf(string,"%d",ThresholdHigh);
                        SetWindowText(GetDlgItem(gProcessingDLG,IDED_THRESHOLDHIGH),
                        string);
                }
        }
        PerformAutoThreshold=FALSE;// finished here...
} // end of auto threshold
```

B2 Particle Scanning (Chapter 3, section 3.2.3)

```
int ImageProcessing::FindParticleParameters()//finds number of particles and size
information etc
{
	long x=NULL; // x/y location
	long y=NULL;

	unsigned char temp=NULL;

	TotalParticles=NULL;// reset particle counter for this pass

	while (y<ImageHeight)
	{
		while (x<ImageWidth)
		{
			temp=*(Image+x+(y*ImageWidth));// get pixel value
			if ((temp==NULL)&&(TotalParticles<MaxParticles)) // has a particle
			been encountered ?
			{
				TotalParticles++; // increase particle count
				ParticleList[TotalParticles-1].MinX=x;
				ParticleList[TotalParticles-1].MinY=y;
				ParticleList[TotalParticles-1].MaxX=NULL;
				ParticleList[TotalParticles-1].MaxY=NULL;
				ParticleList[TotalParticles-1].Pixels=NULL;
				ParticleList[TotalParticles-1].CentroidX=NULL;
				ParticleList[TotalParticles-1].CentroidY=NULL;
				ParticleList[TotalParticles-1].MaxHeight=NULL;
				ParticleList[TotalParticles-1].MaxWidth=NULL;

				ParticleScan(x,y); // find particle parameters

				if(ParticleList[TotalParticles-
				1].Pixels<=IgnoreSize)(TotalParticles--);
				else
				{
					ParticleList[TotalParticles-
					1].MaxWidth=(ParticleList[TotalParticles-1].MaxX-
					ParticleList[TotalParticles-1].MinX);
					ParticleList[TotalParticles-
					1].MaxHeight=(ParticleList[TotalParticles-1].MaxY-
					ParticleList[TotalParticles-1].MinY);
					ParticleList[TotalParticles-
					1].CentroidX=(ParticleList[TotalParticles-
					1].MaxWidth/2)+ParticleList[TotalParticles-1].MinX;
					ParticleList[TotalParticles-
					1].CentroidY=(ParticleList[TotalParticles-
					1].MaxHeight/2)+ParticleList[TotalParticles-1].MinY;
				}
```

```
                }
                x++; // horizontal counter
            }
            x=NULL;//back to the start of the line
            y++; //vertical counter
        }
        return NULL;
} // end of particle parameter scan


void LeanMeanImageProcessing::ParticleScan(long x, long y) //scans particle and finds
size, position etc (called from particle parameter scan routine)
{
        // create a stack pointer
        long stackpointer=NULL;
        long seed=NULL,temp=NULL,size=(ImageWidth*ImageHeight);
        long CurrentX=NULL,CurrentY=NULL;

        // initial location has been given to us
        stack[stackpointer]=x+(y*ImageWidth);

        while(stackpointer>=NULL)//search until there is nowhere left to look
        {
            if(*(Image+(stack[stackpointer]))==NULL) // is the current location valid?
            {
                *(Image+(stack[stackpointer]))=128; // fill the current location

                // particle parameters must be updated...
                // starting with size
                ParticleList[TotalParticles-1].Pixels++;

                // now the current cartesian location must be found...
                CurrentX=stack[stackpointer]%ImageWidth;
                CurrentY=(stack[stackpointer]-CurrentX)/ImageWidth;

                // ...so that the particle co-ords can be updated
                if((ParticleList[TotalParticles-
                1].MaxX)<CurrentX)((ParticleList[TotalParticles-1].MaxX)=CurrentX);
                if((ParticleList[TotalParticles-
                1].MaxY)<CurrentY)((ParticleList[TotalParticles-1].MaxY)=CurrentY);
                if((ParticleList[TotalParticles-
                1].MinX)>CurrentX)((ParticleList[TotalParticles-1].MinX)=CurrentX);
                if((ParticleList[TotalParticles-
                1].MinY)>CurrentY)((ParticleList[TotalParticles-1].MinY)=CurrentY);

                // we must now search all around for other valid pixels...
                seed=stack[stackpointer]; // make a note of the seed location

                // look at the x+1 location - but only if its within the image
                temp=seed+1;
                if((temp>=NULL)&&(temp<size)) (stack[stackpointer]=temp);
```

```
                    else (stackpointer--);

                    // look at the y+1 location - again, with error checking
                    temp=seed+ImageWidth;
                    if((temp>=NULL)&&(temp<size)){stackpointer++;
                    stack[stackpointer]=temp;}

                    // x-1 - with error checking
                    temp=seed-1;
                    if((temp>=NULL)&&(temp<size)){stackpointer++;
                    stack[stackpointer]=temp;}

                    // y-1 - with error checking
                    temp=seed-ImageWidth;
                    if((temp>=NULL)&&(temp<size)){stackpointer++;
                    stack[stackpointer]=temp;}
            }
            else(stackpointer--); //not a valid location so decrement the stack pointer
        }
}//end of particle scan
```

B3 Particle Shape Measurement (Chapter 3, section 3.4.3)

```
int ImageProcessing::FindAspectRatios()//finds the aspect ratios and shape factors of all
the particles in the image
{
        long i=NULL; //particle counter
        int n=NULL; // radii counter
        long Max=NULL;
        long Min=ImageWidth;
        long Xoff=NULL;
        long Yoff=NULL;
        long X=NULL;
        long Y=NULL;
        double MaxTheta=NULL;
        double MinTheta=NULL;
        double Theta=NULL;
        double mean=NULL;
        double RMStemp=NULL;
        double ShapeFactor=NULL;
        int* lengths=NULL;
        unsigned char temp=NULL;
        int Lpos=NULL;
        int Lneg=NULL;
        int LnegMax=NULL;
        int LnegMin=NULL;
        int L=NULL;
```

```
while(i<(ImageWidth*ImageHeight))// most of the image will be a direct copy
{
        *(ImageNew+i)=*(Image+i);
        i++;
}
i=NULL;

if(TotalParticles!=NULL) // prevents unnecessary execution
{
        while(i<TotalParticles)// goes through all the particles
        {

                AspectRadii=(int)(2.0*3.1415927*sqrt((double)ParticleList[i].Pixels
                /3.1415927));
                lengths = new int [AspectRadii];
                ZeroMemory(lengths,sizeof(lengths));

                while(n<AspectRadii)// goes through all the particle radii
                {
                        Theta=(PI/AspectRadii)*(double)n;

                        while(temp<=128)// scans half of the current radii
                        {
                                Xoff=(long)((double)Lpos*cos(Theta));
                                Yoff=(long)((double)Lpos*sin(Theta));
                                X=ParticleList[i].CentroidX+Xoff;
                                Y=ParticleList[i].CentroidY-Yoff;

                                if((X>=ImageWidth)||(Y>=ImageHeight)||(X<NULL)||(Y<N
                                ULL))(temp=255);
                                else
                                {
                                        temp=*(Image+X+(Y*ImageWidth));
                                }
                                Lpos++;
                        }
                        *(ImageNew+X+(Y*ImageWidth))=NULL; // show the end point

                        temp=NULL;
                        while(temp<=128)// scans the other half of the current radii
                        {
                                Xoff=(long)((double)Lneg*cos(Theta));
                                Yoff=(long)((double)Lneg*sin(Theta));
                                X=ParticleList[i].CentroidX-Xoff;
                                Y=ParticleList[i].CentroidY+Yoff;

                                if((X>=ImageWidth)||(Y>=ImageHeight)||(X<NULL)||(Y<N
                                ULL))(temp=255);
                                else
                                {
                                        temp=*(Image+X+(Y*ImageWidth));
```

```
                }
                Lneg++;
        }
        *(ImageNew+X+(Y*ImageWidth))=NULL; // show the end point
        if((Lpos+Lneg)>Max){Max=(Lpos+Lneg); MaxTheta=Theta;
        LnegMax=Lneg;}
        if((Lpos+Lneg)<Min){Min=(Lpos+Lneg); MinTheta=Theta;
        LnegMin=Lneg;}
        lengths[n]=(Lpos+Lneg);// store the lengths for shape factor
        Lpos=NULL;
        Lneg=NULL;
        temp=NULL;
        n++;
}
n=NULL;

// calculate shape factor
// first find the mean radii length
while(n<AspectRadii)
{
        mean=mean+(double)lengths[n];
        n++;
}
mean=mean/AspectRadii;
n=NULL;

// now find the RMS deviation of the maximum and minimum radii
RMStemp=pow((Max-mean),2.0);
RMStemp=RMStemp+pow((mean-Min),2.0);
RMStemp=sqrt(RMStemp/2.0);

// shape factor is the deviation divided by the mean
ShapeFactor=RMStemp/mean;
ParticleList[i].ShapeFactor=ShapeFactor; // store the result

ZeroMemory(lengths,sizeof(lengths));
mean=0;
RMStemp=0;
ShapeFactor=0;

// draw the radii (for aspect ratio)
Theta=MaxTheta;
while(L<=Max)
{
        Xoff=(long)((double)L*cos(Theta));
        Yoff=(long)((double)L*sin(Theta));
        X=(ParticleList[i].CentroidX-
        ((long)((double)LnegMax*cos(Theta))))+Xoff;

        Y=(ParticleList[i].CentroidY+((long)((double)LnegMax*sin(The
        ta))))-Yoff;
```

```
                        if(X>=ImageWidth)(X=ImageWidth-1);
                        if(X<NULL)(X=NULL);
                        if(Y>=ImageHeight)(Y=ImageHeight-1);
                        if(Y<NULL)(Y=NULL);
                        *(ImageNew+X+(Y*ImageWidth))=96;
                        L++;
                }
                L=NULL;
                Theta=MinTheta;
                while(L<=Min)
                {
                        Xoff=(long)((double)L*cos(Theta));
                        Yoff=(long)((double)L*sin(Theta));
                        X=(ParticleList[i].CentroidX-
                        ((long)((double)LnegMin*cos(Theta))))+Xoff;
                        Y=(ParticleList[i].CentroidY+((long)((double)LnegMin*sin(The
                        ta))))-Yoff;
                        if(X>=ImageWidth)(X=ImageWidth-1);
                        if(X<NULL)(X=NULL);
                        if(Y>=ImageHeight)(Y=ImageHeight-1);
                        if(Y<NULL)(Y=NULL);
                        *(ImageNew+X+(Y*ImageWidth))=96;
                        L++;
                }
                L=NULL;
                MaxTheta=NULL;
                MinTheta=NULL;
                LnegMax=NULL;
                LnegMin=NULL;

                if(Max!=NULL)(ParticleList[i].AspectRatio=((double)Min/(double)Max)
                ); //prevents divide by zero errors and records result
                Max=NULL;
                Min=ImageWidth;
                i++;
        }
        delete lengths;
    }

    FlipBuffers();
    return NULL;
} // end of shape routine
```

B4 Lens Distortion Correction (Chapters 4 and 5, sections 4.4.3.1 and 5.3.2)

```
int ImageProcessing::CreateLensDistortionMatrix()
{
	if(DistortionMatrix==NULL) // allocate memory for the geometric distortion matrix
	// - only needs to be done once
	{
		DistortionMatrix=new long[ImageWidth*ImageHeight];
		if(DistortionMatrix==NULL)
		{
			return MemoryError;
		}
	}// end of memory allocation

	if(PincushionBrightnessMatrix==NULL) // allocate memory for brightness correction
	// - only needs to be done once
	{
		PincushionBrightnessMatrix=new float[ImageWidth*ImageHeight];
		if(DistortionMatrix==NULL)
		{
			return MemoryError;
		}
	}// end of memory allocation

	SetWidthHeightmm(); // sets the global image width and height in mm variables

	long	xtot=ImageWidth;// width of image in pixels
	long	ytot=ImageHeight;// height of image in pixels
	double	d=LensDistancemm; // mm from camera to flow
	double	Theta=LensAngleRadians; // lens angle
	double	HalfTheta=Theta/2; // required in equations

	double	Xtot=((2*d)*(tan(HalfTheta))); // width of image in mm
	double	mmPerPixel=(Xtot/xtot);
	double	Ytot=(mmPerPixel*ytot);
	double	h=sqrt((ImageWidth*ImageWidth)+(ImageHeight*ImageHeight));
	double	hmm=(Xtot/ImageWidth)*h;
	double	D=(sqrt((d*d)+((hmm/2)*(hmm/2))))-ImperfectionFactor;//radius of view in mm

	double	xqmm=NULL; // working variables
	double	yqmm=NULL;
	double	Xo=NULL;
	double	Yo=NULL;
	double	Alpha=NULL;
	double	Beta=NULL;
	double	z=NULL;
	double	zp=NULL;
	double	ext=NULL;
	double	ynqmm=NULL;
	double	xnqmm=NULL;
```

```
double  qh=NULL;

long xnq=NULL;
long ynq=NULL;
long xn=NULL;
long yn=NULL;
long x=NULL;
long y=NULL;
long xq=NULL;
long yq=NULL;
long i=NULL;
while(y<ytot)// processing loop
{
        while(x<xtot)// line processing loop
        {
                xq=((xtot/2)-x); // processing equations, correct in first quadrant
                yq=((ytot/2)-y);
                xqmm=(xq*mmPerPixel);
                yqmm=(yq*mmPerPixel);
                qh=sqrt(((xqmm*xqmm)+(yqmm*yqmm)));
                z=sqrt(((qh*qh)+(d*d)));
                zp=(D-z);
                Alpha=acos((d/z));
                ext=((tan(Alpha))*zp);
                Beta=atan((yqmm/xqmm));
                xnqmm=((ext+qh)*cos(Beta));
                ynqmm=sqrt(((ext+qh)*(ext+qh))-(xnqmm*xnqmm));
                xnq=(long)(xnqmm/mmPerPixel); // type casting to avoid data loss...
                ynq=(long)(ynqmm/mmPerPixel);
                xn=((xtot/2)-xnq);
                yn=((ytot/2)-ynq);

                if(x>(xtot/2))(xn=(xtot/2)+((xtot/2)-xn));// correct the value for
                other quadrants
                if(y>(ytot/2))(yn=(ytot/2)+((ytot/2)-yn));

                if((xn>NULL)&&(xn<xtot)&&(yn>NULL)&&(yn<ytot))
                {
                        *(DistortionMatrix+i)=((yn*xtot)+xn);// record the results
                        in the distortion matrix
                        *(PincushionBrightnessMatrix+i)=((float)z/(float)d);
                }
                else
                {
                        *(DistortionMatrix+i)=NULL; // if out of range use NULL
                        *(PincushionBrightnessMatrix+i)=NULL;
                }

                x++;
                i++;
        }//end of line processing loop
```

```
                x=NULL;
                y++;

        }// end of processing loop
        return NULL;
} // end of distortion matrix generation
int ImageProcessing::CorrectLensDistortion()// uses distortion matrix to process an image
{
        AllocBackBuffer(); // will allocate memory for the new image if necessary

        long i=NULL;
        long Size=(ImageWidth*ImageHeight);
        long temp=NULL;
        unsigned char brightness=NULL;
        unsigned int TempImage=NULL;

        while (i<Size)//processing loop
        {
                temp=*(DistortionMatrix+i);
                brightness=(unsigned char)(0+((*(PincushionBrightnessMatrix+i)*255)-255));
                TempImage=((*(Image+temp)));// find the new pixel values
                if(TempImage>255)(TempImage=255); //clip the values
                *(ImageNew+i)=(unsigned char)TempImage;// store the corrected result
                i++;
        }//end of processing loop

        FlipBuffers();
        return NULL;
}
```

B5 Rope Detector (Chapter 5, section 5.4.2)

```
int ImageProcessing::DoRope()// rope detector function
{
        AllocRopeBuffer(); // will allocate memory for the new image if necessary

        long i=NULL;
        long Size=(ImageWidth*ImageHeight);
        int TempRope=NULL;
        long y=NULL;
        long x=NULL;
        double results[9];
        double Max=NULL;
        double Min=300;
        double Mean=NULL;
        ZeroMemory(results,sizeof(results));
        long ZoneSize=(128*96);
```

```
int MaxZone=NULL;

while (i<Size)//decay processing loop
{
        TempRope=int(*(Rope+i)); // get the current pixel value
        if(*(Image+i)<=unsigned char(TempRope))(*(Rope+i)=*(Image+i));//peak detect
        else // no peak - then decay the pixel (toward white)
        {
                TempRope=TempRope+RopeDecay;
                if (TempRope>255)(TempRope=255);
                *(Rope+i)=unsigned char(TempRope);
        }

        i++;
}//end of decay processing loop

// now scan the roping zones to find the concentrations and display the zone edges
i=NULL;

while(y<ImageHeight)// processing loop
{
        while(x<ImageWidth)// line processing loop
        {
                if((x>=0)&&(x<256)&&(y>=0)&&(y<192))
                        (results[0]=results[0]+(255.0-*(Rope+i)));
                if((x>=256)&&(x<512)&&(y>=0)&&(y<192))
                        (results[1]=results[1]+(255.0-*(Rope+i)));
                if((x>=512)&&(x<768)&&(y>=0)&&(y<192))
                        (results[2]=results[2]+(255.0-*(Rope+i)));
                if((x>=0)&&(x<256)&&(y>=192)&&(y<384))
                        (results[3]=results[3]+(255.0-*(Rope+i)));
                if((x>=256)&&(x<512)&&(y>=192)&&(y<384))
                        (results[4]=results[4]+(255.0-*(Rope+i)));
                if((x>=512)&&(x<768)&&(y>=192)&&(y<384))
                        (results[5]=results[5]+(255.0-*(Rope+i)));
                if((x>=0)&&(x<256)&&(y>=384)&&(y<576))
                        (results[6]=results[6]+(255.0-*(Rope+i)));
                if((x>=256)&&(x<512)&&(y>=384)&&(y<576))
                        (results[7]=results[7]+(255.0-*(Rope+i)));
                if((x>=512)&&(x<768)&&(y>=384)&&(y<576))
                        (results[8]=results[8]+(255.0-*(Rope+i)));
                x++;
                i++;
        }//end of line processing loop
        x=NULL;
        y++;
}// end of processing loop

i=NULL;
```

```
        // divide by pixels in zone to find mean luminance
        while(i<9)
        {
                results[i]=results[i]/ZoneSize;
                i++;
        }

        i=NULL;
        RopeStatus=NULL;

        // find stats
        while(i<9)
        {
                if(results[i]>Max){ Max=results[i]; MaxZone=(i+1);}
                if(results[i]<Min)(Min=results[i]);
                Mean=Mean+results[i];
                i++;
        }

        Mean=Mean/9;

        // decide on result
        if((Mean<(Min+((Max-Min)/2)))&&(((Max-Min)/2)>=Min))(RopeStatus=MaxZone);
        else(RopeStatus=NULL);

        if(Min<1.0)(RopeCertainty=TRUE);
        else(RopeCertainty=FALSE);

        return NULL;
}// end of roping detector
```

Publications and Dissemination

Results achieved during the course of the work have been published as journal papers (1-3) and presented at both international conferences (4-7) and national meetings and seminars (8-16). Papers marked * are appended to the end of this thesis for reference.

1. Carter R. M. and Yan Y., 'An Instrumentation System Using Combined Sensing Strategies for On-Line Mass Flow Rate Measurement and Particle Sizing', IEEE Transactions, (in press) 2005

2. *Carter R. M., Yan Y., and Cameron S. D., 'On-Line Measurement of Particle Size Distribution and Mass Flow Rate of Particles in a Pneumatic Suspension Using Combined Imaging and Electrostatic Sensors', Special Issue of Flow Measurement and Instrumentation, (in press) 2005

3. *Carter R. M. and Yan Y., 'On-line Particle Sizing of Pulverised and Granular Fuels using Digital Imaging Techniques', Measurement Science and Technology, vol. 14, pp1099-1109, 2003

4. Carter R. M. and Yan Y., 'An Instrumentation System Using Combined Sensing Strategies for On-Line Mass Flow Rate Measurement and Particle Sizing', Proceedings of the 2004 IEEE Instrumentation and Measurement Technology Conference, Como, Italy, May 2004

5. Carter R. M. and Yan Y., 'On-Line Measurement of Pulverised Fuel Fineness Using Digital Imaging', 5th European Conference on Coal Research & Its Applications , Edinburgh, 2004

6. Carter R. M. and Yan Y., 'Concurrent Measurement of Mass Flow Rate and Size Distribution of Pneumatically Conveyed Particles Using Combined Electrostatic and Digital Imaging Sensors', Proceedings of Sensors and Their Applications XII, Limerick University, Ireland, 2003

7. Carter R. M. and Yan Y., 'Measurement of Solids Concentration in Dilute Phase Particulate Flows Using Digital Imaging Techniques', Proceedings of Sensors and Their Applications XI, City University, London, 2001

8. Carter R. M. and Yan Y., 'Digital Imaging Based On-line Measurement of Size Distribution and Mass Flow Rate of Pulverised Coal', Coal Research Forum Meeting, University of Nottingham, 2005

9. Carter R. M. and Yan Y., 'Monitoring of Pulverised Fuel Flows for Combustion Optimisation Using Advanced Digital Imaging Techniques', SET for Britain, House of Commons, London, March 2004 (won a commendation award)

10. Carter R. M. and Yan Y., 'Emissions Reduction for Coal Fired Power Generation Through Digital Image Processing Based Fuel Monitoring', SET for Britain, House of Commons, London, December 2004

11. Carter R. M. and Yan Y., 'On–Line Measurement of Size Distribution and Concentration of Pulverised Fuel Using Digital Imaging Techniques', BCURA Autumn Meeting, Whetstone, Leicestershire, 2003

12. Carter R. M. and Y Yan., 'Concurrent Measurement of Mass Flow Rate and Size Distribution of Pneumatically Conveyed Particles Using Combined Electrostatic and Digital Imaging Sensors', 1st School of Engineering Research Conference, University of Greenwich, 2003

13. Carter R. M. and Yan Y., 'On-Line Measurement of Pulverised Fuel Fineness Using 3D Digital Imaging Techniques', 4th UK Meeting on Coal and its Applications, Coal Research Forum, Imperial College, London, 2002

14. Carter R. M. and Yan Y., 'On-line Measurement of Pulverized Fuel Fineness Using Digital Imaging Techniques', Combustion Institute (British section) Spring Meeting, London, 2002 (won the prize for best poster)

15. Carter R. M. and Yan Y., 'On-line Measurement of Pulverized Fuel Fineness Using Digital Imaging Techniques', One Day Combustion Related Seminar, Institute of Physics, London, October 2002

16. *Carter R. M., Yan Y. and Tomlins K., 'Digital Imaging Based Classification and Authentication of Granular Food Products', One Day Seminar: Sensors and Instrumentation Systems for the Food and Beverage Industries, Institute of Physics, London, December 2004

JFMI: 398 | DTD 5 | pp. 1–6 (col. fig: NIL)

ARTICLE IN PRESS

Available online at www.sciencedirect.com
SCIENCE DIRECT®

ELSEVIER

Flow Measurement and Instrumentation xx (xxxx) xxx–xxx

Flow Measurement and Instrumentation

www.elsevier.com/locate/flowmeasinst

On-line measurement of particle size distribution and mass flow rate of particles in a pneumatic suspension using combined imaging and electrostatic sensors

Robert M. Carter[a], Yong Yan[a,*], Stuart D. Cameron[b]

[a] *Department of Electronics, University of Kent, Canterbury, Kent CT2 7NT, UK*
[b] *Mitsui Babcock Energy Ltd, Porterfield Road, Renfrew, Glasgow PA4 8DJ, UK*

Received 28 February 2005; received in revised form 23 March 2005; accepted 31 March 2005

Abstract

This paper presents a novel instrumentation system that uses a combination of electrostatic and digital imaging sensors in order to achieve these goals. The results of experimental trials using the system are presented and discussed. An inferential approach is adopted for the mass flow measurement of particles, velocity and volumetric concentration of particles being measured independently. The velocity of particles is determined by cross correlating two signals derived from a pair of electrostatic sensors and the volumetric concentration of particles is obtained using a novel digital imaging sensor, which also provides particle size distribution data. The basic principles and limits of operation of the imaging sensor are discussed and explained. Results obtained from a pneumatic conveyor are presented which demonstrate good performance of the measurement system for both mass flow metering (accurate to about ±6%) and particle sizing (reliable to around ±2.5%). Particle size distribution results are also included and the insensitivity of particle sizing to changes in velocity and concentration is assessed. In addition on-line sizing results are compared to off-line results, measured using an accepted laser diffraction based instrument, and good agreement is observed. In general, the results obtained are encouraging and the system shows great promise.

Keywords: Particulate flow; Pneumatic conveying; Imaging; Electrostatic; Mass flow rate; On-line; Size distribution

1. Introduction

The importance of efficient pneumatic conveyance of particulate materials is widely accepted in many industries. In order for such systems to achieve their full potential it is necessary to measure parameters of the flow such as particle size distribution and mass flow rate. Ideally this should be achieved without affecting the flow in any way. Much research work has been carried out in the field of particulate flow metering [1] and a wide range of techniques have been developed [2]. Instruments based on these techniques are designed to measure various flow parameters but few of them can measure absolute mass flow rate of particles and/or particle size distribution on an on-line continuous basis [2,3].

It is clear that an instrumentation system must be developed that can measure these important parameters on-line and that can be installed in a non-intrusive manner. A novel digital imaging based system capable of measuring particle size distribution and volumetric concentration of particles in the manner required has been developed already [4]. When combined with electrostatic velocity metering technology [5], it is possible to derive absolute mass flow rate. The volumetric concentration of particles is measured by the imaging sensor and the velocity of particles derived from the electrostatic instrument. These two quantities are combined, along with absolute material density, to derive the mass flow rate. This paper presents the basic concepts of both imaging and electrostatic techniques

* Corresponding author.
E-mail address: y.yan@kent.ac.uk (Y. Yan).

0955-5986/$ - see front matter © 2005 Published by Elsevier Ltd
doi:10.1016/j.flowmeasinst.2005.03.005

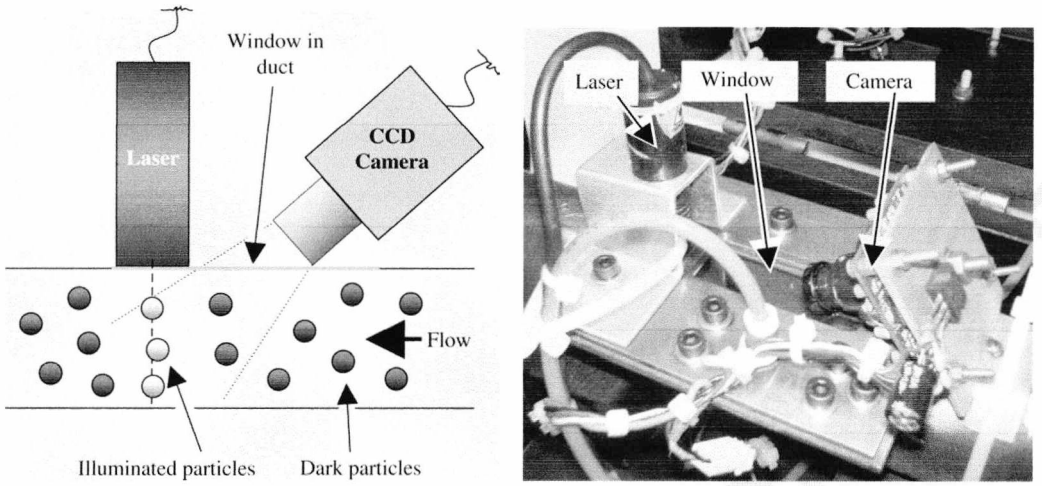

(a) Basic concept. (b) Physical implementation.

Fig. 1. Imaging sensor.

and their novel, complimentary, combination along with experimental results demonstrating the effectiveness of the methodology. The intention here is to develop a system that is worth more than the sum of its parts. Electrostatic sensors, whilst offering proven reliability for velocity measurement, are unsuitable for absolute measurement of mass flow rate due to the high unpredictability of the magnitude of electrostatic charge found on the particles. An imaging based approach, on the other hand, is well suited to performing particle sizing and concentration measurements. Whilst the measurement of particle velocity is possible with some imaging techniques [7], these systems use a different sensing arrangement to the present system and are often optimised for experimental study of turbulence and other such phenomena rather than industrial metering applications. It is believed to be more cost-effective and practical to use electrostatic sensing for velocity measurement than it would be to attempt to perform size, velocity and concentration measurement with the same imaging sensor. The main novelty of the work presented here lies in the novel and effective combination of sensor types rather than the techniques themselves.

2. Measurement principles

The present work focuses on the combination of sensor types rather than the individual techniques—in depth descriptions of the sensors have been reported elsewhere. In view of this only a brief description of the hardware will be given here in the interests of convenience and clarity.

2.1. Digital imaging sensor

Particles flowing through a pipeline can be illuminated using a laser sheet to highlight a 'slice' through the flow. Images of that slice can be acquired using a CCD camera. The basic concept and physical implementation are illustrated in Fig. 1. Once the images have been obtained, digital image processing techniques can be applied to extract information such as particle size distribution and absolute solids concentration. Such a system has been found capable, in its present form, of achieving a basic accuracy of $\pm 1.5\%$ when used with particles in the 150 μm to 25 mm range [4]. Since full details of operation for the imaging sensor have been described elsewhere [4] only a brief summary of the operating principles and limitations of this novel sensor will be given here in the interests of convenience. It should be noted that in previous work [4] the camera was mounted perpendicular to the laser sheet rather than at the angle shown here. This change in interrogation angle is not a severe problem with the optical set-up used (the angle is exaggerated in Fig. 1(a) for clarity) and any trapezoidal distortion is corrected in system software. Another point of interest is that images of particles are not necessarily instantaneous but rather represent accumulated cross sections as the particles pass through the laser sheet—a fast shutter speed is not, therefore, necessary.

Once images of the flow are available they must be processed in order to extract the necessary information. It is this processing that represents the heart of the imaging sensor. After image acquisition it is first necessary to correct the images for any distortion that may arise due to the lens arrangement etc. (typically there will be both 'pincushion' and 'trapezoid' or 'barrel' distortion present in the images). Individual particles must now be detected within the images. This is achieved through the contrast enhancement of images by the application of a high-pass algorithm (which takes advantage of the interlaced nature of the video frames) followed by a novel adaptive thresholding technique tailored specifically toward particle imaging applications [4]. Once the image has been segmented into background and particles it is necessary to count, size and otherwise assess the various particles. It is then a simple matter to determine various statistical quantities such as mean size, concentration and size distribution.

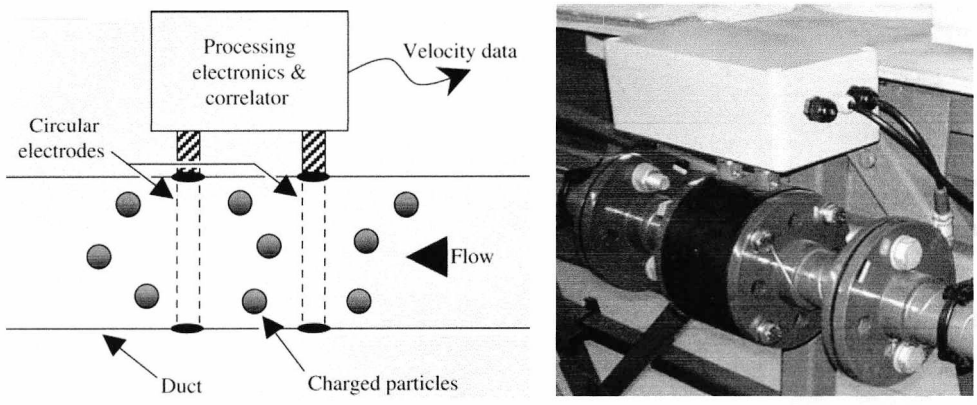

(a) Concept. (b) Experimental installation.

Fig. 2. Electrostatic velocity meter.

Whilst imaging based particle measurement is not entirely new [6,7] the method employed here harnesses novel algorithms and simple optical arrangements in order to achieve rugged and cost-effective operation that is viable in industry. To this end a standard interlaced CCTV type video camera is used. Images are processed using standard PC equipment.

A possible shortcoming of imaging based sensors is that, if the concentration of particles is too high, particles may overlap in the images causing discrepancies in the results. It has been found through experiment that this becomes a measurable problem in the concentration range 2%–3% (by volume) [4] which is well above the 'dilute phase' concentrations used in many industrial situations—coal fired power generation in particular.

2.2. *Inferential mass flow measurement*

Mass flow rate is perhaps the most important parameter related to pneumatic flows. Attempting to measure mass flow rate directly is difficult and it has often been found that an inferential approach is preferable [2]. If solids concentration is measured along with material velocity then these quantities can be combined, along with absolute material density, to yield mass flow rate data. This operation is detailed in Eq. (1).

$$q_m(t) = A\,\rho_t V(t)\beta(t) \tag{1}$$

where, q_m is the mass flow rate of particle (kg/s), ρ_t is the true density of particles (kg/m^3), V is the velocity of particles (m/s), β is the volumetric concentration of particles (%), A is the cross-sectional area of the duct (m^2), and t is time.

One of the novel aspects of the imaging sensor is its ability to provide solids concentration data and it has been shown in the past to be capable of establishing this parameter with accuracies in the order of a few percent [4]. Velocity measurement is widely researched. Instruments capable of measuring velocity are widely available. One of the most cost effective, rugged and repeatable techniques is that of cross correlation of electrostatic signals received from a pair of passive electrodes [5] and it is this technique that is employed here.

The movement of particles in a pneumatic pipeline generates a net electrostatic charge on the particles due to collisions and friction [5]. Although the amount of charge carried on particles is unpredictable, the dynamic changes in charge can be detected through the use of an electrode, electrically insulated from the duct, and suitable signal processing circuitry. As the particles move past the electrode, a constantly changing electrical signal is observed. If two signals are acquired from a pair of circular electrodes that are a known distance apart, then the velocity of particles can be derived by cross correlating the two signals [1]. The general concept and experimental installation are illustrated in Fig. 2.

3. Results and discussion

A small flow loop has been set up for evaluation purposes. This is illustrated in Fig. 3. This loop is approximately six meters in total length and used 40 mm ID pipe. Material is introduced by a vibratory feeder which may be controlled accurately to adjust mass flow rate and a suction fan is use to draw the material through the rig. The power of the fan is adjustable, allowing for varying material velocities.

In order to evaluate the combined sensing system a series of experiments were performed using table salt as a test material. Salt is clean, free flowing and has well defined absolute density [8] (it should be noted that many table salts have anti-caking additives that improve their usefulness in salt cellars but may affect the absolute material density—for the present work care was taken to find an additive free organic salt). Typical examples of results obtained are shown here with both sizing and mass flow measurement being detailed.

Fig. 4 shows a typical size distribution result recorded at four different solids concentrations. This result was recorded at a material velocity of 20 m/s—a reasonable

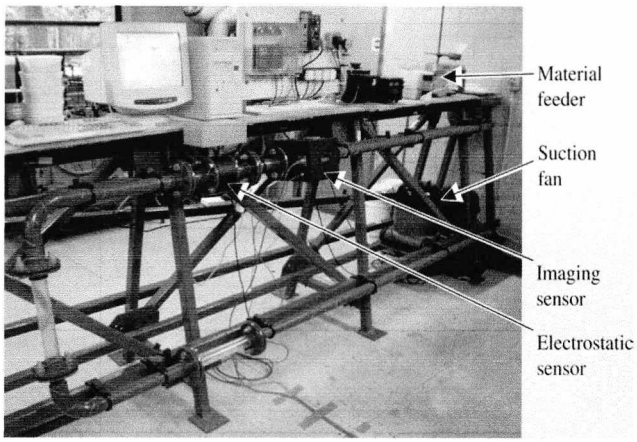

Fig. 3. Experimental flow loop.

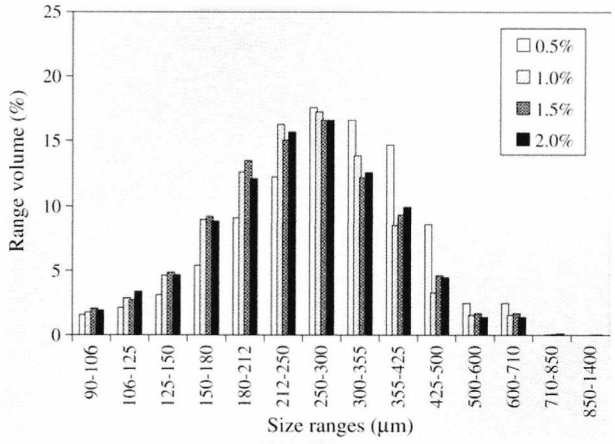

Fig. 4. On-line particle size distribution at four solids concentrations.

value similar to that found in many pneumatic conveyors. Each bar in Fig. 4 represents time averaged values over approximately 10 s. Whilst slight variations are visible between concentrations there is no tendency for perceived particle size to increase or decrease with similar changes in concentration. It is believed that all the variations here can be explained in the natural variation in material during the test runs. In general the agreement is very good.

The independence in size distribution measurement from changes in other parameters is not the only result of interest. The fundamental accuracy must be assessed. Whilst this aspect of the imaging sensor has been assessed in previous work [4,9] it is interesting here to compare the on-line results to those achieved when using an accepted off-line laser diffraction based size analyser which adheres to ISO standards [10]. In this instance a Malvern Mastersizer was employed and a sample of material from the same batch as used for on-line testing was analysed (the exact same sample could not be used in both tests due to practical considerations). It was expected that results would be comparable since both systems take 'in-flight' particle measurements. The comparison is depicted in Fig. 5 where it should be noted that the imaging result represents a mean of the results shown in Fig. 4.

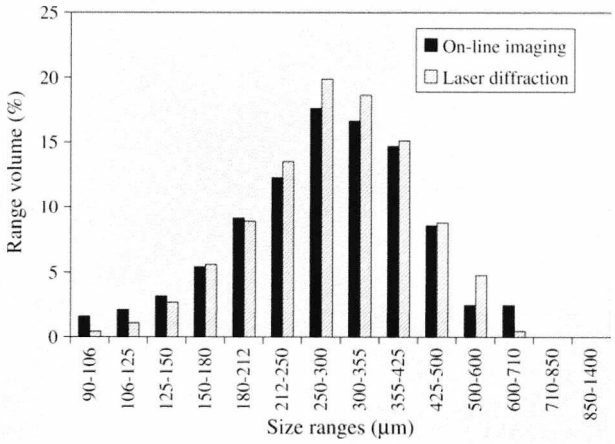

Fig. 5. Comparison between off-line laser diffraction and on-line imaging results.

It can be seen that the agreement between imaging and laser diffraction is excellent. Slight variations can, again, be explained in natural variation in the materials. This variation in material means that the differences between results cannot be considered to be errors since there is no evidence that one result is better than the other. Nevertheless it is interesting to view these variations as percentages and this is presented in Fig. 6. It is evident that the discrepancies between the two methods are no greater than ±2.5%. This demonstrates the suitability of the imaging sensor for on-line size measurement.

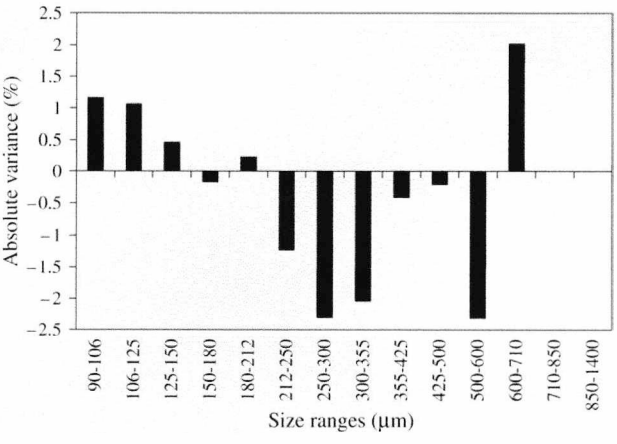

Fig. 6. Variations between off-line laser diffraction and on-line imaging results.

Also of interest is the repeatability of the size measurement. In order to quantify this, five runs were performed using material from the same batch and the normalised standard deviation of results established. For the sake of interest the same procedure was performed with the laser diffraction system, enabling the repeatability to be compared under the particular experimental conditions established here. Results are plotted in Fig. 7.

The standard deviations here seem surprisingly high and it must be assumed that the fundamental repeatability of

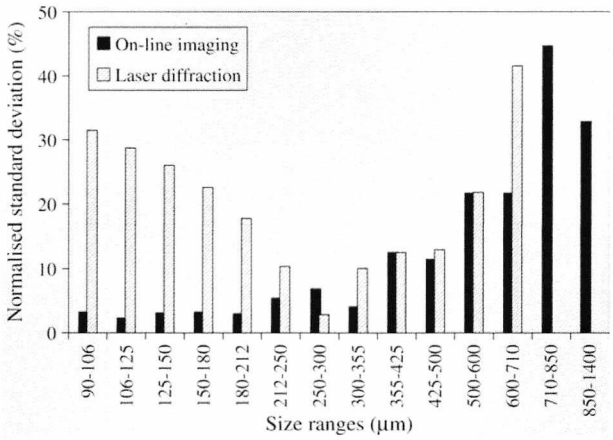

Fig. 7. Repeatability of on-line imaging compared to laser diffraction.

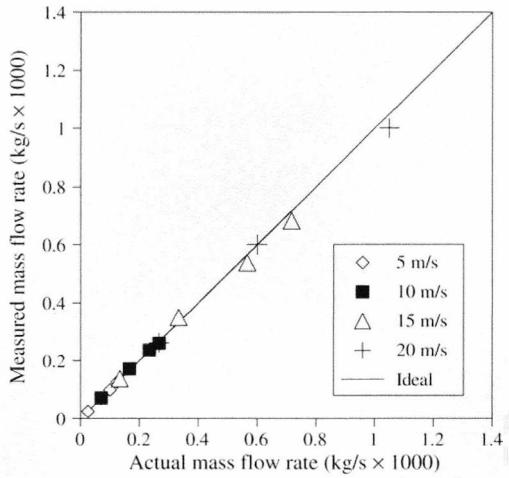

Fig. 8. Comparison between measured and actual mass flow rates.

the instruments is swamped by the variations in material. Despite this, if anything, the imaging system gives better results here than the laser diffraction—this is particularly true in the lower size ranges. Whilst both systems produce in-flight measurements the laser system observes particles as they rotate rather than in cross section as per the imaging system. This, in combination with the large numbers of small particles present, will produce a highly 'averaged' result that may consistently highlight the small differences between material samples from one test to the next. This problem will not be so severe with the imaging approach and it is thought that this difference between measurement techniques may explain the lower deviations in the small size ranges that are seen here.

The ability of the combination of imaging and electrostatic sensors to measure mass flow rate must now be studied. A total of 16 experimental runs were performed at four flow rates and four velocities. Due to practical limitations the same flow rates could not be established at each velocity but, despite this, a good range of conditions was represented. A direct comparison between the measured and actual flow rates is shown in Fig. 8.

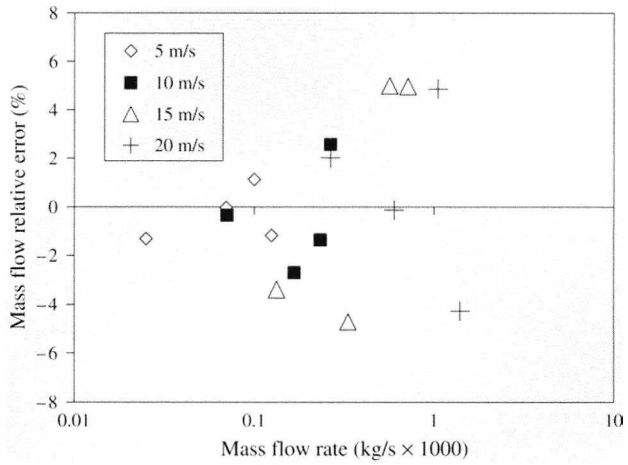

Fig. 9. Relative errors of mass flow measurement.

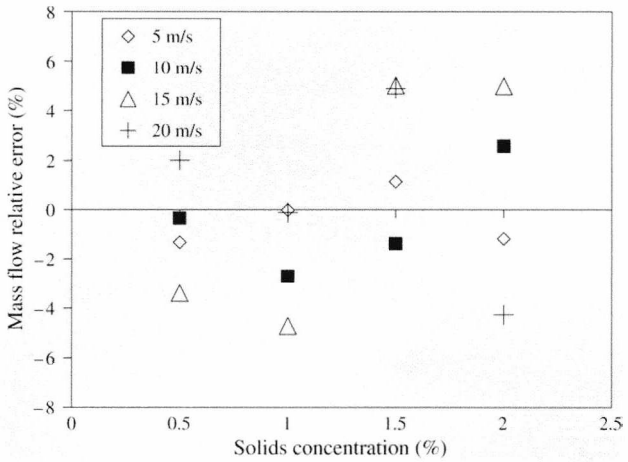

Fig. 10. Relative errors of mass flow measurement versus solids concentration.

General linearity appears good in this graph although the higher velocity points seem to demonstrate greater errors than the others. In order that this might be studied further the relative errors of mass flow measurement are presented in Fig. 9.

Whilst demonstrating that errors are no greater than ±6%, Fig. 9 tends to give the impression that these errors increase with mass flow rate, which is not the case. This can be seen more clearly in Fig. 10 where mass flow rate errors are plotted against solids concentration—i.e. the error in mass flow rate is recorded for each experimental condition. It is evident that the errors tend to increase with velocity – at 5 m/s errors lie within ±2%, at 10 m/s within ±3% etc. – whilst the spread in errors for each concentration point remains constant. It is believed this can be attributed to fluctuations in the correlation velocity data which, whilst highly repeatable, are known to deviate from the true spatially averaged velocity [9]. Despite this a useful mass flow measurement has been achieved in an on-line non-intrusive manner.

4. Conclusions

This paper has assessed the capabilities of a novel combination of sensor types intended to measure the absolute mass flow rate and size distribution of particulate materials in pneumatic conveyance in an on-line and non-intrusive manner. Concentrations of up to 2% have been tested (similar to industrial dilute phase conditions) at velocities of up to 20 m/s. Particle size measurements were comparable with those recorded off line with an ISO13320 compatible laser diffraction instrument, discrepancies between the two lying within ±2.5%. Repeatability was also comparable with the accepted instrument if not a little better. Mass flow rate was established to within ±6% using the sensor combination presented here. In general good results were produced with a level of accuracy that would be acceptable in an industrial setting. It is envisaged that improvements to the camera and optics will lead to similar performance when used with smaller particles such as those found in pulverised coal power generation. Such a system in its final form could solve a long standing industrial measurement problem.

Acknowledgements

The authors wish to acknowledge the British Coal Utilization Research Association (BCURA) for providing funding for the project (Grant Ref B68) and PCME Limited for making the electrostatic velocity meter available for use in this work.

References

[1] Y. Yan, D. Stewart, Guide to the Flow Measurement of Particulate Solids in Pipelines, The Institute of Measurement and Control, London, 2001.

[2] Y. Yan, Mass flow measurement of bulk solids in pneumatic pipelines, Meas. Sci. Technol. 7 (1996) 1687–1706.

[3] M. Pohl, Particle sizing moves from the lab to the process, PBE International, May 2001, pp. 25–31.

[4] R.M. Carter, Y. Yan, On-line particle sizing of pulverised and granular fuels using digital imaging techniques, Meas. Sci. Technol. 14 (2003) 1099–1109.

[5] J. Ma, Y. Yan, Design and evaluation of electrostatic sensors for the mass flow measurement of pneumatically conveyed solids, Flow Meas. Instrum. 11 (3) (2000) 195–204.

[6] R. Kumar, S. Kannan, Drop size measurement in a two-phase swirling flow using image processing techniques, Int. J. Heat Mass Transfer 37 (1994) 559–570.

[7] K. Nishino, H. Kato, K. Torii, Stereo imaging for simultaneous measurement of size and velocity of particles in dispersed two-phase flow, Meas. Sci. Technol. 11 (2000) 633–645.

[8] The Salt Institute, http://www.saltinstitute.org/.

[9] R.M. Carter, Y. Yan, Concurrent measurement of mass flow rate and size distribution of pneumatically conveyed particles using combined electrostatic and digital imaging sensors, in: Proceedings of Sensors and Their Applications XII, 2–4 September 2003, Limerick, Ireland, 2003.

[10] ISO13320-1, Particle Size Analysis—laser diffraction methods, 1999.

INSTITUTE OF PHYSICS PUBLISHING MEASUREMENT SCIENCE AND TECHNOLOGY
Meas. Sci. Technol. **14** (2003) 1099–1109 PII: S0957-0233(03)56686-3

On-line particle sizing of pulverized and granular fuels using digital imaging techniques

R M Carter and Y Yan[1]

Advanced Instrumentation and Control Research Centre, School of Engineering, University of Greenwich at Medway, Chatham Maritime, Kent ME4 4TB, UK

E-mail: Y.Yan@gre.ac.uk

Received 27 November 2002, in final form 23 January 2003, accepted for publication 24 February 2003
Published 17 June 2003
Online at stacks.iop.org/MST/14/1099

Abstract
On-line particle sizing is desirable in many industries, particularly in the power generation industry. This paper presents the principle and design of a prototype, digital imaging based, instrumentation system that can measure size distribution of particles that are largely opaque. The system, which is intended as an industrial rather than a laboratory solution, operates on-line and is non-intrusive. The image processing sequence is discussed in some detail. Experimental results obtained using two common types of particulate material demonstrate the viability of the system. The use of static images has allowed the instrumentation system to be calibrated. The linearity and repeatability of the system are quantified in addition to direct comparisons between the measurements made and those from proven, off-line, industrial solutions. The effects of the illumination sub-system on the spatial sensitivity of the viewing field are discussed along with the turndown ratio. The discrepancies between reference and static measurements are also identified and discussed. The results indicate that the system has good linearity and excellent repeatability and that practical on-line measurement of particle size distribution can be achieved using this technique. As presented the system can be used with particles in the range 150 μm–25 mm.

Keywords: particulate flow, particle size distribution, digital imaging, pulverized fuel fineness

1. Introduction

Pneumatic conveyance of particulate materials is an important technique in many industries. The use of pneumatic conveyers allows time and money to be saved when compared to more traditional handling techniques. In fact, some applications, such as the pneumatic injection of pulverized fuel into power station furnaces, would not be possible without the use of this form of conveyer. In order for these systems to deliver all of their potential benefits it is essential to know the parameters of the flow. Much research work has been carried out in the field of particulate flow metering [1] and many techniques have been developed, ranging from gamma rays to optical attenuation [2]. Instruments based on these techniques are designed to measure various flow parameters but few of them can measure important particle size information on line [3]. Those that can measure this parameter usually do so in an intrusive manner—i.e. they project into the duct, thus changing the characteristics of the flow—which is not desirable. By selecting an imaging approach for the current work a *non-intrusive*, on-line system capable of measuring particle size distribution can be developed. This will represent a major advance over current techniques which may be as primitive as simple sieving.

It is clear that an instrumentation system must be developed that can measure particle size and size distribution

[1] Author to whom any correspondence should be addressed.

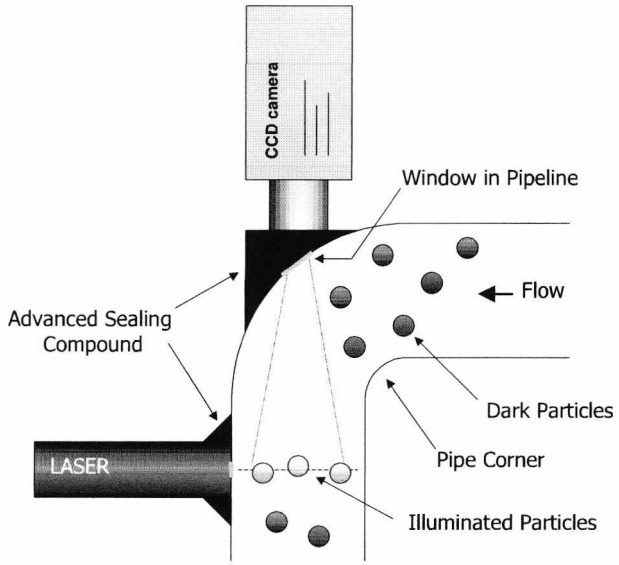

Figure 1. General sensing arrangement.

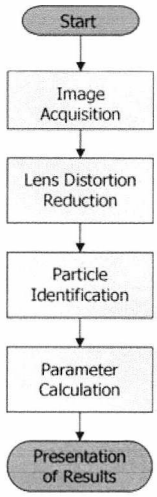

Figure 2. Sequence of operations.

on an on-line continuous basis and that can be installed in a non-intrusive manner. It is accepted that such an undertaking would be 'technically challenging' [2]. This paper presents the results produced by an experimental system of this nature. Digital imaging techniques are used to interrogate the flow and the images obtained are processed in real time using custom software. Accurate static calibration images are used to assess the absolute accuracy of the system and real particulate material examples are used to defend the system's real world viability. The size distribution graph obtained is compared to reference data found using a Malvern Mastersizer—an off-line solution that is accepted in industry. Similar optical work has been carried out in the past [4] but this used simulated flows of unrealistic clarity and resolution. The current research addresses many practical flow related problems that have been left unsolved in the past.

2. Measurement principle

2.1. General sensing principle

When particles are flowing through a pipeline it is possible to acquire images of them using a CCD camera and a suitable illumination source. This general concept is illustrated in figure 1. When a 2D layer of particles is available (made possible, for the on-line system, by the illumination arrangement—see section 2.2) it is a simple matter to focus a CCD camera on this plane and acquire digital images.

2.2. Illumination arrangement

The work, as presented, consists of two systems—a 2D static set-up (for calibration) and an on-line flow rig. These systems have very different illumination requirements. Illumination of a static arrangement of particles is a simple matter. A uniform source of light is shone on to the particles, which are placed on a flat, contrasting background. For the on-line system illumination is more complex.

To process images of a flow in a circular pipeline would be difficult without some means of concentrating only upon a certain plane within the flow. For this reason a low-cost laser sheet generator is used as an illumination source. The laser used in this case emits continuous wave radiation at 633 nm with a power of 1.5 mW. A line generator lens is used to create a sheet thickness of about 0.5 mm. This way an essentially 2D section of the flow—with all the particles in one plane—is illuminated. There are four possible problems with this approach.

(1) *Lateral movement of particles.* It can be assumed, in an on-line system, that the particles will be travelling with a considerable speed (in a real system the speeds may be in the range of 15–40 m s^{-1}). As the particles pass through the laser sheet they are momentarily, and fiercely, illuminated. So long as the particles travel perpendicular to the laser sheet there will be no blurring of the images—at high speeds any lateral movement of the particles would be insignificant during the fraction of a second necessary to traverse the laser beam. For example, a particle travelling at 30 m s^{-1} traverses the thickness of the laser sheet in 17 μs—in order for, say, a 100 μm particle to have moved sideways by one-half of its diameter during this time it would require a lateral velocity component of approximately 3 m s^{-1}—which seems unlikely in a real, high-efficiency, pneumatic conveyer.

(2) *Blurring due to camera shutter speed.* If we refer to the previous example (see above) it can be seen that each particle will, typically, only be illuminated for around 17 μs—or 1/60 000 s. Most low-cost machine vision cameras only support shutter speeds of up to around 1/10 000 s and, as the present system is intended to be cost effective, it would be inappropriate to use a more exotic camera. In point of fact it is unlikely that sufficient detail would be resolved using such a short exposure in any case (unless perhaps a large pixel format CCD were used which, again, would be prohibitively priced). The present system exploits the slow exposure time of the camera and, rather than capturing an instantaneous image of the particles illuminated in the laser beam, integrates the incident light over a relatively long period so that the image obtained represents a cumulative image of the particles as

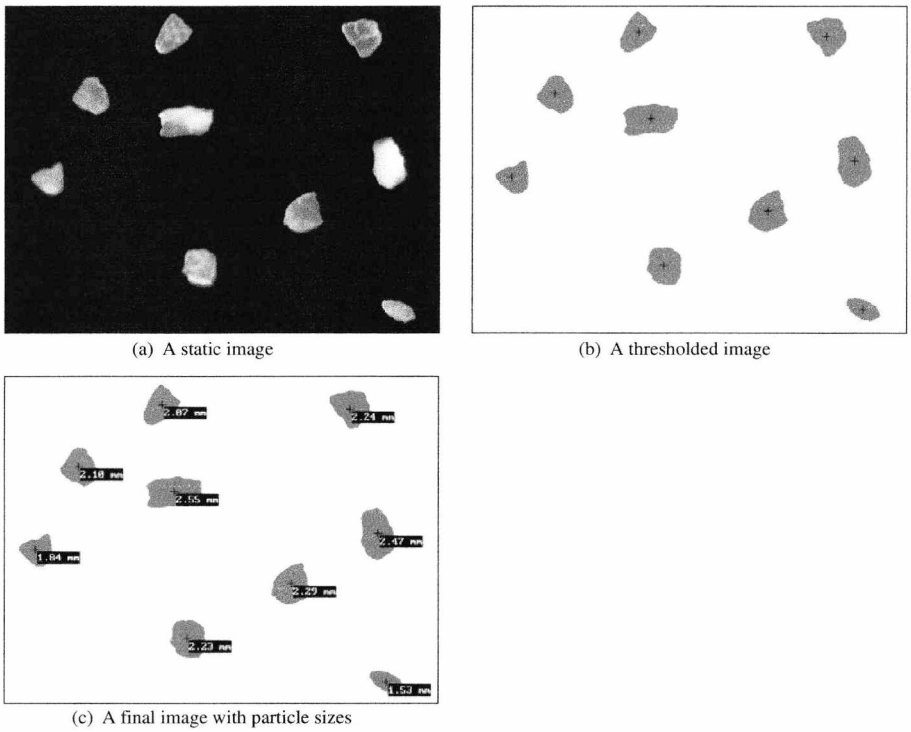

(a) A static image

(b) A thresholded image

(c) A final image with particle sizes

Figure 3. Processing steps used for static images.

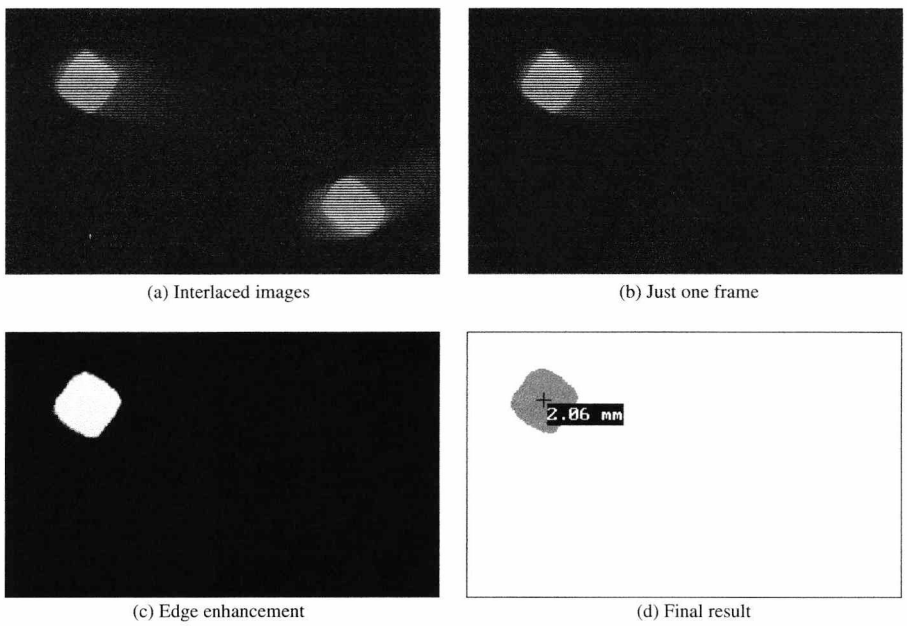

(a) Interlaced images

(b) Just one frame

(c) Edge enhancement

(d) Final result

Figure 4. Processing steps used for on-line images.

they traverse the laser sheet. This approach, though sensitive to lateral movement (largely irrelevant—see above), allows a low-cost camera to acquire bright clear images of the flow. It also prevents problems with particulate self-shadowing. Any rotation of the particles during their illumination will only aid in achieving an accurate mean particle size measurement.

(3) *Overlapping particle images.* It is possible that particle images may overlap in the captured images. This could represent a problem and the phenomenon will certainly limit the system's usefulness at higher concentrations. It is impossible to automatically separate overlapping particle images without prior knowledge of the normal shape of particles. Previous research [4] has assumed that all particles are spherical—an impractical assumption for an industrial system. Due to the low concentrations in question it is believed that overlapping will have little effect on the current system—certainly the results (see section 4) provide good accuracy without taking this phenomenon into account.

(4) *Refraction effects caused by transparent particles, beads or droplets.* When used with highly refractive/reflective particles such as glass beads or liquid droplets the system would prove unreliable and, in some cases, totally impractical. For this reason it is not intended that such materials be used with the present system. Suitable materials must be largely opaque and of such optical properties that they diffusely reflect an appreciable amount of the wavelength in question. The shape of the particles is not critical.

2.3. Image processing

Once the images have been acquired they must be processed in order to extract the desired information, i.e. particle size distribution. The sequence of operations is outlined in figure 2 and details of each processing operation are explained here.

The first processing stage is the reduction of lens distortion based upon the optical parameters of the system—depending upon the lens used there may be significant 'pin-cushioning' or intensity based 'vignetting' to be corrected—this step should not be confused with calibration of pixel size (see section 3.1). It is then necessary for the software to determine which parts of the image are particles and which are background. This is, when accurate sizing information is required, the most complex part of the operation.

2.3.1. Static particle identification. In the static test system the contrast and brightness of the images are easily controlled by the physical and optical set-up. Crisp clear images are produced. In this case separation of the particles from the background can be achieved fairly simply through the use of thresholding.

Simple thresholding has limitations—a small change in threshold level will result in a change in perceived particle size (unless the image is so sharp that it is already a binary representation—an unlikely contingency). For this reason some objective method of setting the threshold level is required. Such a method is employed here—it is based on analysis of the normalized standard deviation of particle size measurement at various threshold settings. An acceptable threshold level 'window' lies between the peaks in this quantity (see section 4.1.4).

Once the image is in binary form it is a simple matter to identify and count the particles and to find their centroids (the exact method used to find the centroid is of no importance here since accuracy of this parameter is not required for particle size measurement).

Figure 3 shows a sequence of images, from the static system, which illustrates the processing steps required (the material is maize, ranging from about 1.5 to 2.5 mm). Figure 3(a) is the starting point—a distortion corrected image—it can be seen that the image is very clear. Figure 3(b) shows the thresholded result with recognized particle locations marked with crosses. Figure 3(c) shows sizes marked by each particle (see section 2.3.3).

2.3.2. On-line particle identification. The images acquired using the on-line system are far less clear than their static counterparts. For this system a simple thresholding operation would not be appropriate. A commonly used method under these circumstances is the gradient based approach as used by

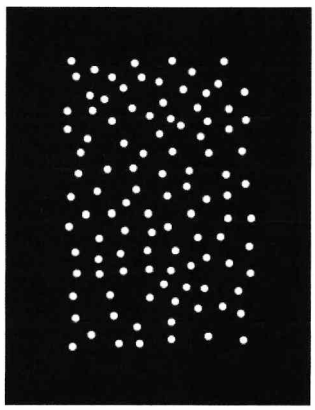

Figure 5. An example of a static calibration image (not to scale).

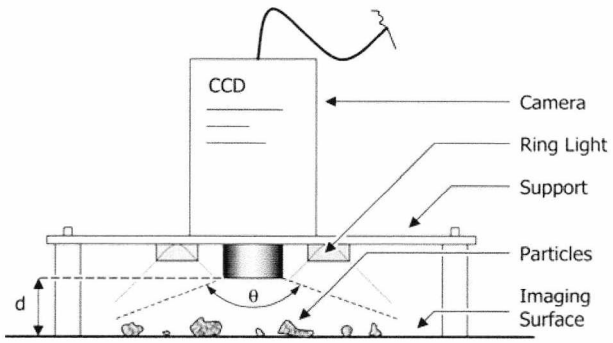

Figure 6. Arrangement of the static set-up.

Li *et al* [5] and modified by Nishino *et al* [6]. Such methods are slow, requiring many particle radii to be processed, and are unsuitable for particles represented by just a few image pixels.

In the current research a gradient approach is used but one that is simpler than accepted methods and that exploits a shortcoming in the *interlaced* images—a series of images, illustrating the sequence of operations, is shown in figure 4 (the material used is rice—this provides large clearly seen particles of about 2 mm diameter for demonstration purposes). As it is the intention to create a cost-effective system a standard, interlaced scan, camera is currently in use. As the particles are moving at high speed both interleaved frames show completely different images (figure 4(a)). Each of these can be processed separately and both used but it is easier to understand if we assume that only one is used and the other discarded—the first step is to de-interlace. The usual method of achieving this would be to interpolate the missing lines from the desired frame, thus covering up the other. In the current system this is not the case. The undesired frame is removed by covering up alternate lines with black (the background colour has been found to be a very consistent black in all on-line images). Now particle pixels—even faint ones from the very edges of particles—represent a large gradient change when compared with pixels directly above and below them (figure 4(b)). An edge-enhancing filter will now allow all particle pixels, and their interposed black lines, to be clearly seen. After some enhancement of the brightness contrast and gamma, using conventional techniques (figure 4(c)), the image may simply be thresholded and processed as for the static system (figure 4(d)).

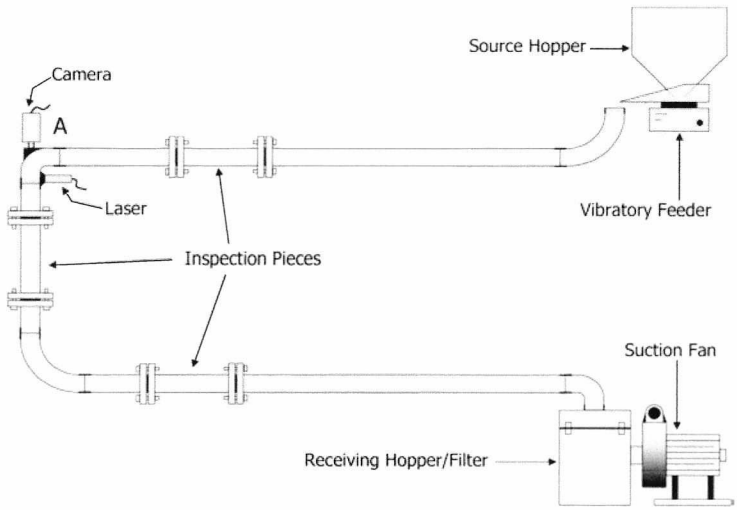

Figure 7. Flow rig.

2.3.3. Parameter calculation. Once a binarized image is available the particle sizes must be found. The system software provides various options including automatic time averaging and statistical analysis. Perhaps most importantly, a real time histogram of particle size distribution is presented to the user. This may provide instantaneous data or represent a rolling average over a period of time.

A single parameter must be used to represent the size of each particle regardless of its shape. If a given particle is not perfectly round (spherical) then this parameter can be hard to define [7]. In this case the area of the particle is determined and its size is expressed as the diameter that a circle of the same area would possess (i.e. the equivalent diameter):

$$D_p = 2\sqrt{\frac{A_p}{\pi}} \tag{1}$$

where D_p is the equivalent diameter of the particle and A_p is the area of the particle.

The software identifies every particle in the image and maintains a list of data that contains information regarding each of the particles. Size distribution measurement, along with the number of particles present, is simply a matter of statistical analysis of these data.

2.4. Turndown ratio and size rangeability

The turndown ratio (accepted term [1] for the range of sizes that a system can successfully interrogate) of the current system is established by two key factors: the resolution of the camera and the size of the area interrogated. The minimum theoretical particle size that the current instrumentation can detect is about 45 μm. This, however, would be inaccurate since only one camera pixel would be used. At 90 μm four pixels are used and greater accuracy is achieved but it is not until about 135 μm is reached ($\approx$9 pixels) that high-accuracy measurements are made. The maximum theoretical particle size is limited only by the size of the interrogation area. In the present system this is about 35 $\times$ 25 mm so a 25 mm particle could easily be interrogated. This gives a turndown ratio of approximately 500:1 in theory and 200:1 if the accuracy of the lower particle sizing is considered. These represent wider ranges than those that are likely to be encountered in a real situation.

Table 1. Specifications of static calibration images.

'Particle' sizes (μm)	Approx. concentration range (%)	Number of 'particles' in images
250	0.005–0.7	1–128
500	0.02–1.7	1–80
1000	0.08–3.3	1–40
2000	0.3–3.3	1–10

It would be possible to interrogate much smaller particles if a higher resolution camera and/or a macro lens were used (the turndown ratio would remain roughly constant for differing lens set-ups but would vary with the resolution of the camera).

3. Test set-up

3.1. Static test arrangement

In the present study two separate set-ups were used: static and dynamic. The static part, used for calibration and assessment of accuracy, consisted simply of a camera accurately fixed over a flat surface. A ring light was used for illumination of the surface, which could be of a light (white) or dark (black) nature depending on the type of material to be interrogated. Particles were placed on the background for size distribution analysis and accurate calibration images, generated using a 2880 dpi inkjet printer, were placed here during the accuracy analysis and calibration phase. An example of such an image is shown in figure 5 and specifications of the images used are given in table 1.

The physical arrangement of the static set-up is shown in figure 6.

As the lens angle and distance from the surface are known the area represented by each frame can be calculated (for the current system a 12 mm focal length f2.5 lens was used in conjunction with a 1/3 in CCD camera). Firstly the distance represented by each pixel's width and height must be found

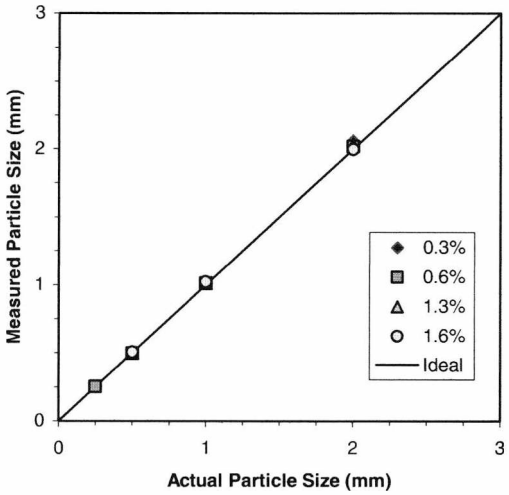

Figure 8. Comparison of measured and actual particle size for different solid concentrations.

(in theory the pixels should be square but in many cameras they are slightly elongated and so both values must be found):

$$P_w = \frac{2d\tan\left(\frac{\theta}{2}\right)}{W_{pix}} \tag{2}$$

$$P_h = \frac{2d\tan\left(\frac{\theta}{2}\right)}{H_{pix}} \tag{3}$$

where P_w and P_h are the equivalent sizes, in millimetres, of each pixel in the horizontal and vertical directions respectively, d is the distance from the focal point to the imaging plane in millimetres and θ is the lens angle (see figure 6). W_{pix} and H_{pix} are the image width and height in pixels. Now the total area represented by each frame can be calculated:

$$A_f = P_w W_{pix} P_h H_{pix}. \tag{4}$$

The images are then processed as described in section 2.3. Note that H_{pix} and W_{pix} are not constant and may be changed during execution of distortion correction or other algorithms. This means that equations (2)–(4) cannot be simply combined. Also, it may be necessary to split the lens angle, θ, into horizontal and vertical components, depending on the camera used.

3.2. Flow rig

For the dynamic part of the experiments a pneumatic flow loop (about six metres of total flow length, using 40 mm ID pipe) was set up. Figure 7 shows the general arrangement of this rig.

In use the laser illuminates a slice of the flow that is perpendicular to the pipe. The camera focuses on this plane in the same way as for the static system (see section 3.1). The same camera/lens was used for both systems.

4. Results and discussion

4.1. Calibration results using static images

4.1.1. Accuracy. Concentrations of 0–4% provided a reasonable coverage of the images without using so many 'particles' that human error in generating the images would have become an issue. This is particularly true with the 250 and 500 μm

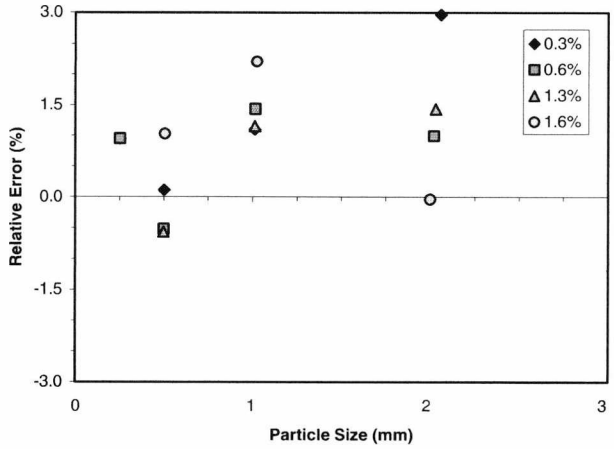

Figure 9. Relative error of particle size measurement.

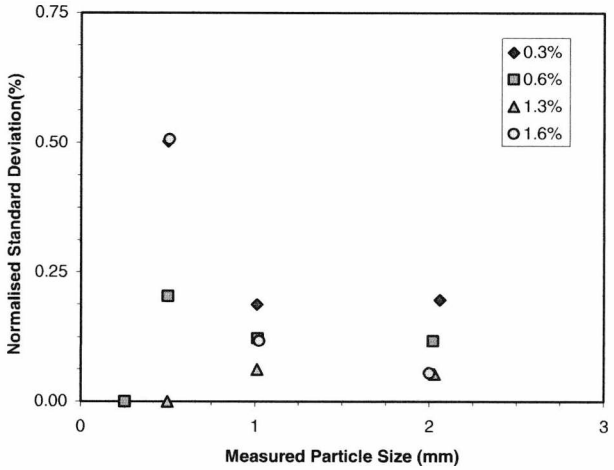

Figure 10. Normalized standard deviation of the particle size measurement.

particles where solid concentrations had to be limited to considerably less than 4%. In the industrial situations to which this technique is intended to apply, the concentration of particles is often very low—in pulverized fuel conveyance, for instance, the concentration of particles is usually below 1%. At high concentrations a system of this nature may become inaccurate due to many overlapping particles in the images—for this reason the current system is only suited to dilute phase conditions.

Figure 8 shows a direct comparison between the measured and actual particle size for four different concentrations. Each point on the graph represents mean particle size data from one accurate calibration image (each containing between one and 128 'particles'—see section 3.1). It can be seen that the instrumentation exhibits good linearity and that the particle size measurement is independent of solid concentration. Figure 9, derived from the direct comparison (figure 8), shows relative error in particle size measurement against actual particle size. In the majority of cases the relative error is within $\pm 1.5\%$. It should be pointed out that the apparent 'systematic error' seen in figure 9 can be attributed to the particular concentrations used and is not, in fact, a genuine error.

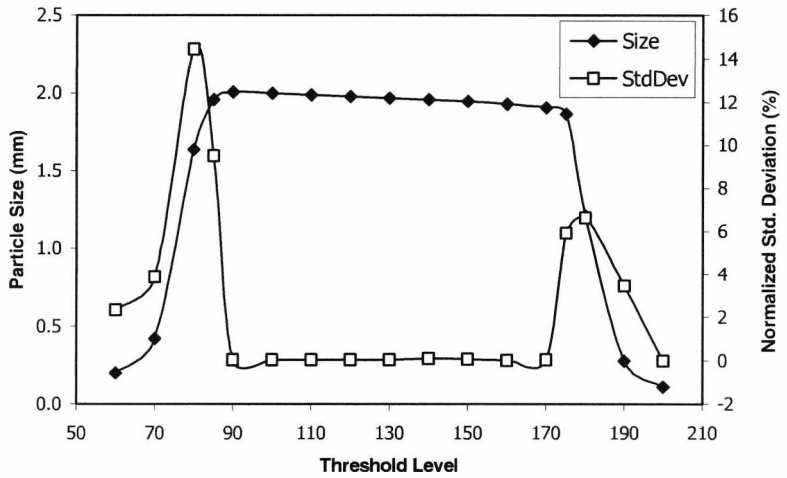

Figure 11. Variation of measured mean particle size and normalized standard deviation for various threshold levels.

4.1.2. Repeatability. In order that the repeatability of the system could be quantified the standard deviation of the 100 averaged readings normalized to their mean value was found. Figure 10 shows the repeatability test results. It is clear that, in most cases, the repeatability is better than 0.25%. The increase in the standard deviation for the smaller particles and lower concentrations is attributed to the effects of the normalization process.

4.1.3. Threshold level sensitivity and automatic setting. The system was tested in order to establish if the measured particle size varied significantly with threshold level variation. The purpose of this testing was twofold. Firstly it was necessary to establish that thresholding was a practical method for this system and that the exact setting was not, within certain bounds, critical. Secondly, through studying threshold variation effects, an automatic threshold level setting method could be found. There have been some research efforts in the past [8] covering the variation of threshold level and its relation to particle size, but these involved old vidicon camera technology. For the present research it was thought necessary to revisit this concept since even a low-cost CCD camera provides markedly superior images to a vidicon in respect of both geometrical and intensity distortion.

The test was performed by interrogating a static test image consisting of 24 2 mm 'particles' and noting the mean particle size and standard deviation for various threshold levels. A total of 100 measurements (video frames) were taken for each result. Figure 11 shows the variation of measured mean particle size and normalized standard deviation for various threshold levels. It can be seen clearly that, whilst at extremes the threshold level affects measured particle size as expected, there is a range of thresholding values for which the particle size measurement is fairly constant. It is easy to think that the measured particle size should start at a very high value and linearly decrease as the threshold level increases. This is not the case—since the particles in the image, and the image background, do not exhibit uniform brightness characteristics. At low thresholding levels small 'particles' appear in the data that are, in reality, artefacts due to background noise. This causes the mean particle size to dramatically reduce when the image background begins to 'break through' and affect the data. At the other end of the scale—when the threshold level is high—the real particles do not simply get smaller and smaller until they vanish but, due to the variations in their brightness levels, begin to break up into many smaller particles when the threshold reaches critical levels. This causes another dramatic reduction in the mean measured particle size. These two sudden reductions can be seen in figure 11. It is these features that may be used to identify the limits of suitable thresholding levels. Such detection can be based either upon inflection point

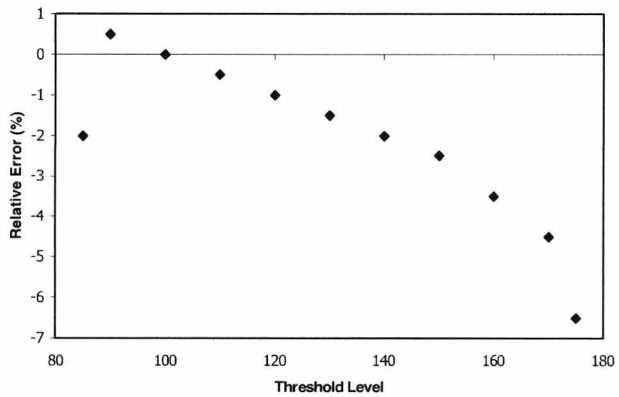

Figure 12. Relative error of particle size measurement within the detected 'suitable' range of threshold levels.

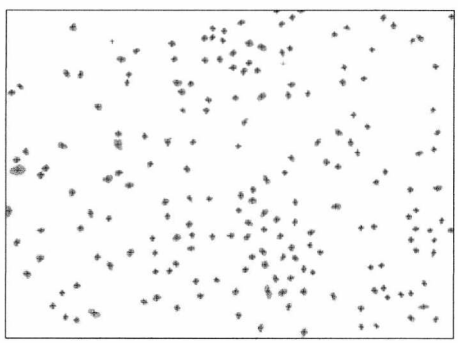

Figure 13. A typical processed image of sand grains taken from the sequence used to generate the results in figure 14—there are about 200 particles here.

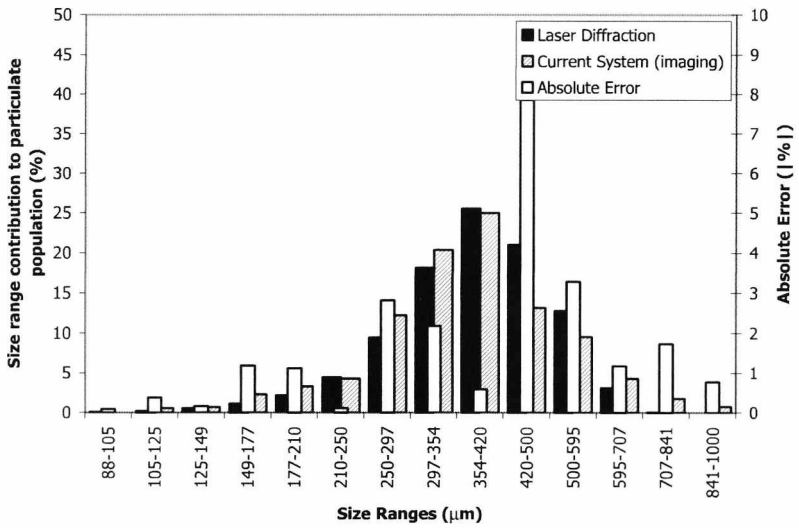

Figure 14. Static size distribution measurement.

detection on the mean sizing data or, as is done by the current system, the peaks in the normalize standard deviation, caused by uncertainty due to the sudden size changes, may be detected.

This method allows a suitable *range* of threshold values to be established. It is important to know how much the measured particle size varies within this range. Figure 12 shows the relative error of particle size measurement within the detected threshold range (≈80–180). It can be seen that the variation is mainly linear and is very small, lying between +0.5 and −7%. The extremes of the detected thresholding range should be treated with suspicion as they occur in the critical threshold level regions. Experiments have shown that a threshold value at 20–25% of the detected range gives best results. In this case (figure 12) a threshold value of 20–25% of the detected range would give relative errors of between 0 and −1.5%—quite adequate in an industrial situation.

4.2. *Static measurement of particle size distribution*

So far the presented results have been produced using accurate calibration images. This section presents results that were found using real particulate materials.

The current research aims to produce a cost-effective replacement for current, industrial, size-distribution measurement systems. In many industries, particularly power generation, methods such as sieving are still in wide use. In these situations any kind of on-line measurement represents a distinct improvement. The most accurate (and accepted) off-line measurement system used in industry is the laser diffraction particle size analyser. For this reason it was thought appropriate to compare the results from the current system to those found using a diffraction based analyser—namely a Malvern Mastersizer.

The ranges of sizes that can be interrogated by the current system and the diffraction based instrument overlap and so, in order to provide the greatest synergy between systems, a material was chosen that contains particles falling within the overlapping range. The best that could be readily sourced was an olivine sand in the range of approximately 100–1000 μm. The same sample could not be used for both instruments

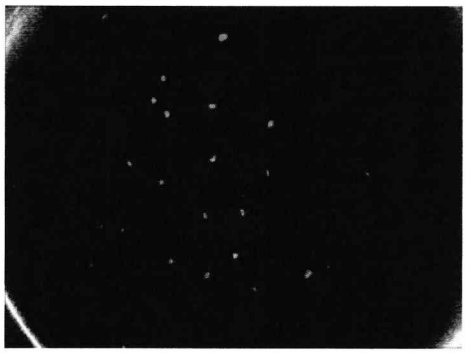

Figure 15. An image of the sand flowing through the test rig.

since the Malvern is a lost sample system but two samples from the same batch were used. Figure 13 shows a typical processed image of this material as captured by the current system and figure 14 shows the size distribution as measured by the two methods—the size ranges used represent standard industrial sieve sizes. It should be noted that five independent measurements were made using the current system, each using a different, random, selection of particles from the sample. The use of a number of particulate samples ensured that the representativeness of the size data was sufficient [9]. Each of these five readings represented a rolling average over a period of 20 frames. In total, therefore, 100 readings were used for each size distribution result. As each frame contained 100–200 particles, in total, between 10 000 and 20 000 particle measurements were taken into account, leading to reduced statistical uncertainty of the size measurement [9, 10].

It can be seen that the agreement between the two systems is good with a mean absolute error of around 3%. The peak absolute error is below 8%. The most obvious reason for such errors is the discrepancy between the two samples—although from the same source there may have been settling or other phenomena that affected the range of sizes found in each sample. Another issue is the fundamental difference between the instrumentation systems used. As the off-line Malvern instrument is a light scattering based system the results it

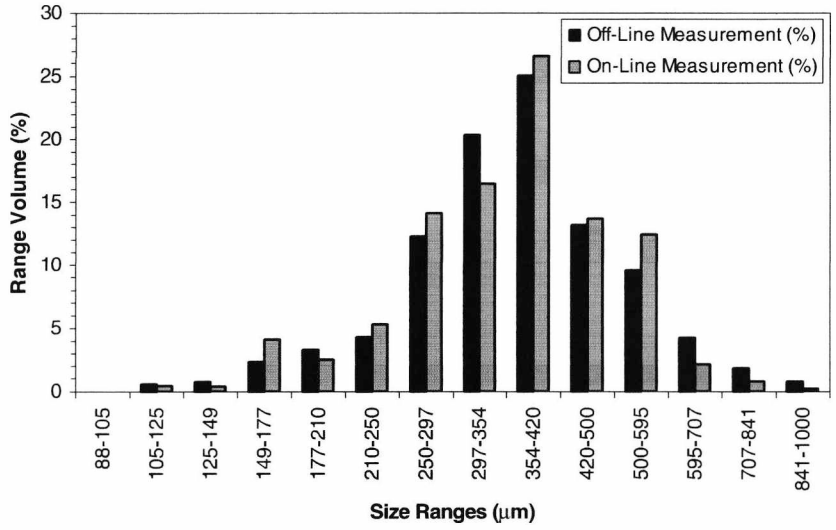

Figure 16. Comparison of on-line and static results for sand grains.

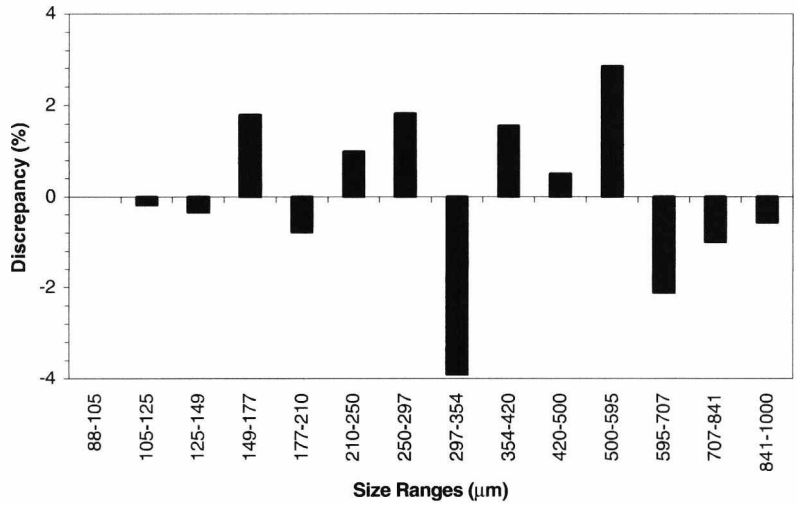

Figure 17. Discrepancy between on-line and static results (figure 16) for sand grains.

generates are susceptible to variations in the materials' shape (the diffraction pattern of an irregular shaped particle is not circular) and refractive index [11]—these limitations are not shared by the present instrumentation and may therefore have strongly contributed to the discrepancies in the results. Lastly, the Malvern particle sizer uses a very large ($\approx$100 g) sample, which is interrogated over a period of several seconds. There are such a vast number of particles in this sample that the result is very much a mean distribution. The present system only interrogates a small section of the total. Although a rolling average is used and five different measurements made the averaging is still far less severe than with the Malvern. It is believed that a combination of these factors can easily account for errors of the magnitude indicated here.

4.3. On-line measurement of particle size distribution

Using the pneumatic flow rig the same sand material was used and an on-line result found. Figure 15 shows a raw, unprocessed, on-line flow image whilst figure 16 compares the static results with those from the live flow (using the same material).

In figure 15 the ring of light around the edge of the frame is caused by the laser sheet shining on the pipe wall. This is ignored by the software.

The results show an absolute discrepancy of less than $\pm$4% (figure 17). Variations in the material samples and the inevitable compounding errors caused by population percentage representation (an error in one size range will always cause an error in one or more other size ranges) can account for errors of this magnitude. It is also possible that particle overlapping could have contributed to this small error (see section 2.2). A further comparison of on-line and off-line results obtained using a different particulate material is provided in figure 18. The absolute discrepancy between measurements (figure 19) is less than $\pm$3%. The material used here is a coarse-grain sea salt. It is interesting to note that the material falls into two distinct groups of sizes—the main, large particles and smaller dust that has been created through abrasion in storage. Causes of errors are as before.

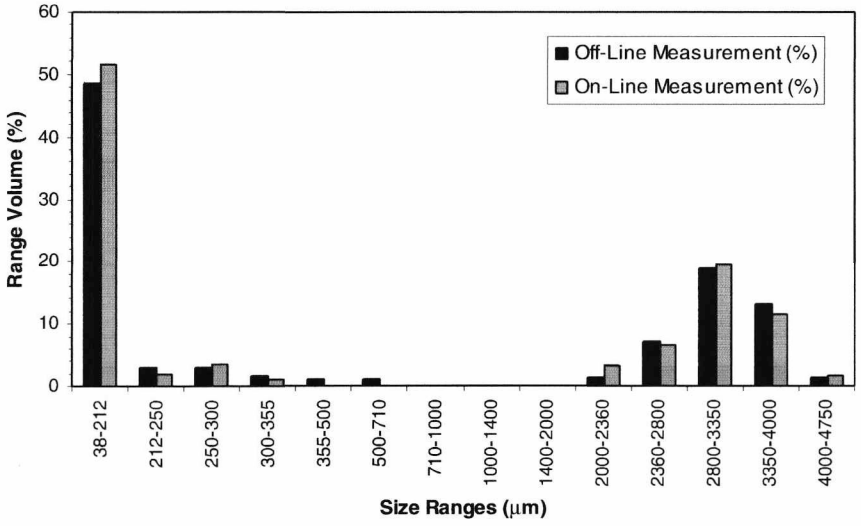

Figure 18. Comparison of on-line and static results for sea salt.

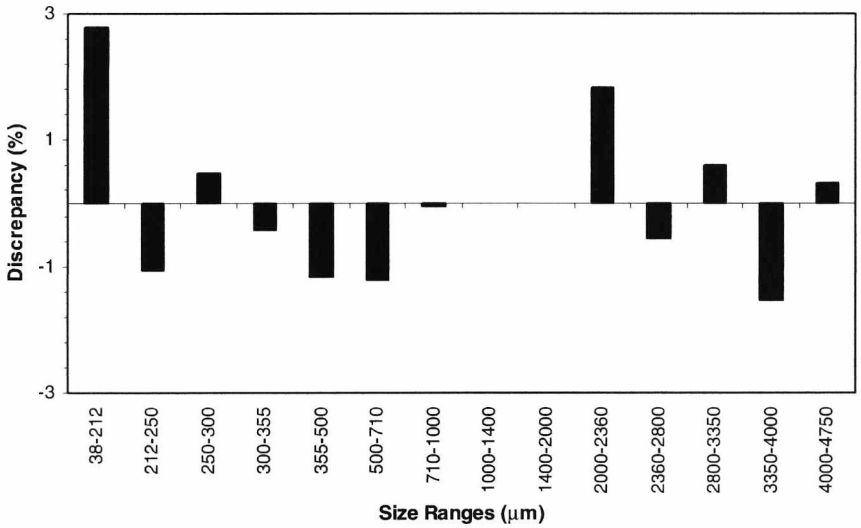

Figure 19. Discrepancy between on-line and static results (figure 18) for sea salt.

5. Conclusions

This paper has presented the concept, operational principle and evaluation of a novel digital imaging based industrial instrumentation system for the on-line measurement of particle size distribution in particulate flows. Results obtained have demonstrated that the system can be calibrated (under static reference conditions) to measure particle size to within $\pm 1.5\%$ irrespective of solid concentration. The repeatability is excellent, being within 0.5%.

Further results have demonstrated that the novel system is capable of measuring particle size distribution with absolute discrepancies no greater than 8%, in relation to reference data. These discrepancies between the measured results and the reference data have been explained. It should be remembered that they do not represent the absolute accuracy of the system but, rather, represent a discrepancy between instrumentation types and were magnified by unavoidable differences in the material samples used. It has also been shown that the technology is capable of operating on-line under real particulate flow conditions with an absolute discrepancy of no more than $\pm 4\%$ when compared to static measurements.

The flexibility of this new approach as presented is clear. It should be noted that all the measurements achieved were made using a low-cost (<£30) CCD board camera. It is envisaged that, using an improved (but still relatively low-cost) camera, higher system performance could be readily achieved. In its final form this instrumentation could provide a complete, cost-effective solution to long-standing on-line particle sizing problems in power generation and other industrial settings.

Acknowledgments

The authors would like to thank their colleagues at the Wolfson Centre for Bulk Solids Handling Technology at the University of Greenwich for providing material samples and reference data.

References

[1] Yan Y and Stewart D 2001 *Guide to the Flow Measurement of Particulate Solids in Pipelines* (London: Institute of Measurement and Control)

[2] Yan Y 1996 Mass flow measurement of bulk solids in pneumatic pipelines *Meas. Sci. Technol.* **7** 1687–706

[3] Pohl M 2001 Particle sizing moves from the lab to the process *PBE International (May 2001)* pp 25–31

[4] Shen L *et al* 2000 Velocity and size measurement of falling particles with fuzzy PTV *Flow Meas. Instrum.* **12** 191–9

[5] Li Z, Yokoi S, Toriwaki J and Fukumura T 1982 Border following and reconstruction of binary pictures using grid point representation *Trans. Inst. Electron. Commun. Eng. Japan* **65** 1203–10

[6] Nishino K, Kato H and Torii K 2000 Stereo imaging for simultaneous measurement of size and velocity of particles in dispersed two-phase flow *Meas. Sci. Technol.* **11** 633–45

[7] Rawle A 2001 *Basic Principles of Particle Size Analysis* MRK034 (Malvern Instruments)

[8] Ahlers K K and Alexander D R 1985 Microcomputer based digital image processing system developed to count and size laser-generated small particle images *Opt. Eng.* **24** 1060–5

[9] Masuda H and Gotoh K 1998 Study on the sample size required for the estimation of mean particle diameter *Adv. Powder Technol.* **10** 159–73

[10] Tate R W 1982 Some problems associated with the accurate representation of droplet size distributions *Proc. 1st Int. Conf. on Liquid Atomisation and Spray Systems (ICLASS) (June 1982)* pp 341–51

[11] Holve D J and Annen K D 1984 Optical particle counting, sizing and velocimetry using intensity deconvolution *Opt. Eng.* **23** 591–603

Digital Imaging Based Classification and Authentication of Granular Food Products

R. M. Carter[(a)] , Y. Yan[(a)1] and K. Tomlins[(b)]

(a) Department of Electronics, University of Kent, Canterbury, Kent. CT2 7NT, UK
(b) Natural Resource Institute, University of Greenwich at Medway, Chatham, Kent. ME4 4TB, UK

Abstract
In the food industry there are many types of product that are in the form of particles, granules or grains. Consistent material size and quality within any given sample is an important requirement that is well known in industry. In addition it is possible that samples of material may be of unknown type or have been subject to adulteration, thus making material authentication a real requirement. The present work implements an advanced, but cost effective, digital imaging and image processing technique to characterise granular foodstuffs either in real time process control or in an off-line, sample based, manner. The imaging approach not only provides cost effective and rugged hardware when compared with other approaches but also allows precise characterisation of individual grains of material. In this paper the imaging system is briefly described and the parameters it measures discussed. Both cluster and discriminant analyses are performed to establish the suitability of the measured parameters for authenticity study and simple fuzzy logic is implemented based on the findings. Tests are performed, using rice as an example, to evaluate the performance of the system for authenticity testing and encouraging results are achieved.

Keywords: Granular food, rice, imaging, particle size distribution, fuzzy logic, authentication, classification

1. Introduction

The requirement for grading granular materials is well known in the food handling industry. Such materials range from ground products such as sugar and flour, through grains or beans such as rice and coffee, to fruit and vegetable produce such as apples, melons and potatoes. The range of sizes represented by these products is large, ranging from a tiny grain of flour to fruits as large as melons. In the past such food products were graded by passing through sieves, sizing plates or other mechanical means. More recently digital imaging has been recognised as a promising technique, capable of meeting this demand in a non-contact manner. In this respect imaging systems have already been applied to material grading [1] and commercial systems are available. Such systems are also capable of determining the quality of a material sample through study of the percentage of abnormally small particles or grains present that may be considered to be broken. Basic grading and simple quality determinations are not, however, the only use of imaging based granular foodstuff analysis. There have been instances in recent years of dishonest material suppliers adulterating their wares with cheap, lower quality, grains. This is particularly true in the commodity food markets such as rice [2] where such practices could have major financial ramifications. In the example of rice it is possible to authenticate material through DNA testing and

[1]Author to whom any correspondence should be addressed, E-mail: y.yan@kent.ac.uk

electronic nose based methods but this is time consuming and expensive. There is clearly a need for a quick, convenient and low-cost system capable of such authentication.

The authors have already developed a digital imaging system for accurate size analysis of particulate materials [3]. This system was not originally designed for use with food products but should be applicable here, the present work representing an investigation into its usefulness for this application. It is believed that this system, being originally intended to accurately size very small particles, is capable of providing considerably higher accuracy and consistency than commercial imaging based food graders (although, as details of these systems are not in the public domain, this belief cannot be quantified). This consistent and accurate sizing opens up the possibility of in-depth analysis of measured material parameters which may be used, through the application of natural algorithms, to identify the material in question and therefore act as an authentication system. Whilst even this work is not entirely new, previous systems reported have been extremely costly and unsuited to convenient transportation from site to site. It is believed that the imaging system discussed here could represent a compact, low-cost alternative to such systems, placing emphasis of novel software processing rather than complex optical and imaging hardware. Such a system could meet a real need that is emerging in the food industry.

2. Measurement Principles

2.1 Imaging Hardware

As already indicated the imaging system used here has been discussed in depth elsewhere [3]. Despite this a brief overview will be presented here in the interests of convenience and in order that the measured parameters of interest for this application are highlighted.

One of the main benefits of the novel processing algorithms used by the present system is that they allow the use of a relatively low resolution CCTV board type camera. Also a simple front lighting arrangement may be used instead of more common shadow imaging techniques [4]. Both of these qualities lead to a compact and low cost physical implementation. Figure 1 shows the imaging arrangement use for the present work. It can be seen that a ring light is used for illumination and particles are laid on a flat objective. It should be noted that such a system could very easily be used for on-line work where particles move in a flat plane, such as in rice grading machines. It should be noted that a fairly wide lens angle is used in the interests of compactness and that the resulting distortion is eliminated through appropriate image processing.

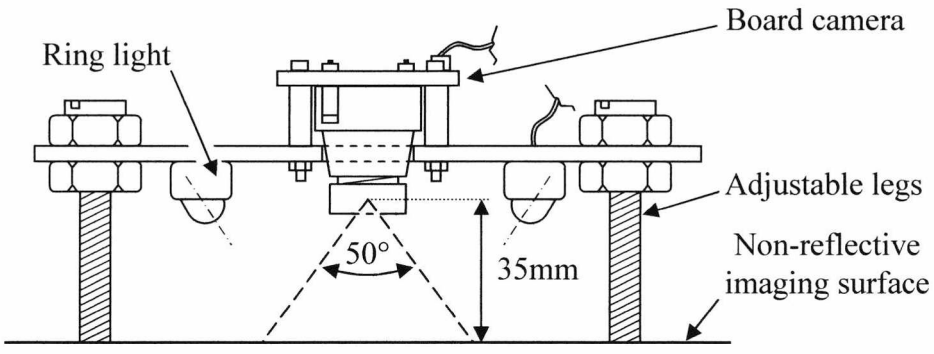

Figure 1. Imaging arrangement.

2.2 Software Processing

Once images of material are available it is necessary to separate the individual particles or grains from image background. Since particles will be imaged against a contrasting background this could be accomplished with simple thresholding. Thresholding, however, has its limitations – perceived particle size may change dramatically with selected threshold value due to particle boundary gradients. This problem may be seen in figure 2 where a maize particle image is shown. Figure 2(a) shows the location of a reasonable looking boundary location (the edge of the particle as might be defined by a particular threshold setting) and figure 2(b) shows the same image with the contrast enhanced. It is clear that the initial boundary location is no longer reasonable and that a different threshold setting could generate significant variation in measured particle size. This problem is widely accepted [5, 6] and may be considered to be the main challenge in image based sizing work. Whilst other particle separation methods have been suggested, such as gradient based techniques [4], these generally require complex processing that is time consuming to perform and unreliable with certain shapes. For this reason the simplicity of thresholding is desirable. Many techniques have been developed in the past for automatic threshold setting [7] but these are generally tailored towards reliable shape separation for optical character recognition rather than consistent and exact grain sizing. Such techniques will reliably separate grains from the background but will not necessarily generate consistent size results under varying lighting and physical conditions. The imaging system discussed here implements a novel auto threshold setting technique designed especially for particle sizing. Whilst discussed fully elsewhere [3, 8, 9] the essential points will now be introduced in the interests of convenience.

A consistent and repeatable method for establishing a suitable threshold level has been achieved in the present research through examining the characteristics of the rice images. It might easily be thought that by varying the threshold level the measured size of the particles could be varied enormously. In practice the image behavior is more complex since there is noise in the images. At very low threshold levels the noise in the image background begins to be detected as a large number of tiny particles and at high threshold levels the noisy particles break up to produce the same effect. Thus, by counting the number of detected particles at a wide range of threshold levels it is possible to establish a range of suitable threshold values by detecting the sudden increase of particle numbers at the extremes of threshold setting. The exact threshold setting within the range is not critical so long as it is consistent since linear systematic errors are easily eliminated through calibration. This method is designed to provide consistent performance under varying conditions. In general it has been found to provide simple high performance processing, achieving particle sizing accuracies in the order of 1% under variable real-world conditions.

Once the particle has been separated from the boundary the resulting binary image may be analysed in order to establish the size of particles in a number of ways. The present software identifies various particle characteristics with parameters of interest here including: Maximum particle length, area equivalent diameter [10] and aspect ratio (defined here as the ratio of the longest to the shortest dimensions that pass through each grain's geometric centre). These parameters are found for each particle and may be extracted as distributions as well as mean values.

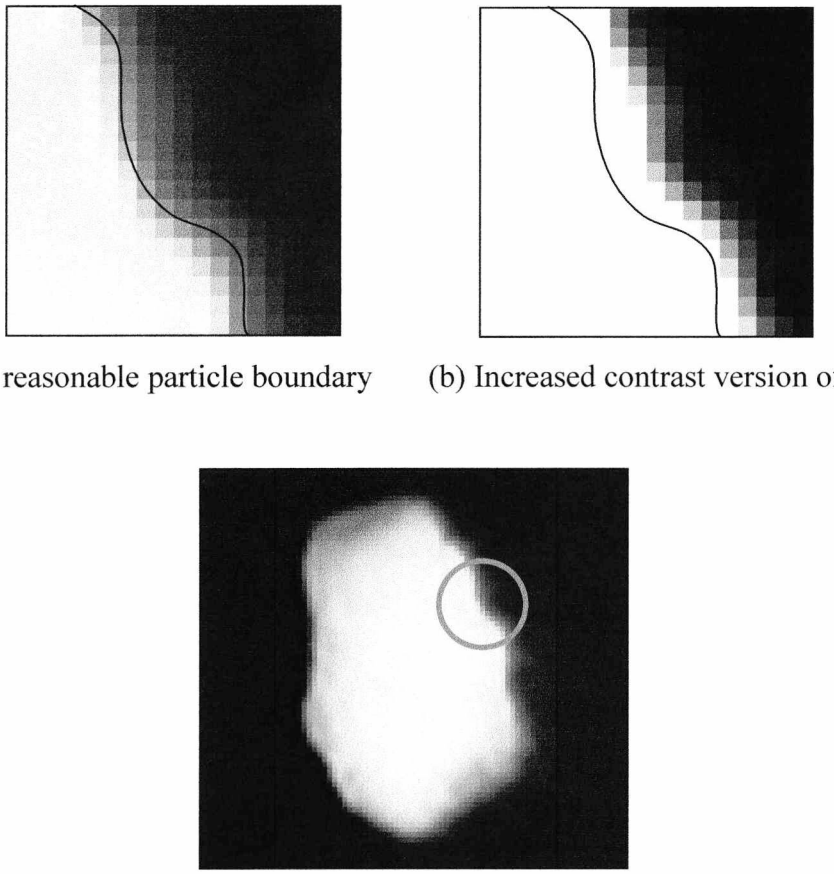

(a) A reasonable particle boundary (b) Increased contrast version of (a)

Figure 2. The difficulty in particle sizing imposed by edge gradients. The circled area is shown in close-up in (a) and (b).

3. Results and Discussion

3.1 Suitability of Measured Parameters

Just because the system measures various particle parameters it cannot be assumed that sufficient information is included in these parameters to allow meaningful differentiation between material samples and therefore successful authentication. In order to assess this, a number of different samples of rice were analysed using the system and the results assessed in order that suitability for authentication could be established. A total of 11 rice samples were used. Their types and the identifiers used in the results are shown in table 1.

Table 1. Rice types used in experiments

Rice Type	Identifiers
Basmati	B1, B2, B3, B4, B5
Thai Fragrant	T1, T2, T3
U.S. Long Grain	L1, L2, L3

Typical images of these rice samples are shown in figure 3, where the three rice types are shown as unprocessed raw images and the US long grain is also shown in its processed form with individual grains identified. Each image contains in the order of 100 grains and during testing ten images of each rice sample were analysed. This led to around 1000 grains being assessed for each result increasing the representative nature of the data [11]. Mean grain sizes for each sample and each rice group along with aspect ratio results are given in table 2. It should be noted that the images in figure 3 contain broken grains – only whole grains were used to train the fuzzy logic system (see section 3.2).

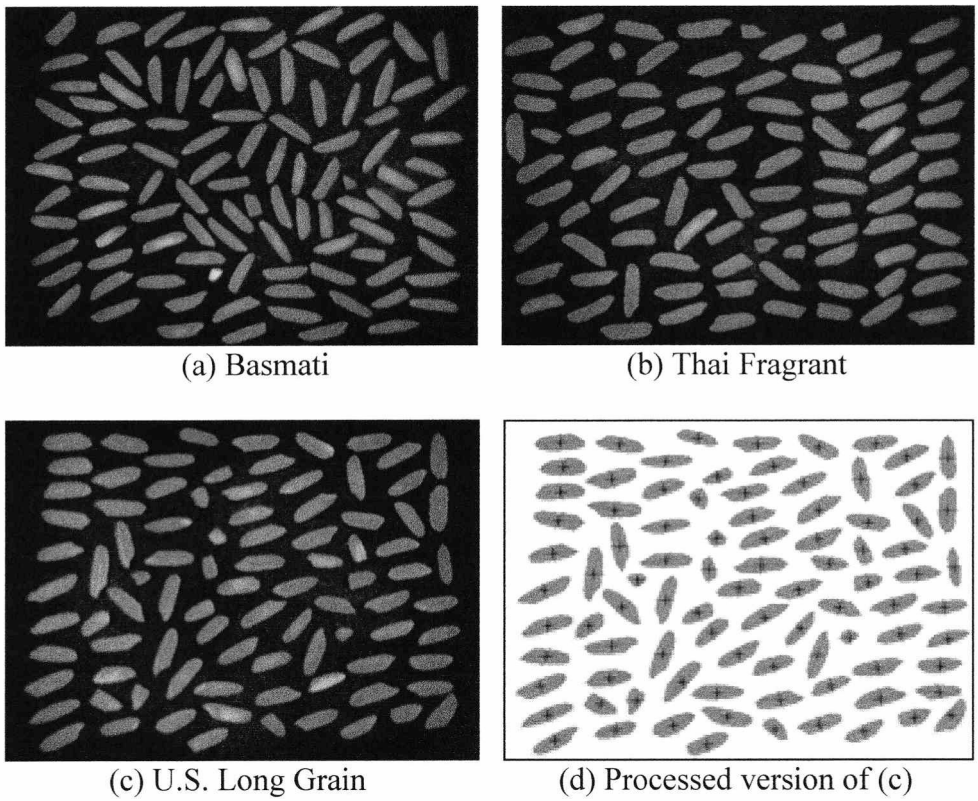

(a) Basmati (b) Thai Fragrant

(c) U.S. Long Grain (d) Processed version of (c)

Figure 3. Typical images of rice samples.

Table 2. Mean result data

Rice	Mean equivalent diameter (mm)		Mean Aspect Ratio	
	Per Sample	Per Rice	Per Sample	Per Rice
B1	3.66		0.33	
B2	3.76		0.33	
B3	3.53	3.63	0.37	0.34
B4	3.55		0.35	
B5	3.64		0.33	
T1	3.92		0.38	
T2	3.98	3.98	0.36	0.37
T3	4.04		0.36	
L1	3.53		0.47	
L2	3.50	3.57	0.48	0.46
L3	3.68		0.42	

It can be seen here that, on initial inspection, the aspect ratio would appear to give the best differentiation between types. These data are also available as distributions and the aspect ratios are presented in this form in figure 4.

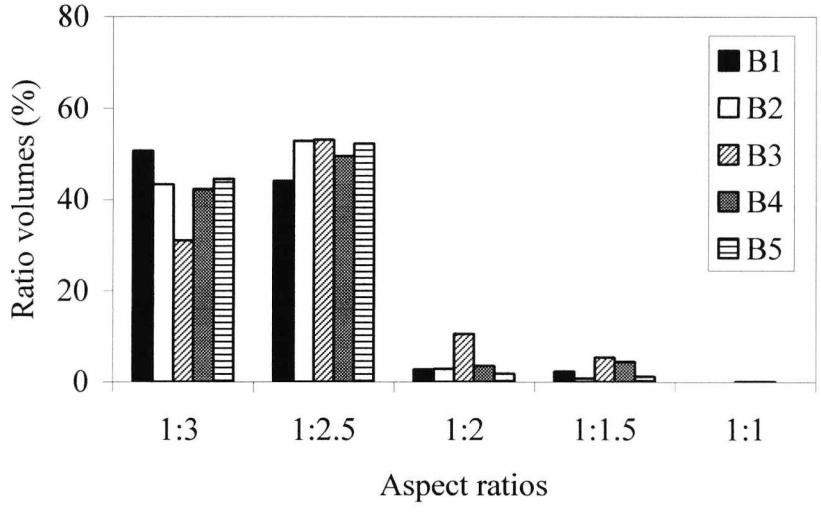

(a) Basmati

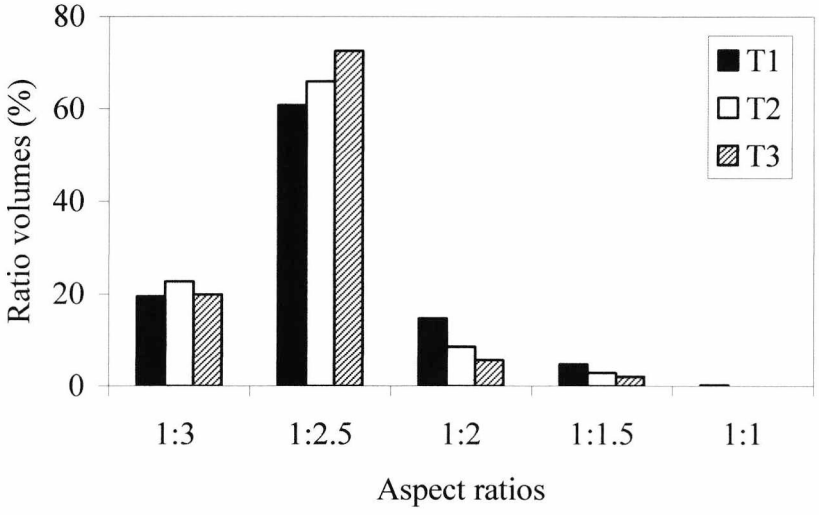

(b) Thai Fragrant

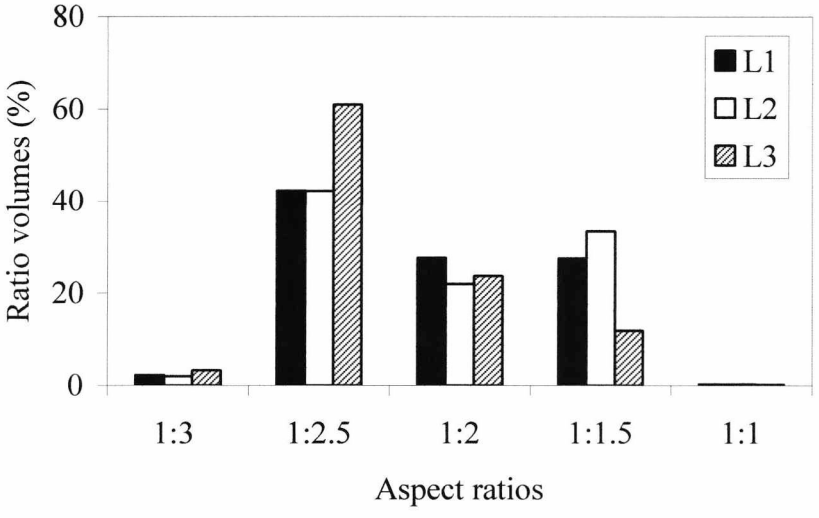

(c) U.S. Long Grain

Figure 4. Aspect ratio distributions.

Study of figure 4 reveals that within each rice type the aspect ratios are similar (though not identical) to one another. Different rice types, however, demonstrate aspect ratio distributions that are different from one another. It can be seen that these distributions represent a form of 'fingerprint' for each rice type and this suggests that the information provided by the imaging system is suitable for authentication purposes. In order to test this, cluster analysis was performed on size and aspect ratio data (Wards method). The resulting Dendrogram is shown in figure 5.

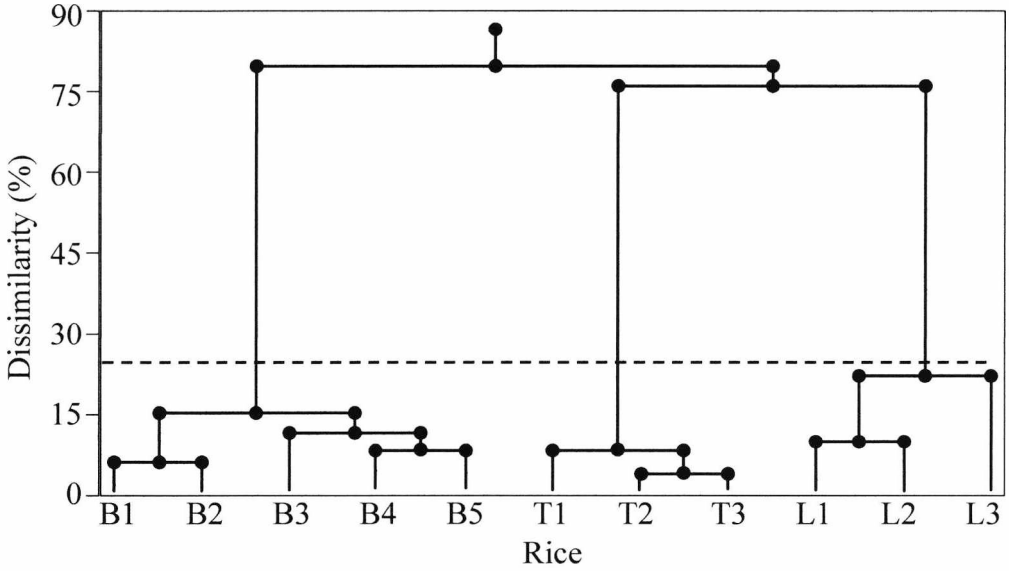

Figure 5. Dendrogram showing the structure of the data with respect to clusters

The differentiation between samples using this unsupervised analysis is extremely good. The main types of rice have been identified clearly, proving the suitability of the data for authentication studies.

3.2 Authentication with Fuzzy Logic

Measurement of parameters and subsequent data analysis is one method of achieving authentication study. It is more useful, however, for the two stages to be combined so that the imaging system identifies material types directly. This may be achieved through the application of natural algorithms and related approaches such as fuzzy logic, neural networks and self organising maps. In the present work fuzzy logic has been employed in order to investigate the practicalities of such a system.

In order to set up a fuzzy system it is necessary to define the input data that will be used. In the previous section cluster analysis was performed using all the size and aspect ratio distribution data. Whilst it would be possible to set up a fuzzy system, using all this input data it would be inefficient and time consuming and so it is preferable to identify key inputs. In this case key inputs will be particular bars in the distributions and mean values. In order to identify these key values a Principal Component Analysis (PCA) was performed. After this analysis the discriminant plot shown in figure 6 was produced. This plot is based upon the combination of a total of six parameters – as presenting the exact parameters would consume considerable space here, it is sufficient to say that bars from both aspect ratio and size distributions were used as well as the mean equivalent diameter. As an example, the 1:3 aspect ratio bar was chosen as a key parameter – this can be confirmed visually in figure 4.

With key parameters established a fuzzy logic system could be set up. Membership functions were created for each of the key parameters highlighted by the PCA. Two examples of these are shown in figure 7.

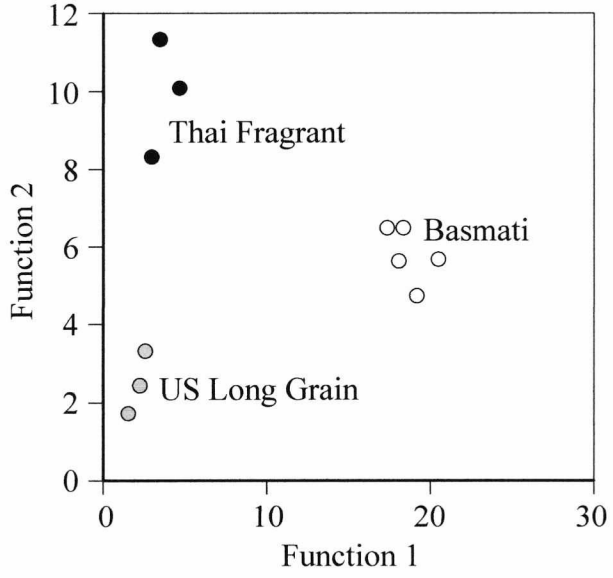

Figure 6. Discriminant plot.

The system software was programmed with the membership functions to identify the individual grains within a sample. Results are presented in the form of percentages of each rice type in the sample and also a percentage of grains that fall so far outside of any known membership function that they must be of unknown type or broken. Tests were performed to ensure correct operation. These tests consisted of mixing rice types together, using the same grains that were used during membership function programming, and observing the results. There are many possible mixture ratios and combinations and, in the interests of brevity only a small sample of typical results, using just two rice types per sample, will be shown here. These results, rounded to the nearest whole percentage, are given in table 3 where B, T, L and U represent Basmati, Thai Fragrant, U.S. Long Grain and Unknown/Broken, respectively.

Table 3. Fuzzy verification results

Rice Types	Mixture Ratio	Results (%)
Basmati / U.S. Long Grain	100/0	B=100 T=0 L=0 U=0
Basmati / U.S. Long Grain	75/25	B=76 T=0 L=24 U=0
Basmati / U.S. Long Grain	50/50	B=50 T=0 L=50 U=0
Thai Fragrant / U.S. Long Grain	100/0	B=0 T=99 L=0 U=1
Thai Fragrant / U.S. Long Grain	75/25	B=0 T=74 L=26 U=0
Thai Fragrant / U.S. Long Grain	50/50	B=0 T=49 L=50 U=1
Basmati / Thai Fragrant	75/25	B=75 T=23 L=1 U=1
Basmati / Thai Fragrant	50/50	B=50 T=49 L=0 U=1

It can be seen that verification was accomplished with almost 100% success. This is to be expected since the same grains are used here that were used to 'train' the system. Absolute 100% accuracy cannot be expected since grains may sit slightly differently from one image to the next – nevertheless, excellent results are demonstrated here.

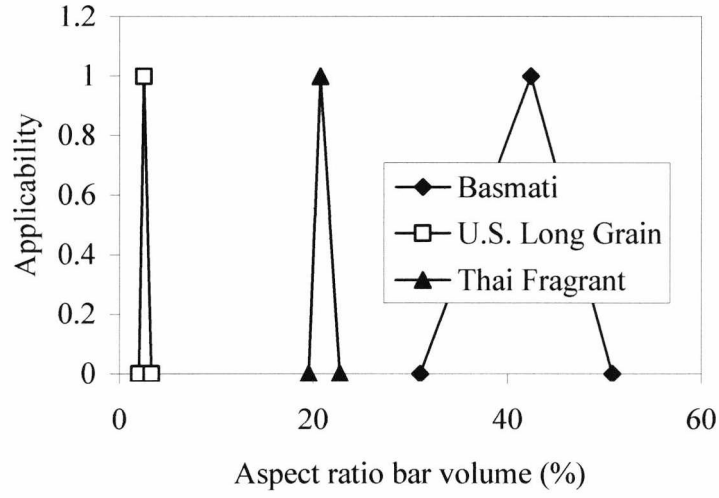

(a) 1:3 aspect ratio bar based

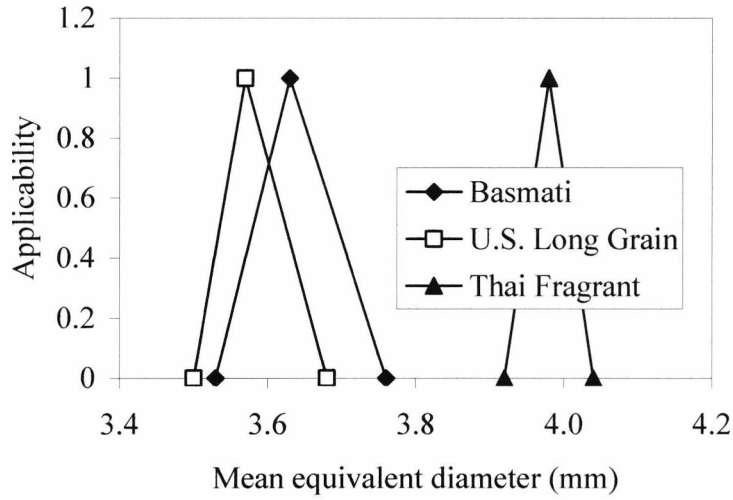

(b) Mean equivalent diameter based

Figure 7. Examples of fuzzy membership functions used.

Interestingly, unknown grains are only detected in samples containing the Thai rice. This could possibly be attributed to the very rounded nature of the grains in this sample which may have increased the slight differences from image to image. This effect only causes 1% discrepancy in results. It can also be seen that there is a very slight tendency for some Thai grains to be detected as U.S. Long Grain. This is only apparent for a very small percentage of the time and is not a problem.

The results given above were conducted in the interests of verification – a system that can only operate with the material samples used to train it is of no use. In view of this further tests were conducted using the same materials, employing only whole, well formed, grains that were not present in the training set. These results are shown in table 4.

Table 4. Fuzzy analysis of whole non-training grains

Rice Types	Mixture Ratio	Results (%)
Basmati / U.S. Long Grain	100/0	B=98 T=0 L=0 U=2
Basmati / U.S. Long Grain	75/25	B=72 T=0 L=21 U=7
Basmati / U.S. Long Grain	50/50	B=48 T=0 L=43 U=9
Thai Fragrant / U.S. Long Grain	100/0	B=0 T=95 L=4 U=1
Thai Fragrant / U.S. Long Grain	75/25	B=0 T=71 L=22 U=7
Thai Fragrant / U.S. Long Grain	50/50	B=0 T=43 L=47 U=10
Basmati / Thai Fragrant	75/25	B=75 T=20 L=3 U=2
Basmati / Thai Fragrant	50/50	B=49 T=43 L=3 U=5

The results in table 4 imply that the accuracy of recognition is not as high as seen in the verification tests (table 3) but is still extremely good. The U.S. Long Grains seem to show the greatest tendency for poor detection here despite the lack of broken grains in the samples used. This could be attributed to the possible presence of more than one variety of rice within the particular sample used. There is evidence here of the same tendency for some Thai grains to be detected as U.S. Long Grain that was seen before. The Basmati sample shows greatest accuracy with a remarkable 98% recognised correctly for a pure sample of whole grains and continued high accuracy for the mixes. In general the results here are very encouraging with a clear indication of the contents of the samples being generated. It is also interesting to test the system with samples of raw, unsorted material, containing broken and malformed grains. These results are shown in table 5.

Table 5. Fuzzy analysis of real samples

Rice Types	Mixture Ratio	Results (%)
Basmati / U.S. Long Grain	100/0	B=93 T=1 L=0 U=6
Basmati / U.S. Long Grain	75/25	B=68 T=0 L=15 U=17
Basmati / U.S. Long Grain	50/50	B=48 T=0 L=40 U=12
Thai Fragrant / U.S. Long Grain	100/0	B=0 T=91 L=2 U=7
Thai Fragrant / U.S. Long Grain	75/25	B=0 T=70 L=17 U=13
Thai Fragrant / U.S. Long Grain	50/50	B=0 T=42 L=40 U=18
Thai Fragrant / U.S. Long Grain	0/100	B=0 T=0 L=79 U=21
Basmati / Thai Fragrant	75/25	B=70 T=22 L=1 U=7
Basmati / Thai Fragrant	50/50	B=49 T=43 L=1 U=7

As Table 5 shows the results of analysing real samples (including broken and malformed grains) the unknown/broken grains detected here are, understandably, more frequent. Results featuring U.S. Long Grain always show the highest unknown/broken values, with the 100% long grain sample featuring 21% of unknown/broken grains. This can be verified visually by observing the typical image shown in figure 3 where approximately 23% of the grains are broken or malformed – this is clearly of the same magnitude as the results shown in table 5 (the table 5 results were not generated solely using the images of figure 3 – these images are typical examples). Basmati continues to give good results here with 93% detection accuracy for an unmixed sample and 6% of grains unknown or broken. Visual inspection of typical images gave a value of around 5% unknown/broken, falling in-line with the value found here. There is a single incidence of basmati grains being detected as

Thai Fragrant but this is not a continuing trend. Thai Fragrant continues to be partly detected as U.S. Long Grain although accuracy of detection for a pure sample is still excellent at 91% for a pure sample with 7% unknown/broken. Once again, visual inspection confirms this value with approximately 8% of unknown/broken grains in evidence (visual inspections are partly subjective, especially if grain damage is slight).

4. Conclusions

Analysis of a set of parameters measured using the imaging system has suggested that these parameters are eminently suitable for material authentication. Both cluster analysis and PCA have been applied in order to support this fact. Fuzzy logic results have suggested that the system can consistently operate with around 1% recognition error using the same material that was used for training (though not the exact same images which would, of course, result in 100% accuracy). Under real conditions, with different samples, accuracy is reduced and whilst no precise error level can be defined in this case results were typically within around 5-10% of the expected values. There is some tendency for a small amount of cross detection between rice types (e.g. Thai Fragrant being detected as U.S. Long Grain) and it is possible that this behaviour could be improved through the use of larger training data sets – i.e. more rice images used during training. The detection of broken and malformed grains within samples appears to be reliable.

The low-cost imaging system that was used in this work is clearly capable of providing sufficient data for successful rice authentication within the scope of the results presented here. There is no reason to presume that similar results would not be recorded with other grains and granular food products. Whilst the fuzzy logic experiments here have concentrated on distinguishing one type of rice from another the clear branching produced during cluster analysis (figure 5), the well separated clusters produced by PCA and the clear differentiation potential of some of the recorded parameters (figure 7a) all point to the fact that it may be possible to distinguish between different varieties of the same rice. This promises many applications in authentication and quality control in terms of rice age and the possible detection of deoxynivalenol contamination. It is possible that the present technique could lead to a compact and cost-effective instrument, capable of operation in the field, which may become a valuable tool, complementing more complex techniques such as DNA analysis, for authentication and quality control of numerous food products.

References

[1] Dalen G. V., 'Determination of the size distribution and percentage of broken kernels of rice using flatbed scanning and image analysis', Food Research International, vol.37, pp.51-58, 2004

[2] Lewis L., 'Japans rice label scandal reveals grain of truth', The London Times, November 15, 2003

[3] Carter R. M., Yan Y., 'On-line particle sizing of pulverised and granular fuels using digital imaging techniques'. Measurement Science and Technology, Vol. 14, pp. 1099-1109, 2003

[4] Nishino K., Kato H., Torii K., 'Stereo imaging for simultaneous measurement of size and velocity of particles in dispersed two-phase flow', Measurement Science and Technology, vol. 11, pp633-645, 2000

[5] Kim I. G., Lee S. Y., 'A simple technique for counting and sizing spray drops using digital image processing', Experiments in Thermal Fluid Science, vol. 3, pp214-221, 1990
[6] Kumar R., Kannan S., 'Drop size measurement in a two-phase swirling flow using image processing techniques', Int. J. Heat Mass Transfer, vol. 37, pp559-570, 1994
[7] Sankur B., Sezgin M., 'Image thresholding techniques: a survey over categories', Bogazici University, Istanbul, Turkey, 2002
[8] Carter R. M., Yan Y., 'An instrumentation system using combined sensing strategies for on-line mass flow rate measurement and particle sizing', Proceedings of IEEE Instrumentation Measurement Technology Conference 2004, vol.2, pp.864-868, Como, Italy, 18-20 May 2004
[9] Carter R. M., Yan Y., 'Concurrent measurement of mass flow rate and size distribution of pneumatically conveyed particles using combined electrostatic and digital imaging sensors', Proceedings of Sensors and Their Applications XII, Limerick, Ireland, 2-4 September 2003
[10] Black D. L., Mardson Q. M., Bonin M. P., 'Laser-based techniques for particle-size measurement: a review of sizing methods and their industrial applications', Energy Combustion Science, vol. 22, pp267-306, 1996
[11] Masuda H., Gotoh K., 'Study on the sample size required for the estimation of mean particle diameter', Advanced Powder Technology, vol. 10, pp159-173, 1999